OCS Study
BOEM 2022-078

Central Beaufort Sea Wave and Hydrodynamic Modeling Study

Report 1: Field measurements and model development

Central Beaufort Sea Wave and Hydrodynamic Modeling Study

Report 1: Field measurements and model development

February 2023

Authors:
Jeremy Kasper
Li H. Erikson
Thomas Ravens
Peter Bieniek
Anita Engelstad
Kees Nederhoff
Paul Duvoy
Stephanie Fisher
Eloise Petrone Brown
Yaman Man
Borja Reguero

Prepared under Cooperative Agreement
M17AC00020
by
Alaska Center for Energy and Power
University of Alaska Fairbanks
1764 Tanana Loop
Fairbanks, AK 99775

and

Civil Engineering Department
University of Alaska Anchorage
(EIB) 301P
2900 Spirit Way
Anchorage, AK 99508

Prepared under Interagency Agreement
M17PG00046
by
U.S. Geological Survey
Pacific Coastal and Marine Science Center
2885 Mission Street
Santa Cruz, CA 95060

DISCLAIMER

Study collaboration and funding were provided by the U.S. Department of the Interior, Bureau of Ocean Energy Management (BOEM), Environmental Studies Program, Washington, DC, under Agreement Number M17AC00020 with University of Alaska and through Intra-Agency Agreement Number M17PG00046 with the U.S. Geological Survey Pacific Coastal and Marine Science Center.

This report has been technically reviewed by BOEM, and it has been approved for publication. This report has been peer reviewed and approved for publication consistent with USGS Fundamental Science Practices (https://pubs.usgs.gov/circ/1367/). The views and conclusions contained in this document are those of the authors and should not be interpreted as representing the opinions or policies of BOEM. Any use of trade, firm, or product names is for descriptive purposes only and does not imply endorsement or recommendation by the U.S. Government.

CITATION

Kasper J, Erikson LH, Ravens T, Bieniek, P, Englestad A, Nederhoff K, Duvoy P, Fisher S, Petrone Brown E, Yaman M, Reguero B (University of Alaska, Fairbanks and Anchorage, AK; U.S. Geological Survey, Santa Cruz, CA; Deltares-USA; University of California Santa Cruz). 2023. Central Beaufort Sea wave and hydrodynamic modeling study. Report 1: Field measurements and model development. Anchorage (AK): U.S. Department of the Interior, Bureau of Ocean Energy Management. 100 p. Report No.: OCS Study BOEM 2022-078. Contract No.: M17AC00020 and IAA No. M17PG00046.

ABOUT THE COVER

A calm day in Foggy Island Bay amidst scientific data collection. Photo credit: Jeremy Kasper, 2020.

ACKNOWLEDGMENTS

JK led the field data collection campaigns. LE led the model developments in Section 2. TR led the coastal change modeling in Section 3. PB led the dynamic atmospheric downscaling. PD, SF, and EPB processed the field data. Wave, hydrodynamic, and sediment transport models were developed and implemented by KN, AE, and LE. BR computed the representative sea states. All authors contributed to the writing of the report. In-kind funding to further support this study was provided by the USGS Coastal and Marine Hazards Program (CMHRP) for LE and by the University of California Santa Cruz for BR. We thank Heather Crowley, Thomas Kilpatrick, and Caryn Smith at BOEM and Babak Tehranirad at USGS for their thoughtful reviews. LE additionally wishes to thank Chris Flanary, Diana Bull, and William Eymold for collaboration on the CMIP5 circum-Arctic wave model simulations.

Contents

List of Figures

List of Tables

List of Abbreviations and Acronyms

ADCP	acoustic Doppler current profiler
ADV	acoustic Doppler velocimeter
BOEM	Bureau of Ocean Energy Management
cm	centimeter(s)
CTD	conductivity/temperature/depth
CTP	conductivity/temperature/pressure
DPP	Development and Production Plan
DWDB	downscaled wave database
GMT	Greenwich mean time
GNSS	global navigation satellite system
GPS	global positioning system
IARC	International Arctic Research Center
kg	kilogram(s)
km	kilometer(s)
LDI	Liberty Development Island
m	meter(s)
MAE	Mean absolute error
MBES	multibeam bathymetric echo sounder
RMSE	root-mean-square error
SCI	scatter index
s	seconds
TSS	total suspended solids
UAA	University of Alaska Anchorage
UAF	University of Alaska Fairbanks
USGS	U.S. Geological Survey
VMDS	vessel mounted data acquisition system

1 Introduction

Renewed interest in nearshore oil exploration and production in the shallow waters of the Central Beaufort Sea Shelf has created a need to advance our understanding of the past, current, and future atmospheric and oceanographic conditions. At the time of writing this report, Hilcorp Alaska LLC has received BOEM approval for an oil and gas Development and Production Plan (DPP) that includes the construction of the Liberty Drilling Island (LDI) in Foggy Island Bay located within Stefansson Sound, circa 30 km east of Prudhoe Bay (Figure 1.1). The aim of this study is to investigate how longer periods of open water, decreased sea ice, and changes in ocean and atmospheric conditions might affect wave and storm surge conditions, sediment transport patterns, and coastal erosion rates within Foggy Island Bay as well as the potential influence of the offshore artificial island on sediment transport patterns.

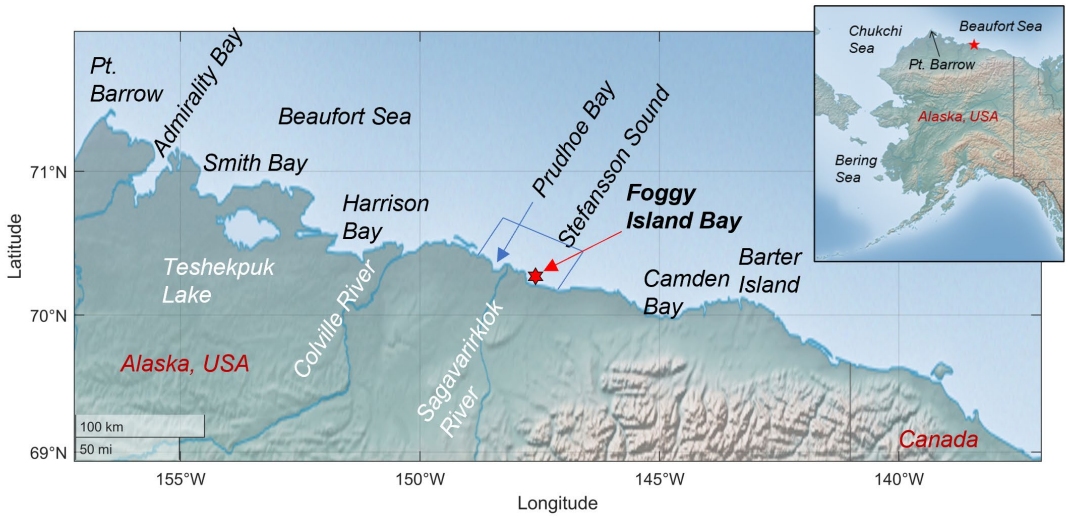

Figure 1.1 Map of the Alaska Beaufort Sea coast, showing major rivers, Stefansson Sound, and the Foggy Island Bay study site.
Red star denotes the location of Foggy Island Bay and approximate bounds of Figure 1.2. Shaded relief basemap created with Mathworks™ MATLAB ver. 2022a and *Natural Earth* blended with a land cover palette (https://www.naturalearthdata.com/).

The study presented here included the collection of field data in 2018 through 2020 and the development, calibration, and validation of a suite of numerical models that simulate waves, hydrodynamics, and sediment transport within Foggy Island Bay and shoreline change along the mainland coast of the Bay. Model results of the hindcast period from 1979 through 2019, supported by and in combination with both historical and the newly acquired 2018 – 2020 field measurements, elucidate on the physical oceanographic processes within the Bay that are relevant to development and management, such as the influence of the LDI construction on sediment transport patterns. The hindcast runs are additionally used to calibrate and evaluate model uncertainty. The calibrated models are then applied for the future period to develop time series of wave and hydrodynamic conditions from 2020 through 2050 and the effect on shoreline change rates and sediment transport patterns within Foggy Island Bay, with and without the LDI construction.

This report (Report 1 of a 2-part series) provides a synopsis of field measurements and model setup, calibration, and validation with a focus on the field measurements, the hindcast period, forcing conditions

for the projection time-period, and projected coastal change. Report 2 describes results and findings of model production runs that were done to compute summary wave statistics and sediment transport patterns within Foggy Island Bay with and without the LDI construction for the entirety of the hindcast (1979 – 2019) and projection time-periods (2020 – 2050).

1.1 Environmental Setting

Foggy Island Bay is relatively shallow with a mean water depth of ~7 m and is sheltered by several offshore shoals and barrier island complexes along the seaward portions of Stefansson Sound (Figure 1.2). Within and to the west of Foggy Island Bay, exists a relatively unique and isolated marine algal flora benthic community in an area termed the Boulder Patch (Figure 1.2: Dunton et al. 1982, Wilce and Dunton 2014). The Boulder Patch is located 6 – 8 km from the coast and covers roughly 125 km^2. In contrast to the soft-sediment seabed present throughout most of the north Alaskan coast, the Boulder Patch seabed is a rare occurrence of localized gravel, cobbles, and small boulders (generally < 1 m diameter). These localized rock accumulations, the result of Pleistocene glacial deposits (Dunton et al. 1982), provide habitat for attached vegetation and a diverse fauna (Dunton and Schonberg 2000). Under past conditions, along-shore currents have been reported to be sufficiently strong to maintain the Boulder Patch as a non-depositional environment, despite its immediate proximity to the Sagavanirktok River Delta (Dunton et al. 1982, Wilce and Dunton 2014).

Meteorological conditions and sea ice along the Beaufort Sea coast are a major controlling factor in determining the physical environment of the entire region. The region experiences subfreezing temperatures for nine months of the year when air temperatures can reach to -45°C (Overland, 2009) and with strong winds can produce even colder wind chills. The mean annual temperature is ~-10°C, but during the summer months, air temperatures occasionally exceed +20°C (Curchitser et al. 2018). Air temperature controls the timing of sea ice formation and breakup.

Historically, the annual return of landfast sea ice initially forms in the shallows of Foggy Island Bay in late September and early October, then slowly thickens and grows seaward until the Beaufort Shelf is ice-covered by the second or third week of October (Coastal Frontiers, 2016). In the fall, when the floating ice sheet grows seaward, the ice gradually attaches to the near-freezing seabed, gradually thickens to ~1.7 to 2.2 m by mid-March, and then remains constant through early to mid-June (Mahoney et al. 2014; Curchister et al. 2018). However, over the course of the satellite era (1979 to present), when consistent sea ice observations have been collected, it is evident that the timing of ice break-up and freeze-up are occurring earlier and later in the year, respectively (Figure 1.3). In the 1980s (blue colored lines in Fig 1.3), partial sea ice cover was intermittently present during the summer and early fall months (July-September), but by 2019, little to no sea ice was common between August to mid-October. The open-water season (here defined as when sea ice concentrations are less than 15%) has on average increased from 60 days in 1979 to nearly 160 days in 2019.

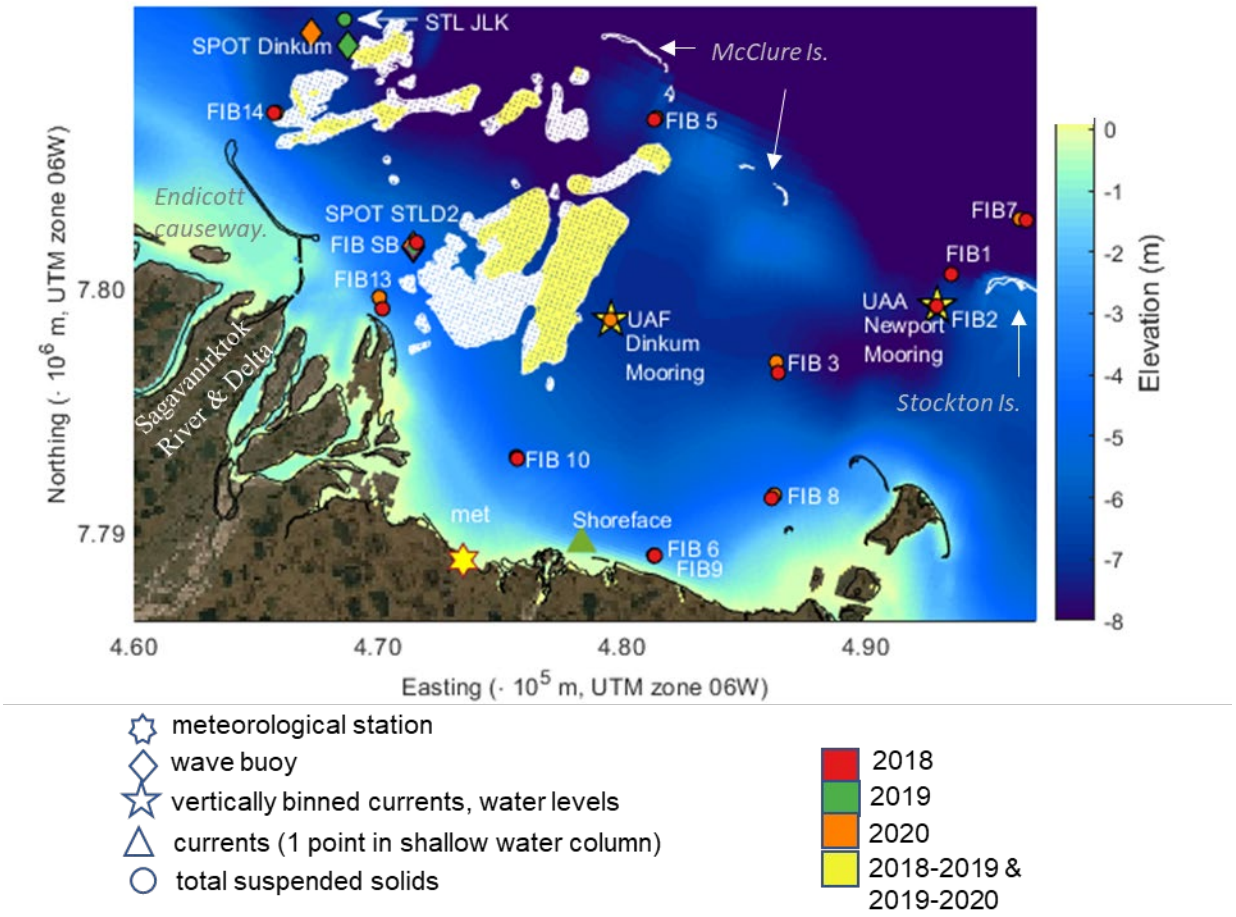

Figure 1.2 Map showing locations of key 2018 – 2020 monitoring stations in Foggy Island Bay and immediate surrounding area.

Black diamond denotes the location of the proposed construction of the Liberty Development Island (Hilcorp, 2017). The Boulder Patch area is represented by white and yellow stippling, denoting light (10-25% coverage) and heavy (>25%) boulder cover, respectively, as measured by geologic surveys conducted in 1980 and 1987 (Toimil and England, 1980; Coastal Frontiers and LGL, 1998; Bonsell and Dunton, 2018). Colored symbols denote key monitoring locations and years that data were collected as part of this study for use in model calibration and validation.

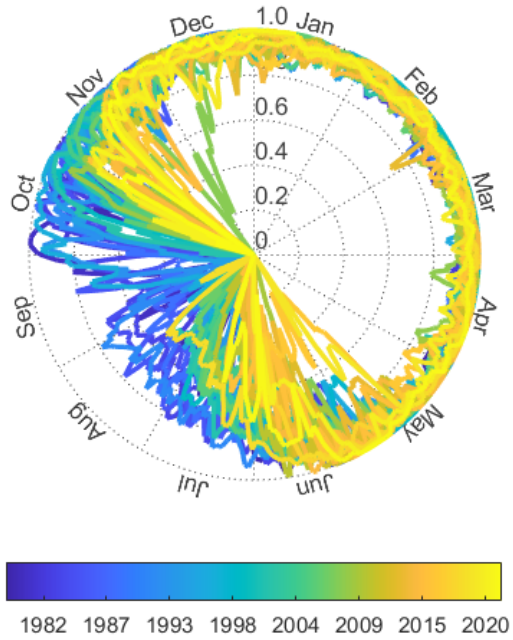

Figure 1.3 Spiral plot showing daily sea ice concentrations at Foggy Island Bay from 1979 through 2021. Radial axis shows the fraction of ice cover (0 to 1, completely ice free to full coverage). Colors denote the year.

Data source: ERA5 derived from satellite passive microwave brightness temperatures (https://cds.climate.copernicus.eu/). Sea ice concentration is defined as the fraction of a pixel in a satellite image that is covered with sea ice. Source data are 15 – 60 km resolution, depending on the year and available satellite data. Data have been gridded to 25 km resolution.

During spring/early summer break-up, coastal rivers discharge warmer fresh sediment-laden water at the coast, hastening nearshore melting. The peak discharge period for most rivers is short and occurs in late May to early June when 60 to 80% of the total annual discharge often occurs within a two-week period (Bjerklie, 1993; Kasper, 2010). Fresh water from the Sagavanirktok River flows both underneath the sea ice and penetrates the ice cover from above through stress or thermal cracks and seal breathing holes, forming "strudel" vortices which can scour bottom sediments (Dickins et al. 2011). This process freshens the surface waters and disperses large amounts of sediment and organic matter into the water column (Reimnitz and Kempema 1983).

Wind directions in the region are largely bimodal, blowing from either east or west. Winds from the east are more persistent in the early summer season (June-July), with a tendency for increased frequency of winds from the west as the season progresses. Wind speeds during open water season are about 10 m/s, with maximum winds typically occurring in September/October (Figure B.2 in Appendix B). Historical trends in storm tracks generally do not show coherent signals, but there is evidence that strong or extreme storms are becoming more frequent in the Arctic basin, especially in winter (Rinke et al. 2017; Sepp and Jaagus 2011). For the Foggy Island Bay region, enhanced storminess is corroborated by a trend toward a weakened Beaufort High (Kenigson and Timmermans 2021) and recent years that experienced a "collapse" of the same feature (Ballinger et al. 2021, Moore et al. 2017 2018).

Surface winds have a strong influence on nearshore currents, waves, water level variations, ice floes and ultimately drive sediment transport and coastal processes (Erikson et al. 2020). Wave directions are similarly bimodal as the wind, with a predominant direction from the east (Erikson et al. 2020; Hamilton et al. 2021; Bieniek et al. 2022). During the frozen months from early to mid-November through May, no wave action is observed. However, once ice concentrations start to decrease, waves begin to emerge in the region (e.g., Thomson et al. 2016). High wave heights increase throughout the open water season due to higher wind speeds and larger fetch. The highest wave heights are typically observed in late October when wind speeds are high and ice is not yet present (e.g., Stopa et al. 2016).

During the open water season, pressure gradients and winds are the main driving force of surface and subsurface currents and mixing of the water column (Weingartner et al. 2017). Because wind stress is proportional to the square of wind speed and tides are feeble, periods of strong winds (storms) dominate the circulation in this region. Summer (July – September) winds along this east-west oriented portion of the Beaufort coast are nearly always alongshore. Over-water easterly winds (winds that blow from the east) are 10 to 50% more frequent compared to westerlies (winds that blow from the west) (Fig. 1.4) and cause surface waters to advect seaward under the influence of the Coriolis acceleration. The Coriolis effect veers currents to the right of the wind stress, and in Stefansson Sound during times of freshwater fluvial inputs, this rotation transports less saline surface water offshore. The offshore transported surface waters are replaced by subsurface colder and more saline water, a process known as coastal upwelling (e.g., Hachmeister and Short, 1985; Danek and Tourtellote 1987). In contrast, when the winds blow from the west (westerlies), offshore surface waters are pushed landward, effectively raising the water level near the shore, setting up an across-shore pressure gradient that causes nearshore bottom waters to move seaward, a process referred to as downwelling. Downwelling conditions typically result in a vertically mixed water column nearshore.

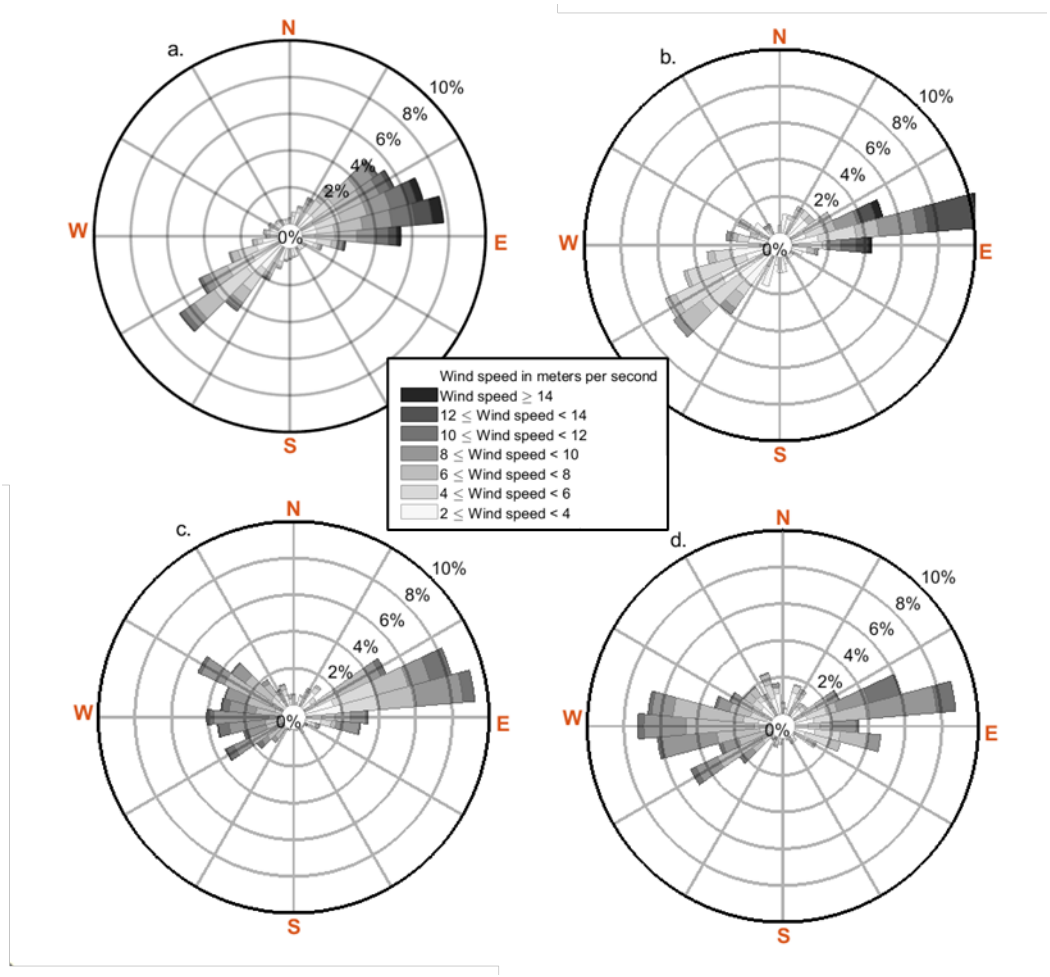

Figure 1.4 Wind rose plots of measurements obtained at one land-based and two over-water sites within Stefansson Sound in 2019 and 2020.

(a.) Land-based meteorological station: July 27, 2019, at 00:00 hours through December 20, 2020, at 23:00 hours. (b.) Same as in (a.) but for the open water time-period that overlaps with the over-water measurements at the Dinkum and STLD2 wave buoys in 2019 (August 20 (first measurement at met station) – September 9). (c.) Over-water wind measurements obtained with the SPOT 0156 buoy at STLD2: August 6 22:35 hours through September 9 19:21, 2019. (d.) Over-water wind measurements obtained with the SPOT 0107 buoy at Dinkum: August 7 18:41 hours through September 9 18:44, 2019. Winds that blow from the east are ~10% (Dinkum) and ~50% (land-based and STLD2) more frequent compared to winds blowing from the west. Station locations are shown in Figure 1.2. All times are Greenwich Mean Time (GMT = Alaska Standard time + 9 hours) here and throughout the report.

2 Field Measurements

2.1 Methods

2.1.1 Field Work

Field work for this effort was carried out in the summers of 2018, 2019 and 2020. A brief synopsis of each season is included below. More details on the field campaigns are included in field reports provided in Appendix A. The Research Vessel (R/V) *Ukpik* was chartered to carry out this work.

2.1.1.1 2018 Field Summary

In 2018 field work took place between July 15 – 30. Approximately 224 km were surveyed using a Multibeam Bathymetric Echosounder (MBES, seafloor elevations and backscatter strength) within and adjacent to Foggy Island Bay. In addition, two bottom-founded oceanographic moorings equipped with internally recording instruments to measure currents, surface wave spectra, near-bottom velocity and hydrography, and water levels were deployed within Foggy Island Bay. A third, seasonally deployed shallow water instrument package, the "shoreface" mooring was deployed to capture wave and water level fluctuations in the shallows at the southern end of Foggy Island Bay. The shoreface mooring was recovered during a short field trip in September 2018. A fourth mooring, the "LTER Cross Island mooring" equipped with sensors to measure currents, wave spectra, and near bottom hydrography, was deployed offshore of Cross Island as part of the Beaufort Lagoons LTER project. The goal of this latter mooring deployment was to provide data useful to both the Beaufort Lagoons LTER project and this project. The LTER Cross Island mooring could not be located in 2019, as it was likely crushed or moved beyond the range of the acoustic release by sea ice. Water column hydrographic information were collected (conductivity/temperature/pressure, or CTP) during the 2018 cruise to provide sound speed corrections for multibeam sonar data. A total of 14 CTP + discrete water samples stations (using a Seabird Electronics SBE25/55 CTD + Water Sampler) and 50 sensor-only stations (using an AML Oceanographic CTP+Turbidity probe) were completed during the cruise. A total of 18 seafloor samples were also collected during the 2018 cruise using a "Ponar"-type grab for seafloor sediment size characterization.

In addition to the hydrographic data collection, a meteorological station was deployed at the southern end of Foggy Island Bay (70.204075°N, 147.701386°W; E 473,490 m, N 7,788,784 UTM zone 06W). The station was equipped with sensors to measure barometric pressure, temperature, and relative humidity. Two cameras mounted on the met station were configured to capture images of the nearby coast once per hour.

2.1.1.1 2019 Field Summary

In 2019, work took place on the R/V *Ukpik*, between August 16 – 26. Between August 22 and August 25, work on other projects was carried out from the same platform. For this study, MBES data were gathered between August 12 and August 29 within and outside of Foggy Island Bay. A pole-mounted Acoustic Doppler Current Profiler (ADCP) was also deployed from the gunwale of the R/V *Ukpik* to measure water column velocity and acoustic backscatter. The two bottom-founded oceanographic moorings deployed in

2018, were recovered to download data and refresh batteries and then were redeployed. The seasonally deployed shallow water shoreface mooring was also deployed at this time.

Water column conductivity, temperature, and pressure (CTP) data were also collected for sound speed corrections for the MBES. A total of 3 water samples were collected in 2019 using a 3.2 liter Van Dorn water sampler and 4 "sensor only" stations were completed during the 2019 cruise (using an AML Oceanographic CTP + Turbidity probe). The met station installed in the prior year was serviced in 2019. Two Sofar Ocean "Spotter" buoys (SPOT 0107 and SPOT 0156) for measuring winds and surface wave spectra in real-time were deployed on August 6 and 7 and retrieved on September 7, 2019, at the same time the shoreface mooring was recovered. Finally, a small unoccupied aerial vehicle was also deployed at this time to image coastal position and topography at the southern end of Foggy Island Bay.

2.1.1.2 2020 Field Summary

In 2020 field work took place between August 3 – 13. Between August 3 – 6, work on other projects was carried out from the same platform. The two bottom-founded oceanographic moorings deployed in prior years were recovered at this time. A pole-mounted Acoustic Doppler Current Profiler (ADCP) was deployed from the gunwale of the R/V *Ukpik* to measure water column velocity and acoustic backscatter for the duration of the 2020 cruise. Water column hydrographic information were collected (conductivity, temperature, and pressure) during the cruise as well. A total of 31 discrete water samples were collected in 2020 using a 3.2 liter Van Dorn water sampler and 41 "sensor only" stations were completed during the 2020 cruise (using an AML Oceanographic CTP + Turbidity probe). An unoccupied aerial vehicle was deployed to image coastal position and topography near the met station. In addition to the work between August 3 – 13, two Sofar Ocean Spotter buoys (SPOT 0158 and SPOT 0159) and the shoreface mooring were deployed prior to the start of the cruise from the R/V *Ukpik* on July 16. The Spotter buoys and shoreface mooring were recovered on August 12, 2020. Locations of these sensors used in model calibration and validation are shown in Figures 1.2 and 2.1. Parameters used in model calibration and validation are shown in Table 2.1.

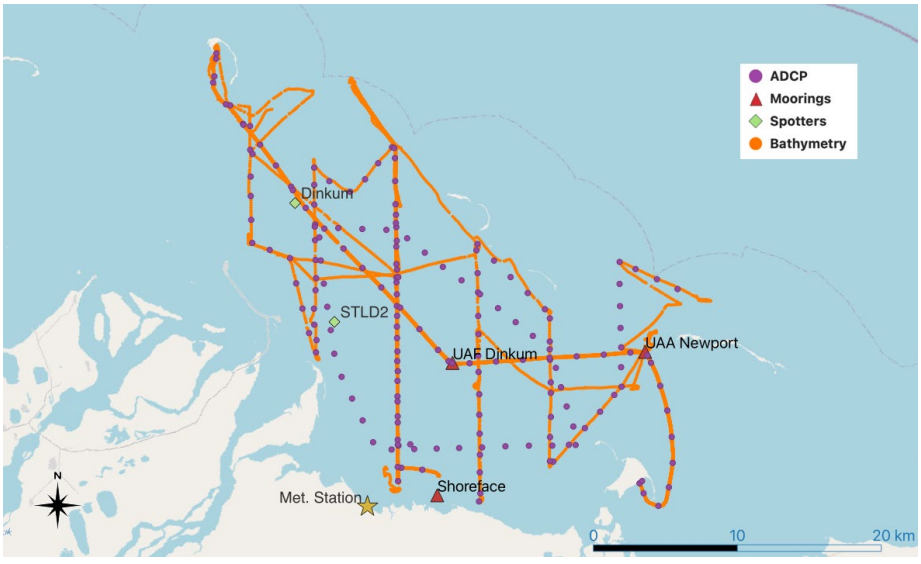

Figure 2.1 Overview map of field measurements employed in calibration and validation of the wave-hydrodynamic-sediment transport model.

Table 2.1 Summary of measurement data collected as part of this study that were used for model calibration and validation of the wave-hydro-sediment transport model.

Identifier	Temporal space	Use			Instrument(s)	Parameter(s)	Date start (UTC)	Date end (UTC)	Latitude (DD)	Longitude (DD)	Depth (m)
		input	calib.	valid.							
multibeam	instantaneous	x			MBES	bathymetry	2018				-
ponar bottom grabs	instantaneous	x			bottom grabs	bed composition	2018-07-10	2018-07-10	Table 2.3		-
UAF Sofar Spotter0156	time series		x		SPOT_0156	waves	2019-08-07	2019-09-09	70.31882	-147.76044	3.2
UAF Sofar Spotter0107	time series		x		SPOT 0107	waves	2019-08-07	2019-09-09	70.39285	-147.83368	7.0
UAA Newport Mooring 2018-2019	time series		x	x	RDI ADCP CTP	currents, waterlevels	2018-07-20	2019-08-18	70.29879	-147.18768	6.5
UAF Dinkum mooring 2018-2019	time series		x	x	RDI ADCP CTP	currents, waterlevels	2018-07-20	2019-08-18	70.29313	-147.54327	6.6
Shoreface TempMooring 2018	time series		x	x	vector ADV	near bottom velocities	2018-07-20	2018-09-25	70.21078	-147.57308	1.1
SBE25/SBE55+LISST	instantaneous				SBE25/SBE55+ LISST	TSS; requires calibration	2018-07-10	2018-07-10	16_stations		-
UAA Newpor tMooring 2019-2020	time series			x	RDI ADCP CTP	currents, waterlevels, near bottom velocities	2019-08-19	2020-08-08	70.29920	-147.18763	6.5
UAF Dinkum mooring 2019-2020	time series			x	RDI ADCP CTP	currents; waterlevels	2019-08-19	2020-08-08	70.29315	-147.54302	7.1
Shoreface TempMooring 2019	time series			x	vector ADV	near bottom velocities	2019-08-19	2019-09-07	70.21109	-147.57363	0.6
Shoreface TempMooring 2020	time series			x	vector ADV	near bottom velocities	2020-07-16	2020-08-11	71.21092	-147.57323	0.6
T1	instantaneous			x	Niskin bottle	TSS	2019-08-18	2019-08-18	70.46321	-147.64539	surface
STLJLK (surface)	instantaneous			x	Niskin bottle	TSS	2019-09-11	2019-09-11	70.40239	-147.83824	surface
STLJLK (7m depth)	instantaneous			x	Niskin bottle	TSS	2019-09-11	2019-09-11	70.40286	-147.84153	7.0

Table 2.1 continued

Identifier	Temporal space	Use			Instrument(s)	Parameter(s)	Date start (UTC)	Date end (UTC)	Latitude (DD)	Longitude (DD)	Depth (m)
		input	calib.	valid.							
UAF Sofar Spotter0518	time series			x	SPOT_0518	waves	2020-07-16	2020-08-12	70.39757	-147.87539	6.4
UAF Sofar Spotter0519	time series			x	Sofar_Spotter_buoy_0519	waves	2020-07-16	2020-08-12	70.30639 70.31921	-147.72044 -147.76081	4.6
FIB1FIB16	instantaneous		x		Niskin bottle	TSS	2020-08-01	2020-08-11	Table 2.5		-

2.1.2 Precision and uncertainty

The reader is referred to manufacturer specifications for instrument precision and uncertainty.

2.2 Measurement Synopsis

2.2.1 Bathymetry and Topography

Bathymetric track line data collected for this study were compared to National Ocean Service (NOS) data collected in 1945 – 1953 (Zimmerman et al. 2021). NOS post-World War II data provide the most comprehensive bathymetric coverage to date, with a resolution of <100 m distanced soundings throughout most of Stefansson Sound, and therefore are used as a reference. Comparison of depth measurements show consistent (81%) but low deposition east of the Boulder Patch. A large area of high deposition was measured landward of the Narwhal/ Jeanette/ McClure barrier islands (total number of points n = 1,527, mean and 1 standard deviation $\bar{x}$ = -1.26 m, ± 0.88; Figure 2.2), and the expanded footprint of the 2018 data showed this high deposition extended west to Dinkum Sands, and Cross and Bartlett islands. The highest deposition (n = 654, $\bar{x}$ = -2.29 m, ± 1.18) in the Dinkum Sands region occur immediately to the west of the area of the high erosion (n = 391, $\bar{x}$ = 1.90 m, ± 0.76). However, the deposition rates are within the range of uncertainty considering measurement precision of both datasets but particularly the post-World War II data for which reporting was given in increments of one foot (±30 cm).

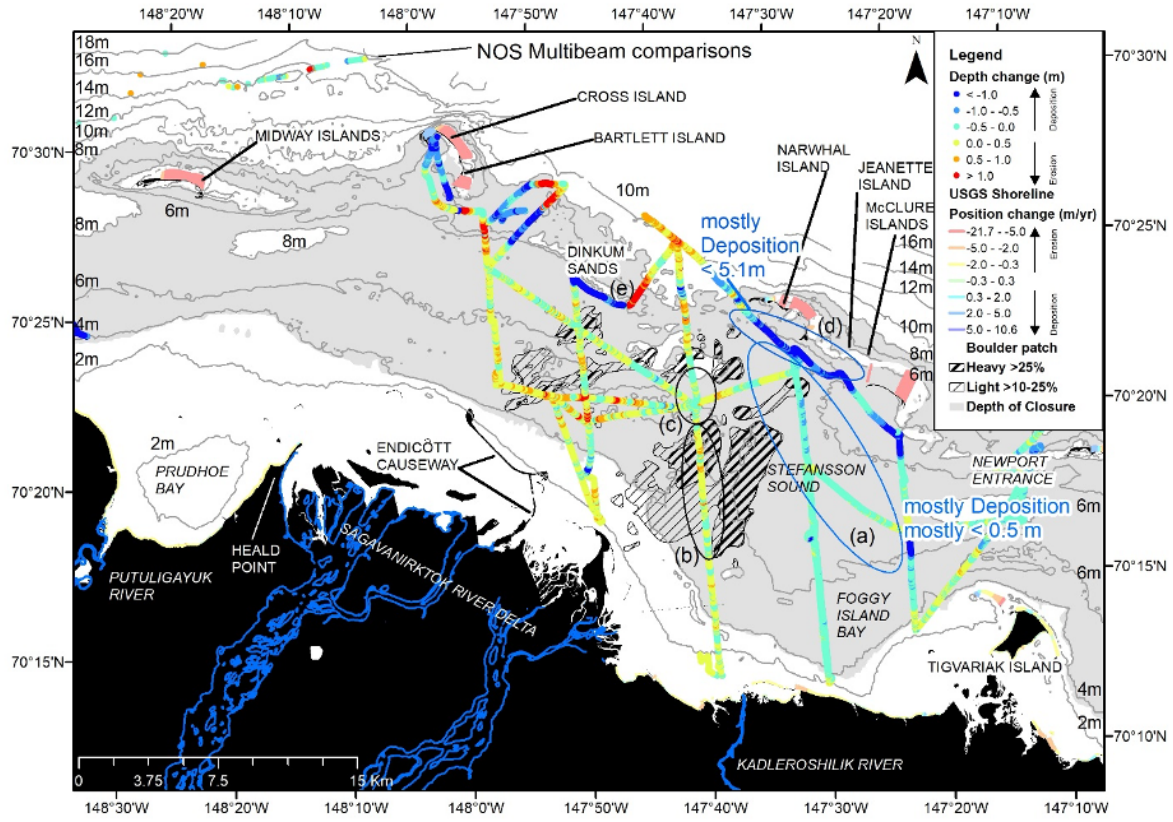

Figure 2.2 Map showing depth differences between post-World War II hydrographic (1945-53) and 2018 MBES survey collected for this project. Warm colors (yellow to red) indicate erosion, whereas cool colors (teal to blue) indicate deposition. Bathymetric contours were generated from post-World War II era NOS smooth sheet bathymetry raster, shoreline change is from Gibbs and Richmond (2017), and the land is from IFSAR (Interferometric Synthetic Aperture Radar: https://elevation.alaska.gov/). Boulder Patch rock coverage digitized from Bonsell and Dunton (2018). Figure reproduced from Zimmerman et al. (2022).

A drone survey of the area immediately surrounding the met-station was successfully executed in 2019 using a UAF-owned DJI Phantom 3 Uncrewed Aerial Vehicle (UAV). The digital elevation map produced using the Agisoft photogrammetric software package of the surveyed area is shown in Figure 2.3. Three survey lines were occupied using a survey-grade GPS system (a UAF-owned Trimble R10 base and rover). Repeat aerial surveys are planned to assess near coast elevation changes.

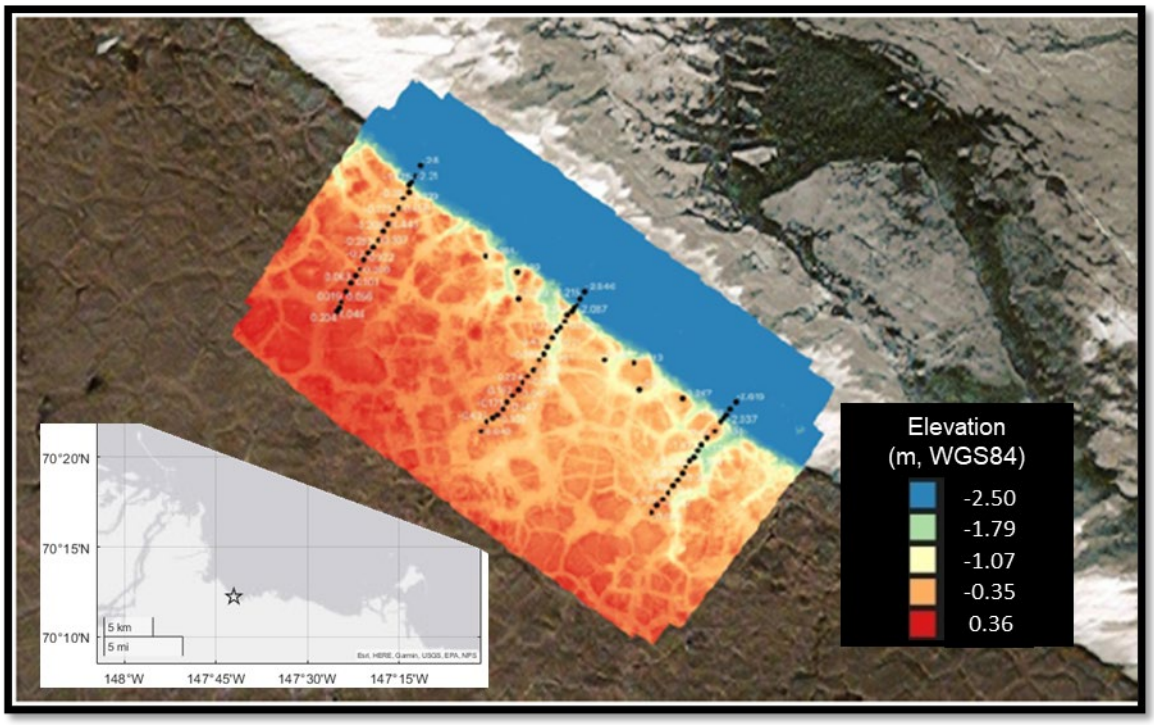

Figure 2.3 Map showing topographic elevations produced from the 2019 UAV photogrammetry survey.
Black dots denote locations of GNSS transects. Inset shows the location of the aerial survey.

2.2.2 Sediment character

Seabed sediment grab samples collected within and immediately west of Foggy Island Bay in 2018 primarily consisted of silt and sand (Table 2.2). Visual inspection of grab samples report silt and mixed silt with sand or rocks at 5 of the 16 sites, whereas sand and mixtures thereof were noted at 10 of the 16 sites. Median grain sizes (d_{50}, including all fractions) ranged from 0.01 mm to 1.56 mm with an average of 0.23 ± 0.45 mm (Table 2.2 and Figure 2.4a). The grab sample collected at FIB3, located in the approximate center of Foggy Island Bay and outside the Boulder Patch region, contained silt and rocks with a sieve analysis showing a d_{50}= 1.56 mm and 90th percentile passing (d_{90}) at 14.17 mm. A similarly high d_{90} was measured at FIB5, located within the Boulder Patch area. Overall, 90th percentile grain sizes (d_{90}, including all fractions) ranged from 0.14 to 14.84 mm with a mean of 2.12 ± 5.33 mm (Table 2.2 and Figure 2.4b).

Table 2.2 List of sediment grain size and description of seabed samples collected within Stefansson Sound in July 2018.

Name	Latitude (DD)	Longitude (DD)	Date	Visual Description [pre-sorting]	d_{50} [mm]	d_{90} [mm]
FIB 1	70.29932	-147.18681	July 21, 2018	sand	0.11	0.24
FIB 2	70.22792	-147.36653	July 21, 2018	sand	0.13	0.22
FIB 3	70.31373	-147.49621	July 21, 2018	silt with rocks	1.56	14.17
FIB 4	70.24251	-147.64471	July 22, 2018	---	0.12	0.23
FIB 5	70.29576	-147.64484	July 22, 2018	silt with rocks	0.37	14.84
FIB 6	70.40370	-147.64656	July 22, 2018	sand	0.13	0.23
FIB 7	70.41986	-147.79726	July 22, 2018	---	0.14	0.24
FIB 8	70.39996	-147.79713	July 22, 2018	sand	0.14	0.23
FIB 9	70.34500	-147.79457	July 22, 2018	sand	0.14	0.36
FIB 10	70.31763	-147.79630	July 22, 2018	sand	0.14	0.24
FIB 11	70.29669	-147.79380	July 22, 2018	silt	0.01	0.51
FIB 12	70.36002	-147.84536	July 22, 2018	sand	0.14	0.25
FIB 13	70.39898	-147.91583	July 22, 2018	sand	0.13	0.19
FIB 14	70.42614	-147.91481	July 22, 2018	sand with small pebbles	0.23	1.53
FIB 15	70.45346	-147.91867	July 22, 2018	silty sand	0.08	0.14
FIB 18	70.35673	-147.83833	July 25, 2018	silt	0.12	0.33
Minimum					0.01	0.14
Maximum					1.56	14.84
Mean					0.23	2.12
St. Dev.					0.45	5.33

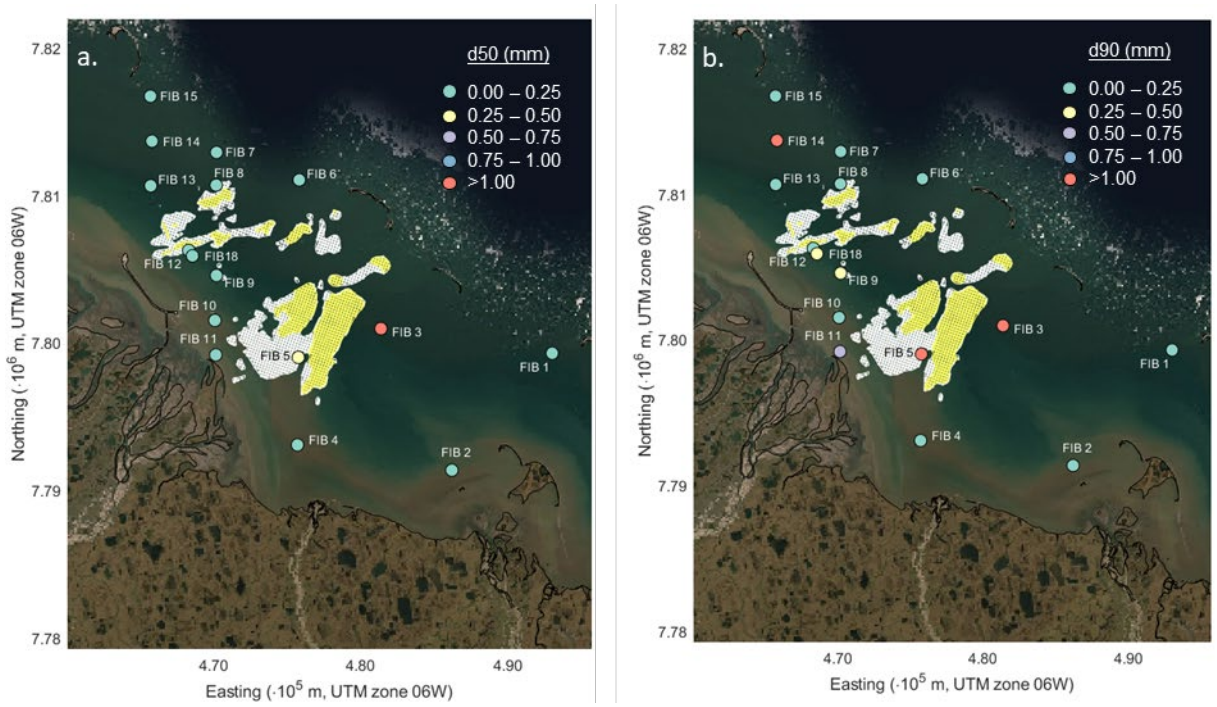

Figure 2.4 Maps showing seabed sediment grain sizes within Stefansson Sound in 2018.
Measured a.) median (d_{50}) and b.) 90th percentile (d_{90}) grain sizes of seabed grab samples. See Table 2.2 for qualitative descriptions of grab samples. Boulder Patch rock coverage is shown with yellow (> 25% cover) and white (10-25% cover) as digitized from Bonsell and Dunton (2018).

2.2.3 Waves

The 'metocean' (wave + wind) buoys in 2020 were re-deployed at the same location as in 2019 but were dragged from their original position, presumably by ice floes. Figure 2.4a shows the deployment locations in 2019 as green and blue dots. The buoys are tethered to a bottom weight, allowing movement within a diameter of ~100-150 m (example point locations of the stationary buoy in 2019 are shown in Figure 2.4b). In 2020, the buoys became untethered from the bottom weight and moved in a net westward direction (red and salmon-colored circles in Figure 2.5a).

Maximum measured wave heights in 2019 reached 2 – 2.5 m, with an incidence from the northeast (Figure 2.5c,d). Commensurate mean wave periods (T_m) were 10 – 12 s (Fig. 2.5e,f). Wave heights and mean periods are generally ~44% higher and ~16% longer at Dinkum compared to measurements at STLD2 (Fig. 2.6a,c). Most frequent incident wave directions are from the north-northwest at Dinkum, in contrast to STLD2 where the most frequent incident wave directions are from the north-northeast (compare Figures 2.5c,d).

Wave periods measured in 2020 reach more than 25 s in some instances; these are considered as outliers possibly associated with the horizontal displacement of the buoys and have been removed from Figures 2.7 and 2.8.

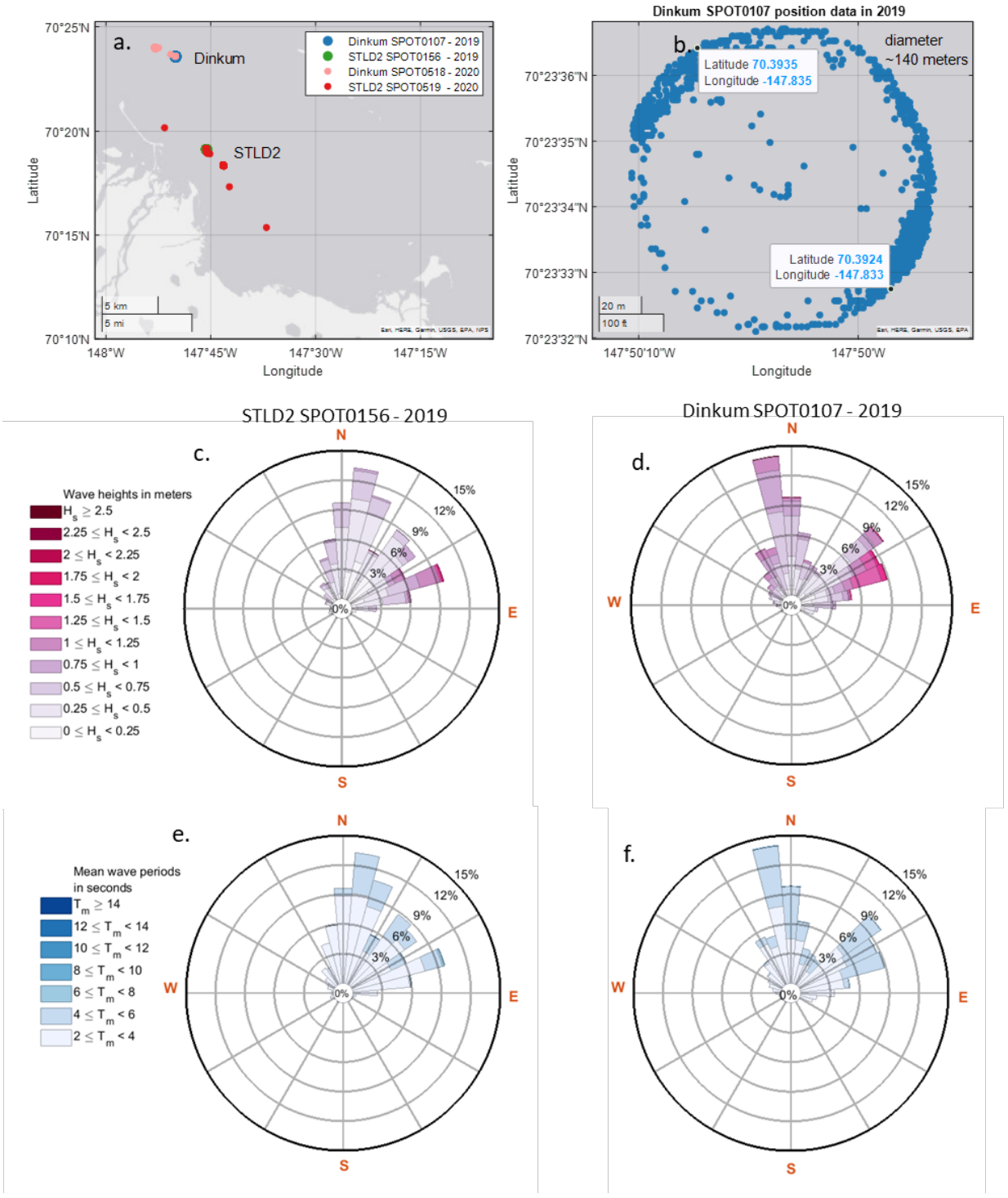

Figure 2.5 Mapped locations of buoy deployments and wave rose plots for the 2019 deployments. a) Wave buoy deployments in 2019 and 2020. Note the horizontal displacement of the buoys deployed in 2020, presumably dragged by ice floes. (b) Horizontal displacement of the tethered 2019 SPOT0156 buoy. (c,d) Wave rose of measured wave heights at SPOT0107 and SPOT0156 in August through September 2019. (e,f) Same as in (c,d) but for mean wave periods.

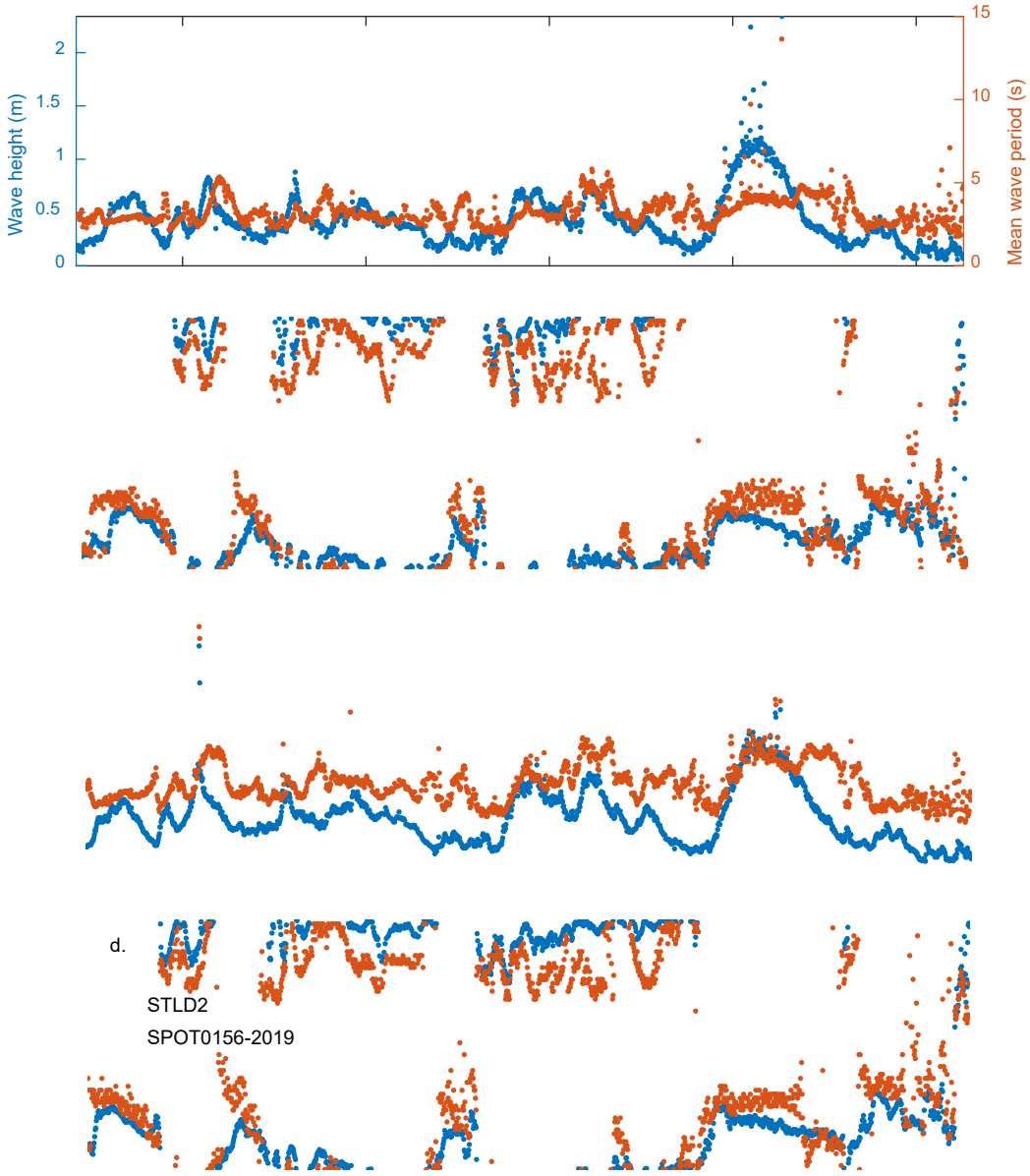

Figure 2.6 Time-series plots of measured waves and winds at the 2019 buoy deployment locations.

(a,c) Significant wave heights and mean wave periods measured at Dinkum (SPOT0107) and STLD2 (SPOT0156), respectively. (b,d) Mean incident wave directions and wind directions at Dinkum (SPOT0107) and STLD2 (SPOT0156), respectively. See Figures 1.2 and 2.5a for locations.

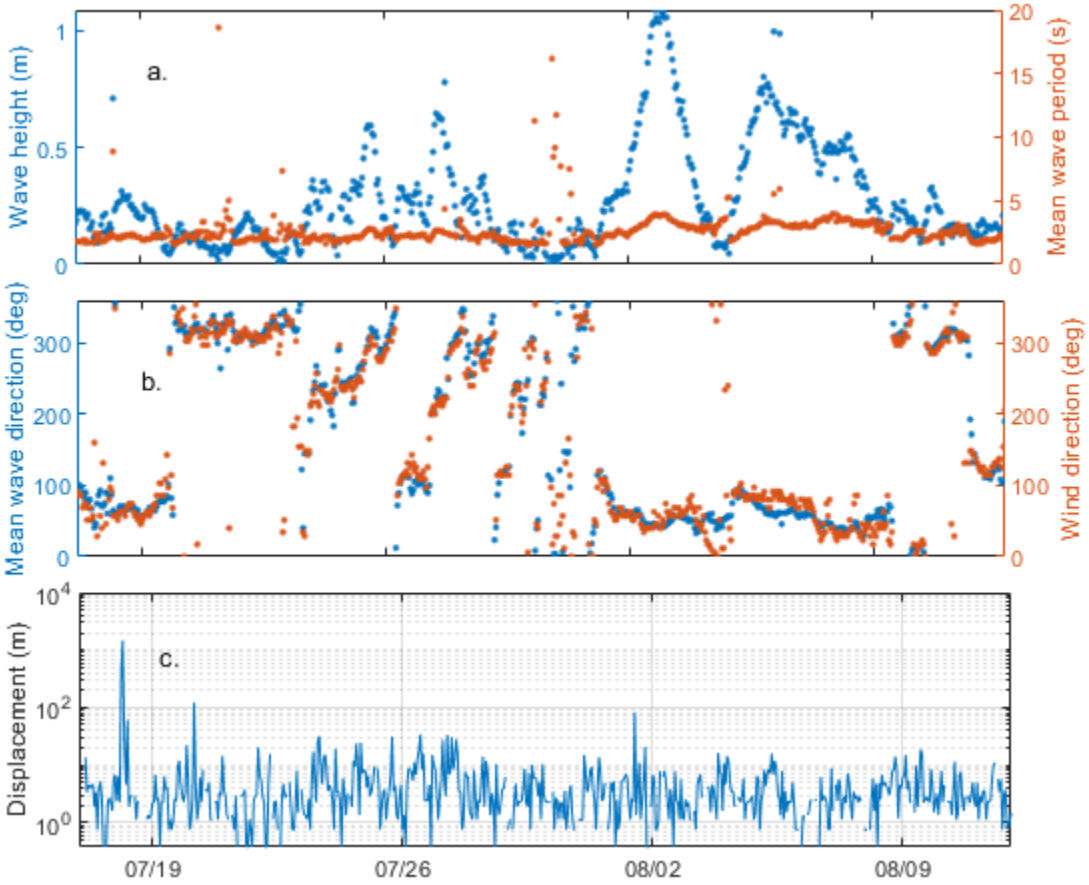

Figure 2.7 Time-series plots of measured waves, winds, and horizontal displacement of the 2020 SPOT 0158 buoy at the Dinkum site.

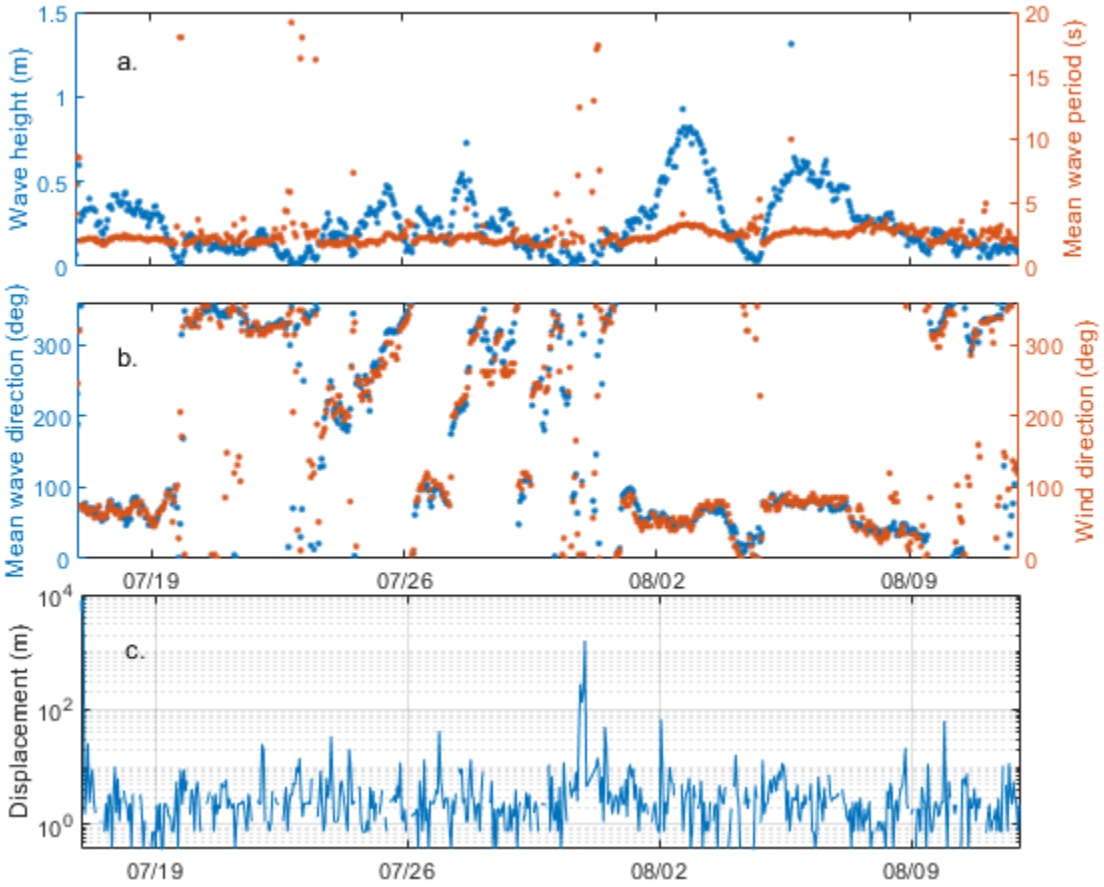

Figure 2.8 Time-series plots of measured waves, winds, and horizontal displacement of the 2020 SPOT 0159 buoy at the STLD2 site.

2.2.4 Sea ice, currents, and winds

The UAF and UAA bottom-founded moorings (see Figures 1.2 and 2.1 for locations) measured sea ice, currents, and water levels from July 20, 2018, through August 11, 2020, excepting the retrieval redeployment for servicing on August 18 and 19 in 2019. Each year-long time series provides a glimpse into the seasonal characteristics of currents and water levels in Foggy Island Bay during freeze-up, break-up, fully open water conditions, and beneath sea ice.

Sea ice thickness at each mooring was estimated following the method described in Weingartner et al. (1999). Sea ice thickness, was computed from the ADCP data as the difference between the bottom depth, Z_b (Table 2.1), and the sum of the height of the transducer above the bottom, $H_T = 0.68\ m$, and the range from the transducer at which the intensity of the reflected acoustic signal was maximum, R (e.g., $H_{ice} = [Z_b - (H_T + R)] \cdot 1.12$), where the factor 1.12 is the ratio of sea water and sea ice density. Because the ADCP bins were set to integrate acoustic signals over 0.5 m vertical bins, there is an uncertainty in the sea ice thickness of at least 0.5 m. To reduce high-frequency noise in the data resulting from the bin averaging, Weingartner et al. (1999) suggested smoothing the ice thickness time series with a 5-day running mean. The resulting time series of ice thickness from the initial deployment spanning July 20, 2018, to August 18, 2019, is shown in Figure 2.9a. The signal suggests that the onset of the winter

landfast ice season started in late October with sea ice gradually thickening until reaching a maximum thickness of ~2 m in March/April. By mid- to late-June, the thaw appears to have begun, with full break-up by late June. The sea ice thickness and timing are generally consistent with previously reported values of landfast ice formation and ablation (e.g., Envirosphere 1991; Weingartner et al. 2009, 2017). Based on field crew comments that the 2018 summer field season was difficult due to generally icy conditions, it is thought that the noisy sea ice thickness signal in August through October 2018 (Figure 2.9a) is indicative of wind-driven ice floes intermittently passing over the ADCP beams.

During winter sea ice cover, measured depth-averaged currents were generally low: 5.0 ± 1.7 and 4.8 ± 2.5 cm/s at the UAF and UAA moorings, respectively, but did reach as high as 15 cm/s on occasion (November 15, 2018 through June 15, 2019 in Figure 2.9c). Maximum currents over the course of the year were measured on August 15, 2018, and July 20, 2019, at the UAA (65 cm/s) and UAF (77 cm/s) moorings, respectively. The presence of sea ice was not recorded by either mooring at the time of maxima currents, but other peak values >40 cm/s were recorded during the 'noisy' time of the year in September and October 2018 when presumably free-moving ice floes affected the signal (circles in Figure 2.9c). During this same time-period (September and October 2018), the mean current directions were from southeast, with the UAA currents rotated ~30 º clockwise from the UAF principal axis and corresponding to steady winds from the east-southeast (~100º, Figure 2.9b). In contrast, under sea ice current directions measured at the UAF mooring appear chaotic during the winter season.

Overall, the measured depth-averaged currents were ~33% stronger at the UAF mooring compared to the UAA mooring. The difference might be attributable to the fact that the blanking distance for the UAA mooring was set at a higher value resulting in measurements only being recorded in the upper 2 m of the water column. An example of the vertical structure (shear) can be seen in Figure 3.15 presented in the model/measurement comparison section. For the most part, it is apparent that vertical structure exists primarily during times of low current speeds from the east and breaks down during times of higher current speeds (>25 cm/s) from the west and north (Figure 3.15a,c). Vertical velocities are largely uniform except within the upper parts of the water column (Figure 3.15e).

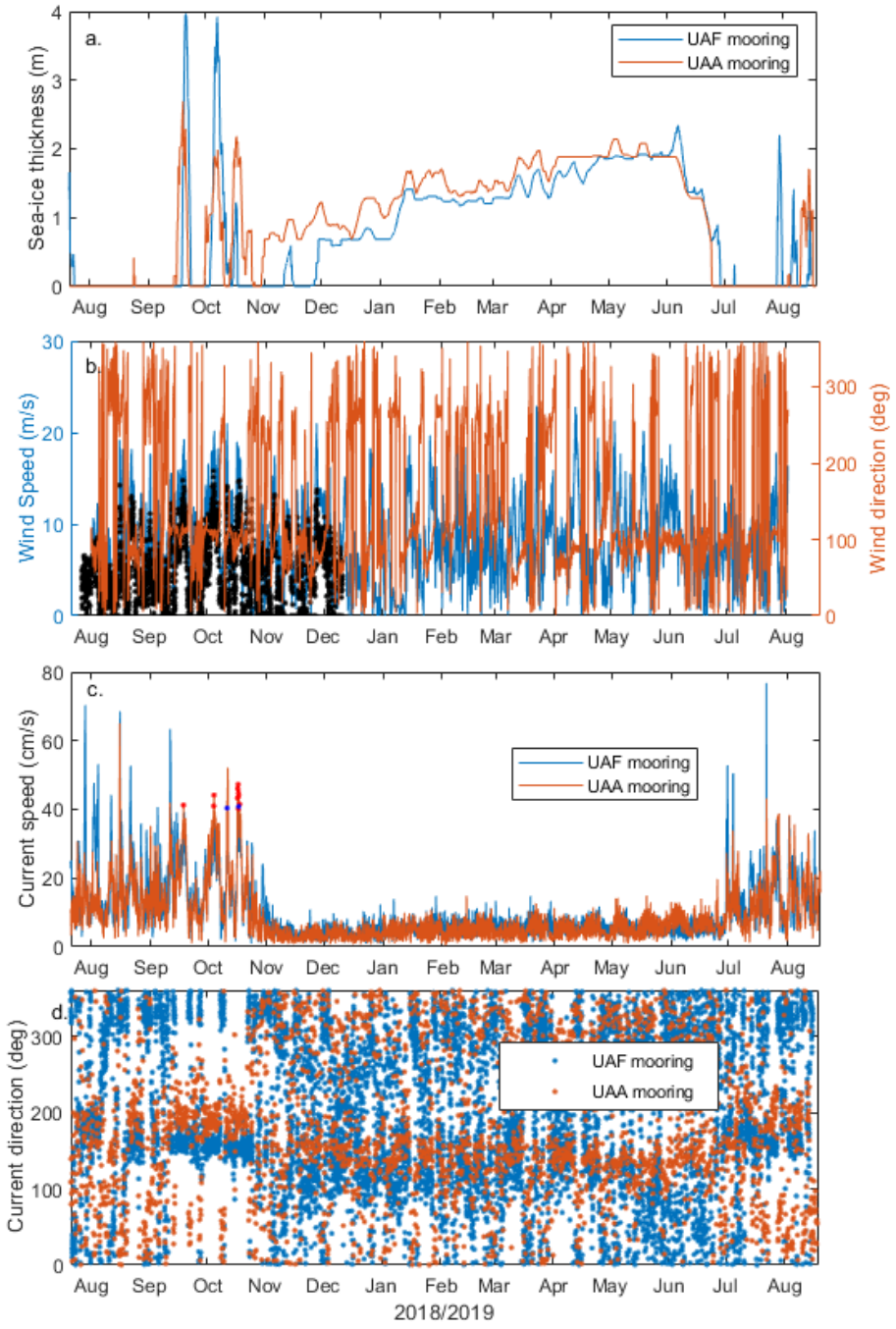

Figure 2.9 Time-series plots of depth averaged currents measured at the UAF and UAA moorings between August 2018 and August 2019.

a.) Sea ice thickness calculated from the ADCP return signal strength at the UAF mooring. (b.) Wind speed and direction measured at Prudhoe Bay tide station (NOAA station #9497645). Black dots are wind speeds measured at the Foggy Island Bay shore-based meteorological station (see Figure 1.2 for location). Wind anemometer was installed less than 2 m above the ground. No corrections for elevation have been made. (c.) Depth averaged currents measured at the UAF and UAA moorings. The weak currents from ~November through June correspond to the presence of sea ice in (a.). Small circles at peaks in September and October 2018 correspond to current speeds >40 cm/s and under the presence of sea ice. (d.) Directions of depth-averaged currents at the UAF and UAA moorings.

2.2.5 Total Suspended Solids

Total suspended solid concentrations within the water column were collected in 2018 (Figure 2.10) and many locations repeated in 2020 at which time both surface and near bed samples were collected (Tables 2.3 and 2.4). TSS concentrations in June 2018 ranged from 8 to 32 mg/L; in September of the same year, two samples were collected with one measuring 134 mg/L (first row in Table 2.3). It is unclear at this time why the sample returned such high concentration levels. Surface and near bed samples collected in 2019 ranged from 5 to 19 mg/L with the highest concentrations obtained at the UAA and UAF mooring sites. Three additional single point measurements (*T1* and *STL_JLK*) were collected in September 2019 (see Table 2.1 for locations) and measured 23 mg/L at the surface of location T1. At the *STL JLK* locations (sited approximately 100 m apart), TSS concentrations were 2 mg/L at the surface and 20 mg/L at 7 m water depth.

Figure 2.10 Map showing measured total suspended solid (TSS) concentrations and locations in 2018.

Table 2.3. List of total suspended solids measured in 2018

Name	Latitude (decimal degrees North)	Longitude (decimal degrees West)	Date	TSS (mg/L)
FIB SB	70.32078	-147.75615	25-Sep	134
FIB1	70.31060	-147.17230	20-Jul	8
FIB1	70.31060	-147.17230	20-Jul	17
FIB10	70.24170	-147.64380	22-Jul	12
FIB10	70.24170	-147.64380	22-Jul	15
FIB11	70.42780	-147.64720	22-Jul	20
FIB11	70.42780	-147.64720	22-Jul	28
FIB12	70.42020	-147.79770	22-Jul	8
FIB12	70.42020	-147.79770	22-Jul	11
FIB13	70.29620	-147.79260	22-Jul	17
FIB13	70.29620	-147.79260	22-Jul	15
FIB14	70.36770	-147.91420	23-Jul	21
FIB14	70.36770	-147.91420	23-Jul	13
FIB15	70.45350	-147.91880	23-Jul	32
FIB15	70.45350	-147.91880	23-Jul	13
FIB16	70.46850	-147.72200	25-Jul	11
FIB2	70.29890	-147.18810	20-Jul	9
FIB2	70.29890	-147.18810	20-Jul	18
FIB3	70.27410	-147.36050	20-Jul	24
FIB3	70.27410	-147.36050	20-Jul	9
FIB5	70.36680	-147.49780	20-Jul	18
FIB5	70.36680	-147.49780	20-Jul	6
FIB6	70.20640	-147.49390	20-Jul	22
FIB6	70.20640	-147.49390	20-Jul	20
FIB7	70.33050	-147.09040	21-Jul	9
FIB7	70.33050	-147.09040	21-Jul	31
FIB8	70.22790	-147.36690	21-Jul	13
FIB8	70.22790	-147.36690	21-Jul	11
FIB9	70.20650	-147.49320	21-Sep	11
FIB9	70.20650	-147.49320	21-Jul	12

Table 2.4. List of total suspended solids measured in 2020

Name	Latitude (decimal degrees North)	Longitude (decimal degrees West)	Date	Depth (m below surface)	TSS (mg/L)
FIB3	70.27800	-147.36260	11-Aug	surface	5
FIB3	70.27800	-147.36260	11-Aug	7.30	13
FIB5	70.36743	-147.49557	11-Aug	surface	3
FIB6	70.20663	-147.49418	11-Aug	surface	5
FIB6	70.20663	-147.49418	11-Aug	2.90	5
FIB7	70.33089	-147.09720	11-Aug	surface	5
FIB8	70.22908	-147.36411	11-Aug	surface	5
FIB8	70.22908	-147.36411	11-Aug	3.05	5
FIB10	70.24233	-147.64466	10-Aug	surface	8
FIB10	70.24233	-147.64466	10-Aug	4.50	7
FIB11	70.42809	-147.65094	10-Aug	surface	5
FIB13	70.30040	-147.79613	10-Aug	surface	8
FIB13	70.30040	-147.79613	10-Aug	2.75	8
FIB14	70.36784	-147.91153	10-Aug	surface	8
FIB15	70.45299	-147.91799	9-Aug	surface	4
FIB15	70.45299	-147.91799	9-Aug	7.00	5
FIB15	70.45299	-147.91799	9-Aug	7.00	4
FIB16	70.46780	-147.72162	9-Aug	surface	3
FIB16	70.46780	-147.72162	9-Aug	14.00	7
UAA	70.29878	-147.18921	8-Aug	surface	4
UAA	70.29878	-147.18921	8-Aug	6.95	19
UAF	70.29314	-147.54381	8-Aug	surface	15
UAF	70.29314	-147.54381	8-Aug	7.00	10

3 Modeling of hydrodynamics, waves, and sediment transport

In this section we describe the development and application of a model system and variants thereof to generate spatial statistics of waves and sediment transport pathways within Foggy Island Bay. This report (Report 1 of a 2-part series) provides a synopsis on the model setup, calibration, and validation for the hindcast period and describes forcing conditions for the projection time-period. Report 2 describes a schematization to derive representative sea states and implementation of model simulations, using the sediment transport model described herein, that were done to compute sediment transport patterns for the entirety of the 40-year hindcast (1979 – 2019) and 30-year projection time-periods (2020 – 2050). The following sections provide an overview of the modeling system and details of each model in that system.

3.1 Model system overview

Sediment transport patterns within Foggy Island Bay are modeled with a coupled wave-hydrodynamic-sediment transport model (Figure 3.1: Tier 2 Model C). Horizontal grid resolutions within Foggy Island Bay are 50 and 200 m for the hydrodynamic (currents and sediment transport) and wave grids, respectively. The rather fine resolution was deemed necessary to accurately represent wave transformation, currents, and sediment transport patterns within Foggy Island Bay, but at the cost of increased computation time (~30 hours runtime for a one-month long simulation, running on 3.8GHz 30 core machine),

To allow for continuous multidecadal long simulations of 40-year hindcast and 30-year projected wave conditions that are necessary for computation of time-series based statistics, the 200 m resolution wave model was additionally run as a stand-alone model without two-way communication with the hydrodynamic model (Figure 3.1: Tier 2 Models A and B). Two variants of the stand-alone Tier 2 wave model were developed and used to generate time-series statistics: the Tier 2A wave model, consists of three subsequent finer resolution grids and was implemented in 'brute-force' (continuous) mode using hourly time-steps for the entire hindcast time-period, but only using the two coarser outer and intermediate wave grids. Model Tier 2B employs the finest nested nearshore grid and calibration settings derived from the Tier 2A wave model, and using a set of representative sea-states, was used to develop nearshore wave fields at 3-hourly time-steps for the entire hindcast and projected time-periods whilst accounting for mitigation of wave-energy brought about by the presence of barrier islands. Further details can be found in Sections 3.2 and 3.5, and Table 3.1.

Two types of boundary conditions are used for the Tier 2 stand-alone and coupled models: 1) spatiotemporally varying winds, sea ice fields, and atmospheric pressures (Model Tier2C only) that are applied across the domains, and 2) time-varying waves and water levels (Model Tier2C only) that are applied at the open boundaries.

The spatiotemporally varying fields are derived from dynamically downscaled global scale atmospheric models and reanalysis products for the hindcast period (1979 – 2019) and from high-resolution climate models ($\leq 25°$) for the projection time-period (2020 – 2050).

The second set of boundary conditions, time-varying wave and water levels at the open boundaries, are derived from two separate Tier 1 models,

- an Alaska-statewide hydrodynamic model with a coastal grid resolution of ~2 km (Figure 3.1: Tier 1 hydrodynamic model), and
- circum-arctic (18 km nearshore resolution) and global- to local scale (7 km nearshore resolution) WaveWatch3 wave models and ERA5 reanalysis products (30 km resolution) (Figure 3.1: Tier 1 wave models).

The individual Tier1 and Tier 2 models are described in Sections 3.2 through 3.4 of this report. Model sensitivities to parameter settings and comparisons to observations collected as part of this study (Section 2 of this report), and prior to this study, are summarized in Section 3.5. A summary of findings is presented in Section 3.6.

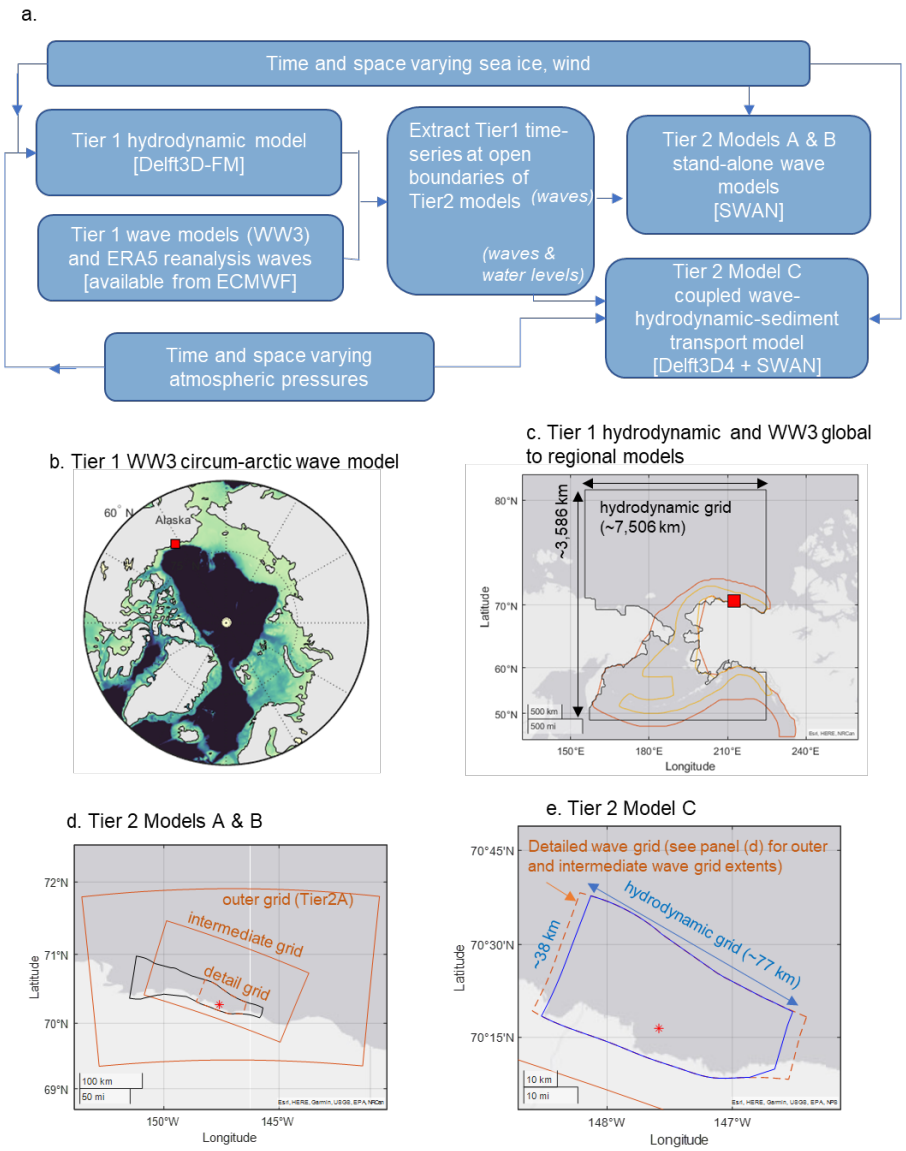

Figure 3.1 Model framework and extents of Tier 1 and nested Tier 2 models.
Overall framework and summary of models developed and employed for this study to simulate waves, hydrodynamics, and sediments transport are shown in (a.). The Tier 1 models are used to derive wave and water level boundary conditions along the sides (open boundaries) of the Tier 2 model grids. Time and space varying wind, sea ice, and atmospheric pressure fields are used as inputs across the domains of both Tiers 1 and 2. (b.) Extent of the circum-arctic Tier 1 WaveWatch3 (WW3) wave model that was used to compare hindcasted waves using 4 different wind products with that of the ERA5 reanalysis (produced by ECMWF – see text for further explanations) and additionally, to produce a projected time series of waves using winds from a 5th generation Coupled Model Intercomparison Project (CMIP) global climate model. (c.) Extents of the Tier 1 hydrodynamic model (black line) and WW3 grids (orange and yellow outlines) nested in a global-scale WW3 model. The global scale and Alaska WW3 models (developed by NOAA and formerly used as an operational forecast model) was applied to simulate historical and projected wave time series by winds from the 6th generation CMIP campaign. The red square indicates the location of Foggy Island Bay. (d.) Extents of the Tier 2 stand-alone wave model domains. Orange lines are for wave model Tier 2A. Black line shows the full extent of the Tier 2B wave model. Note that the smallest nested grid of model Tier 2A (shown with a dashed line) is identical to Tier 2B with respect to resolution and cross-shore extent. (e.) Extents of the hydrodynamic model grid (blue) and nested wave model grid (orange) in the coupled Tier 2C wave-hydrodynamic-sediment transport model. Red star denotes the preliminary LDI construction.

Table 3.1 Summary of models used for quantification of wave statistics and sediment transport patterns in Foggy Island Bay.

	Tier 1 regional hydro-dynamics	Tier 1 regional waves	Tier 1 regional wave reanalysis (hindcast only)	Tier 2 Models A&B: local waves	Tier 2 Model C: local wave-hydrodynamic-sediment transport
Modeling package	Delft3D FM modeling suite	WaveWatch3	ECMWF ERA5 (https://cds.climate.copernicus.eu/#!/home)	SWAN	Delft3D4 modeling suite (Delft3D structured + SWAN)
Simulation mode	Two-dimensional depth-averaged	Surface fields	Surface fields and assimilation of altimeter data	Surface fields	Three-dimensional (6 equally portioned sigma layers)
Domain(s) extents	7,506 km by 3,586 km	Variant 1: Circum-arctic Variant 2: global + Alaska coast	Global	77 km by 38 km	Hydro grid: 57 km by 30 km Wave grid: 77 km by 38 km
Mesh	unstructured flexible mesh; resolution: 10 km offshore to 500 m nearshore	Variant 1: 18 km Variant 2: 7 km	Structured 31 km	Tier 2A: outer: 5 km intermediate: 1 km detail: 200 m Tier 2B: 200 m	structured, curvilinear Hydrodynamic grid: 600 m offshore to 45 m nearshore Wave grid: 1.7 km to 130 m nearshore
Time step	Variable and based on mesh size and flow velocity (Courant number)	hourly	hourly	Stationary mode. Tier 2A: hourly Tier 2B: individual sea states, time component depends on input time series	FLOW model: 12 seconds Wave model: 20 minutes (stationary mode)
Bathymetry	TCarta (90 m) IBACO (200 m) GEBCO 200 m	ETOPO1	ECMWF	UAF; instrumented depth measurements; Coastal Frontiers; UAA; Oasis; NOS smoothsheets	UAF; instrumented depth measurements; Coastal Frontiers; UAA; Oasis; NOS smoothsheets
Open boundary conditions	FES2014 tidal constituents	Not applicable	Not applicable	Tier1 waves along all open boundaries	Hydrodynamic grid: water levels from Tier 1 at the along-coast offshore boundary, Neumann at lateral boundaries. Wave grid: Tier1 waves along all open boundaries
Forcing fields	10 m neutrally stable east-west and north-south winds; atmospheric pressures; sea ice concentrations	10 m neutrally stable east-west and north-south winds; sea ice concentrations	10 m neutrally stable ECMWF east-west and north-south winds; sea ice concentrations	10 m neutrally stable east-west and north-south winds; sea ice concentrations (Tier2A)	Water levels and waves from Tier hydrodynamic & regional wave models; 10 m neutrally stable east-west and north-south winds; atmospheric pressures; sea ice concentrations

3.2 Tier 2 Model Description and Methods

3.2.1 Tier 2A: standalone wave model, continuous time series

The spectral wind-wave model SWAN (Simulating WAves Nearshore, Booij et al. 1999) is widely used to compute wavefields over shelf seas, in coastal areas, and in shallow lakes. SWAN computes the evolution of wave action density $N = E/\sigma$, where E is the wave variance density spectrum and σ the relative radian frequency, using the action balance equation. SWAN was run in third-generation mode and includes parameterizations for wind input, quadruplet interactions, triads, and whitecapping. Numerical frequency resolution ranged lognormally from 0.03 Hz up to 2.5 Hz in 46 frequency bins (33.3 – 0.4 seconds). Five-degree bins were used to resolve wave directions.

3.2.1.1 Effects of air-sea temperature gradients

SWAN was run with physics package ST6 (Rogers et al. 2012) that allowed for a multiplier on the drag coefficient. The coefficient for drag was based on the work of Le Roux (2009), which accounts for differences in air-water temperatures. SWAN normally does not include this effect, but the Le Roux formulation based on temperature difference was added via the ST6 implementation. Based on the analytical wave height formulation of Le Roux, variations to the wave height because of variations in the drag coefficient were estimated to be between -10 to +10% (95% confidence interval, CI) equivalent to a drag coefficient multiplier of ±20% (Figure 3.2a).

3.2.1.2 Effects of sea ice

Rogers (2019) implemented input/output for sea ice in SWAN, a dissipation source term, and scaling of wind input source functions by sea ice (Figure 3.2b). This functionality is built on lessons learned during the implementation of sea ice in WAVEWATCH III (Collins and Rogers 2017). The formulations use a simple empirical parametric model (polynomial function) for dissipation by sea ice, following Meylan et al. (2014) and Collins and Rogers (2017), which prescribe the dissipation rate as a function dependent on the wave frequency. Thus, the temporal exponential decay rate of energy can be written as:

$$D_{ice} = \frac{S_{ice}}{E} = -2c_g k_i, \tag{3.1}$$

where S_{ice} is the sea ice sink term, and E is the wave energy spectrum. Here, k_i has units of 1/m and is the linear exponential attenuation rate of wave amplitude in space. Factor 2 provides a conversion from amplitude to energy decay. The group velocity, c_g, enables conversion from spatial decay to temporal decay. S_{ice} and E vary with frequency and direction. In the implementation of Rogers (2019), k_i varies with frequency according to:

$$k_i(f) = c_0 + c_0 f + c_2 f^2 + c_3 f^3 + c_4 f^4 + c_5 f^5 + c_6 f^6, \tag{3.2}$$

with c_0 to c_6 being the user-defined empirical (calibration) polynomial coefficients.

Furthermore, the scaling of the wind input source functions allows the user to control the scaling of wind input by open water fraction with the variable Ω_{iw} (Rogers 2019). The default value of $\Omega_{iw} = 0$, used throughout this study, corresponds to the case where wind input is scaled by the total fraction of open water.

These formulations, also referred to as IC4M2, have been implemented in the main sub-version of SWAN version 41.31 used in this study. Here, a three-level SWAN nested grid setup is used with grid resolutions of 5,000, 1,000, and 200 meters for the overall, intermediate and detail grids, respectively.

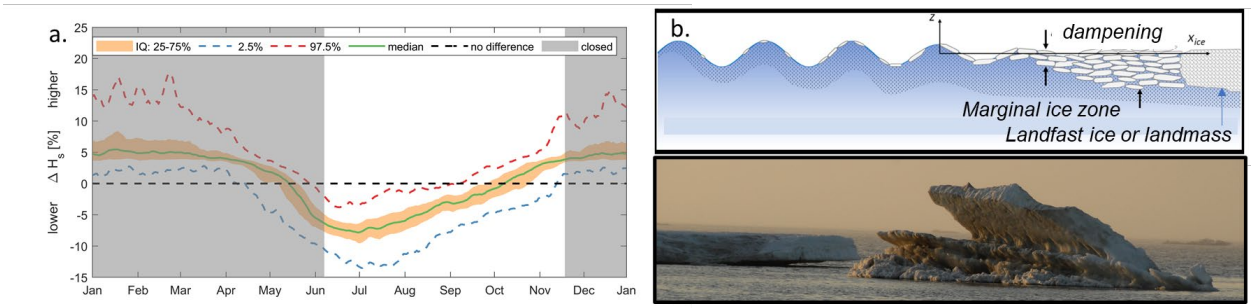

Figure 3.2 Modifications made to the Tier 2A wave model to account for high-latitude conditions. a.) Effects of air-sea temperature gradients on wave height growth. Plot shows the percent difference in wind-waves when considering changes in the drag coefficient brought about by air/sea temperature differences, based on Le Roux 2009. b) Schematic showing damping of wave energy due to the presence of sea ice.

3.2.1.3 Bathymetry

Model bathymetry was derived from datasets listed in Table 3.2. All bathymetry data were refenced to NAVD88 (any necessary transformations were done using VDATUM, version 4.0; NOAA 2019) and to local mean sea level (MSL). A published offset between NAVD88 and MSL is not available and thus was estimated by comparing three months of water level measurements at the UAA Newport mooring in 2018 (Section 2) with bathymetry collected the same year and referenced to GEOID12. Using these measurements, MSL was estimated to be 2.2 m above NAVD88.

Bathymetry of the 50 and 200 m resolution hydrodynamic and wave 'detail grids' were built primarily from single- and multi-beam track data collected in the 1980s through 2018 (Figure 3.3 and Table 3.2). Bathymetry collected as part of this study (see Section 2.2.1 and 'UAF 2018' in Figure 3.3) were given priority where overlap with previously collected data occurred. Time-series depth measurements obtained at the UAA and UAF mooring sites in 2018 – 2020 (Section 2.2.4) were also used to adjust depths surrounding those deployment locations. Bathymetry in grid cells of the intermediate and outer grids extraneous to the detail grid were populated with 200 m gridded bathymetry data from the International Bathymetric Chart of the Arctic Ocean (IBCAO) Version 4.0 (Jakobsson et al. 2020).

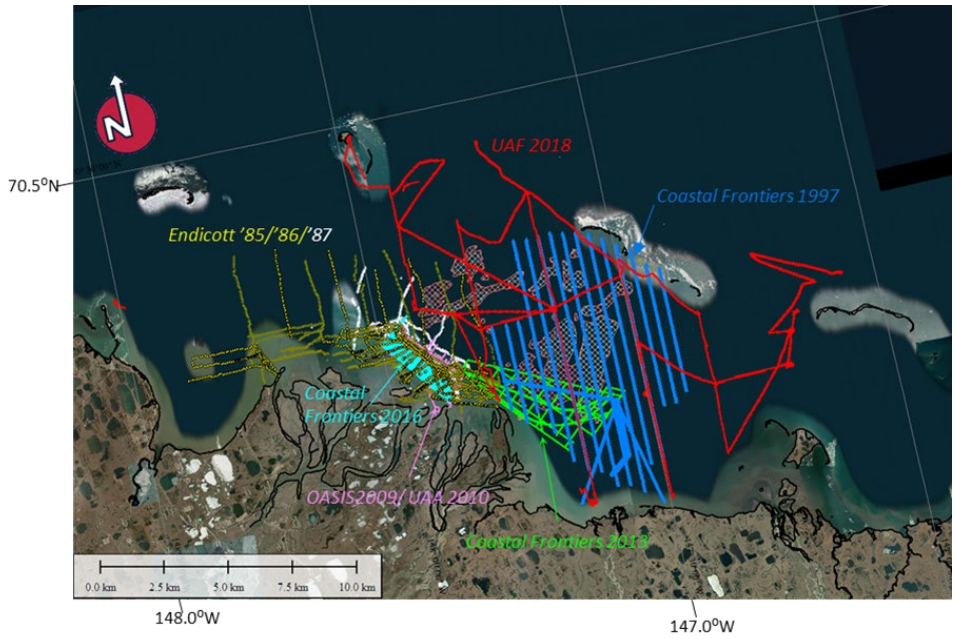

Figure 3.3 Map showing track lines of available bathymetry used to build the Tier 2(A-C) grid bathymetries.
Measurement year and source are indicated on the figure and in Table 3.2. Background image from DigitalGlobe.

Table 3.2 Data sources for model bathymetry within Stefansson Sound.

Time-period	Source	Year	Resolution
Foggy Island Bay ***region higher resolution products***			
1949/50	NOS smoothsheets	1949/50	~500 m soundings
	DHI, gridded from NOS	1949/50	90 m gridded
1980s	Endicott	1985	transects 2-3 km apart
	Endicott	1986	transects 100s m to 4 km
	Endicott	1987	transects 100s m to 4 km
late 1990s	Coastal Frontiers/Hilcorp	1997	transects ~1 km apart
2000s	Oasis	2009	transects ~150 m apart
	UAA	2010	transects ~150 m apart
	Coastal Frontiers/Hilcorp	2013	transects ~1 km apart
	Coastal Frontiers/Hilcorp	2016	transects ~150 m apart
	UAF, this study	2018	transects ~ 5 km apart

The landward boundary followed NOAA's 2017 Continually Updated Shoreline Product (CUSP) vector shoreline supplemented with hand-digitized positions for the missing region along Foggy Island Bay shores. Hand-digitizing was done using Google Earth imagery from 2019. Land elevations abutting Foggy Island Bay were obtained from 2010 lidar (Gibbs and Richmond, 2017) and assigned an elevation of 3 m above MSL for the remaining areas not measured with the lidar. Due to a lack of elevation data and the ephemeral nature of the Sagavanirktok Delta, that region was only crudely represented in the hand digitized shoreline and model bathymetry. Main channels were set at 1 m depths to ensure that discharge reached the shore, shallows were set at 0.20 m depths and

shoals at 0.20 m above MSL (Yager, 2011). Inshore bathymetry between the shoreline and available depth soundings was filled in by linear interpolation. A volume-conserving smoothing algorithm available in the Delft3D Quicken toolbox was applied across isolated regions to avoid large depth gradients which could result in spurious hydrodynamic and wave simulation results.

3.2.2 Tier 2B: standalone wave model, reconstructed time series

Wave summary statistics were computed with the numerical model SWAN. Model settings were largely the same as for the Tier 2A model (Section 3.2.1), with the exception that only the ice-free periods (open seasons) were considered (no implementations for sea ice concentrations were made). The computational grid used for this model is the detail grid (Figure 3.1d) and is part of a larger modeling effort extending from the Canadian border to the Bering Sea (Engelstad et al. in press). Shoreline and barrier island locations along the Alaska coast were extracted from USGS Topographic maps from the 1950s to 1990s at a scale between 1:63,360 and 1:250,000. Barrier island chains, located roughly 20 km offshore where the grid cells are mostly larger than the cross-shore island widths, were represented in the model using the SWAN option 'obstacles.' The use of obstacles provides a means for the model to compute flow re-routing and wave energy blocking as well as overwash during high wave events. The obstacles were assigned transmission coefficients valued at 2.6 (alpha) and 1.5 (beta) and average heights as computed from 2010 lidar data (Hamilton et al.-, 2021). Because of the high computation cost (about 1.6 hours of wall-clock time for a 24 hour simulation on a high-performance computing system) SWAN was forced with a reduced set of binned combinations of wind and wave parameters derived from the hindcast and projected wind and wave time series at the open boundary of the grid and, hereafter termed 'sea states.' The use of representative sea-states follows modified methods outlined in Camus et al. (2011), Reguero et al. (2013), and Lucero et al. (2017). Hourly time series of wave heights (H_s), mean wave periods (T_m), and mean incident wave directions (D_m), were first extracted from Tier 1 model grid points along the Tier 2 model boundary (Figure 3.4). For the hindcast period (1979 – 2019), these parameters were obtained from the ERA5 reanalysis. For the projection period (2020 – 2050), wave time series were extracted from the downscaled Tier 1 wave model (Section 3.3.2), while wind time series from CMIP6 products were used directly by choosing the closest output location to the grid. Sea states were established with a multivariant maximum-dissimilarity algorithm (MDA) which identified various combinations of significant wave heights, mean wave periods, mean wave directions, wind speeds and wind directions. The MDA method allows for a full representation of the marine climate since the determined sea states are uniformly distributed over all the data, including extreme events (Camus et al. 2011). A total of 2,000 sea states were identified for the hindcast period, while for the projections 4,000 sea states were established to ensure that differences between the CMIP6 models were captured.

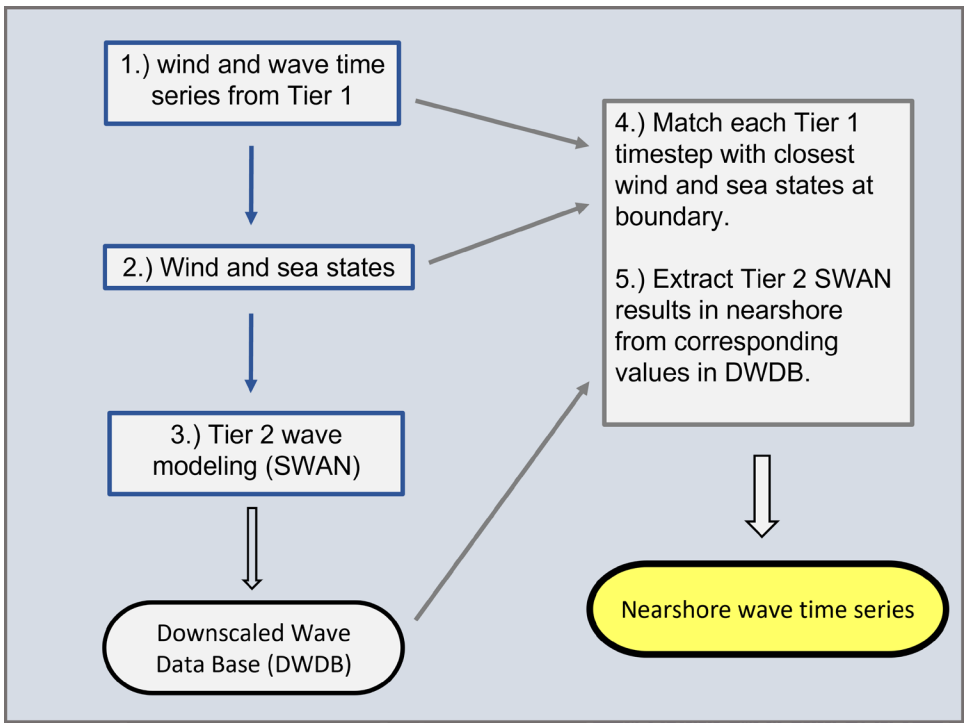

Figure 3.4 Flow chart outlining the steps involved in constructing the nearshore wave time series using Model Tier 2B.

SWAN was then forced with these sea states to develop a downscaled wave database (DWDB). The DWDB in combination with a known offshore wave and wind time series is then used to construct time series of nearshore wave conditions from the ~20 m depth contour to the shore (steps 4 and 5 in Fig. 3.4). Nearshore time series were generated by first matching sea states at the boundary with wave and atmospheric conditions at each time-point of a given Tier 1 offshore (seaward of the 20 m isobath) time series. For each 3-hourly timestep, the closest combination of H_s, T_m, D_m, wind speed, and wind directions to the Tier 1 time series was found. The algorithm initially allowed for a combination of small differences between time series and sea states ($H_s \leq 0.05$ m, $T_m \leq 0.5$ s, $D_m \leq 5^o$, wind speed < 2 m/s and wind direction < 5^o), and if no sea state could be found the bins were gradually widened up to a difference in H_s of 0.15 m, in T_m of 1 s, in D_m of 20^o, in wind speed of 3 m/s and in wind direction of 20^o. The number of values that could not be found under these requirements was less than 5%. After the sea states representing the time series at the boundary were determined, the corresponding DWDB values at all grid-points were extracted to form a set of mapped wave height, period, and direction time series.

3.2.3 Tier 2C: coupled wave-hydrodynamic-sediment transport model

The Delft3D-FLOW, WAVE, and MOR modules of the Deltares Delft3D4 Modeling Suite (Lesser et al. 2004; Deltares 2022) were used to compute water motion and sediment transport within Foggy Island Bay. The Delft3D-FLOW module simulates water motion due to tidal and meteorological forcing by solving the unsteady shallow-water equations, that consist of the continuity equation and momentum equations, discretized in time (time step) and space (grid). The numerical model SWAN (version 41.31) served as the backbone for the Delft3D-WAVE module. The Delft3D-WAVE and FLOW modules were

two-way coupled ('online mode'), enabling communication between the two modules so that depth variations and currents simulated with the FLOW module are implemented in the WAVE module and vice-versa.

Sediment transport was modeled with the online morphology module Delft3D-MOR (Lesser et al. 2004). Both cohesive and non-cohesive sediment were simulated. The TR2004 transport equations were used to model the movement of non-cohesive sediment and are implemented in the Delft3D FLOW solver. The Delft3D implementation of this formulation follows the principal description of Van Rijn (2007a,b), which separates the sediment transport into suspended and bed-load components. Suspended sediment transport is computed by the advection-diffusion equation and includes the effect of fluid density of sediment in suspension. Bed-load transport represents the transport of sand particles in the wave boundary layer in close contact with the bed surface, and when coupled with the WAVE module, includes an estimate of the effect of wave orbital-velocity asymmetry. The bed level was held constant in all simulations, to reduce computations times, decrease the uncertainties associated with morphodynamic updating, and isolate the role of changing flows on the sediment-transport patterns that result from interactions with observed (known) morphologic features.

The Tier 2 hydrodynamic and sediment-transport model domain consisted of a structured, curvilinear 143,600 cell grid that extended 57 and 30 km in the along- and cross-shore directions (Figure 3.1e and Table 3.1). Grid resolution varied from 500 m offshore to <50 m in the nearshore within Foggy Island Bay. The hydrodynamic model grid was run in both 2D vertically averaged and 3D modes. For the 3D simulations, six equally spaced vertical sigma layers were used. Blocking effects caused by the Endicott and West Dock land-connected causeways were represented with 'thin dams' in the FLOW module. Care was taken to not include thin dams where three breaches were constructed as part of the original Endicott Causeway design (1985-1987) and later added in 1994; these breaches allow exchange between Stefansson Sound saline and Sagavanirktok River freshwater flows and fish passage (Fechhelm 1999). Depth variations associated with specific boulders and rocks within the Boulder Patch region (see Figure 1.2) were not represented in the model bathymetry; instead, flow variations brought about by the presence of boulders were represented with a spatially varying bottom roughness map that varied from 0.030 $s/m^{1/3}$ in high density boulder areas to 0.020 $s/m^{1/3}$ outside the Boulder Patch region and 0.015 $s/m^{1/3}$ along the boundaries of the model grid.

Simulations of currents and sediment transport under sea ice were done using an ice-module beta-version. The ice-module is based on the approach from Semtner (1976) for which space and time-varying ice concentration and thickness maps are additional inputs. Ice is treated as a floating structure exerting pressure on the water column (Figure 3.5), with the same time step as the hydrodynamic FLOW model. Delft3D4 developments are ongoing for inclusion of ice drift velocity, growth, and decay, and as such were not explicitly modeled; instead, daily ice concentrations and thickness maps were used to represent any such changes in the forcing fields. Gridded sea ice fields (concentrations and thickness) from the ERA5 reanalysis and individual CMIP6 GCMs were re-gridded from their native resolution (25 km) to the hydrodynamic model grid and used for the hindcast and projection simulations, respectively. The lack of finer scale projected spatiotemporal sea ice products, relative to the model grid and time-step, precludes the use of finer spatial scale reanalysis products (e.g., the U.S. Navy Global Ocean Forecasting System, GOFS, ~5 km spatial resolution, Metzger 2014).

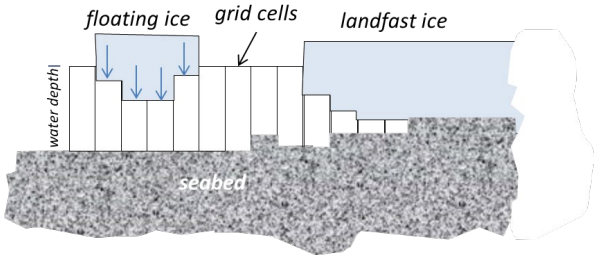

Figure 3.5 Schematic representation of how sea ice is treated in the hydrodynamic model.

3.2.3.1 Seabed sediment composition

Seabed sediment composition was derived from 18 samples collected within Foggy Island in support of this study (Section 2.2.2) and augmented with previously collected samples throughout Stefansson Sound (Table 3.3; Figure 3.6). The 2018 sediment samples collected in support of this study indicate mixed silt and sand compositions with some small pebbles, ranging in median grain size (d_{50}) from <0.01 to 1.56 mm. Grab samples collected in 1999–2015 indicate a dominance of sand (92%) at the west and east ends of Foggy Island Bay and approximately equal amounts of sand and silt immediately seaward of the inner portions of Foggy Island Bay (areas 1 and 2 in Figure 3.6, respectively).

Table 3.3 Sources for seabed sediment composition used in the model

Identifier	Year of data collection	Method
UAF/UAA	2018	Surface grab samples
ANIMIDA **cANIMIDA** **ANIMIDAIII**	1999–2001 2005–2006 2014–2015	Surface grab samples
Duane Miller & Associates	1997	Boring logs

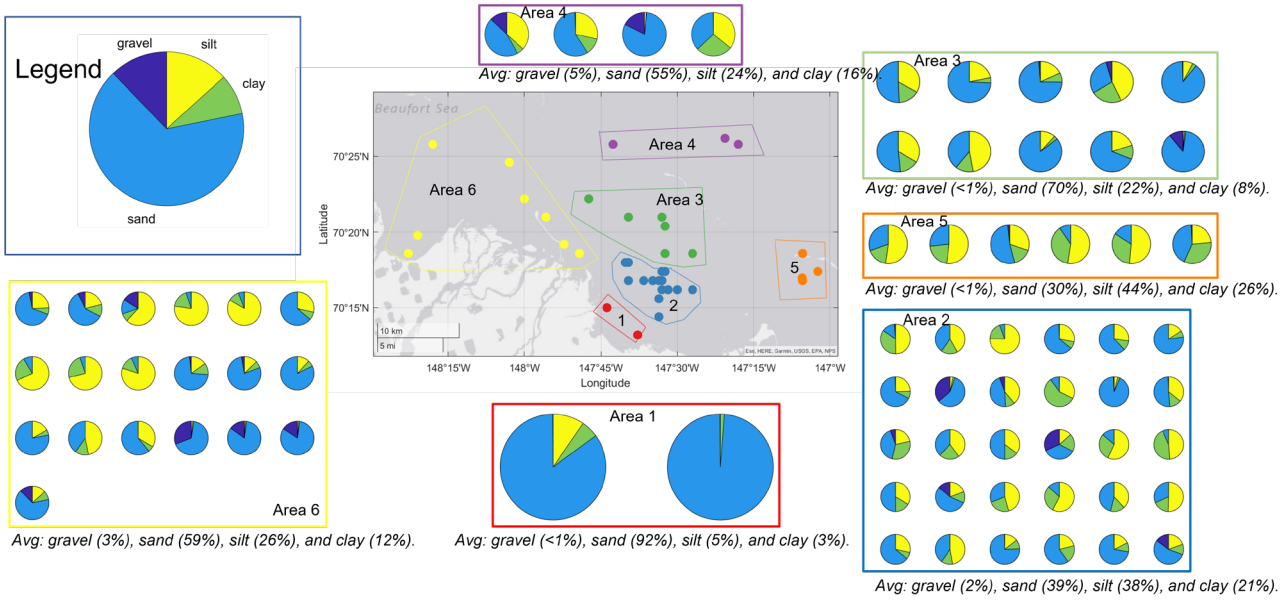

Figure 3.6 Pie charts showing relative abundance of gravel, sand, silt, and clay of seabed sediment samples collected and analyzed for ANIMIDA and ANIMIDAIII and used to develop model bed sediment maps.

Model bed composition maps were generated by assuming a uniform 2 m bed thickness proportioned to be gravel, sand, silt, and clay based on measured grab sample concentrations of those sediment types. The selection of a 2 m thickness is based on studies done in temperate environments (e.g., Stevens et al. 2022) where higher thickness values are often used but only achieved in long-term high-energy environments, and second, based on nearshore subsurface resistivity measurements of subsea permafrost and active layer depths along shore-perpendicular profiles (e.g., Figure 9 in Angelopoulos et al. 2019). Boring logs (Duane Miller & Associates 1997) were used to qualitatively assess the validity of assuming that surface grab samples were representative of the upper layer of sediment available for transport. Measured grab sample point data were interpolated using Delaunay Triangulation algorithm in the Deltares Quicken tool yielding one bed composition map for each sediment class (Figure 3.7).

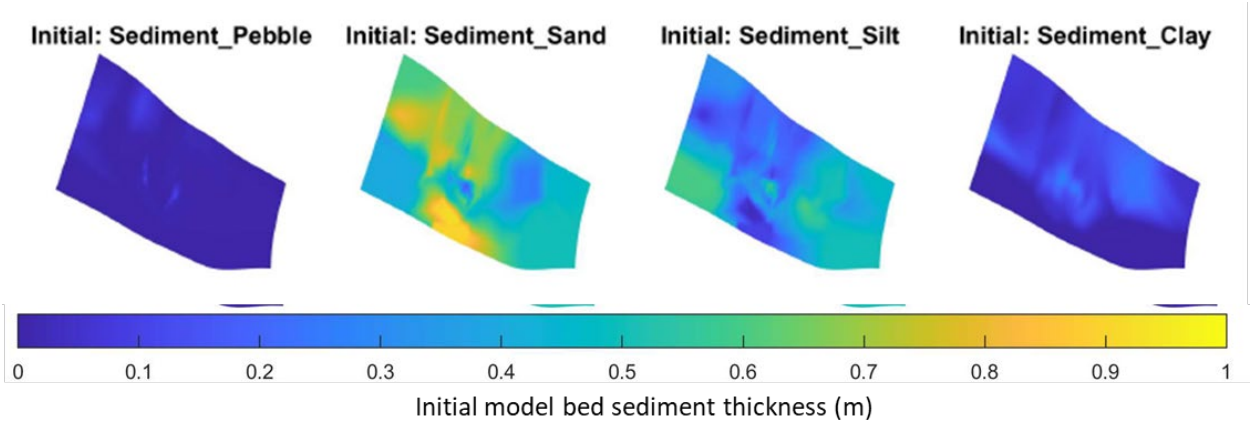

Figure 3.7 Gridded model maps of sediment type distributions at the onset of each model simulation.

Bed sediment maps were generated by interpolating grab sample point data collected in 1999 through 2018.

3.2.3.2 Seabed sediment character

Assigned grain sizes of each sediment class (clay/silt/sand/gravel) defined in the ANIMIDA studies (Figure 3.6) are based on the 18 samples collected in 2018 (Section 2) and settings used for an earlier analytical sediment flux model (Coastal Frontiers, 2014). The grain sizes and transport formulae used are listed in Table 3.4. Critical shear stress for deposition was set at 1,000 N/m^2, which effectively implies that deposition is a function of concentration and fall velocity (Winterwerp and van Kesteren 2004). Particle density and density of salt water were set at 1,787 and 1,026 kg/m^3, respectively (Coastal Frontiers 2014). Acceleration due to gravity was set to 9.83 m/s^2 (for 70.4°N). The fall speed velocity, critical shear stress and mobility parameters for the cohesive fractions (clay and silt) were treated as calibration parameters (see Section 3.5.1.3). These and other parameter settings are provided in Appendix B.

Table 3.4 Seabed sediment characteristics and model transport formulae

Sediment class	Grain size (median, mm)	Transport formula
Clay	0.005	Krone and Ariathuai-Partheniades
Silt	0.020	Krone and Ariathuai-Partheniades
Sand	0.074	Van Rijn 2007
Pebble to gravel	Not applicable	Van Rijn 2007

3.3 Tier 1 wave model

Three wave products were used to assess and generate boundary conditions for the nested Tier 2 models: wave time series computed with two variants of the WAVEWATCHIII (WW3, The WAVEWATCH III Development Group, WW3DG, 2016) model and one wave reanalysis product (ERA5) that became available ~midway through this study in 2019.

3.3.1 ERA5 reanalysis

The fifth generation of European Centre for Medium-Range Weather Forecasts (ECMWF) global atmospheric reanalysis combines model data with vast amounts of past re-processed observations from across the world into a globally complete and consistent dataset (Hersbach et al. 2020). The wave data are derived from a fully coupled atmosphere-ocean-wave model (ecWAM (Baordo et al. 2020)), which assimilates satellite radar altimeter-derived wave height data from 1991-present. The ecWAM wave model is based on wind-wave growth parameterizations of WAM cycle 4 (commonly known as ST3). ERA5 provides hourly wave estimates on a 30 km global grid from 1979-onward (https://cds.climate.copernicus.eu/cdsapp#!/home).

3.3.2 WW3 models

The WW3 model is a phase-averaged numerical model that solves the random phase spectral action density balance equation for wavenumber-direction spectra based on the assumption that water depths, currents, and wave fields vary on time and spatial scales much larger than that of a single wave. WW3 is

generally more computationally efficient compared to SWAN and therefore is commonly used to compute large scale wind wave growth across ocean basins; nearshore physics such as depth induced breaking has traditionally been better represented with SWAN (used in the Tier 2 nearshore models).

3.3.2.1 Polar Circum-Arctic WW3 Model

Version 5.16 of the WW3 model was run with a circum-Arctic stereographic computational grid (Rogers and Orzech, 2013; Stopa et al. 2016; Rogers, written and oral pers. comm. 2018; Casas-Prat and Wang, 2020) covering latitudes poleward of 60°N at a resolution of about 18 km at the coast. The conventional parametrizations of wave physics in WW3 (ST4, NL1 switches) were used (Ardhuin et al. 2010; Hasselmann & Hasselman, 1985) with the Naval Research Laboratory Digital Bathymetry Data Base 2-min resolution (NRL DBDB2). Damping and scattering by sea ice was not included.

This version of the WW3 model was forced by three different wind field products to assess performance compared to buoy observations and ERA5 reanalysis waves across the Beaufort Sea (Table 3.5). Waves were computed hourly for time-points when available buoy measurements exist. Additionally, a 3-hourly time series was computed for the months of June through December of each projection year (2020 – 2050) with wind forcing from dynamically downscaled winds using the Weather Research and Forecasting Model (WRF, version 3.5) forced with winds from the CMIP5 GFDL-CM3 global climate model, RCP8.5 climate scenario. These downscaled winds were produced in part for this study and are available at https://catalog.snap.uaf.edu/. A second set of CMIP5 simulations were anticipated but following in-depth analyses of the parent and WRF-downscaled winds and atmospheric pressures of the CCSM Global Climate Model (GCM) it was decided to exclude this product from further wave downscaling as it contains a known bias toward lower sea level pressures and does not well represent the historical Beaufort High atmospheric pressure pattern (De Boer et al. 2012; Bieniek et al. 2022).

Table 3.5 Wind products used to simulate waves with the polar circum-Arctic WW3 model

Wind product	Resolution (time and space)	Simulation period	**Product type**	**Reference and data source**
WRF-ERAI	hourly at 20 km	Overlapping with buoy measurements	WRF dynamic downscale	Bieniek et al., 2016 https://catalog.snap.uaf.edu
ASRv2	3-hourly at 15 km	ditto	WRF dynamic downscale + data assimilation	NCAR/UCAR, 2017. Browmwich et al., 2018 https://rda.ucar.edu
NARR	3-hourly at 32 km	ditto	NCEP dynamic downscale + data assimilation	NCEP/NWS/NOAA, 2005 https://rda.ucar.edu
WRF-GFDL-CM3	hourly at 20 km	2020-2050 (June-December)	WRF dynamic downscale	Bieniek et al., 2016 https://catalog.snap.uaf.edu

3.3.2.2 Global to Alaska-scale WaveWatchIII (WW3) model

Version 6.07.1 of the structured WW3 model was employed with a 0.5° global grid and two subsequent nested grids at ~18 km and ~7 km resolution, with the finest grid aligning with outer coast of Alaska. The finer resolution nested grids each take inputs along their open boundaries from the increasingly coarse grids. Bathymetries and landmasks for all grids were obtained from the 1arc-minute ETOPO1 global relief model (Amante and Eakins, 2009). This version of the WW3 model includes transitional-

and shallow-water equations. Source terms for physical processes include parameterizations for wind-driven wave growth, parametrized forms for nonlinear resonant wave-wave interactions, scattering due to wave-bottom interactions, triad interactions, bottom friction, and interactions with ice. An exponential decay source term for wave energy dissipation due to sea ice (switch IC4_M1; Wadhams et al. 1988) that has been shown to perform well compared to the ERA5 reanalysis (Shao et al. 2022) was used.

This version of the WW3 model was forced by five different wind field and sea ice products produced by HighRes CMIP6 global climate models for the RCP8.5 climate scenario, years 2020 – 2050: CMCC, CNRM, EC-EARTH, GFDL, HadGEM-SST (Table 3.6). The GFDL model runs are excluded from further analysis in this report because the sea ice fields were not fully ingested by the model simulations resulting in wave heights of unlimited fetch and seasonal extent. The CMCC model runs were also excluded from further consideration of nearshore conditions as it was found that these wind fields produced strongly biased wave heights compared to the other products (due to low biased winds, see Appendix B, Figures B1-B3).

Table 3.6 CMIP6 wind and sea ice products used to simulate waves with the global to Alaska scale WaveWatchIII (WW3) model.

Global Climate Model (GCM)	Spatial and temporal wind resolution	Spatial and temporal sea ice resolution	**Variant**
CMCC*	25 km / 6 hrly	25 km / daily	CMCC-CM2-VHR4-r1i1p1f1_gn
CNRM	100 km / 3 hrly	25 km / daily	CNRM-CM6-1-HR-r1i1p1f2
EC-Earth	50 km / 3 hrly	25 km / daily	EC-Earth3P-HR-r1i1p1f1_gr (wind) EC-Earth3P-HR-r1i1p2f1_gr (ice)
GFDL*	50 km / 3 hrly	25 km / daily	GFDL-CM4C192-highresSST-r1i1p1f1_gr3 (wind) GFDL-CM4_ssp585_r1i1p1f1_gr2 (ice)
HadGEM-SST	50 km / 3 hrly	25 km / daily	HadGEM3-GC31-HM_highresSST-future_r1i1p1f1_gn

The grayed and starred GCMs are excluded in the further downscaling to Foggy Island Bay as it was found that the CMCC product produced strongly biased wave heights compared to the other products (due to low biased winds; see Figures B1-B3 in Appendix B), and for GFDL, the sea ice fields were not fully ingested into the WW3 model runs. At the time of writing this report, the cause for the corrupt ice-field files is unknown.

3.4 Tier 1 hydrodynamic model

The Delft3D Flexible Mesh Suite (Delft3D FM; Kernkamp et al. 2011) was used to obtain estimates of water motion across the state of Alaska. The main component used was the hydrodynamic module D-FLOW Flexible Mesh (D-FLOW FM). D-FLOW FM implements a finite volume solver on a staggered unstructured grid. The higher-order advection treatment and near-momentum conservation make the solver very suitable for supercritical flows. The handling of wetting-and-drying makes it suitable for flooding computations. The continuity equation is solved implicitly for all points. Furthermore, Coriolis forcing, horizontal eddy viscosity, tide generating forces and meteorological forcings were added, making the system suitable for tidal, estuarine or river computations.

The Delft3D FM hydrodynamic model encompasses the entire State of Alaska, covers an area of 7,506 km by 3,586 km and includes 29,656 nodes. Delft3D FM allows for unstructured variable grid resolution and varies in this application from 10 km offshore to 500 m nearshore. Since advection is resolved

explicitly, the time step is variable and depends on the mesh size and flow velocity (i.e., Courant number). The hydrodynamic model grid was run in two-dimensional depth-averaged (2DH; barotropic) mode, and, thus, we assume that time-dependent baroclinic pressure gradients are essentially much smaller than the dominating tide and surge signals in coastal regions and are justifiably neglected. Bathymetry was interpolated onto the Delft3D FM mesh based on IBACO (200 m) and GEBCO (200 m). A grid cell averaging approach ensures a correct average depth when the number of bathymetry points per model cell is large. Boundaries were based on FES2014 tidal constituents and tide-generating forces were activated (484 components). Atmospheric forcing was based on ERA5 and CMIP6 products for the hindcast and projections, respectively. Winds, atmospheric pressures, and sea ice fields were used in the simulation. Wind drag was based on Garratt (1977) in combination with Lüpkes et al. (2012) to account for sea ice concentration on the atmospheric drag coefficients (Joyce et al. 2019).

3.5 Model evaluation

3.5.1 Tier 2

Wave, current, and water level data collected in 2019 and total suspended solids (TSS) data collected in 2020 as part of this study (Section 2) were used to evaluate model sensitivities to variations of parameter settings and calibrate the Tier 2C wave-flow-sediment-transport model. Model skill was evaluated against independent measurements collected during the 2018–2020 field campaign (Section 2) and complemented with historical data from previous field efforts.

In this section, the calibration and validation procedures for hydrodynamics, waves, and sediment transport are discussed.

3.5.1.1 Waves

Calibration and sensitivity to model settings

Review of historical data revealed that wave data in the form of statistical summaries and one time series station in the early 1980s are available near the current location of the Endicott causeway immediately west of the study area, but no wave measurements within Foggy Island Bay itself had been collected, thus prompting the need for wave data measurements of this study (Section 2). To that end, data collected in 2019 for this study were used to calibrate the model. Testing of model skill was then done by running the model with calibrated settings and comparing to measurements obtained in 2020 and 1982 (Table 3.7; Figure 1.2).

Table 3.7 Time-series observation data used for calibration and validation of the Tier2 wave model

Identifier	Lat (DD)	Lon (DD)	Depth (m)	Month/Year	Use	Source
Spotter 0107 (Dinkum)	70.39285	-147.83368	7.0	Aug / Sept 2019	validation	this study
Spotter 0156 (STLD2)	70.31882	-147.76044	3.2	Aug / Sept 2019	calibration	this study
Spotter 0158* (Dinkum)	70.39757	-147.87539	6.4	Jul / Aug 2020	validation	this study
Spotter 0159* (STLD2)	70.30639 70.31921	-147.72044 -147.76081	4.6	Jul / Aug 2020	validation	this study
LGL	70.37500	-147.83167	5.5	Aug 1982	validation	Gallaway, 1983

Note: buoy was dragged (see Figures 2.5, 2.7 and 2.8) presumably by ice floes; positions at specific time-points were used in the validation

Calibration and sensitivity testing of two primary model settings were considered: bottom friction and formulations for inclusion of sea ice on wave growth and energy propagation. For this reason, an open-water wave calibration time-period (2019) extending from August 7 through September 4, 2019, was considered for the bottom friction calibration followed by a marginal sea ice season extending from October 25 through December 1 for testing the sea ice formulations. The division was made by partitioning the observations based on the mean ice concentration within the outer SWAN wave model domain. When the mean ice concentration was higher than 5%, it was deemed part of the ice season. When the mean IC was smaller than 5%, it was deemed part of the open-water season. In particular, 2019 observations were used for open-water season calibration and ~20% of the available timestamps in the data from 2007 – 2013 were used for the ice season calibration. [Note that the 5% threshold of sea ice concentrations for defining the open/closed -water season varies somewhat throughout the literature and that in cases when satellite data are used to assess ice concentrations, a threshold of 15% or greater is preferred as this is the minimum at which space-based measurements give reliable measurements (Strove et al. 2016; Crawford et al. 2021). In report 2 of this 2-part report series the 15% threshold is used.]

Observed and computed wave heights and periods for the 2019 measurement period are shown in Figure 3.8. Individual combinations of bottom friction formulation and friction coefficient are plotted with different colors. Observed wave heights and periods are plotted as black dots. The figure shows strong sensitivity to different friction options used for both the wave height and period. The range of coefficients used for the Madsen et al. (1988) formulation (Madsen-BFF) resulted in too much dissipation due to bottom friction and under-estimated wave heights. Whereas default SWAN values for Collins-BFF and JONSWAP (see Table 3.8) performed well, the overall best fit, based on visual inspection of the time series in Figure 3.8 and residual plots (not shown) as well as quantitative error statistics, was the formulation of Collins-BFF with a coefficient of 0.020 (RMSE = 0.13 m; bias < 0.01 m).

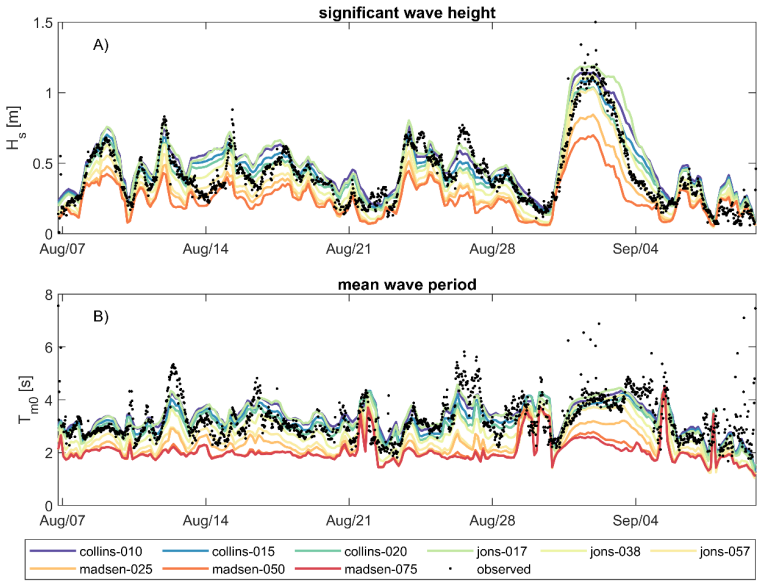

Figure 3.8 Calibration and sensitivity testing of bottom friction settings for the nested Tier 2 wave model.

Modeled (colored lines) wave heights (A) and periods (B) using various bottom friction formulations and coefficients are compared to observations (black dots) at SPOT_0156 deployed in ~3 m water depth during ice-free observations in 2019. Figure reproduced from Nederhoff et al. (2022).

Table 3.8 Skill scores used to evaluate model performance with variations of the wave related bottom roughness.

Friction		RMSE (cm)	MAE (cm)	Bias (cm)	SCI (%)
Formulation	**Coefficient**				
Colins-BFF	0.010	0.146	0.297	0.077	11
Colins-BFF	0.015*	0.129	0.261	0.036	9
Colins-BFF	0.020	0.126	0.256	0.005	8
JONSWAP	0.017 m^2/s^3	0.149	0.302	0.077	11
JONSWAP	0.038* m^2/s^3	0.123	0.249	-0.033	8
JONSWAP	0.057 m^2/s^3	0.151	0.307	-0.092	1
Madsen-BFF	0.025 m	0.187	0.379	-0.133	14
Madsen-BFF	0.050* m	0.227	0.461	-0.169	18
Madsen-BFF	0.075 m	0.237	0.482	-0.175	18

*default model values

Model skill

The combined performance of the model and DWDB, as well as the performance of the continuous model, was assessed by calculating several statistical test scores. The mean-absolute error (MAE) between model and observations was calculated as

$$MAE = \frac{1}{N}\sum(|y_i - x_i|) \tag{3.3}$$

Here, N is the number of data points, y_i is the i[th] modeled variable and x_i is ith the observed variable. Further, the root-mean-square error and unsystematic root-mean-square errors were estimated as

$$RMSE = \sqrt{\frac{1}{N}\sum(y_i - x_i)^2} \tag{3.4a}$$

$$uRMSE = \sqrt{\frac{1}{N}\sum\left(y_i - x_i^*\right)^2} \tag{3.4b}$$

where x_i^* is the least-squares regression fit between the modeled and observed values, and the scatter index is defined as,

$$SCI = \frac{\sqrt{\frac{1}{N}\sum(y_i - x_i)^2}}{\sqrt{\frac{1}{N}\sum x_i^2}} \tag{3.5}$$

and is a relative measure of the RMSE compared to the variability in the observations. The model bias was calculated as the mean difference between model and observations.

The comparison between SWAN results and observations shows good agreement (Figure 3.9) for H_s, T_m, and D_m, suggesting that the models can reproduce the wave field in the area. Skill scores for wave heights computed with the DWDB method are 0.12 and 0.09 m for the RMSE and MAE, respectively (Table 3.9), while the SCI is 24%. Wave periods have a RMSE of 0.76 s, a MAE of 0.48 s, and a SCI of 23%. Further, SWAN runs with the DWDB method have similar reproductive skill as the time-consuming continuous method (Figure 3.9). Skill score differences for H_s between the two methods are 0.01 m for the RMSE, 0.01 m for MAE and a bias in of 0.03 m, while the SCI is the same. For T_m, the difference between the two methods is 0.1 s for the RMSE, 3% for the SCI and a -0.1 s bias, while the MAE is the same. The largest discrepancies in H_s between models and observations can be seen between October 31 and November 2, 2019. This could have been caused by the fact that SWAN was run in stationary mode with hourly wind input so that the onset of the sudden large wave events was missed (e.g., from H_s = 0.85 m on September 2 hour 20:30 to H_s = 2.34 m on September 2 at 21:00 hours), or the difference might have been caused by measurement errors. Mismatches between modeled and observed H_s, appear to be mostly caused by differences between ERA5 and local winds (e.g., August 26, September 4, and September 8).

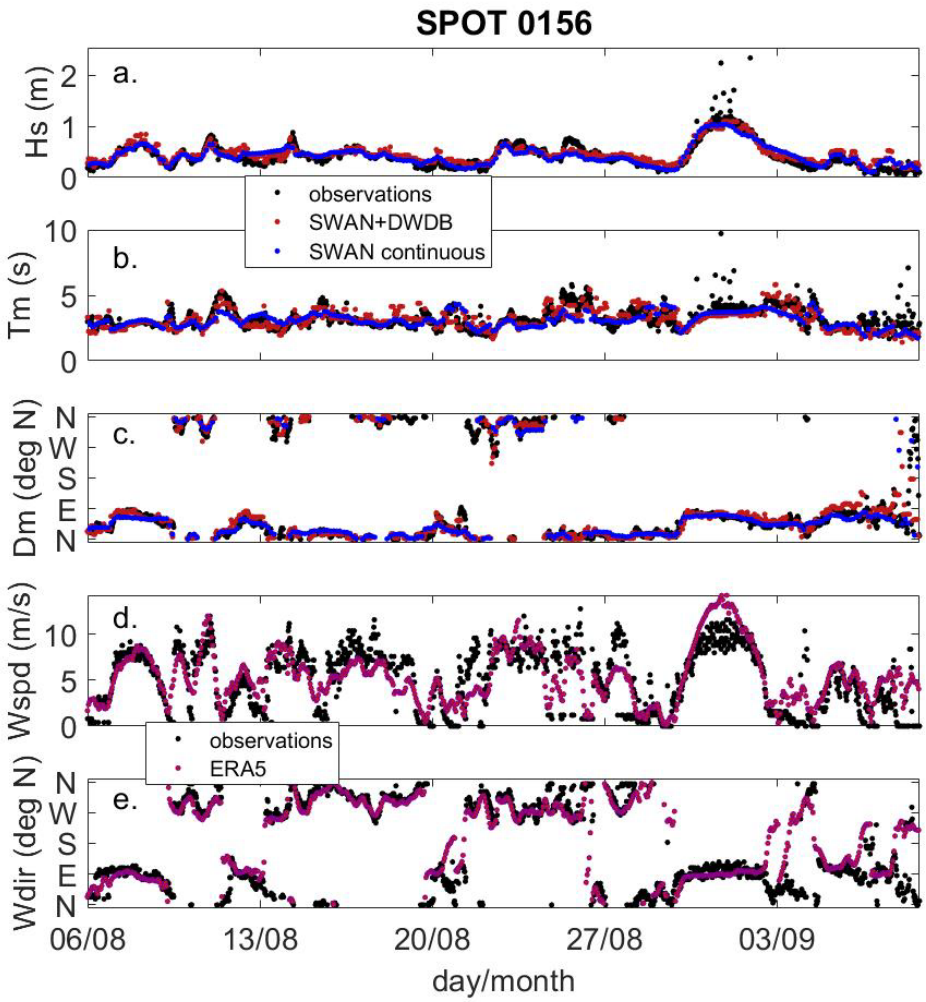

Figure 3.9 Time-series plots of wave and wind model comparisons to observation at site STLD2 in 2019.

Comparison of wave heights (a.), mean wave periods (b.) and mean wave directions (c.) for the time series created with the DWDB (red dots) and the continuous model runs (blue dots), compared to observations (black dots). (d. and e.) Offshore wind speed (Wspd) and direction (Wdir) from ERA5 (magenta dots) are compared to local winds measured with the SPOT 0156 (black).

Discrepancies between modeled and observed H_s at the Dinkum and STLD2 locations in 2020 (Figs. 3.10 and 3.11) coincide with times of disagreements between ERA5 and local winds (see e.g., July 25, July 29 – August 1, and August 7). In general, modeled and observed T_m agreed well (Figs. 3.10b and 3.11b), aside from some single higher than modeled periods, as between July 30–31 when T_m at Dinkum was as high as 12 s while modeled T_m was around 2 s. This was not observed at STLD2. Wave directions were mostly aligned with the wind directions, and differences between modeled and observed D_m (Figures 3.10c and 3.11c) are apparent when local and ERA5 wind fields differ.

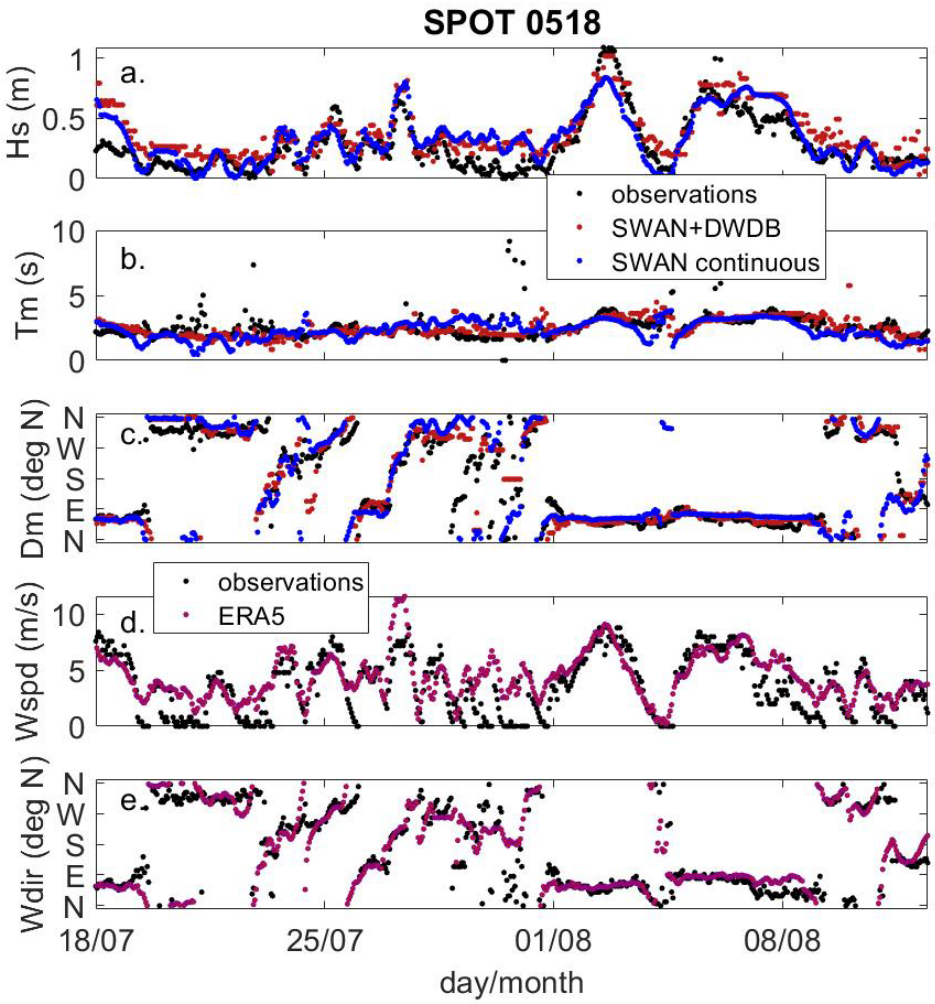

Figure 3.10 Time-series plots of wave and wind model comparisons to observation at site Dinkum in 2020.

Comparison of wave heights (a.), mean wave periods (b.) and mean wave directions (c.) for the time series created with the DWDB (red dots) and the continuous model runs (blue dots), compared to observations (black dots). (d. and e.) Offshore wind speed (Wspd) and direction (Wdir) from ERA5 (magenta dots) are compared to local winds measured with the SPOT 0158 (black).

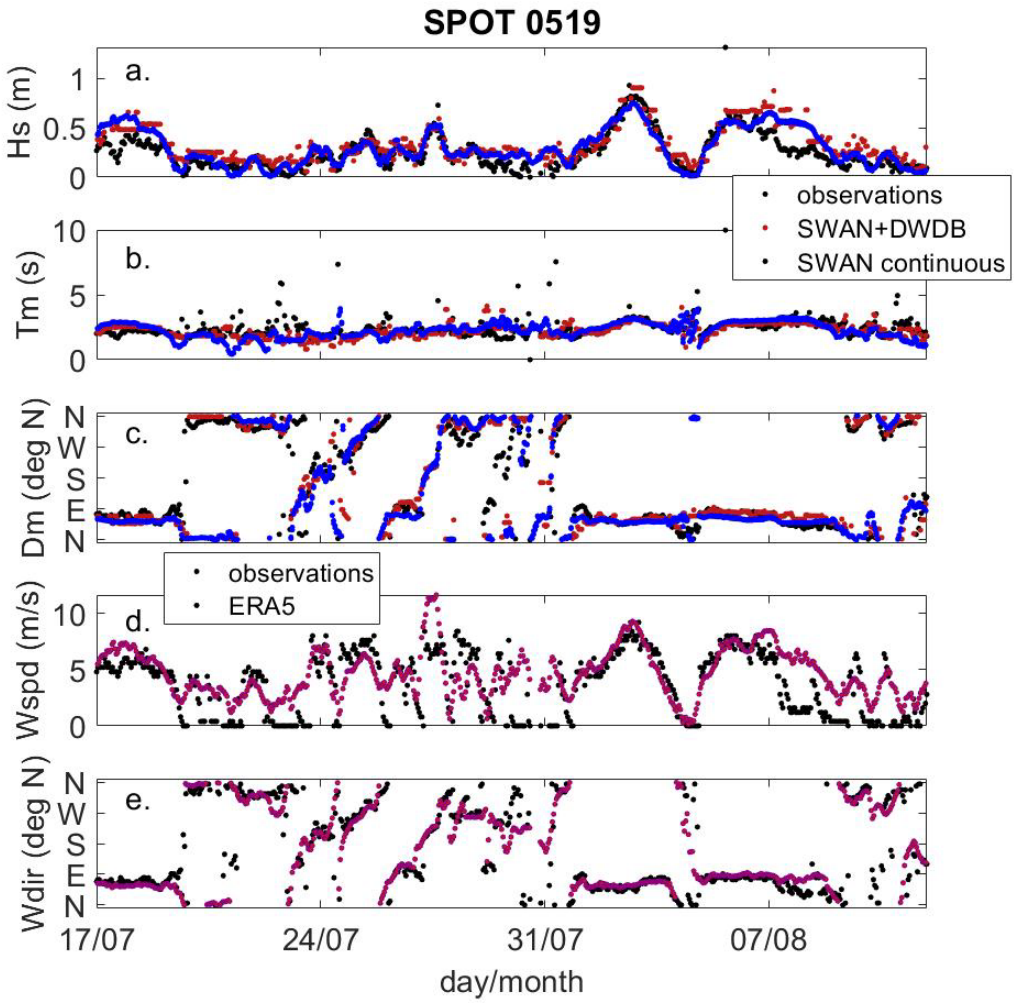

Figure 3.11 Time-series plots of wave and wind model comparisons to observation at site STLD2 in 2020.

Comparison of wave heights (a.), mean wave periods (b.) and mean wave directions (c.) for the time series created with the DWDB (red dots) and the continuous model runs (blue dots), compared to observations (black dots). (d. and e.) Offshore wind speed (Wspd) and direction (Wdir) from ERA5 (magenta dots) are compared to local winds measured with the SPOT 0159 (black).

Table 3.9. Model skill statistics for wave heights and wave periods comparing the DWDB and continuous (Cont) methods for using measurements collected at STLD2 and Dinkum.

Location (identifier)	Wave model	H_s				T_m			
		RMSE (m)	MAE (m)	SCI (%)	bias (m)	RMSE (s)	MAE (s)	SCI (%)	bias (s)
STLD2 (SPOT 0156)	**DWDB**	0.12	0.09	24	0.04	0.8	0.5	23	-0.1
	Cont	0.11	0.08	24	0.01	0.7	0.5	20	-0.2
Dinkum (SPOT 0518)	**DWDB**	0.14	0.12	38	0.09	2.1	0.7	61	-0.3
	Cont	0.14	0.11	38	0.05	2.0	0.8	60	-0.4
STLD2 (SPOT 0519)	**DWDB**	0.13	0.11	42	0.08	3.1	0.9	76	-0.6
	Cont	0.12	0.09	39	0.05	4.0	1.0	80	-0.6

RMSE: root-mean-square-error
MAE: mean absolute error
SCI: scatter index

3.5.1.2 Water levels

Water level gradients across the Tier2 domain are small as can be seen in both observations and model results (Figure 3.12). Winds from the west produce water level setup, while winds from the east produce water level setdown, as expected. A monthlong simulation was compared to observations in 2019, during a time of significant water level variations, resulting in an overall MAE of 10 cm, RMSE of 13 cm, and a bias of 0.5 cm (Figure 3.12d,e).

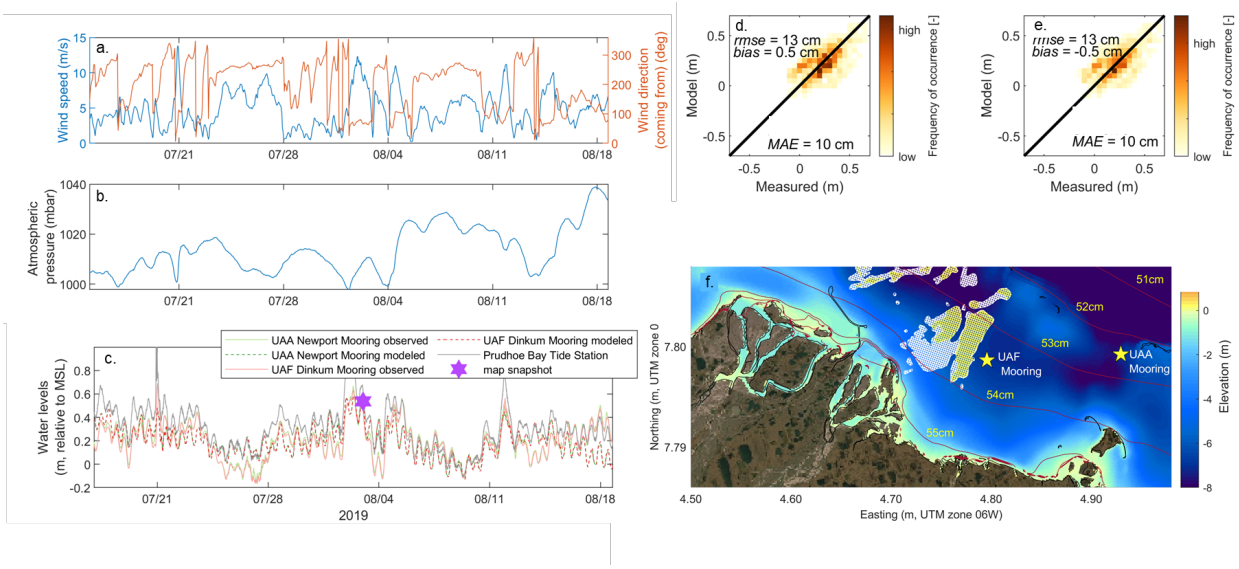

Figure 3.12 Water level variations simulated with the Tier 2C model in 2019.
(a and b) Time-series plots of wind speed/direction and atmospheric pressures measured at NOAA station #9497645. (c) Modeled and measured water levels at the UAF and UAA moorings. Purple star depicts time at which simulated water levels and gradients are shown in the mapped output of panel (f). (d and e) Scatter plots comparing measured and modeled water levels at the UAF (d) mooring and UAA (e) moorings.

3.5.1.3 Currents

Calibration and sensitivity to model settings

Changes in bed roughness values ranging from 0.015 to 0.030 $s/m^{1/3}$ extraneous to the Boulder Patch region were tested and found to yield little change on the modeled currents. Although results were not found to be very sensitive to bottom roughness, a spatially varying Manning roughness map was employed, whereby all regions were set to 0.015 $s/m^{1/3}$ except along the model boundaries and within the Boulder Patch where Manning's roughness were set to 0.025 and 0.030 $s/m^{1/3}$, respectively. The higher roughness values along the open boundaries of the model domain were implemented in an effort to reduce sediment stirring that occurs in continuous multi-month-long simulations. The impact of the greater roughness is, however, minimal.

The influence of winds and waves on currents and sediment mobility stirring was tested by simulating hindcast time-periods and running the model with and without 2-way coupling of waves. Consistent with hydro- and sediment-dynamic theories and previous studies of the region, currents increase in response to increases in wind speeds. For example, the time series in Figure 3.13, representative of a location near the proposed LDI in ~6 m water depth, shows that depth-averaged currents respond to peaks in wind speeds, and that when wind speeds reach ~10 m/s, corresponding depth-averaged currents ≥15 cm/s are capable of initiating sediment motion (Figure 3.13b). The threshold for sediment motion by near-bed orbital velocities resulting from waves are much lower (O(5cm/s), black dashed line in Figure 3.13b). The elevated TSS concentrations at the end of the time series are a result of the entrainment of sediment from the seabed into the water column by both elevated wind- and wave- induced currents; the lagged response of the TSS concentrations compared to the depth-averaged currents result from the sediment being held in suspension by the elevated currents and the sediment-specific settling velocity and critical shear stress determined through calibration.

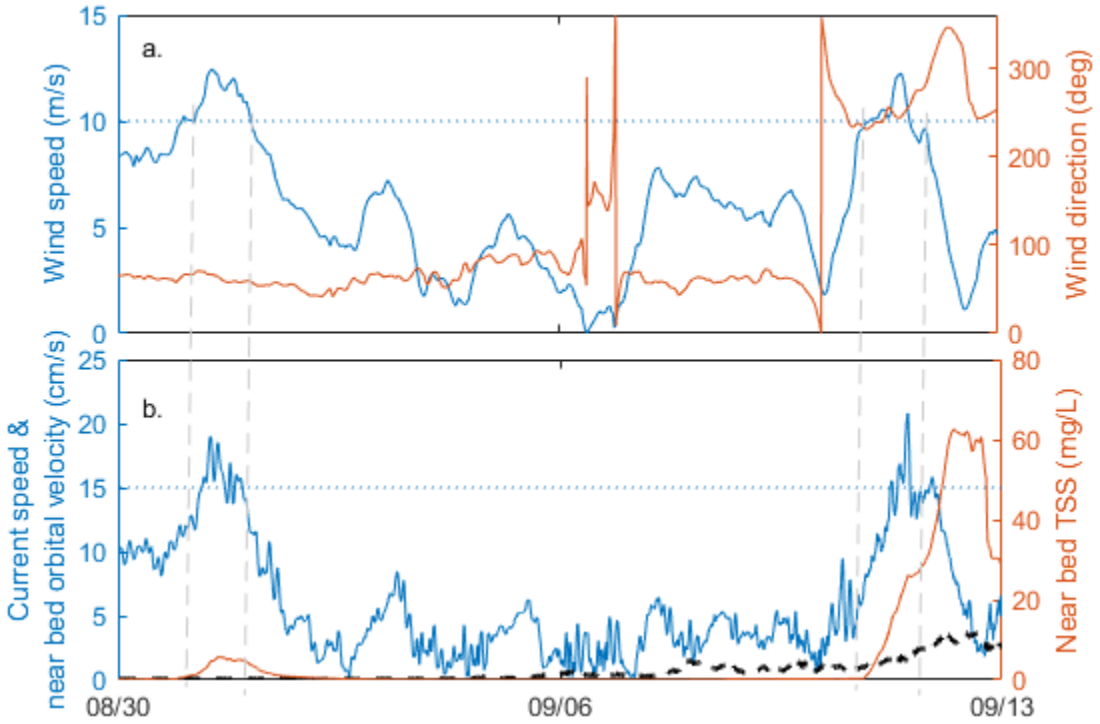

Figure 3.13 Time-series plots exemplifying the influence of winds and waves on currents and sediment mobilization.

The plots show example time series from September 2020 at a location near the proposed Liberty Drilling Island site in approximately 6 meters water depth: (a.) wind speed and wind direction, (b.) depth-averaged currents and near bed orbital velocities (black dashed line) plotted against the left-hand axis, and TSS in the bottom bin of the model (near the bed) plotted against the right-hand axis. Dashed vertical gray lines highlight the times during which currents exceed a threshold value of ~15 cm/s and sediment are mobilized.

Model skill

Modeled and measured depth-averaged currents are compared in Figure 3.14 for part of the measurement period in July 2019 when relatively strong currents were observed. Wind speeds reached nearly 15 m/s on July 21 when modeled wave heights at the UAA and UAF moorings reached 1.4 to 1.5 m. Modeled depth-averaged velocities were estimated to be 35 and 40 cm/s. Those results compare well with the UAA mooring where currents reached 40 cm/s, but under-estimate the currents at the UAF mooring, measurements were significantly greater reaching nearly 80 cm/s.

Reasons for the discrepancy might be related to spatial wind variations not captured in the model forcing or the vertical structure of the current fields, which are poorly resolved in the 3D model since density gradients due to temperature and salinity variations in the water column are not simulated. Note that the lower current measurement bins of the UAA mooring did not register and thus less vertical structure is apparent (Figure 3.15g,i,k).

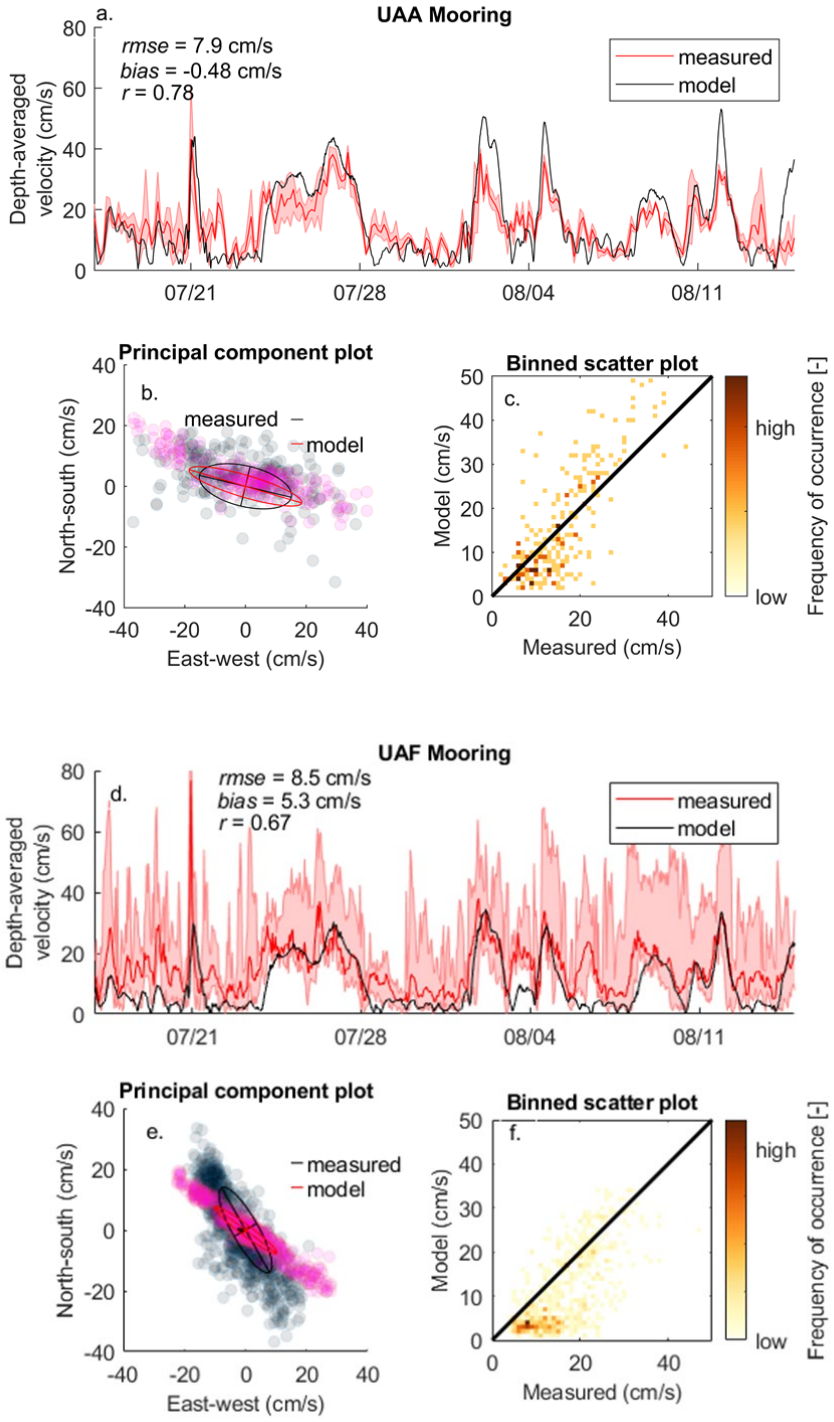

Figure 3.14 Time-series and scatter plots comparing measured and modeled depth-averaged currents at the UAA and UAF moorings in July and August 2019.

(a and d) Times-series plots show depth-averaged velocities from a 3D model simulation (black solid lines) and measurements (red lines). Red shading indicates maximum and minimum measured current speeds in the water column. (b and e) Principal component plots comparing observed and modeled major and minor directions. (c and f) Binned scatter plots indicating agreement between magnitudes and frequency of occurrence within each 1 cm/s bin.

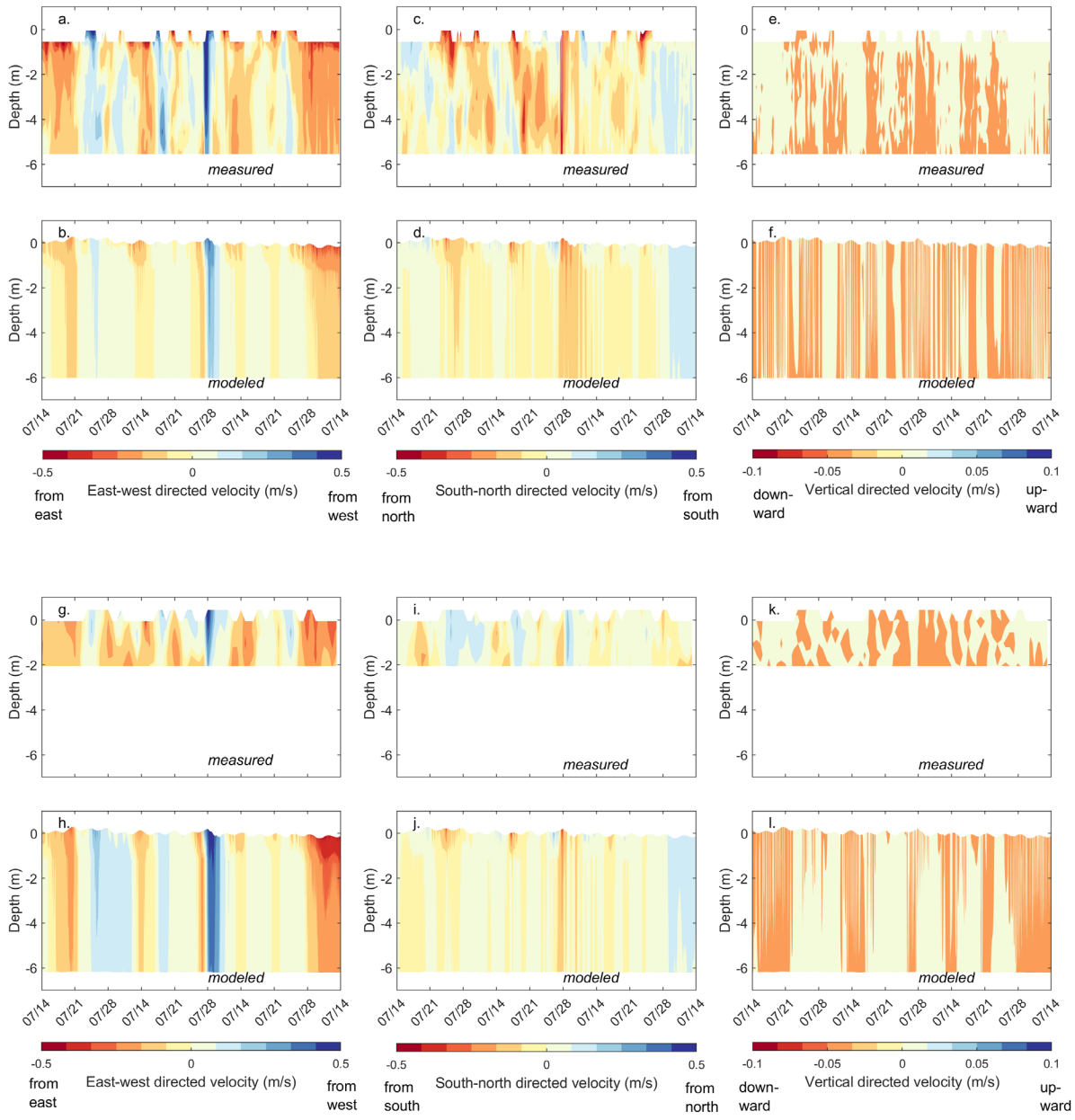

Figure 3.15 Time-series comparison of measured and modeled 3D currents.
(a-f) UAF and (g-l) UAA moorings in July 2019.

Considering the near entirety of the 2019 open water season, modeled depth-averaged currents show an overall uRMSE = 5.3 cm/s and a slight negative bias of -3.2 cm/s compared to observations (Table 3.10, row1). The significantly larger bias persists at the UAF mooring (-7.1 cm/s). Simulated currents beneath the sea ice at the same location is significantly better with a bias of only 0.9 cm/s and uRMSE = 5.7 cm/s. The shorter length of the simulation (1 week, compared to > 3 months for the open water season) and the

more uniform vertical temperature and salinity profiles (Section 2) likely contribute to better skill scores. This notion is further supported by the good skill scores (< 3 cm/s bias and uRMSE) obtained for the same open water time-period at the Shoreface monitoring site, which was located in ~1 meter water depth near the shoreline where the water column was likely well-mixed (Figure 3.16).

Comparison of modeled currents to historical measurements dating back to 1982 show reasonable overall agreement (-5 cm/s ≤ *bias* ≤ 1 cm/s, 5 cm/s ≤ uRMSE ≤ 8 cm/s, Table 3.9). In general, the model is generally biased low, particularly in the vicinity of the Endicott causeway (Figure 3.16). The 1982 measurements were obtained prior to construction of the causeway; this was accounted for in the model by removal of the hard structure and smoothing of the bathymetry, which may have introduced greater uncertainties.

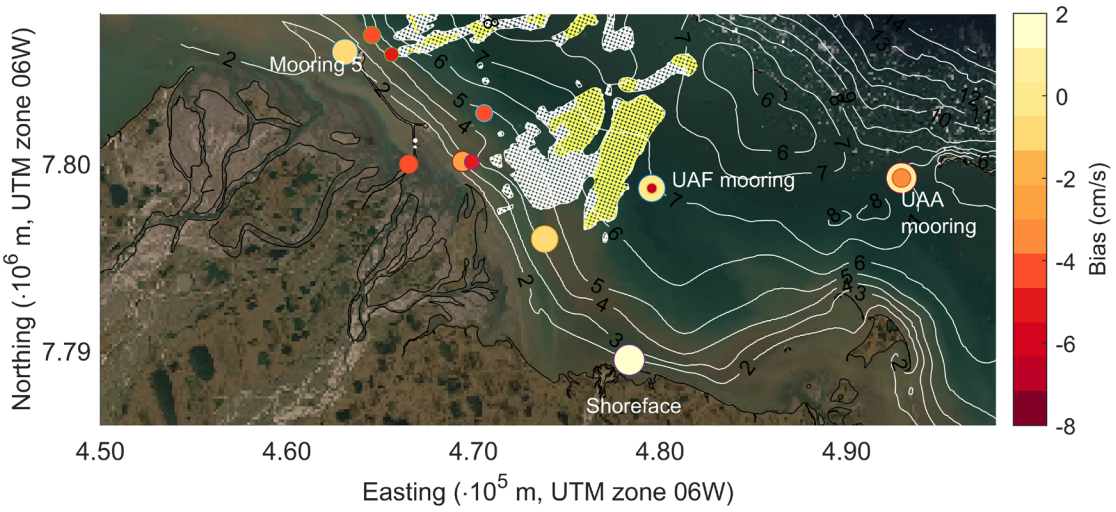

Figure 3.16 Map showing biases in modeled currents within Foggy Island Bay for years 1982 through 2019.

Color and size of circles indicate the level of bias (cm/s) between modeled and measured currents (negative values denote model under-estimates). Time-periods over which the bias was calculated varies by site as listed in Table 3.10.

Table 3.10. Model skill statistics of currents measured within Foggy Island between 1982 and 2019.

Identifier	Date	Location (meters, UTM zone 06W)	Depth (m)	*Bias* (cm/s)	*uRMSE* (cm/s)	Instrument	Source
UAA mooring	Jul 21–Oct 01, 2018	E 492,938 N 7,799,204	6.5	-3.2	5.3	ADCP	this study
UAF mooring	Jul 21–Oct 01, 2018	E 479,554 N 7,798,654	6.6	-7.1	4.8	ADCP	this study
UAA mooring	March 02–09, 2019	E 492,938 N 7,799,204	6.5	2.5	6.4	ADCP under sea ice	this study
UAF mooring	March 02–09, 2019	E 479,554 N 7,798,654	6.6	0.9	5.7	ADCP under sea ice	this study
Shoreface	Jul 20–Aug 22, 2018	E 478,346 N 7,789,480	1	2.6	2.4	ADV	this study
Mooring 1	Jul 30–Sep 02, 1982	E 464,560 N 7,806,853	4	-3.8	5.9	current meter	Gallaway, 1983
Mooring 3	Jul 27–Sep 13, 1982	E 470,570 N 7,802,677	4.5	-4.0	7.6	current meter	Gallaway, 1983
Mooring 4	Jul 31–Sep 01, 1982	E 469,409 N 7,800,090	2.5	-2.3	6.9	current meter	Gallaway, 1983
Mooring 5	Jul 31–Sep 01, 1982	E 463,108 N 7,805,946	2	0.5	7.0	current meter	Gallaway, 1983
CM8510	Jul 28–Jul 30, 1985	E 466,522 N 7,799,941	3	-3.5	4.6	current meter	Hachmeister et al. 1985
CM8517	Jul 28–Aug 27, 1985	E 473,812 N 7,795,943	2	0.5	5.0	current meter	Hachmeister et al. 1985
ER01N1	Jul 27–Aug 03, 1986	E 469,910 N 7,800,061	4	-5.0	4.9	current meter	Short et al. 1986
ER12N1	Aug 25–Aug 27, 1986	E 465,606 N 7,805,810	5	-5.3	6.1	current meter	Short et al. 1986

3.5.1.4 Total Suspended Solids

Calibration and sensitivity to model settings

Guided by seabed surface grab samples collected within and in the immediate vicinity of Foggy Island Bay, four sediment fractions were simulated in the model; two non-cohesive classes (sand and gravels/pebbles) and two fractions of cohesive fine material. Spatial distributions and bed composition were derived from ANIMIDA samples collected between 1999 and 2006 (see Section 2.2.2).

Non-cohesive sediment fractions were characterized by specific densities of 2650 and 1784 kg/m^3 for the gravel/pebble and sand fractions, respectively. A dry bed density of 1600 kg/m^3 was assumed for both fractions. Median grain sizes (D50) of the sand fraction were set at 74 μm, similar to previous studies (Coastal Frontiers, 2014) but finer compared to the 8 seabed samples obtained and analyzed in 2018 ($113 \pm 0.9\ \mu m$; see Figure 3.16). The gravel/pebble sediment grain size was set to 600 μm, corresponding to the upper limit of the van Rijn TR2004 wave-related sediment transport formula used in this study (Van Rijn, 2007) (see Section 3.2).

Sensitivity of the TR2004 wave-related bed- (*BedW*) and suspended-load (*SusW*) transport tuning parameters were tested by varying these coefficients between 0.1 and 0.4 (Stevens, in press). The coefficients relate wave asymmetry on bedload transport and influence the magnitude and direction of transport in the direction of wave propagation and near bed currents. Identical simulations for the 2019 open water season, when waves reached nearly 1.5 m at the 2019 Dinkum wave buoy showed that TSS was nearly doubled with a higher coefficient value of 0.4. Although these coefficients affect the transport results, the model is more sensitive to settings for the cohesive fractions.

Transport of the cohesive mud fractions was modeled with the Krone and Ariathurai–Partheniades formulations (Krone, 1962; Ariathurai, 1974). A mid-range dry bed density of 850 kg/m^3 was assigned to both cohesive fractions (Porterfield, 1980). The critical shear stress for deposition (τcrd) was set to 1,000 N/m^2, which effectively implied that deposition was a function only of concentration and fall speed velocity (Winterwerp and Van Kesteren, 2004). The critical shear stress for erosion (τcre), fall speed velocity (ws), and erosion rate constants (M) were treated as calibration parameters. These parameters were varied within the bounds of previously published values and different combinations were tested by running otherwise identical simulations (Table 3.11; all with *SusW* and *BedW* = 0.2). The time-period of August 2020 was used as the calibration time-period to allow for comparison to TSS measurements collected throughout the study area. Calibration parameter sensitivities were evaluated by computing the bias between measured and modeled TSS concentrations (mg/L) across 13 stations. Instantaneous samples were collected at both the surface and near the bed at most stations, resulting in a total of 23 measurements across which the bias was computed. Because the precise hours of sample collection are not available, modeled TSS values were averaged over 24hrs corresponding to the day that samples were collected.

Results show that the model is highly sensitive to all three calibration parameters and that switching the orders of magnitude in the *M* and *ws* parameters can yield similar results (e.g., compare *calib2020h* and *calib2020i*). Daily model outputs are compared to observations in Figure 3.17. At most sites (8 of 13), measured TSS concentrations fall within the modeled range. Exceptions are at FIB3, FIB5, FIB7, and FIB11 where the model under-estimates TSS. The high modeled values at FIB13 are related to

accelerated flow velocities influenced by the Endicott causeway. The flow velocities reach as high as 2 m/s within this region and warrant further comparisons and possibly model adjustments.

Table 3.11. Sensitivity testing of cohesive model calibration parameters.

ID	Silt fraction			Clay fraction			Bias (mg/L)
	Mobility (kg/m^2/s)	***Fall speed*** (mm/s)	***Critical shear stress for erosion*** (Newtons/m^2)	***Mobility*** (kg/m^2/s)	***Fall speed*** (mm/s)	***Critical shear stress for erosion*** (Newtons/m^2)	
calib2020b	1e-5	0.147	0.500	1e-4	0.009	0.135	>100
calib2020d	1e-4	0.147	0.050	1e-4	0.147	0.050	52 ± 130
calib2020e	1e-4	0.147	0.050	1e-4	0.147	0.005	51 ± 125
calib2020g	1e-4	0.147	0.005	1e-5	0.147	0.005	>100
calib2020h	1e-5	0.147	0.050	1e-4	9.200	0.050	4 ± 12
calib2020i	1e-5	0.200	0.050	1e-5	0.092	0.050	-1 ± 7

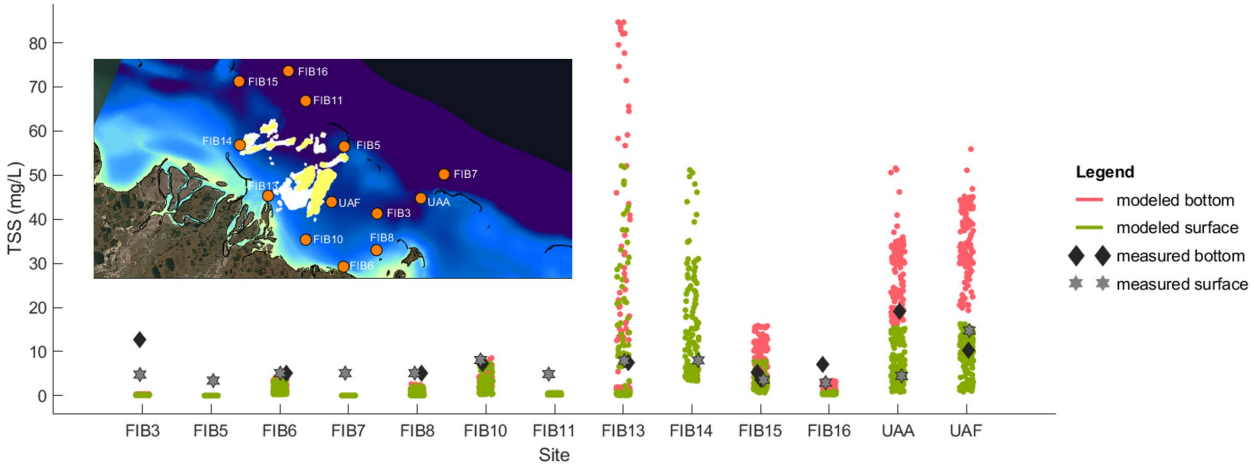

Figure 3.17 Comparison of measured and modeled total suspended sediment (TSS) concentrations (mg/L) in August 2020.

Plot shows the station location name (horizontal axis) versus TSS concentrations. Inset map shows the sample locations. Measurements near the surface (gray stars) and at a depth close to the bed (black diamonds) were obtained by weighing non-dissolved particles filtered from instantaneously collected 1 liter water samples. The exact time of day that samples were collected is unknown. Colored circles show modeled TSS concentrations at 10-minute intervals corresponding to the day of sampling and the vertical bin closest to the reported sampling depth. Model settings are those of run 'calib2020i' in Table 3.11. The inset shows the locations of TSS samples collected on August 8–11, 2020.

Model skill

Model skill was assessed by running the model with the *calib2020i* settings and comparing to point measurements obtained in September 2019, July 2018, and July through September 1985. Measurements

collected in the upper water column on Sept 11, 2019, are well within the modeled range (measured = 2.6 mg/L; modeled: 0.5 to 4.5 mg/L). High sea ice concentrations were documented during the July 2018 measurement campaign conducted for this study yet range between 6 and 32 mg/L (Figure 2.10). Model simulations resulted in negligible TSS values due to high sea ice cover as estimated with the ERA5 sea ice concentration; the mismatch between modeled and observed TSS for this time-period might be due to an under-estimate of TSS due to exaggerated sea ice concentrations in the model and possibly an over-estimate of measured TSS due to stirring of sediment by vessel maneuvering to avoid ice floes. The discrepancy highlights the need for improved measurements of nearshore sea ice concentrations for accurate modeling of sediment transport.

TSS measurements beneath sea ice and within Foggy Island Bay were collected for the ANIMIDA-I Project in April 2000 (row 3 in Table 3.12). The model was run for the same time-period with atmospheric forcings turned on and with ERA5-estimated sea ice concentrations and thickness. Modeled TSS concentrations in the vicinity of the measurement sites and commensurate with the sampling day resulted in TSS concentrations from <1 mg/L to a max of 1.4 mg/L, which compare well with the low measured TSS concentrations that were <1 mg/L.

Two additional TSS samples were collected within Foggy Island Bay as part of the ANIMIDA-I project in August 2001 under ice-free conditions (row 4 in Table 3.12). Analyses of those samples showed TSS concentrations between 5 and 8 mg/L; the model was consistent in that site 4A had higher concentrations compared to 4B, but modeled concentrations were underestimated, ranging from 1-3 and 3-6 mg/L, respectively.

As part of the Endicott study in 1985, which aimed to evaluate background conditions associated with the construction of the nearby causeway, water samples were collected during the summer and analyzed for TSS at 22 locations near the west end of Foggy Island Bay (last row in Table 3.12 and Figure 3.18). Measured concentrations ranged from 4 mg/L to 17 mg/L, with an overall mean of 8.8 ± 5.6 mg/L. Simulated TSS concentrations are found to be biased low with an overall negative bias of -2.5 ± 6.3 mg/L. Model results (±1 day on both sides of the reported sampling date) vary substantially and do bracket observed values (e.g., sampling sites C03 and E02 in Figure 3.18) but in many cases, the modeled TSS concentrations are well below the measured concentrations (e.g., site I03, Figure 3.18). Whereas the model results are biased, the order of magnitude and overall pattern of higher and lower values are well represented.

Table 3.12 Suspended sediment concentration data used for validation of the wave-hydrodynamic-sediment transport model.

Identifier	Date	Number of sites; Location	Depth (m)	Measured (mg/L)	Modeled range (mg/L)	Source
STL_JLK	September 11, 2020	2 locations ~100 m apart	surface	2.6	0.5 – 4.5	this study
FIB2-FIB16_2018	July 10, 2018*	16 stations within Foggy Island Bay	surface and bottom	6 - 32	1 - 5	this study

LA2 & LA3	April 28, 2000 beneath sea ice	70.31°N / 147.63°W 70.27°N / 147.55°W	1 - 6	<1	<1 to 1.4	ANIMIDA
4B & 4A	August 4 and August 6, 2001	70.34°N / 147.6°W 70.30°N / 147.6°W	0.20 - 5	5 8	1-3 3-6	ANIMIDA
3 letter codes	intermittent days from Jul 23 – Sept 9, 1985	22 stations within Foggy Island Bay	surface and bottom	Figure 3.18	Figure 3.18	Endicott

Note: An asterisk (*) denotes that exaggerated sea ice concentrations may have affected both measurements and the model results which are biased very low.

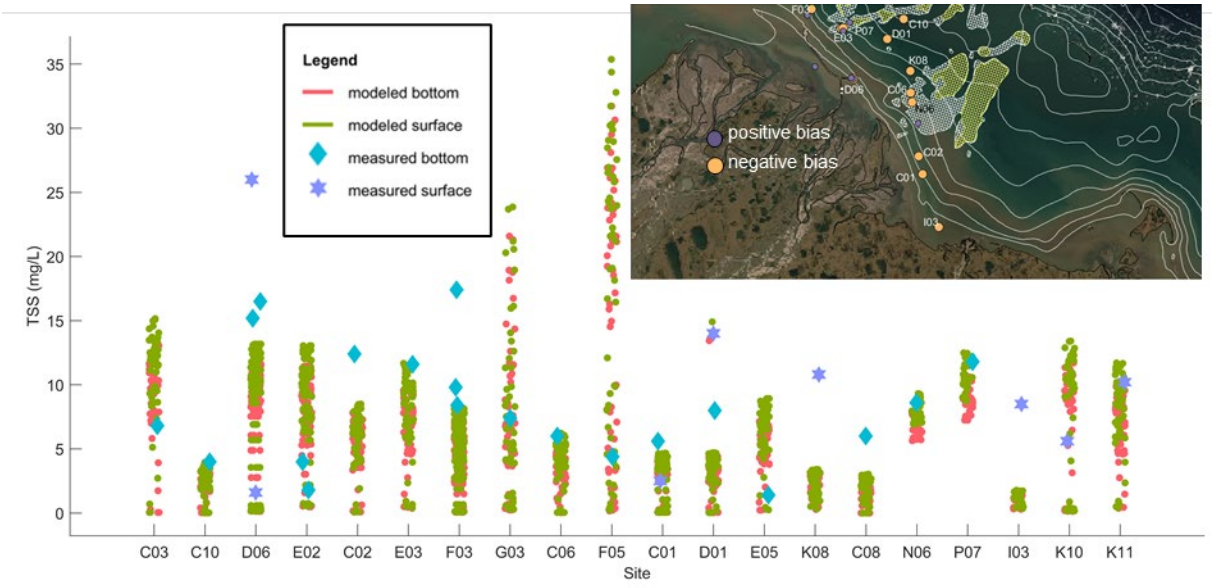

Figure 3.18 Comparison modeled total suspended sediment (TSS) concentrations (mg/L) to measurements obtained in 1985 as part of the 'Endicott Study.'
Plot shows the station location name (horizontal axis) versus TSS concentrations. Inset map shows the sample locations. Endicott measurements shown with diamonds and stars and labelled on the x-axis according to the Endicott naming convention (Short et al. 1986) were obtained by weighing non-dissolved particles filtered from 1 liter water samples (Niskin bottle samples). Concentrations of 10-minute interval TSS, computed with the calibrated model and corresponding to the upper and lower bins of the water column at each location, are shown with colored circles. Inset shows sample locations and bias (colors) of the model compared to measurements (a negative value indicates that the modeled daily mean under-estimates the measured TSS concentration obtained with an instantaneous water sample).

To evaluate the consistency of the model with previous guidelines of winds and TSS concentrations, a set of experimental model runs were done with constant easterly winds increasing in speed according to the ranges denoted in the first column of Table 3.13. Winds were set to increase over a 24 hr time-period to stay within the bounds of storm duration not exceeding 10 hrs (Coastal Frontiers) and with no distant

swell allowed to enter the model domain. Model results obtained from a location in ~2 m water depth in central Foggy Island Bay compare well with ranges of TSS and current speeds summarized by Trefry (2009) and Coastal Frontiers (2014). Modeled current speeds are estimated somewhat low for the 2.5 to 5 m/s constant wind bin but otherwise bracket the values provided by Coastal Frontiers (compare columns 4 and 5 in Table 3.13). Modeled TSS concentrations are well within the guidelines presented by Trefry (compare columns 2 and 3 in Table 3.11), except for the higher wind speeds (>10 m/s) where the model predicts 25 to 85% lower suspended sediment concentrations. A maximum upper wind speed of 15 m/s was assumed in the model simulation, which may be lower than the actual wind speeds on which Trefry based their observations upon.

Table 3.13 Comparison of modeled current speeds and total suspended solids to published guidelines for open water conditions in Foggy Island Bay.

Wind speed	TSS (mg/L) Trefry (2009)	TSS (mg/L) This study	Current Speed (cm/s) Coastal Frontiers, 2014	Current Speed (cm/s) This study
0 – 0.25 m/s (5 knots)	1 – 4	1 - 3	3	2 ± 1
2.5 - 5 m/s (5 – 10 knots)	3 – 8	4 - 7	12	7 ± 2
5 - 10 m/s (10 – 20 knots)	5 -15	7 - 14	19	16 ± 4
>10 m/s (>20 knots)	50 -100	8 – 74*	27	26 ± 6

*a maximum of 15 m/s winds were used for this experimental simulation

3.5.2 Tier 1 wave model

Here we compare hindcast wave height time series from newly available datasets against buoy measurements. Additionally, we compare buoy observations with results of the Polar Circum-Arctic Tier 1 WW3 model using WRF-ERA and CBHAR winds to assess the level of improvement using these downscaled wind products.

A total of 10 short-term buoy deployments that measured waves in 20-50 m water depths across the Beaufort Sea within a ~110 km radius of Foggy Island Bay during the 2011-2013 open water seasons were identified and collated as part of this study (Figure 3.19b; Table 3.14). The data were collected primarily by private industry and have been approved for release to this study. Buoy measurements were compared to wave heights and periods available from the ERA5 reanalysis product, Ifremer, and ERAI wave hindcasts, as well as model outputs from the Tier 1 circum-Arctic WW3 model. The circum-Arctic WW3 model was forced with winds from the ASR, NARR, and WRF-ERAI products (see Section 3.3.2.1 for details on sources). Based on various skill statistics between measured and modeled wave heights and periods, the ERA5 reanalysis performed best overall (Figure 3.20). The overall median bias in wave heights and periods of ERA5 is < 0.10 m and <0.5 s, respectively. Root-mean-square errors are also good with median values at 0.30 m and 1.35 s, for wave heights and periods, respectively. Wilmott Skill Scores

range from 0.71 to 0.99 at each site, and for all sites within 60 km of Foggy Island Bay, the skill scores are all >0.80.

Table 3.14 Buoy observation data used for validation of the Tier1 wave model

Identifier	Latitude (decimal degrees North)	Longitude (decimal degrees West)	Approximate distance from Foggy Island Bay (km)	Depth (m)	Date start (month/day/year)	Date end (month/day/year)
2012_HB01	70.80075	-149.99400	109	22	10/3/2012	11/7/2012
2013_HB01	70.81250	-149.99400	109	24	10/4/2013	11/12/2013
2014_HB01	70.81250	-149.99400	110	24	7/11/2014	10/5/2014
2011_A	70.36720	-145.99880	58	31	10/2/2011	11/3/2011
2012_A	70.36720	-145.99690	97	31	10/6/2012	11/9/2012
2013_A	70.36720	-145.99690	58	31	6/1/2013	10/1/2013
2013_CB01	70.37000	-146.04000	56	32	8/6/2013	10/4/2013
2013_V	70.36715	-146.13660	53	34	7/10/2013	9/30/2013
2012_V	70.63307	-146.13660	65	43	10/5/2012	11/8/2012
2011_V	70.63338	-145.13560	97	55	10/2/2011	11/3/2011

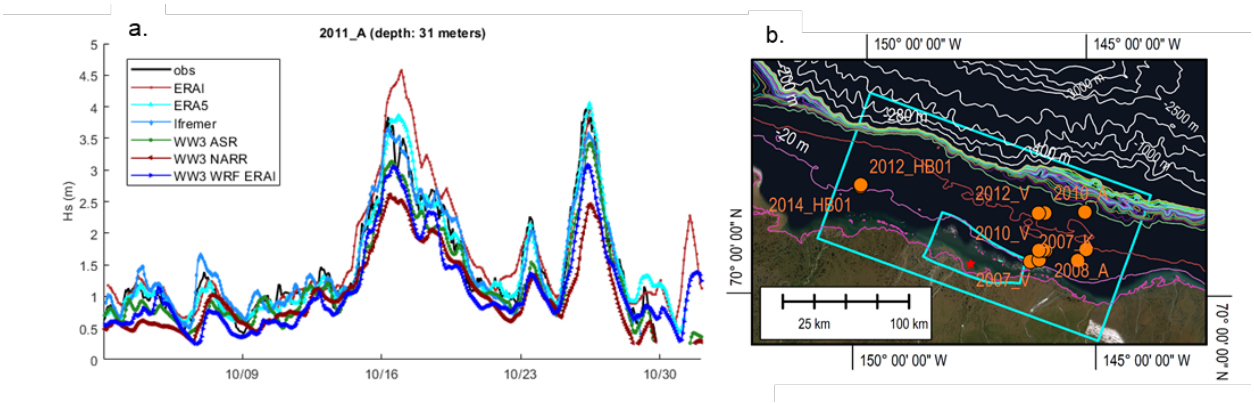

Figure 3.19 Buoy locations and measurements used for Tier 1 wave model comparisons.
(a) Sample time series comparing measured and hindcasted wave heights in 2011 at buoy 2011_A. (b) Map showing locations of buoys used for validation and selection of optimum hindcast wave hindcast product. Bounds of the intermediate and detail Tier 2A wave model grids are shown with cyan-colored lines for reference.

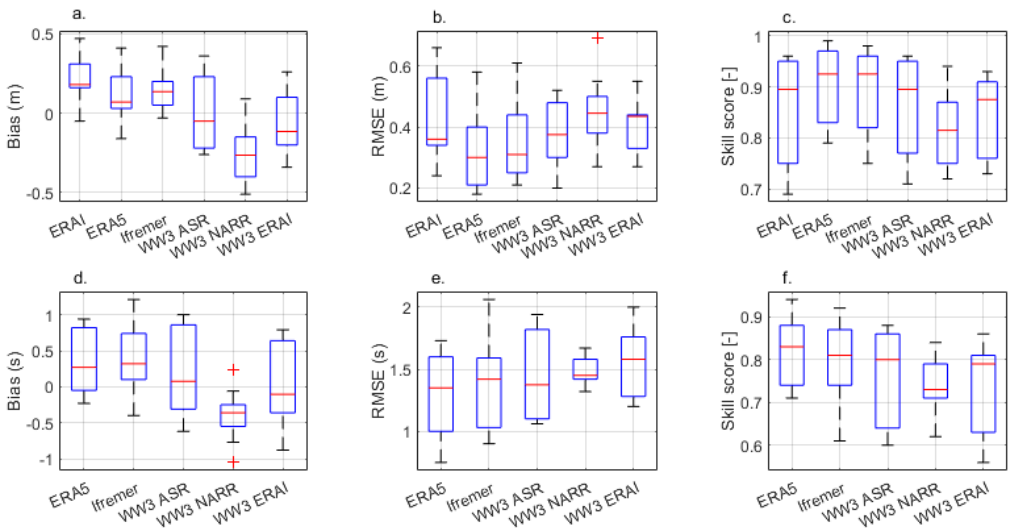

Figure 3.20 Box plots of error statistics between deep water (>20 m) observation buoys (Table 3.14) and hindcast Tier 1 wave model and reanalysis products.

(a-c) Box plots of bias, RMSE, and Skill score metrics between measured and modeled wave heights. (d-f) Box plots of bias, RMSE, and Skill score metrics between measured and modeled wave periods. Wave periods were not available for the ERAI hindcast at the time of this analyses.

3.5.3 Tier 1 hydrodynamic model

Sensitivity testing of several model settings was performed. Tidal constituents, bottom friction and wind drag relationships were varied. In total more than 30 runs were run as part of the sensitivity testing. For example, different sources for boundary conditions were tried (TPXO 7.0, TPXO 8.0, FES2014), bottom friction formulations (Chezy, Manning) were varied and different drag relationships for the wind were used (with and without the effect of ice). The settings used in this study are presented in Appendix B and Section 3.5.3. Changes in the tidal boundary conditions and wind drag formulations resulted in the greatest variance.

Modeled water levels from 1980 until 2020 were validated for the entire model domain. An example time series of two weeks of storm water level at tide gauge station Prudhoe Bay (NOAA station #9497645), including the decomposition into the tide and non-tidal residuals (NTR), is shown in Figure 3.21. Tidal variations are generally small, and the model can reproduce large surge events as depicted in the figure with good accuracy. In general, water levels at Prudhoe Bay are mainly driven by non-tidal residuals. Tidal amplitudes are small (< 20 cm). The difference in observed and modeled tidal amplitudes is smaller than few centimeters and the phase differences are within the acceptable range (Figure 3.22). NTR are reproduced with an unbiased uRMSE of 13.3 cm. The model does have a bias of ~12 cm, which would likely be reduced if large-scale steric effects from a barotropic model were included.

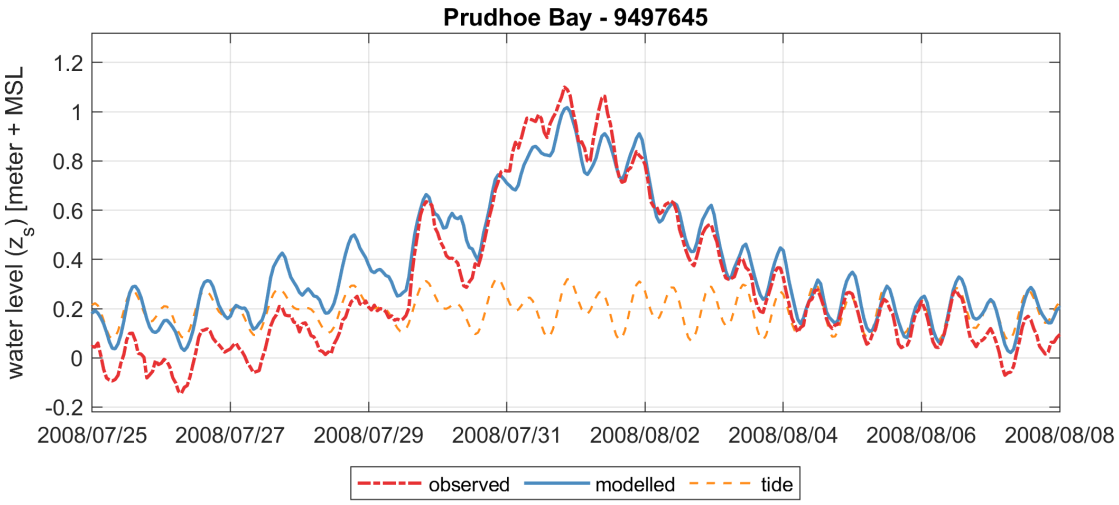

Figure 3.21 Example time series comparing water levels computed with the Tier 1 hydrodynamic model with observations at the Prudhoe Bay tide gauge (#9497645).
Observed water levels (red) are decomposed into a tide-only signal (orange) and non-tidal residuals (red line). Modeled non-tidal residuals are shown in blue.

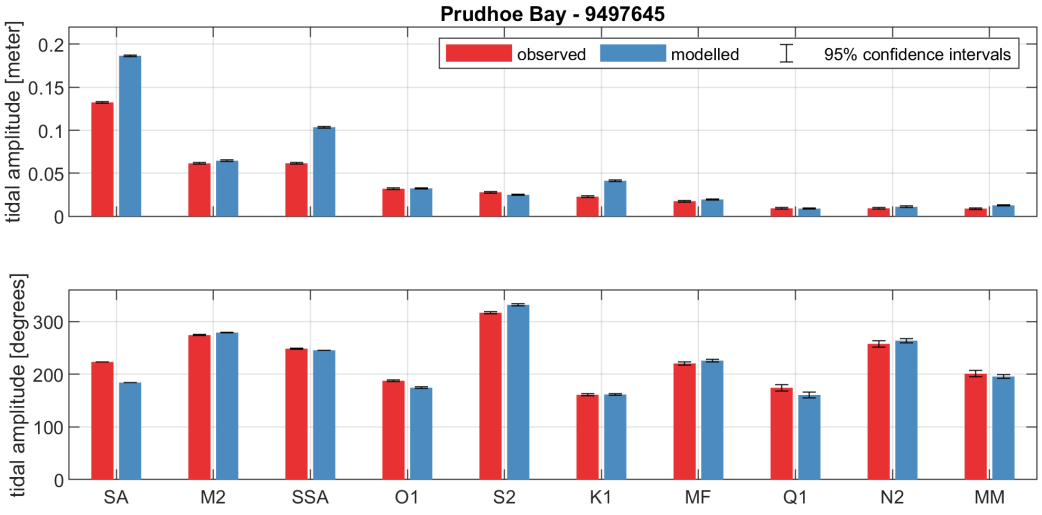

Figure 3.22 Bar charts comparing measured and modeled tidal amplitudes (top panel) and phases (bottom panel) using the Tier 1 hydrodynamic model at Prudhoe Bay (#9497645).
Values for the 10 highest observed tidal amplitudes are shown.

3.6 Results

Comparison of simulation results to observations show an overall acceptable model skill. After model calibration, comparison of results from the local scale stand-alone wave models and the coupled wave-hydrodynamic-sediment transport model with observations show *RMSE*s of <15 cm for significant wave heights and water levels, <1s for wave the mean wave period, and less than <10 cm/s for currents. Depth-averaged currents are biased low overall (<-5 cm/s), which likely contribute to the overall negative bias of modeled TSS concentrations (on the order of -2.52 ± 6.29 mg/L). Whereas the model results are biased low, the order of magnitude and overall pattern of higher and lower values appear well represented.

3.6.1 Wave hindcasts

A 41-year hindcast of nearshore wave conditions show a two-fold increase of the spatial median annual wave height from 1979 to 2019 (Figure 3.23a). Early in the time series, highest events typically occurred in mid-September and have since shifted toward early to mid-October (approximately 20 days later in the season). The shift correlates strongly with changes in sea ice concentrations. In the 1980s, partial sea ice cover was intermittently present during the summer and early fall months (July-September), but by 2019, little to no sea ice was common between August to mid-October (Figure 3.23b). The open-water season (when sea ice concentrations are less than 15%) has on average increased from about one month in the early 1980s to more than 5 months (152 days) between 2015 – 2019. A linear trend analysis (not shown) reveals a statistically significant decrease in the median sea ice concentrations of -1.3% per year and -1.7% per year for the summer (June through July) and fall (September through November), respectively. Over the same analyzed time-period from 1979 to 2019, no statistically significant trends in wind speed were found.

The longer open-water season and expansion of fetch (surface area over which winds blow to build waves) has also affected the frequency of high wave events. For example, the number of 'rough wave days' have increased from approximately 1.5 days/year at the start of the time series in 1979 – 1984 (range 0 to 7 days/year) to 13.1 days/year toward the end of the hindcast period, and primarily occur in September and October. Rough wave days is a threshold-based extreme wave index defined as the annual number of days when daily max wave heights exceed 2.5 m (World Climate Research Programme (WCRP) Expert Team on Climate Change and Detection). Whereas wave heights and wave power increased significantly over the 1979-2019 time-period, only minor trends in median wave period (0.03 sec/year) and wave steepness (wave height divided by wave period) were found. Mean wave periods rarely exceed 11 s; this, in combination with the weak trend, suggest that while some increase in swell (waves generated by distant storms and characterized by wave periods greater than 12-15s) energy has occurred, local seas still dominate the full wave energy spectrum. A barrier island chain located <20 km offshore of Foggy Island Bay mitigates offshore wave energy reaching the study area and additionally limits the fetch for local wave growth within Foggy Island Bay. The ephemeral barrier islands changed shape and configuration over the study time-period but have thus far generally remained intact, effectively filtering offshore wave energy from the north-northwest to northeast from reaching Foggy Island Bay.

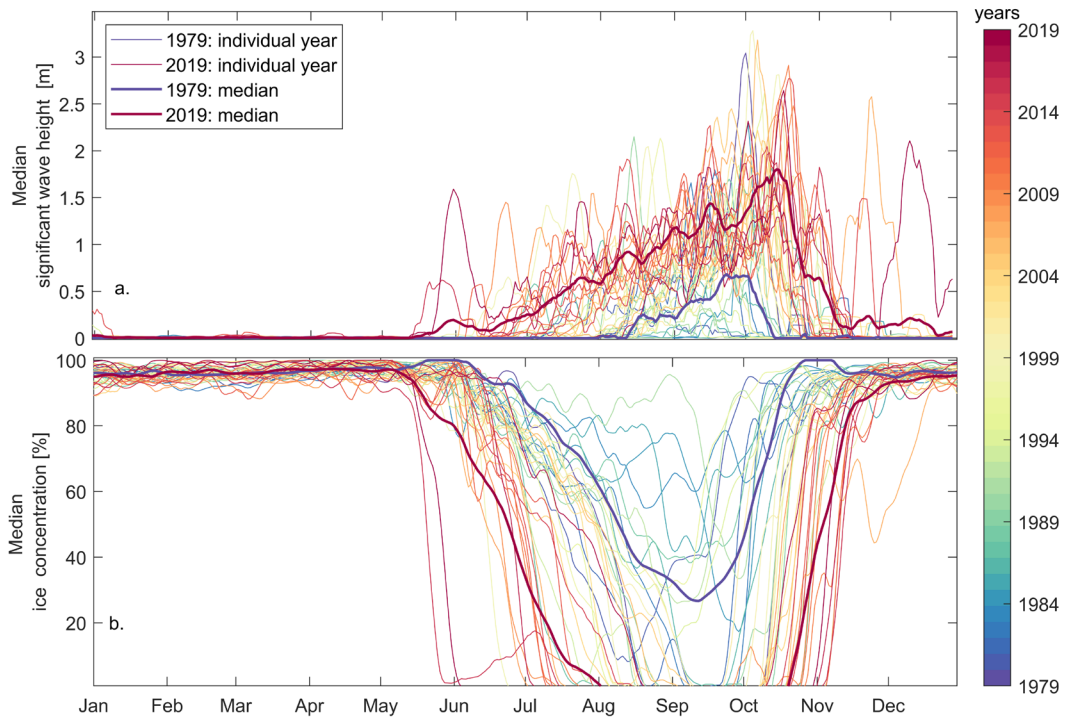

Figure 3.23 Monthly changes in wave heights and corresponding sea ice concentrations from 1979 through 2019 within Foggy Island Bay and immediate vicinity.
(a.) Daily spatial median wave heights throughout the calendar year. The median estimates for 1979 and 2019 are based on linear fits per day of the individual years. (b.) Daily sea ice concentrations computed as for wave heights in (a.). The time series in (a.) and (b.) are smoothed by applying a weekly moving filter. Reproduced from Nederhoff et al. (2022).

3.6.2 Storm surge hindcasts

Open water season storm surge events, which are much less influenced by the presence of barrier islands, reached a maximum of 65 cm (excluding astronomic tides) seaward of Foggy Island Bay during the 41-year hindcast from 1979 through 2019. Loglinear and GEV fitted curves suggest surge levels of 30 and 70 cm above mean sea level for the annual and 50-year return periods. These summary statistics are computed from 10-minute time series outputs of the Tier 1 model at the 20 m isobath seaward of Foggy Island Bay. Variations in water levels produced with the finer resolution Tier 2 model are generally within 10% (higher and lower during setup and setdown events) at the proposed LIB site (6 m water depth) compared to the offshore 20 m isobath location, except during high surge events when inshore water levels are ~40% higher for the Tier 2C model. Because of the finer grid resolution and better representation of bathymetric and coastline variations, the Tier 2 model better resolves water level variations in the nearshore shallow regions. Water level gradients across the domain and seaward of the very shallow areas (deeper than ~1 m) are small, on the order of a couple centimeters across 10 km at a particular point in time.

A small (-0.2 cm/year) but statistically significant ($pVal < 0.05$) negative trend of the 3-year moving mean annual maximum storm surge was found. Moreover, the annual maxima and minima surge levels exhibit decadal and semi-decadal oscillations, respectively (Figure 3.24a). The signals were compared to established climate indices, such as the Arctic Oscillation (AO) and Pacific Decadal Oscillation (PDO).

No clear dependency was found except a qualitative correspondence between elevated storm surge levels with the negative PDO phase and that the decrease in annual maximum surge levels appears to correspond with an overall change of the PDO from a positive to negative phase (Figure 3.24a). The decadal and semi-decadal cycles warrant further investigation into relations of these variations to westerly and easterly winds for the setup and setdown events, respectively, but a robust analysis would require a longer time series to account for multi-decadal long atmospheric variability.

Akin to the increase in frequency of larger waves, the occurrence of surge and setdown events are also found to increase with time, which is a reflection in the increasing number of open water days. The number of surge and setdown events, relative to the 25th and 75th climatological quantiles (calculated from the 30-year 1980 to 2010 time series), increased at a rate of 0.13 events per day of increase in the open water season (R^2 = 0.79; *pval*<0.05; Figure 3.24b). Since 1979, the number of open water days have increased at a rate of 2.5 days/year (R^2 = 0.50; *pval* <0.05).

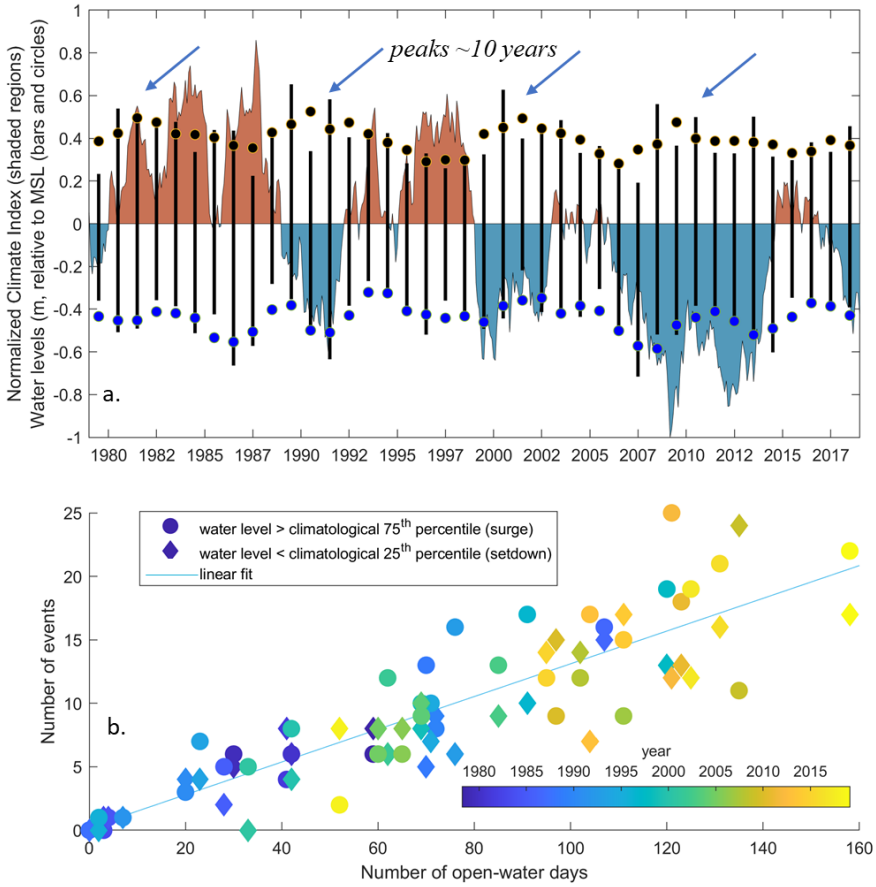

Figure 3.24 Extreme water level variations and its correspondence to the Pacific Decadal Oscillation and length of the ice-free season.

(a.) Time-series plot showing modeled annual maxima and minima water levels (vertical bars) at a model grid point in about ~20 m water depth seaward of Foggy Island Bay plotted against the (normalized) positive (red shading) and negative (blue shading) phases of the Pacific Decadal Oscillation climate index. Colored circles are the 3-year moving mean of the annual maxima (black) and minima (blue) water levels. (b.) Scatter diagram showing the annual count of water levels greater than or less than climatological threshold water levels plotted against the number of

open water days for the same year. Climatological thresholds are the 75th (5 cm) and 25th (-10 cm) percentile water levels computed from the 30-year time series from 1980 to 2010.

3.6.3 Total suspended solids

Previous studies have shown that total suspended sediment (TSS) concentrations are strongly correlated with wind and sea conditions during the summer open-water period (Trefry et al. 2009). Measurements show that TSS concentrations tend to be less than 15 mg/L until wind speeds exceed 10 m/s when current and wave action intensifies. Under these stormy conditions, bottom sediments are re-suspended and TSS levels increase to 50 – 100 mg/L or more (Coastal Frontiers, 2014). Results from the calibrated Tier 2 wave-hydrodynamic-sediment transport model developed for this study fall within these guidelines (Table 3.13) and additionally illuminate on the spatial variability and relative contribution of swell and wind-waves compared to just wind-induced currents on elevated TSS concentrations.

Accounting for natural spatiotemporal variability in the wind fields illuminates the effect of winds and waves on TSS. For example, Figure 3.25 shows a week-long modeled time series of winds, waves, current speeds, and TSS in August 2020 at the UAF mooring site. At the beginning of the time series it is seen that 6-7 m/s winds from the east (100º) produce currents on the order of 12 cm/s (Figure 3.25b,c) and in combination with half meter high waves (Figure 3.25a) initiate suspension of bottom sediment to concentrations on the order of 10 mg/L (Figure 3.25d). The wind then subsides on August 8 and the horizontal currents decrease to <4 cm/s, but simultaneously remnant wave energy propagates past the point causing the near-bed orbital velocities to peak at ~20 cm/s (dashed black line in Figure 3.25a) which imparts a vertical water flux (Fig 3.25d) and TSS silt concentrations to reach 50 mg/L near the bed. As the wave energy subsides and winds remain low (<4 m/s) the sediment falls out of suspension and TSS silt concentrations diminish by the early hours of August 10. Later the same day, winds from the northwest pick up speed and in response, TSS concentrations increase slightly

Clays and silts dominate the TSS concentration signal, with sand transport (suspended and bedload) only occurring during higher wave events (>1 m). Modeled silt and sand sediment concentrations are compared in Figure 3.25e,f at the UAF mooring to illustrate the difference in magnitude. Silt concentrations tend to be the greatest due to their high mobility, low fall speed, and relative abundance at the seabed (compared to clay).

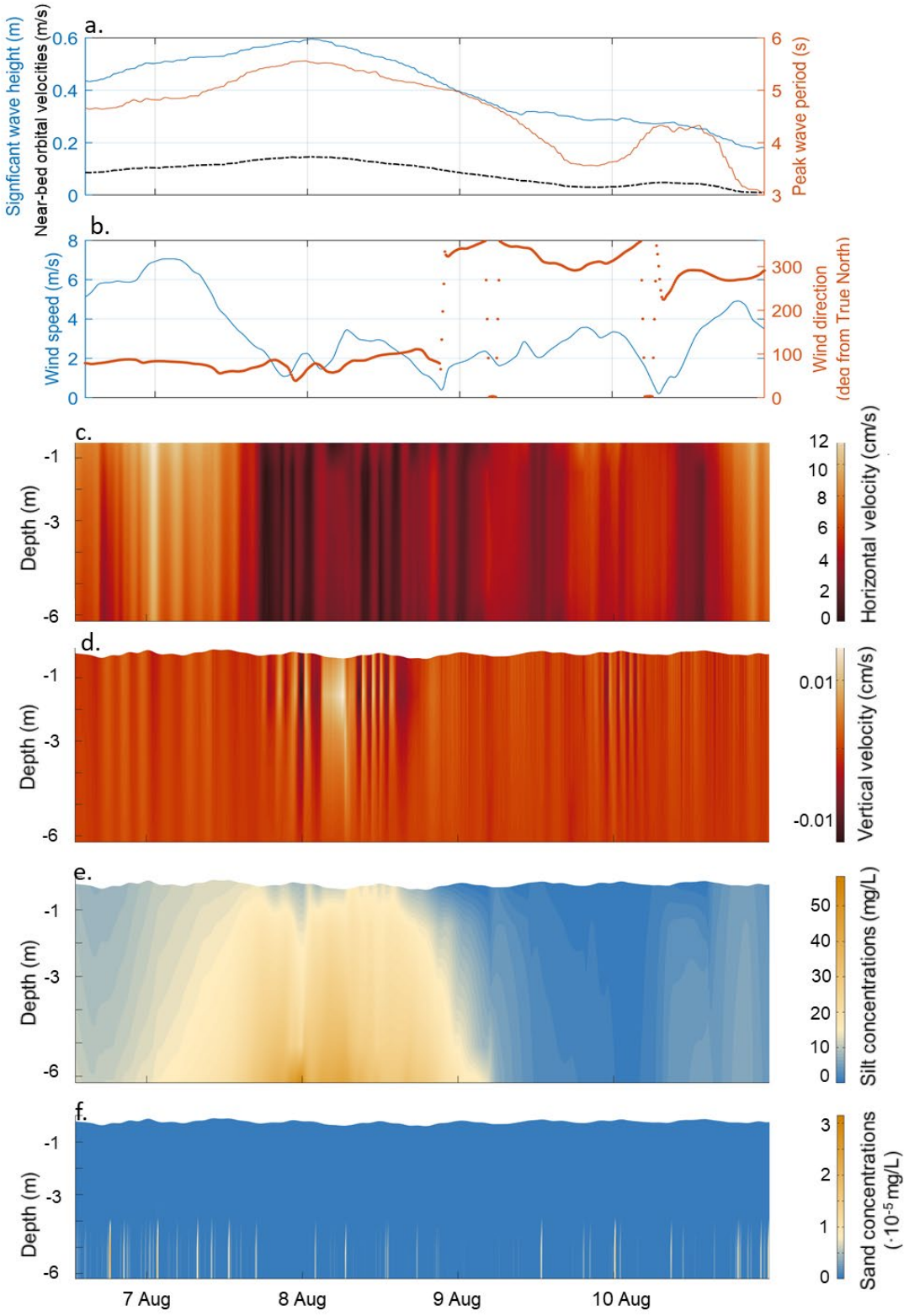

Figure 3.25 Modeled waves, water levels, currents, and sediment concentrations throughout the water column at the UAF mooring in August 2020.

3.6.4 Under-ice currents and suspended sediment concentrations

During the winter landfast ice season, under-ice currents are known to be weak (<5 cm/s), variable, and uncorrelated with wind and sea level fluctuations (Weingartner et al. 2009, 2017). Observations collected across the Alaska Beaufort Shelf suggest that circulation beneath the landfast ice is controlled by time-varying along-shore pressure gradients (order 10^{-6} m/s^2) and frictional coupling of the currents to the seabed and sea ice (Weingartner et al. 2009; Weingartner and Kasper, 2011). The origin of the pressure gradients is in part due to along- and cross-shore variations in ice width and/or under-ice friction (Kasper and Weingartner, 2012) and additionally larger scale atmospheric or ocean circulation fields (Weingartner and Kasper, 2011). While density differences were not accounted for in these model simulations, indications are that modeled current magnitudes beneath the sea ice are reasonable and that they are insufficient to mobilize meaningful volumes of seabed material, even though much of it is within the cohesive silt fraction. For example, modeled currents beneath the sea ice in March 2019 when winds reached nearly 15 m/s did not exceed 6 cm/s (colors in Figure 3.26) 5 mg/L of TSS (contour lines in Figure 3.26).

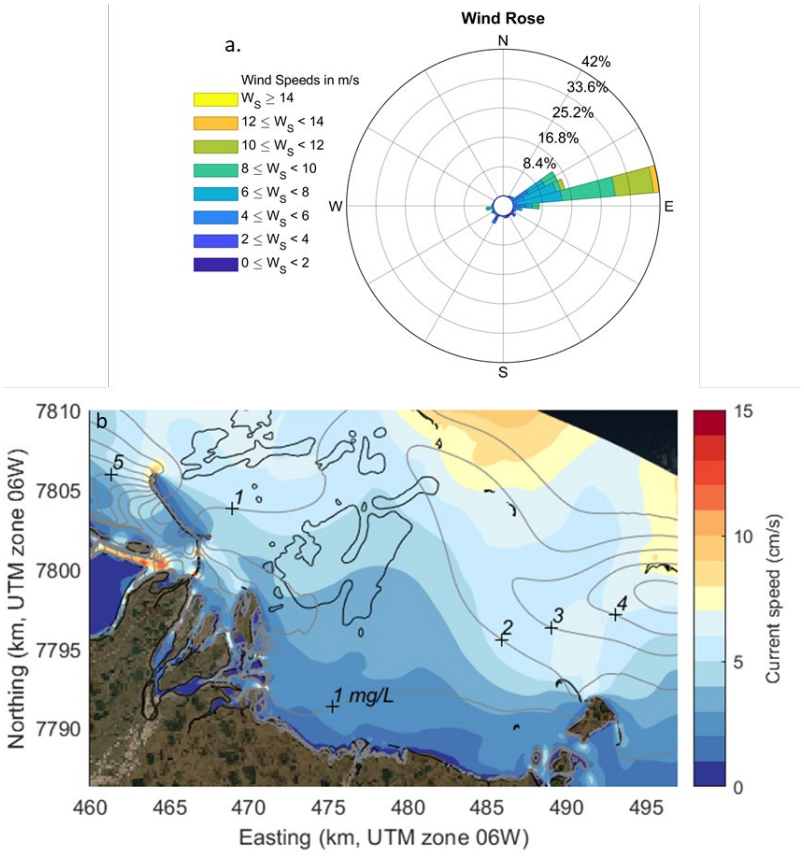

Figure 3.26 Modeled under-ice currents and suspended sediment flux in March 2019.
(a.) Wind rose showing the ERA5 wind speed, direction, and frequency of occurrence within the center of the model domain in March 2019. (b.) Map showing modeled maximum currents and TSS beneath the sea ice in early March 2019. Colors denote the current speed and contours the total TSS concentrations. Contour levels are indicated with the '+' sign. The Boulder Patch area is shown with a black outline.

4 Modeling of Coastal change

Coastal change modeling (CCM) included long-term hindcasting and forecasting of shoreline change within Foggy Island Bay (part 1 (Section 4.1)), as well as process-based modeling of geomorphic change during the course of an open-water season accounting for individual storm events (part 2 (Section 4.2)). For the long-term hindcasting and forecasting of shoreline change, we used the Coastal One-line Assimilated Simulation Tool (CoSMoS-COAST, Vitousek et al. 2017). CoSMoS-COAST is a numerical, transect-based, one-line model used to simulate long-term shoreline evolution. The model accounts for long-shore sediment transport, cross-shore sediment transport, sea-level rise, and sediments supplied by natural and anthropogenic sources. Data assimilation in the form of an extended or unscented Kalman filter was used to improve the model skill. To make the CoSMoS-COAST model applicable to the Arctic, a thermal component was added to the model. Thermal processes, such as thawing permafrost and decreasing ice protection, were accounted for by modifying the last term in the governing equation (Kupilik et al. 2020). Hindcasting covered the period from 2007 to 2017 in which annual shoreline position data were available, and the projection covered the period from 2019 through 2049 (30 years). Shoreline position data from 2018 were used for model validations. In contrast to Section 3 modeling for which the projection time-period starts in 2020, the forecasting/projection time-period used for the coastal change model starts in 2019 in order to provide a continuum following the last measured shoreline position in August 2018. The projection time-period extends 30 years, with a stop date of August 2049. Hindcasted and projected wave time series from the stand-alone Tier 2B wave model (Section 3.2.2) were used as boundary conditions for the CoSMoS-COAST model.

In addition to the CoSMoS-COAST model that was developed to estimate decadal scale projections of shoreline change (further described in Section 4.1 below), a process-based, coastal geomorphic change model was also developed to assess the fate and transport of eroded bluff sediment (mass wasting) from individual storms along the Foggy Island Bay coast (Section 4.2). The coast in this portion of the Alaska Beaufort Sea erodes via the bluff face thaw / slump mechanism in which bluff sediment thaws and slumps to the beach face and then is transported offshore via storm waves (Ravens and Peterson 2021). The first step of the bluff face thaw / slump erosion mechanism (i.e., the bluff face thawing and slumping) was simulated using a 1D thermal model oriented perpendicular to the bluff face. In this model, any bluff-face sediment which thawed was transferred to the beach face fronting the bluff on a daily basis. The second step of the erosion mechanism (cross-shore sediment transport during storm events) was modeled using the open-source, coastal geomorphic change model, XBeach (Roelvink et al. 2010). The combination of the two models, referred to as Arctic XBeach, simulates a series of two-step sequences to determine the total shoreline and geomorphic change of the open water period. To evaluate the fate of mass wasted bluff sediment due to the combination of cross- and along-shore currents, a test case was conducted whereby the mass wasting event of 2017 was introduced into the coupled wave-hydrodynamic-sediment transport model ‘Tier 2C’ (Section 3.2.3).

4.1 CCM1: Long-term hindcasting and forecasting of shoreline position

4.1.1 Methods

As indicated above, we used the one-line model, CoSMoS-COAST, to hind-cast and forecast shoreline position. CoSMoS-COAST solves a coupled set of differential equations along a series of cross-shore

transects. The central governing equation states that the time rate of change of shoreline position, $\frac{\partial Y}{\partial t}$ $(\frac{\mathrm{m}}{\mathrm{s}})$ is the sum of four terms (Equation 4.1). The first term represents the contribution to shoreline change due to alongshore variation in longshore sediment transport, where the Q is the longshore sediment transport rate, and X is the spatial coordinate in the alongshore direction, D_c is the depth of the active beach (sum of the depth of closure and berm height), and K is an empirical coefficient. The second term represents the shoreline change contribution due to cross-shore sediment transport due to wave energy disequilibrium (Yates et al. 2009). The Yates model asserts that for a given short-term (seasonal) shoreline position (Y_{st}), there is a corresponding equilibrium wave energy $E_{eq}(Y_{st})$. Further, for simplicity, the equilibrium wave energy can be assumed to be linear with short-term shoreline position (i.e., $E_{eq} = aY_{st} + b$). When, for a given shoreline position, the wave energy (E) differs from E_{eq}, there will be a tendency toward shoreline change related to the amount of disequilibrium ($\Delta E = E - E_{eq}$), as quantified in the second term on the right-hand side of Equation 4.1. Here, C is an equilibrium shoreline change magnitude parameter. The third term represents shoreline retreat due to relative sea-level rise, where $\frac{\partial S}{\partial t}$ is the rate of relative sea level rise, tanβ is the beach slope, and c is a calibration coefficient. The model assumes a sea level rise of 0.30 m by 2050, relative to 2007.

$$\frac{\partial Y}{\partial t} = -\frac{K}{D_c}\frac{\partial Q}{\partial X} + CE^{1/2}\Delta E - \frac{c}{tan\beta}\frac{\partial S}{\partial t} + V_{lt} \quad (4.1)$$

The fourth term represents unresolved natural and anthropogenic processes. To capture processes specific to the Arctic, such as decreasing ice protection and thawing permafrost, the White formulation (White et al. 1980, Equation 4.2) has been used to represent the V_{lt} term (Kupilik et al. 2020):

$$V_{lt} = \lambda X \frac{R^{0.2}H^{0.8}}{\tau}(T_w - \delta_w) \quad (4.2)$$

where:

- T_w is the water temperature (ºC),
- δ_w is the melting point of frozen water (ºC),
- X is an empirical constant with a value of 0.000146 ($ºC^{-1}$),
- R is the surface roughness (taken as 0.1 m following White et al. 1980),
- H is the wave height (m),
- τ is wave period (s), and
- λ is the ratio of energy required to melt a unit volume of pure ice at 0 ℃ relative to the energy required to bring a unit volume of composite material to 0 ℃ and melt it (Equation 4.3).

$$\lambda = \left[\frac{L_w p_i}{L_w p_i W + p_b C_b (T_w - \delta_w)}\right] \quad (4.3)$$

Here:

- L_w is the latent heat of fusion of water (J/kg),
- p_i is the ice density (kg/m^3),
- W is the water fraction of the composite material,
- p_b is the bulk density (kg/m^3), and
- C_b is the bulk specific heat capacity (J/(kg C)),

For this study, additional transect-specific model training of the thermal erosion term was achieved by adding a factor referred to as "t_factor" to the V_{lt} equation (Equation 4.4).

$$V_{lt} = \lambda X \frac{R^{0.2} H^{0.8}}{\tau} (T_w - \delta_w) * \text{t\_factor} \quad (4.4)$$

The solution to Equation 4.1 is achieved by breaking up shoreline position (Y) into a short term and a long-term component (i.e., $Y = Y_{lt} + Y_{st}$) and splitting the overall governing equation into a pair of equations, with Equation 4.5 and Equation 4.6 addressing short term and long-term shoreline change, respectively (Vitousek et al. 2017). The splitting procedure allows addressing short term (seasonal) shoreline change due to wave energy disequilibrium (where $\Delta E = E - E_{eq}$, with $E_{eq} = aY_{st} + b$) separately from long-term shoreline change. The split model equations are written:

$$\frac{(Y_{st})_k^{n+1} - (Y_{st})_k^n}{\Delta t} = C_k (E_k^n)^{1/2} (E_k^n - a_k (Y_{st})_k^n) - b_k) \quad (4.5)$$

$$\frac{(Y_{lt})_k^{n+1} - (Y_{lt})_k^n}{\Delta t} = -\frac{K_k}{d_k} \frac{Q_{k+\frac{1}{2}}^{n+\theta} - Q_{k-\frac{1}{2}}^{n+\theta}}{\Delta X_k} - \frac{c_k}{tan\beta_k} \left(\frac{\partial S}{\partial t}\right)_k^n + (V_{lt})_k \quad (4.6)$$

In these equations, the subscript n represents the time step index, Δt is the time step (1 day), k indicates the particular cross-shore transect under consideration, and ΔX_k is the distance between adjacent transects. Note, the sediment transport coefficient (K_k), normally a part of the equation for alongshore transport, Q, is pulled out of Q so that it can be adjusted in the data assimilation procedure. Note also, most of the terms in Equation 4.5 and 4.6 have "k" subscripts indicating that they are defined at individual transects. However, two of the subscripts are "k+1/2" and "k-1/2," and they are subscripts of the alongshore transport Q. In principle, the gradient of alongshore sediment transport is estimated based on the transport between transects on the upstream and downstream side. Finally, the variable Θ ($0 \leq \Theta \leq 1$) in Equation 4.6 defines the implicitness of the calculation scheme.

4.1.2 CCM1 Inputs

To represent the shoreline at Foggy Island Bay adequately, 318 shore-perpendicular transects were generated. Transects are shore-normal to the extent possible. The transects usually start a few hundred meters landward of the bluff edge and end at the 5 m depth contour (Figure 4.1). Most transects are spaced approximately 50 m apart with the exception of some transects spaced about 100 m apart. Based on the location of the main distributary of the Sagavanirktok River delta, the CoSMoS-COAST model was split up into two parts. Model 1 includes transects 1-151 (west of the main distributary) and Model 2 includes transects 152-318 (east of the main distributary).

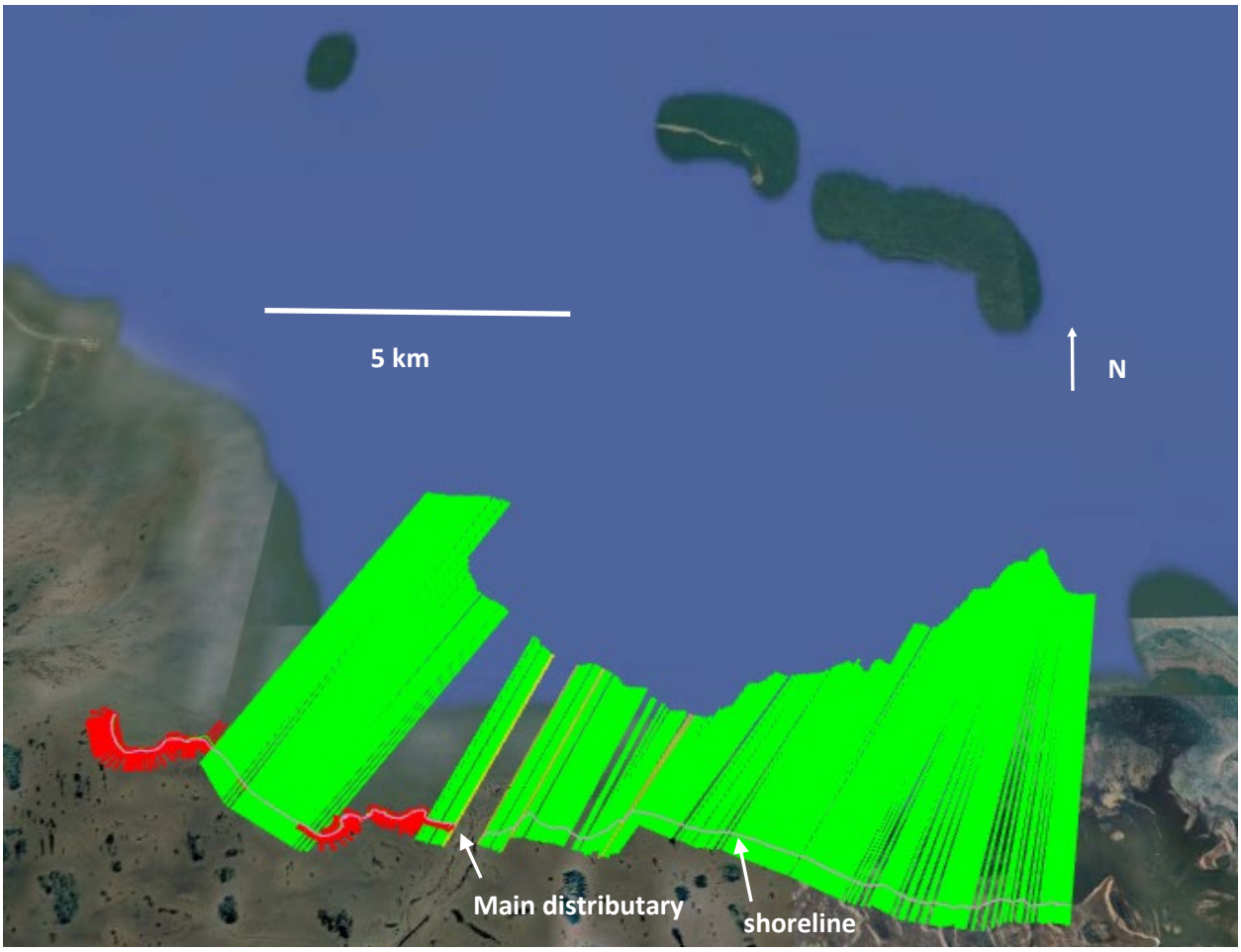

Figure 4.1 Map showing transects used in Foggy Island Bay study.
Red transects indicate that only the cross-shore terms are included and green transects indicate that both longshore and cross-shore terms are included. The gray line is the shoreline. The T-shaped structure in the upper left is the Endicott Causeway for which the eastern-most point is 70.320 N, -147.859 E.

Within CoSMoS-COAST there is an option to either use the Full Model (using all 4 terms on the right-hand side of Equation 4.1) or Cross-Shore Only Model (using only the second, third, and fourth terms on the right-hand side). In Figure 4.1, the green transects indicates that the Full Model was used on these transects, in the first set of model runs. The red transects indicate that only the Cross-Shore Model was used. While it's ideal to run the Full Model whenever applicable, the Cross-Shore Only model was used along transects where the incident wave angle at the 5 m depth contour did not seem applicable to nearshore conditions. Therefore, longshore sediment transport was turned off for those transects. Note, in the final set of model runs and particularly for the forecasts, we opted to use the Cross-Shore Model for all of the transects because the longshore transport term caused significant instability in the forecasted shoreline position that was deemed to be physically unrealistic.

All known variables, such as beach slope, water temperature, sea ice, and wave climate act as model inputs and are used as forcing parameters. On the north coast of Alaska, such data can be difficult to obtain, and the data are expected to vary spatially. All unknown input variables were estimated using an

unscented Kalman filter based on known historical shoreline positions. Below, we discuss the model inputs used to drive the CoSMoS-COAST model.

The nearshore sea ice concentration and water temperature in the historical period were obtained from the Marginal Ice Zone Modeling and Assimilation System (MIZMAS, Schweiger and Zhang 2015). Sea ice concentration, water temperature, and land surface temperature for the forecasted 2019–2049 period were obtained from the HadGEM-SST GCM available from the World Climate Research Program (WCRP) coupled Model Inter-comparison Project (Phase 6), https://esgf-node.llnl.gov/projects/cmip6/. USGS North Slope of Alaska LiDAR from 2010 in conjunction with the composite bathymetric dataset of Foggy Island Bay (Section 2.2.1) were used to determine representative beach slope along each transect. Hindcasted wave climate at the 5 m isobath from the wave model Tier 2B (Section 3.2.2) and hind-casted storm tide time series at the 15 m isobath computed with the Tier 1 hydrodynamic model (Section 3.4) were used as forcing.

Annual georeferenced aerial images of Foggy Island Bay were supplied by BP Alaska from 2006 through 2018. Based on the quality of the images and ease of delineating observed shorelines, images from 2006, 2008 and 2011 were excluded. Timestamps were not available for the aerial images. Therefore, it was assumed that the acquisition date was August 1 every year.

4.1.3 Estimation of Parameters

To solve the governing equation (Equation 4.1), all of the unknown variables are included a state vector, ψ, defined: $\psi = [Y_{lt}\ V_{lt}\ Y_{st}\ C\ a\ b\ c\ K\ t\_factor]^T$. With nine state variables in the state vector, there are nine nonlinear equations. Each transect at Foggy Island Bay has a state vector specific to that transect. The long-term shoreline component Y_{lt} and the short-term shoreline component Y_{st} vary temporally, while the other seven unknown variables are estimated using a Bayesian filter. The unscented Kalman filter (UKF) was chosen for this study to avoid some of the limitations associated with the extended Kalman filter (EKF).

Based on rigorous testing of both models, the error covariance matrix and the additive noise matrix were set as follows for both models, following Kupilik et al. (2020):

$$P = [1\ \ 0.1\ \ 1\ \ 0.1\ \ 0.1\ \ 0.1\ \ 1e-10\ \ 0.1\ \ 1e-2]^2$$

$$Q1 = [1\ \ 1e-3\ \ 1\ \ 1e-3\ \ 1e-2\ \ 0.05\ \ 1e-10\ \ 1e-2\ \ 1e-3]^2$$

4.1.3.1 Initial Values

Setting appropriate initial values for all state variables ensures state variables converge to a stable solution. While the initial values for some of the variables were computed, others were set based on a trial-and-error approach, where we selected the value, which resulted in a stable model with a reasonably low Root Mean Square (RMS) error. The long-term shoreline component Y_{lt} was set to the coastal position in 2007. The short-term shore component Y_{st} was set to zero. Yates shoreline equilibrium coefficient, C, was set to -0.005, while coefficient, a, was set to -0.1. The Yates equilibrium coefficient, b, was set to the average wave height between 2007 and 2018. The Bruun coefficient, c, was set to 1. The longshore transport coefficient, K, was set to 15. The thermal coefficient, t_factor, was set to 0.80 and 0.65 in Model 1 and Model 2, respectively.

4.1.3.2 Unscented Kalman filter versus Extended Kalman filter

The EKF has become a standard technique for nonlinear estimation and machine learning applications. However, the EKF has some inherent flaws. The EKF propagates a Gaussian random variable (GRV) through the system dynamics. In the EKF, the state distribution is approximated by a GRV, which is then propagated analytically through the first-order linearization of the nonlinear system. Large errors can be introduced through this approach in the posterior mean and covariance of the transformed GRV. The UKF, on the other hand, uses a deterministic sampling approach. The state distribution is approximated by a GRV, but it's now represented by a number of sampling points. These sampling points capture the mean and covariance of the GRV more accurately. While an EKF only captures the mean and covariance to the first-order, the UKF captures the mean and covariance to the third-order for any nonlinearity (Wan and Van der Merwe, 2000).

For this study, the UKF was chosen for its performance in the context of state-estimation for nonlinear systems.

4.1.4 Results

4.1.4.1 Shoreline erosion hind-casting with CoSMoS-COAST (2007-2018)

Time-averaged observed and modeled erosion rate in the model domain (transects 1-318) between 2007 and 2018 is plotted in Figure 4.2. Averaged observed and modeled erosion rate was 1.16 and 1.19 m/year, respectively, though there was great spatial variability. The peak in observed erosion rate was about 8 m/year on transect 44, and erosion rates were elevated in transects 43-46. At this location, there was a low elevation spit that served as the creek bank, rather than an elevated bluff (Figure 4.3a). There was a second area of rapid erosion at transects 191-195, where the shoreline was again a sand spit (Figure 4.3b).

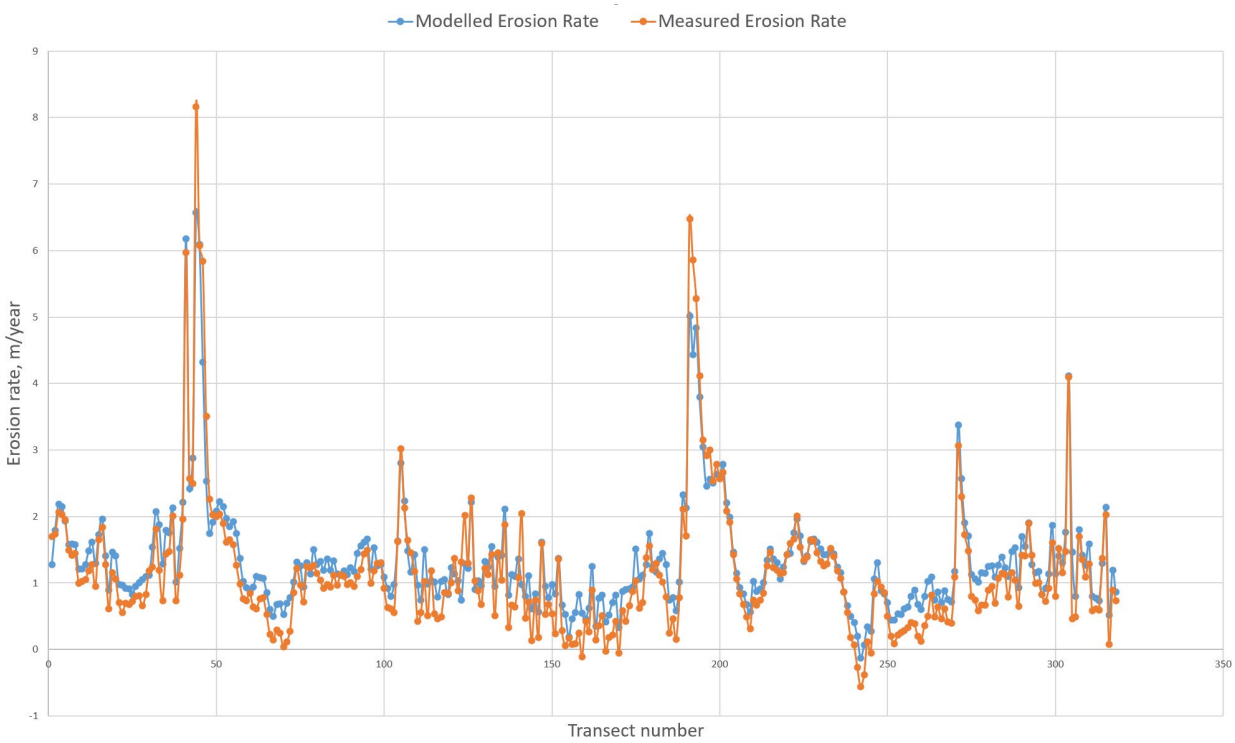

Figure 4.2 Measured and modeled average erosion rate (m/year) between 2007 and 2018 at transects 1-318, including Model 1 and 2.
Erosion rates (vertical axis) are plotted against transect ID numbers **(horizontal axis)**.

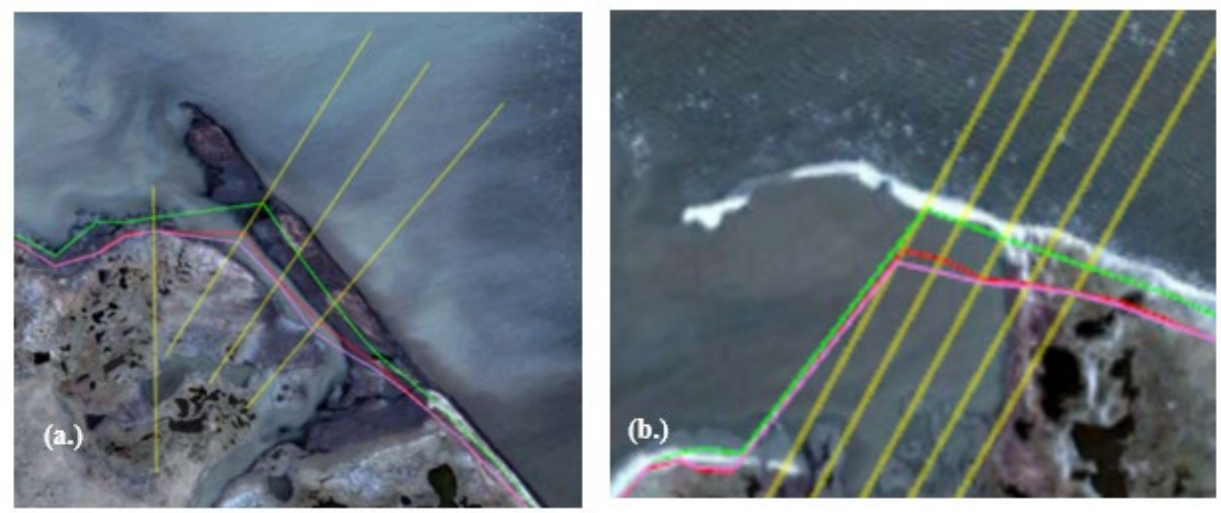

Figure 4.3 Mapped figures showing the observed 2007 (green) and 2018 (pink) shorelines, along with the modeled 2018 shoreline (red), at (a) transects 43-46 and (b) transects 190-194.
Both plots show a 2010 Google image in the background. The green line is the initial (2007) shoreline position, the pink line is the measured 2018 shoreline, and the red is the modeled 2018 shoreline. Note, there is a minor "disconnect" between the 2007 shoreline and the 2010 Google image. The 2010 Google image may have been taken at low tide, and there may have been shifting of the Google image relative to the high resolution geotiff used for the designation of the shoreline position

Model error was calculated based on the difference between the predicted and observed 2018 shoreline (Figure 4.4). The overall RMS error of the original model (including the longshore term) was 3.59 and 3.70 m for Model 1 and Model 2, respectively. The overall RMS error of the final model (excluding the longshore term) was 3.88 and 3.53 m for Model 1 and Model 2, respectively. Thus, the use of the longshore term did not affect the error assessment in a significant way. The error was relatively large (greater than 15 m) at the locations where the shoreline was part of a sand spit (e.g., transects 44-46, 191-193). Note that the one-line model employed in this study was not designed to account for sand spit migration.

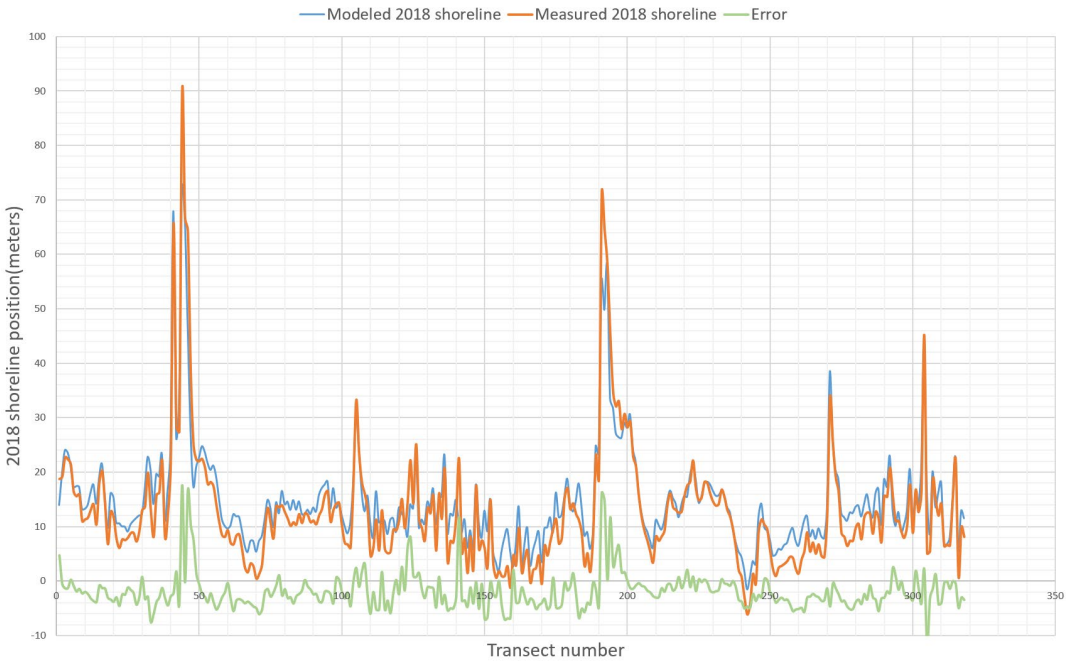

Figure 4.4 Modeled and measured 2018 shoreline position relative to the 2007 shoreline position, along with the model error.
Shoreline positions (vertical axis) are plotted against transect ID numbers (horizontal axis).

The percent contribution to total change along each transect between 2007 and 2018 was calculated for each of the processes including: longshore transport, cross-shore transport due to non-equilibrium wave conditions, relative sea level rise, and thermal processes (Figure 4.5). Note that the long-shore component was turned off for a number of transects (particularly in Model 1) where the incident wave angle at the 5 m bathymetric contour did not seem applicable to nearshore conditions (Figure 4.1). It is noteworthy that the cross-shore term contributed positive (accretionary) shoreline change, while both thermal erosion and the sea-level rise term contributed negative shoreline change. The contribution of the longshore transport term was positive or negative, depending on the shoreline orientation.

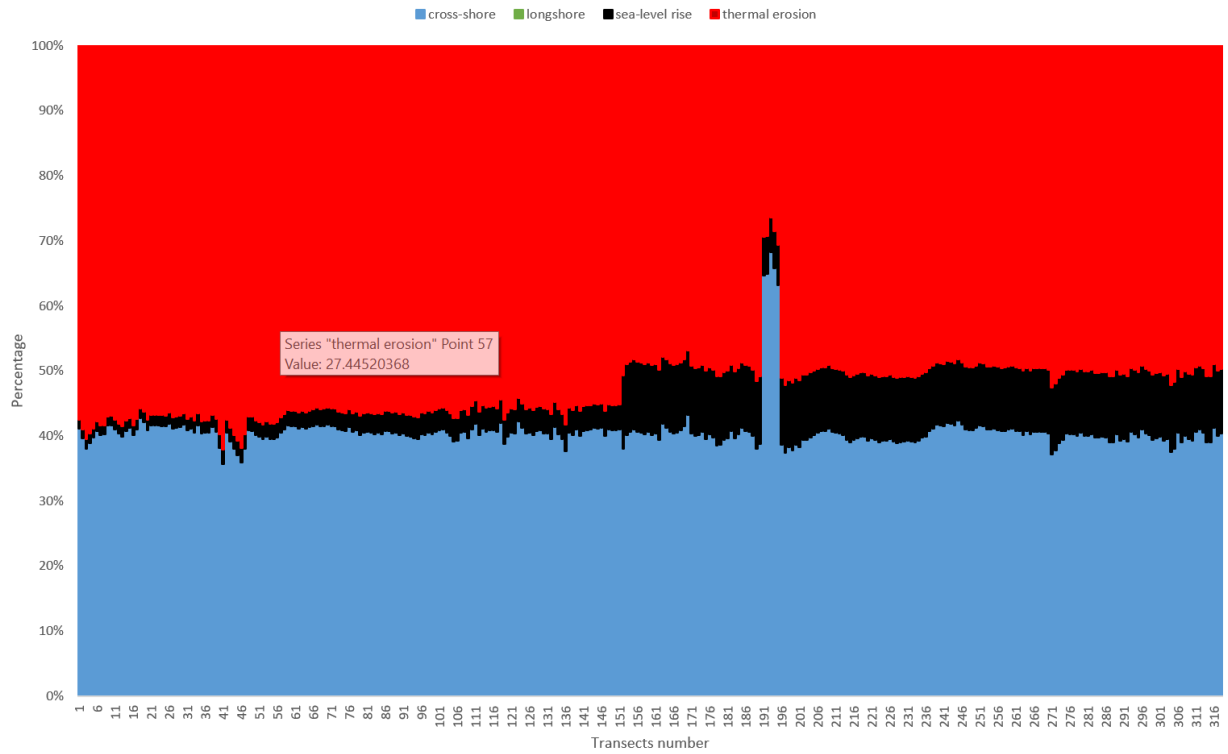

Figure 4.5 Percent contribution of cross-shore transport, sea-rise, and thermal erosion to retreat between 2007 and 2018 for transects 1-318.
Percent contributions (vertical axis) are plotted against transect ID numbers (horizontal axis).

4.1.4.2 Shoreline erosion forecasting with CoSMoS-COAST (2019–2049)

The CoSMoS-COAST model, calibrated with the 2007-2018 period, was used to predict Foggy Island Bay shoreline into the future (2019–2049). Data on sea ice, nearshore water temperature, and a wave times-series produced with the nearshore wave model Tier 2B (Section 3.2.2) and the HadGEM-SST GCM were used for the 2019–2049 time-period projection. Figure 4.6 provides plots of the 2018, 2030, and 2049 model-calculated shoreline positions relative to 2007 as a function of transect number. Figures 4.7 and 4.8 provide the 2007 (green), 2018 (red), and projected 2030 (pink) and 2049 (yellow) shorelines on a 2006 Google image background, for the Model 1 domain and the Model 2 domain, respectively.

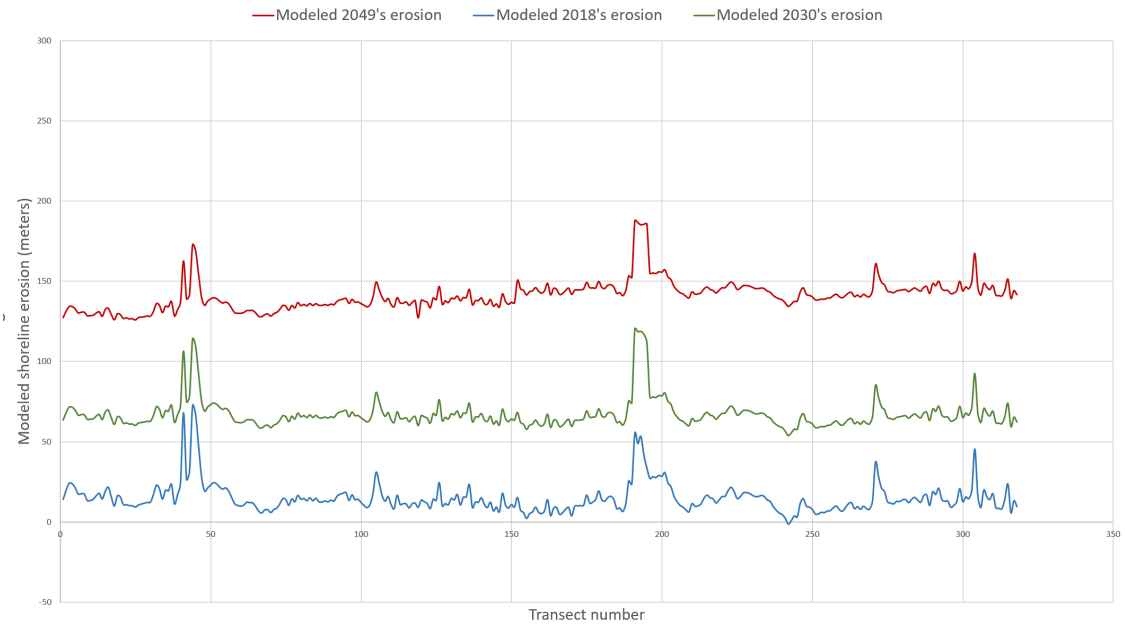

Figure 4.6 Plot of modeled shoreline erosion in 2018, 2030, and 2049 relative to the 2007 shoreline position.

Figure 4.7 Plots of the observed 2007 (green) and 2018 (red) shorelines, along with the projected 2030 (pink) and 2049 (yellow) shoreline, for the Model 1 domain.
The background is a 2006 Google image and the transects shown are transects 43-46, also shown in Figure 4.3a.

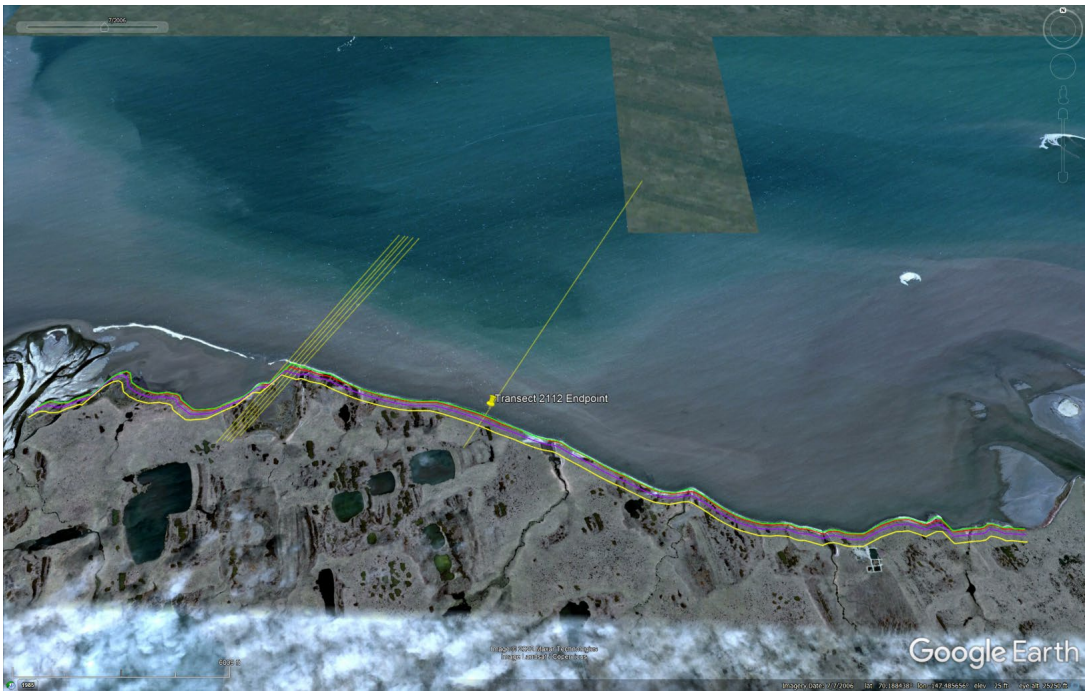

Figure 4.8 Plots of the observed 2007 (green) and 2018 (red) shorelines, along with the projected 2030 (pink) and 2049 (yellow) shoreline, for the Model 2 domain.
The background is a 2006 Google image and the transects shown are transects 190-194 and 231, which is coincident with USGS Transect #2112 (the focus of Section 4.2 in this report).

The average Modeled shoreline retreat (erosion) over time at transect 231, which is coincident with USGS Transect #2112, indicates that the erosion rate is projected to increase in the future (Figure 4.9). Examination of the individual contributions to erosion rate at transect 231 indicates that the increased erosion rate is due to a reduced positive contribution from the cross-shore term, and due to accelerating sea level rise (Figure 4.10).

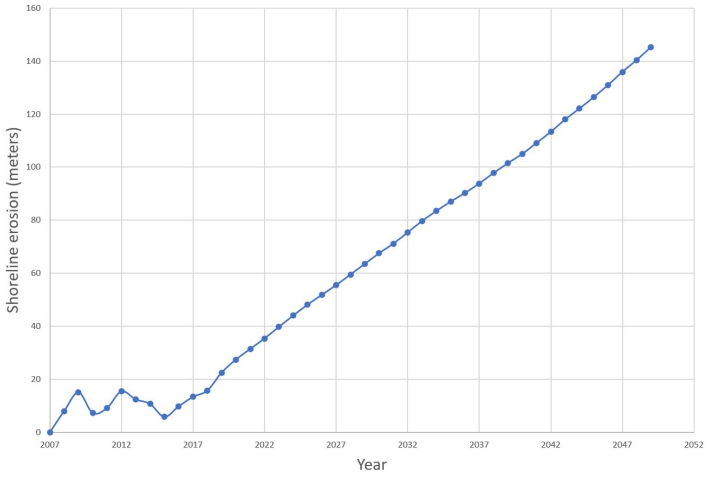

Figure 4.9 Hind-casted and projected shoreline erosion at transect 231 (USGS #2112) through the year 2049, relative to 2007.

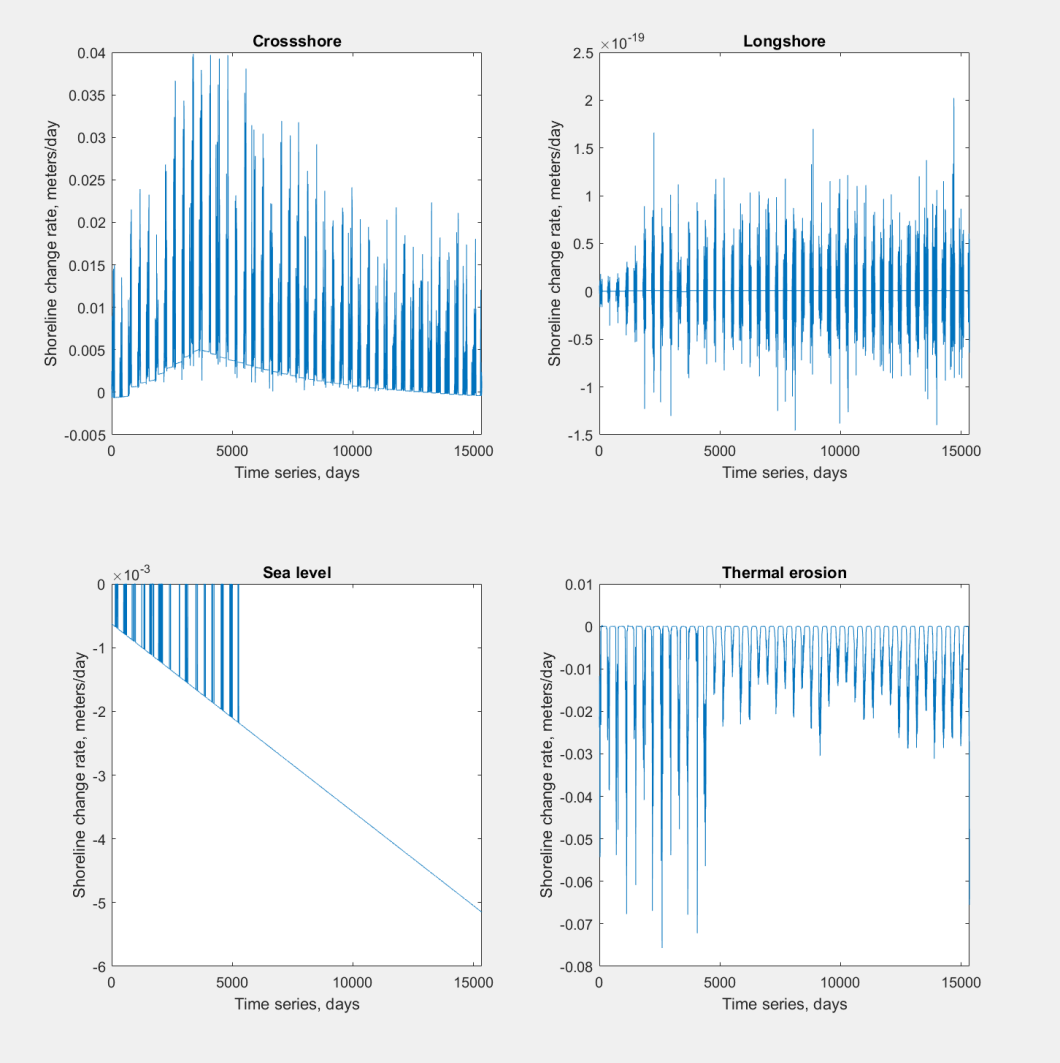

Figure 4.10 Contributions to shoreline change rate at transect 231 over time between 2007 and 2049.

A negative shoreline change rate (e.g., due to sea level rise and thermal erosion) indicates a positive erosion rate.

The projected increase in erosion rate at transect 231 is indicative of erosion rate increase at all of the transects. Figure 4.11 shows the average erosion rate between 2007 and 2018 and between 2040 and 2049, as a function of transect number. The data show that the Foggy Island Bay average erosion rate increases from 1.16 m/year for 2007–2018 to 4.5 m/year for 2040-2049.

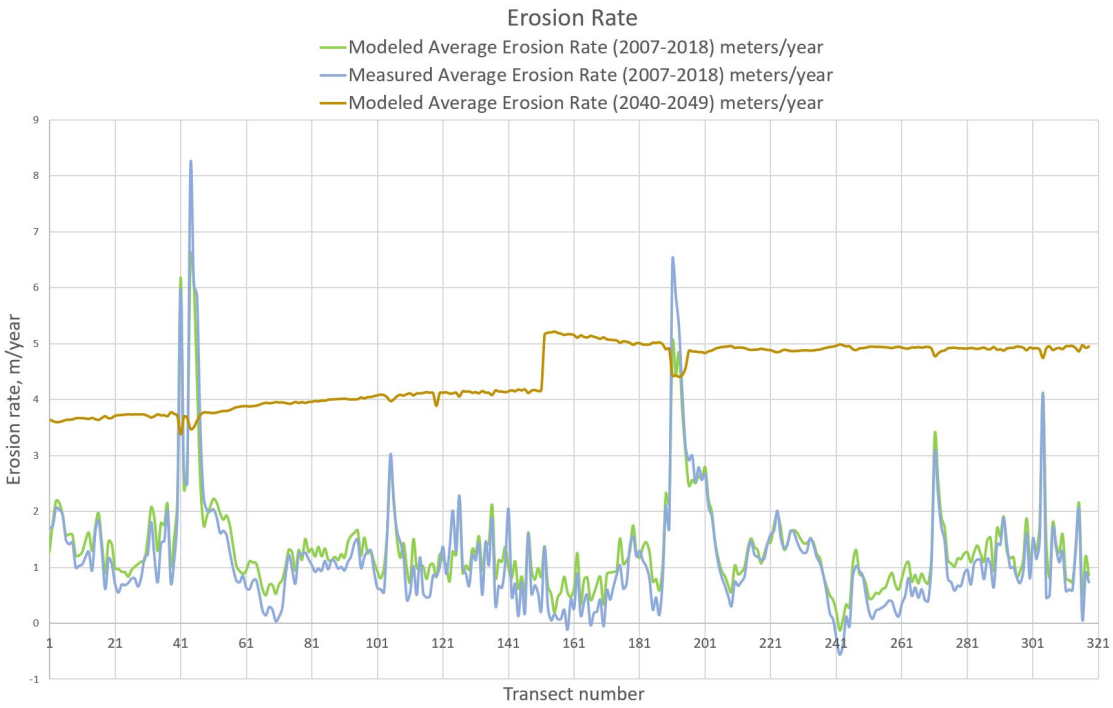

Figure 4.11 Plot of modeled and measured erosion rate in 2007-2018 and modeled erosion rate in 2040-2049.

4.1.4.3 Discussion

As indicated above, the average measured and modeled erosion rate in Foggy Island Bay, for 2007-2018, was 1.16 and 1.19 m/year, respectively. In comparison, Jones et al. (2008) reported the erosion rate to be 2.5 m/year for the Alaska Beaufort coast. The relatively low erosion rate at Foggy Island Bay is consistent with its erosion mechanism - bluff face thaw / slump (or thermal denudation). Ravens and Peterson (2021) identified bluff face thaw / slump and niche erosion / block collapse as the principal erosion mechanisms active on the Alaska Beaufort coast, and they noted that the erosion rate with the bluff face thaw slump is relatively low.

The CoSMoS-COAST model forecast indicates that the Foggy Island Bay erosion rate will increase from the historical 1.2 m/year in the historical period (2007-2018) to 4.5 m/year in the 2040-2049 period. This is a surprisingly large increase in erosion rate. In order to gain confidence in this result, a number of activities were undertaken. The activities included:

1. We double checked that the input parameters were reasonable. All of the important variables from 2007 – 2049 were plotted (Appendix C). All of the input variables were deemed to be reasonable with the exception of the nearshore water temperature from the HadGEM-SST Global Climate Model.
2. We explored alternative thermal erosion formulations. The White formulation used in this study was developed originally to model iceberg thaw. The actual mechanism of erosion at the Foggy Island Bay coast is quite different from iceberg thaw. As we will see in the second part of this study, a reasonable alternative approach would be to tie the thermal erosion to the land surface temperature. Preliminary calculations indicated that driving the thermal erosion model using the

land surface temperature led to an improvement in the accuracy of the 2018 model calculation. The calculation also led to 2049 erosion amounts similar to what was determined with the White formulation (Appendix C).

4.2 CCM2: Process-based modeling of coastal geomorphic change

4.2.1 Methods

4.2.1.1 Description of the two-step erosion model

In order to provide more detailed information about the coastal geomorphic change in Foggy Island Bay and, in particular, to provide data on the amount of "mass wasting" during individual storms, a coastal geomorphic change model, Arctic XBeach, was developed. For simplicity, the model was developed for a single USGS transect (#2112), with offshore and onshore end points of 481849.7 E, 7788118.9 N and 481607.2 E, 7787625.2 N, UTM Zone 6, respectively (Figure 4.12). Analysis of shoreline position data by USGS transect #2112 from 2007 to 2018 (Figure 4.13) indicates that the average bluff and shoreline retreat rate is about 1.5 m/year.

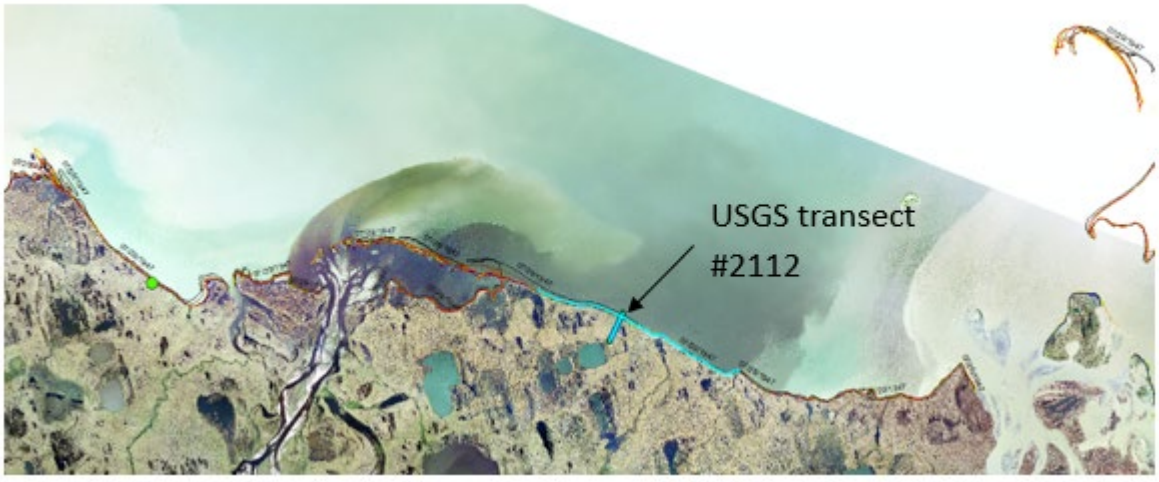

Figure 4.12 Aerial photo of Foggy Island Bay coastal zone and the location of USGS transect #2112.

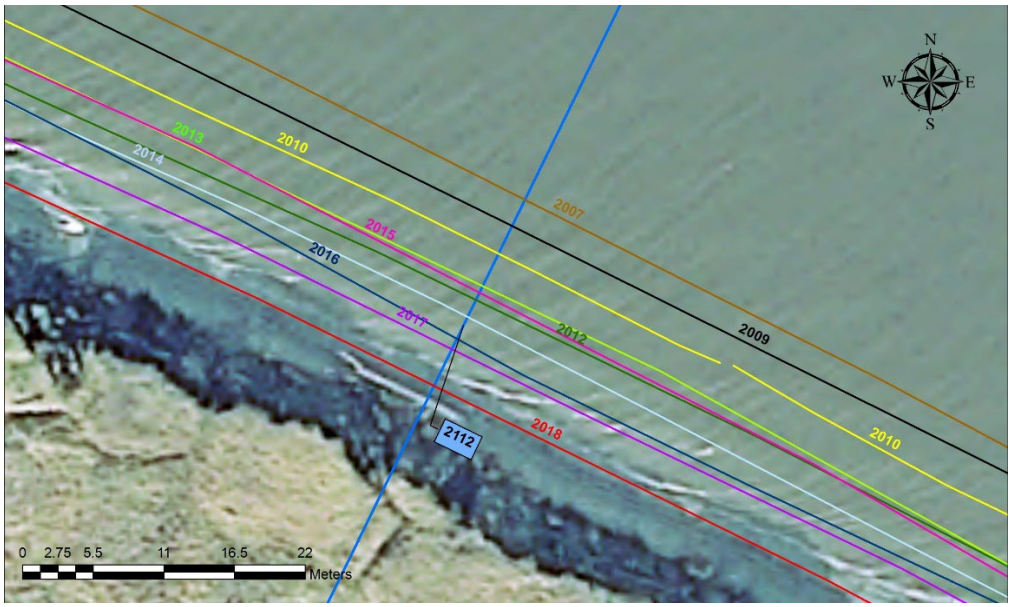

Figure 4.13 Mapped image showing Foggy Island Bay shorelines between 2007 and 2018, proximal to USGS transect #2112.

Figure 4.14 provides an aerial photo of the bluff and beach face proximal to USGS transect #2112, and it enables insight into the erosion mechanism. A close look at Figure 4.12 shows tundra vegetation sliding down the bluff face, indicating thawing of the bluff face and slumping of bluff face materials to the beach face. Coastal erosion at this location (and at most locations on the Alaska Beaufort coast) proceeds via a two-step process (Ravens and Peterson, 2021). In the first step, which occurs mainly during inter-storm periods, the bluff face thaws and thawed material slumps and deposits on the beach face (Figure 4.15). Solar radiation, longwave radiation (emitted from the earth surface and downward from the atmosphere), sensible heat, and latent heat fluxes combine to thaw the bluff face. In the second step, which occurs during storm periods, storm surges and waves transport slumped materials offshore.

Figure 4.14 Clip of a USGS aerial photo image of shoreline by USGS transect #2112.

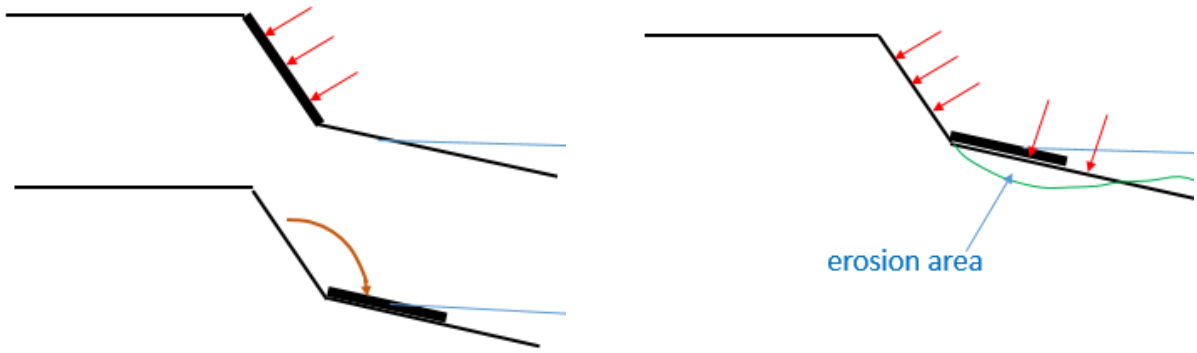

Figure 4.15. Schematic of the two-step erosion mechanism featuring (a) bluff face thaw / slump, followed by (b) offshore transport during storm surge events.

To represent the first step of the two-step sequence, a 1D thermal model – oriented perpendicular to the bluff face – was developed to predict ground temperature and phase, and it has been validated using available ground temperature data. For the second step, we have coupled the heat transfer model with an open-source coastal geomorphic change model, XBeach, creating Arctic XBeach. The XBeach user provides the bluff and beach topography and bathymetry, sediment grain size, and the offshore wave and water level boundary condition – and XBeach provides the change in the beach profile. With Arctic XBeach, the material is allowed to move only if it has been thawed. However, in this particular application, we expected limited benefits from using Arctic XBeach and ran the simpler XBeach model to represent storm-driven offshore transport in step 2.

The concept of the inter-storm / storm sequence is illustrated in Figure 4.16. The figure depicts nearshore water levels (including tides and storm surge at 5 m depth offshore) as well as wave height for the month of June and July 2017, computed with the Tier 1 hydrodynamic and Tier 2A wave models (Sections 3.4 and 3.21). The data show some storm surge events in the month of June. However, due to the presence of sea ice, there is little wave action until the month of July 2017. For effectual offshore transport of sediments, it is necessary to have both significant surge ($\eta > 0.4$ m) and significant wave height ($H_s > 0.4$ m). Since, coincident significant surge and wave height do not occur until July 20, the period between June 1 and July 19 can be considered an inter-storm period.

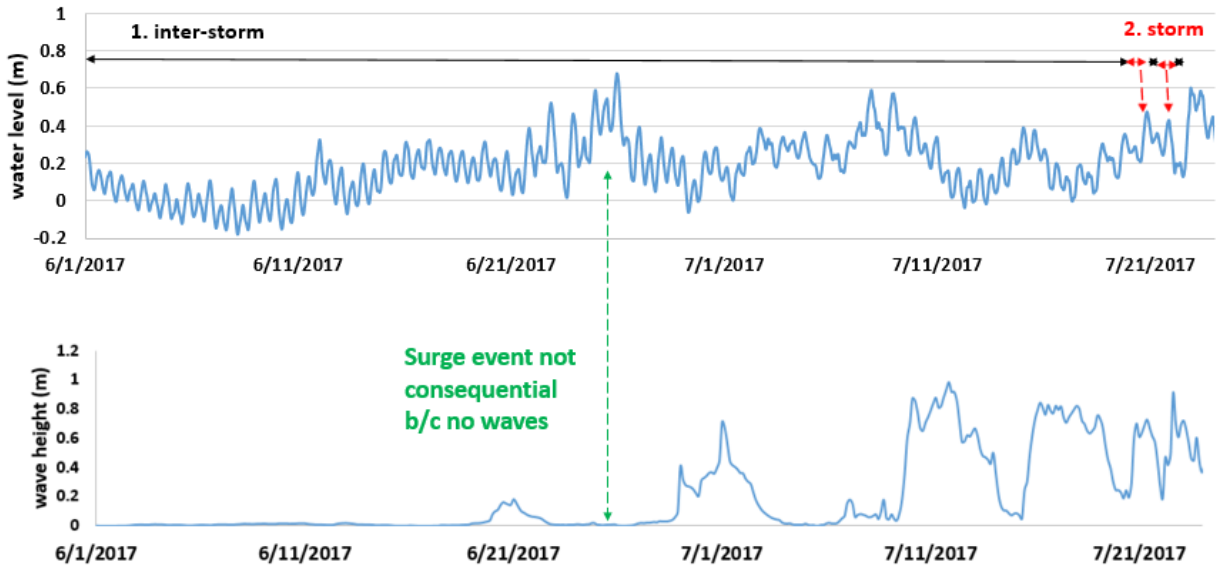

Figure 4.16. Time-series plots of water level and wave height in June and July 2017.
Black and red double arrows at the top of the figure depict the inter-storm and storm periods.

The 1D numerical thermal model to determine the bluff face thaw during the inter-storm periods is developed based on the 1D time-dependent heat balance equation in terms of enthalpy, H (Hu and Argyropoulos 1996, Equation 4.7).

$$\rho \frac{\partial H}{\partial t} = \nabla \cdot (K \nabla T) \qquad (4.7)$$

Where $H = c_s T \qquad for\ T < T_m$

$H = c_l T + (c_s - c_l) T_m + L \qquad for\ T \geq T_m$

c_s = specific heat of the solid phase

c_l = specific heat of the liquid phase

T_m = temperature of melting

L = latent heat

4.2.1.2 The solar flux calculator

In order to model heat flow along an axis perpendicular to the bluff face, it was necessary to develop a "solar flux calculator" that provided the solar (shortwave) radiation on the typical north-facing coastal bluff, which had a face angle of 45 degrees relative to the horizontal. Although both modeled and measured data on solar radiation on a horizontal surface were available for our study site on the Foggy Island Bay coast, data on north-facing, and angled coastal bluff face were not.

Solar intensity [W/m^2], I, on a flat surface is given by the equation (Buffo 1972):

$$I=I_0 p^{1/\sin(A)} \sin(\theta) \quad (4.8)$$

where: I_0= solar constant: radiation at the top of the atmosphere normal to the sun,
p = atmospheric transmission coefficient (based on altitude, weather),
A = altitude angle off of the horizontal that the sun's rays strike a horizontal surface,
sin (A) = sin (ϕ) sin (δ) +cos(ϕ)cos(δ)cos(h),
ϕ = latitude,
δ = declination (time of year),
h = hour angle,
θ = angle between the surface and the radiation,
Sin (θ)= sin (A)cos($\boldsymbol{\alpha}$)-cos(A)sin($\boldsymbol{\alpha}$)sin(Z-$\boldsymbol{\beta}$),
$\boldsymbol{\alpha}$ = surface slope from horizontal,
Z = azimuth (AZ) CCW from south + 90 degrees,
sin AZ = -cos(δ)sin(h)/cos(A), and
$\boldsymbol{\beta}$ = slope aspect from north (0 is north facing)

The details of the solar flux calculator are provided in Appendix C.

4.2.2 Validation of the two-step erosion model

The 1D numerical model was validated by simulating the "Stephan problem" and comparing the numerical solution to the published analytical solution (Hu and Argyropoulos 1996). In the Stephan problem considered here, there is a 1D bar with the properties of water, extending from y = 0 to ∞. The initial temperature is -5ºC (Figure 4.17). At t = 0, the surface (y = 0) is set to 2ºC, and heat flows from the surface into the bar (in the positive y direction). The numerical solution and the analytic solution (Hu and Argyropoulos 1996) at 10^5 seconds are shown to be in reasonable agreement (Figure 4.17).

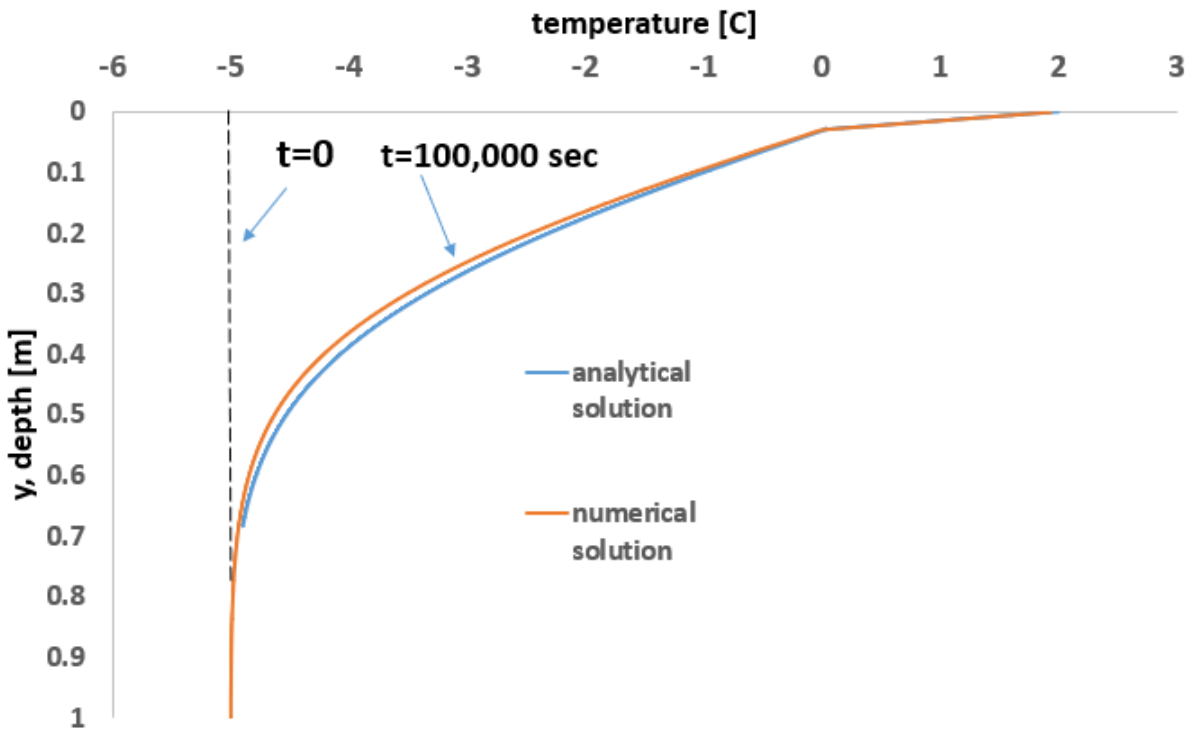

Figure 4.17 Depiction of the initial temperature and the analytical and numerical solution to the Stephan problem at 10^5 seconds.

The 1D thermal model was also validated using ground temperature data from West Dock, which is proximal to Foggy Island Bay. In this situation, we defined an initial, June 1, 2017, temperature distribution from the surface to a depth of 10 m, based on West Dock ground temperature data (https://permafrost.gi.alaska.edu). The model was "forced" using measured surface temperature data. Comparison of the modeled and measured ground temperature data on August 24, 2017, with the thermal properties shown in Figure 4.18, demonstrated a second validation of the 1D thermal model.

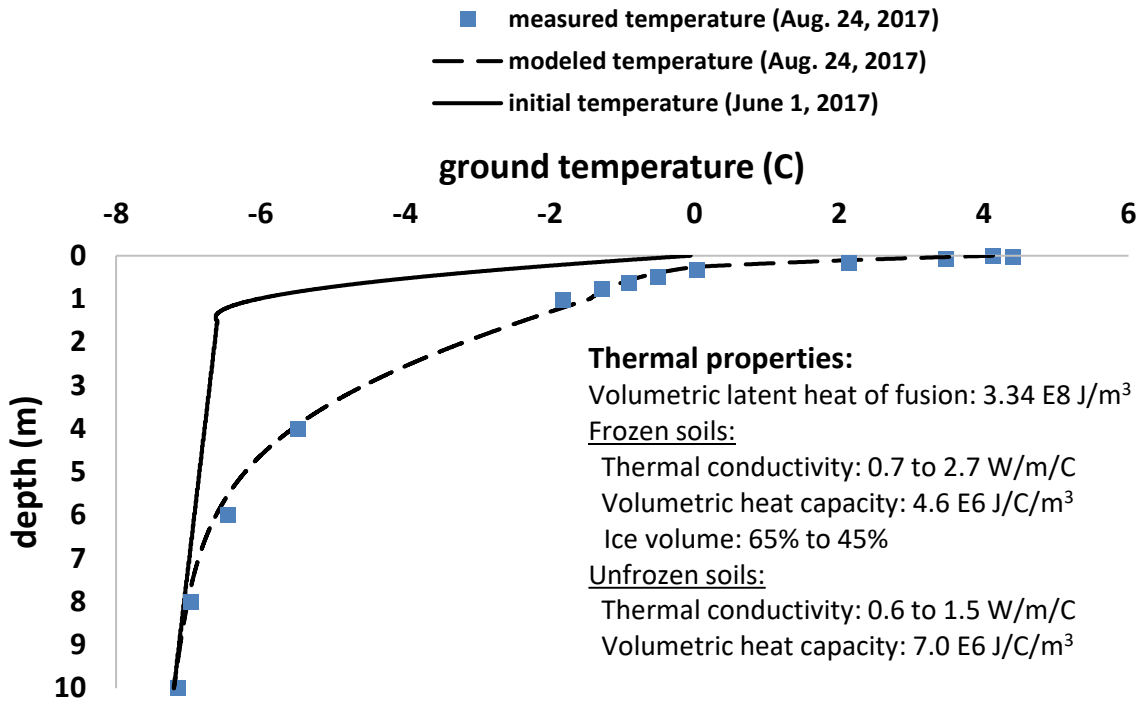

Figure 4.18 Depiction of the initial temperature distribution on June 21, 2017, along with the modeled and measured temperature distribution on August 24, 2017.

In addition, the 1D thermal model was validated for the case where a flux-type boundary condition was used at the tundra surface. The net heat flux was sum of the solar (short wave) radiation, the longwave radiation emitted from the earth's surface, the downward longwave radiation from the atmosphere, the latent heat flux, and the sensible heat flux (Figure 4.19). Note, over the time-period used in the figure (between July 14 and August 13, 2017), solar shortwave radiation (in red) diminishes significantly and so does the net heat flux (in blue). As shown in Figure 4.20, the modeled and measured August 24, 2017, ground temperatures were in reasonable agreement when the flux-type boundary condition was used. In addition, the modeled and measure thaw depths were also in agreement when the flux-type boundary was employed (Figure 4.21).

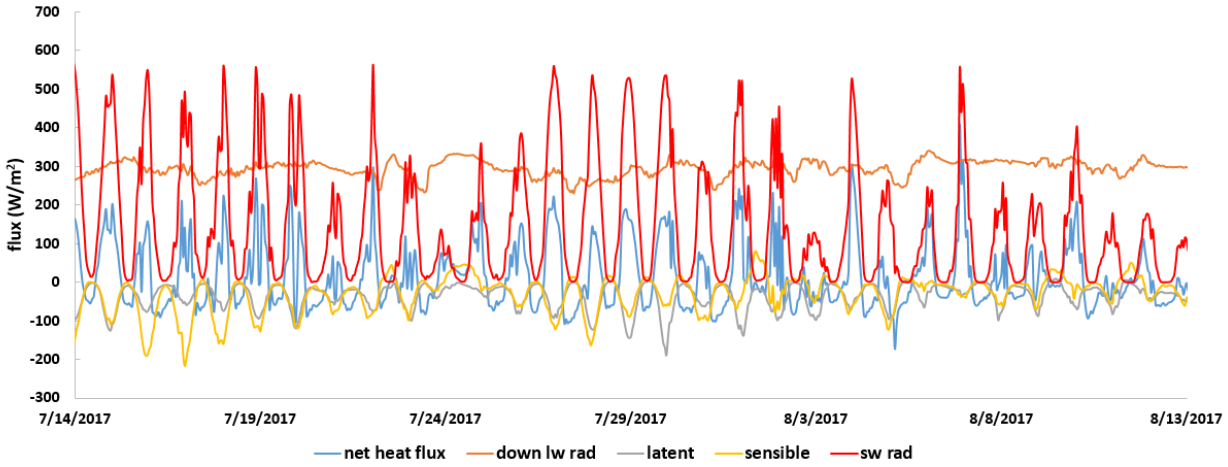

Figure 4.19 Plot of the 4 of the 5 computed heat fluxes as well as the net heat flux between July 14 and August 13, 2017, at West Dock.

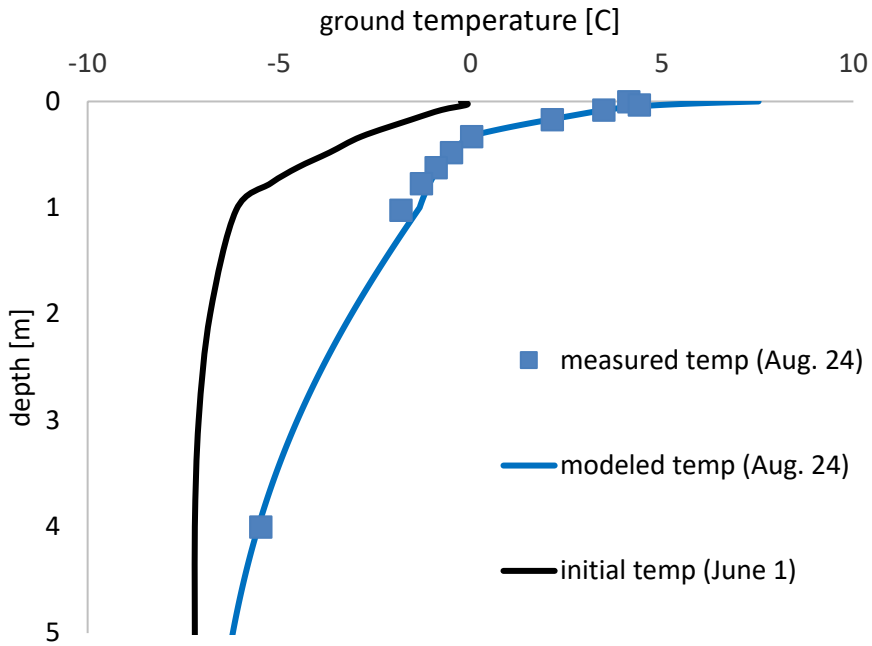

Figure 3.2

Figure 3.3

Figure 3.4

Figure 3.5

Figure 3.6

Figure 3.7

Figure 3.8

Figure 3.9

Figure 4.20 Initial (June 1, 2017) and measured and modeled August 24, 2017, ground temperature, with a flux-type boundary at the tundra surface.

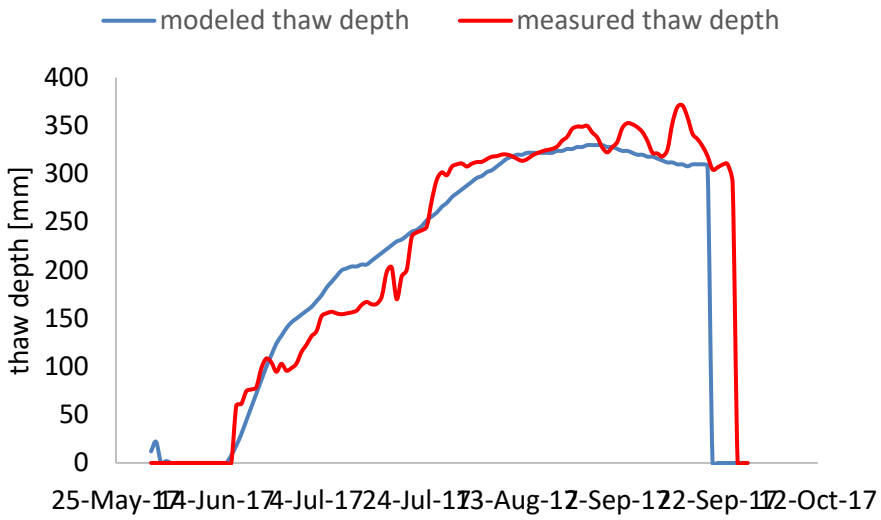

Figure 4.21 Plot of the measured and modeled thaw depth during the summer of 2017.

The *validation* effort described above concerned a vertically oriented temperature profile from the bluff top to a depth of 10 m (Figure 4.22a). We chose the vertical orientation because the available validation data (at West Dock) are along a vertical profile. The *application* of the 1D thermal model in the two-step erosion model, however, requires that the axis of the 1D thermal model be perpendicular to the bluff face as illustrated in the schematic in Figure 4.22b. In addition, the 1D thermal model in the two-step model removes any thawed material on the bluff face and daily deposits that material on an equivalent width of the beach face, adjacent to the bluff toe.

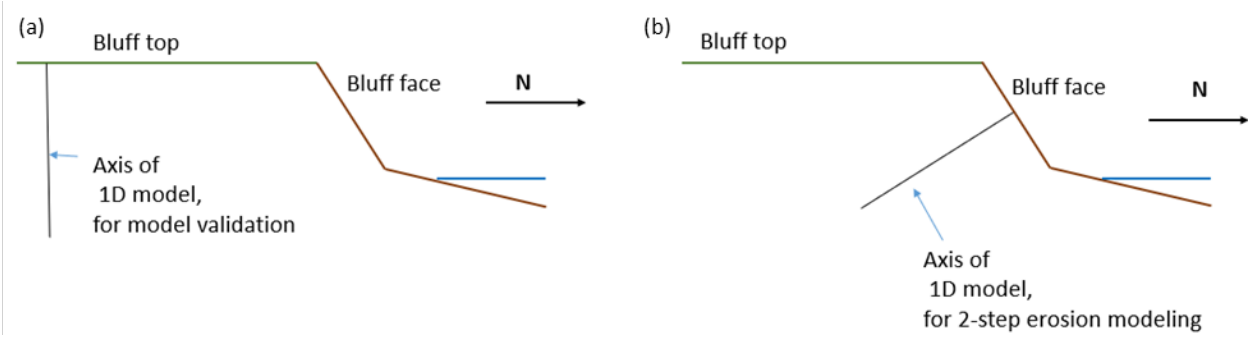

Figure 4.22 Schematics showing (a) the vertical axis of the 1D thermal model used for model validation and (b) the bluff face-perpendicular axis of the 1D thermal model used for the 2-step erosion modeling.

4.2.3 Results – application of the step 1 and step 2 models

The results of the application of the 2-step erosion model for the summer of 2017 are provided in Figure 4.23. The first inter-storm period extended from June 1 to July 19, 2017. During this time, there were no consequential storms as there were no instances where the water level and wave height simultaneously

exceeded 0.4 m. As shown in Figure 4.17, the solar radiation and the net heat flux are relatively high, so there would have been significant thawing and slumping of the bluff face. Calculations of thaw depth, using the 1D thermal model (step 1 model), find a total thaw depth of 0.51 m during this time-period. It is noteworthy that this is significantly above the thaw depth computed and observed with the vertically oriented axis (Figure 4.21). Since thawed material is removed from the bluff face and placed on the beach face on a daily basis, there is less material on the bluff face to insulate the deeper layers of the bluff from heat transfer from the atmosphere. The thaw area corresponding to the 0.51 m thaw depth is the product of the depth and the length of the bluff face in the cross-shore direction (about 9.4 m). The deposition of the slumped material is depicted in the beach and bluff profile shown in the upper right of Figure 4.23.

The first consequential storm of the summer of 2017 occurred on July 20, and it had an offshore surge and wave height of 0.47 and 6.4 m, respectively. The XBeach model of this storm computed an erosion area of 1.4 m^2. The eroded portion of the beach face during the July 20 storm is depicted in the profile in the lower right of Figure 4.21. Given that the depth of the active beach was about 7 m, this erosion area corresponds to a linear erosion distance of 0.2 m. Given that the net depositional area from the first inter-storm period was 4.8 m^2 and given that the first storm eroded only 1.4 m^2, we conclude that there was still 3.4 m^2 of material left on the beach face. For simplicity, that material would be assumed to be distributed over the 9.4 wide section of beach face proximal to the bluff toe. The second inter-storm period lasted only 1 day, and it yielded a thaw depth of 0.03 m (corresponding to a depositional area of 0.3 m^2). Hence, following the second inter-storm, the net depositional area was 3.7 m^2 = 3.4 m^2 +.3 m^2 (Figure 4.21). The two-step model was applied for the remainder of the open water period until freeze-up on August 30, a date determined by temperature observations from the study site.

As a final step to investigating the potential fate of the eroded bluff material, we introduced the estimated volume of the mass wasting event into the coupled wave-hydrodynamic-sediment transport model (Tier 2C) described in Section 3.2.3. Assuming ice-free conditions through mid-October and using ambient wind, and atmospheric pressures to drive the Tier 2C model, the resulting tide, surge, and wave conditions would have caused the eroded bluff material to move alongshore with the predominant concentrations toward the northwest during a high wave event (Figure 4.25).

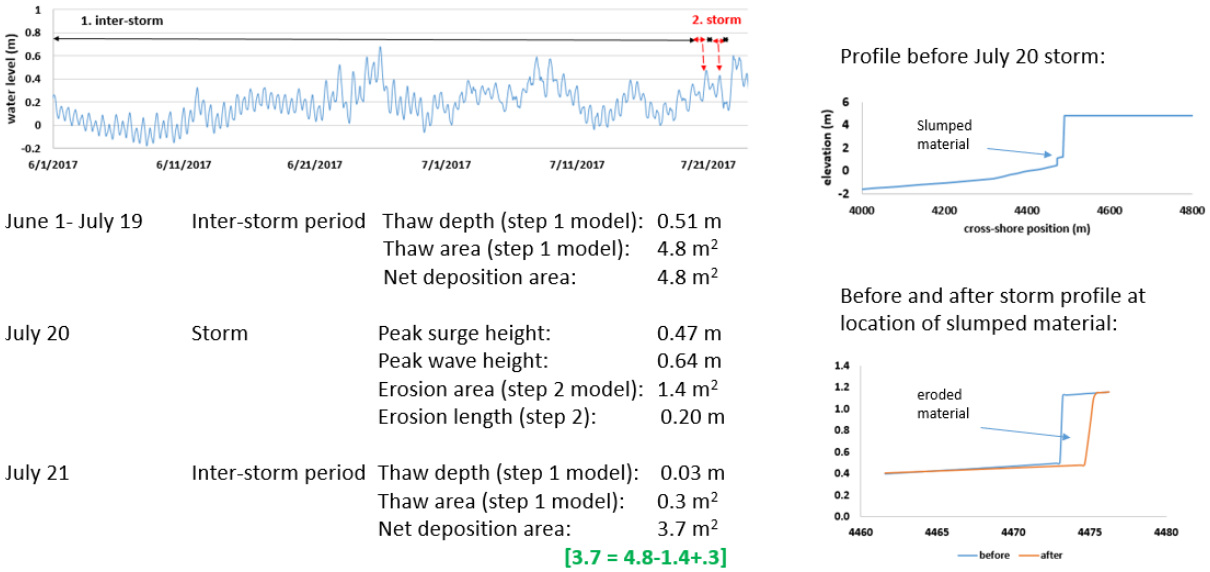

Figure 4.23 Depiction of details of the two-step erosion model for the summer of 2017.

Figure 4.24 depicts the modeled shoreline erosion between June 1 and August 30, 2017, based on the two-step model, along with the annual observed erosion (1.48 m), based on high resolution aerial photos from 2012-2018. The two-step erosion model and erosion measurements are in rough agreement.

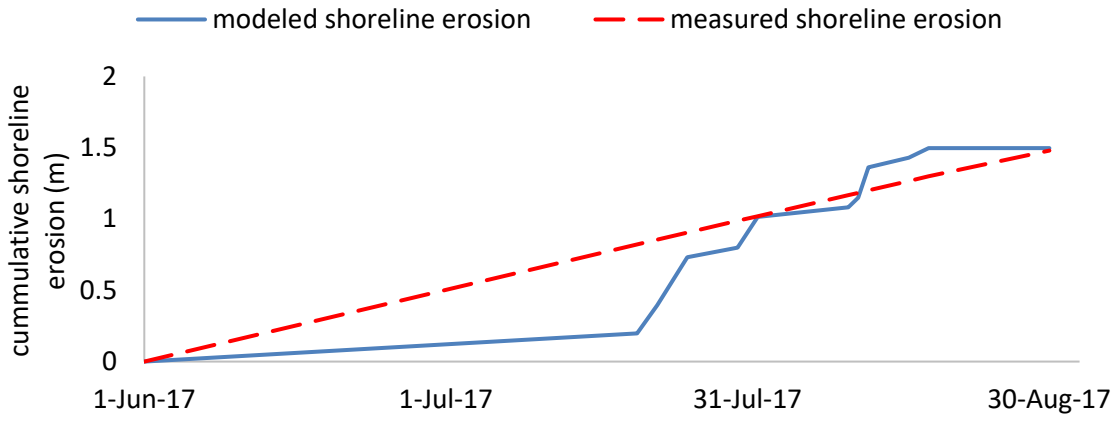

Figure 4.24 Plot of the modeled and measured shoreline change between June 1 and August 30, 2017.

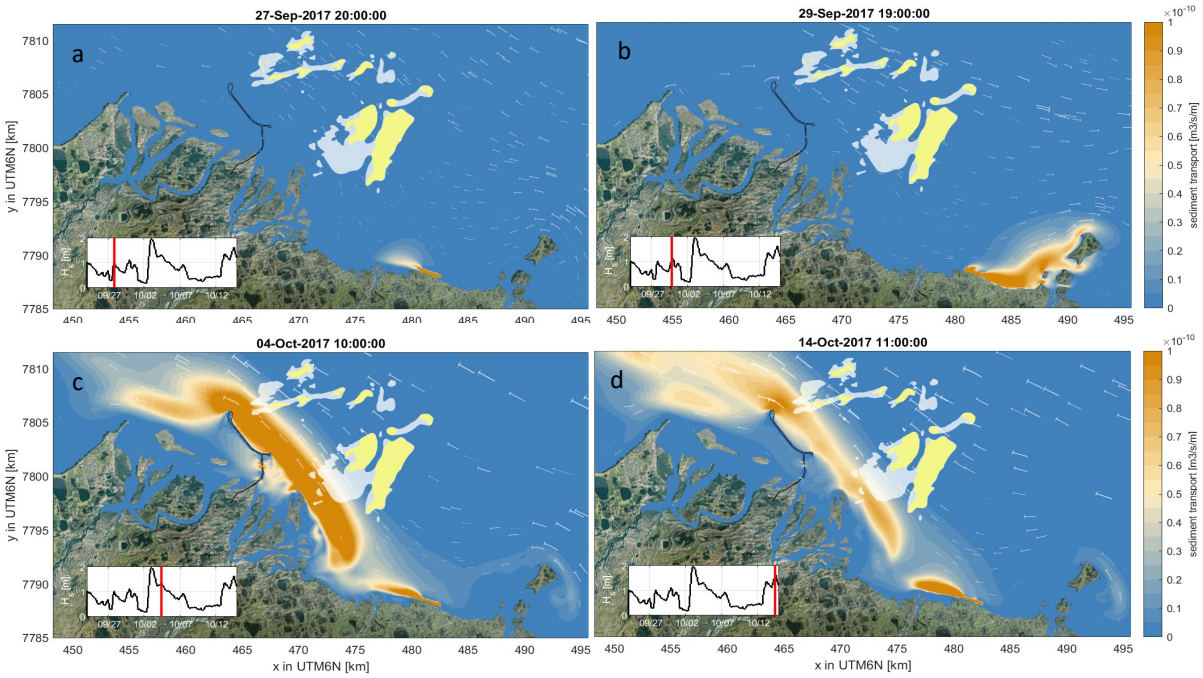

Figure 4.25 Maps showing modeled fate of eroded bluff material after the hindcasted mass wasting event in September 2017.
(a-d) Time snapshots showing concentration and transport of eroded bluff material. The volume of eroded material was estimated using model CCM2 and inputs from the Tier 2B wave and Tier 1 hydrodynamic models. Shown sediment concentrations (light to dark brown colors) and velocity vectors (white arrows) are derived with the coupled wave-hydrodynamic-sediment transport model Tier 2C. Inset shows a time series of the wave heights (vertical scale 0 to 2 m) with the red bar depicting the time-point of the mapped image.

5 Conclusions and future directions

The research described in this report culminates a unique set of numerical models specifically designed to evaluate past (1979-2019) and future (2019-2049) conditions of waves, hydrodynamics, sediment transport and shoreline erosion within Foggy Island Bay. Model development was supported by oceanographic, meteorological, bathymetric, topographic, and water quality data collected specifically for this study and complemented with historical data obtained within Stefansson Sound and beyond (e.g., Gallaway 1983; Short et al. 1986, 1987).

The local-scale wave-hydrodynamic-sediment transport numerical model, resolved at 50 – 200 m horizontal resolution across Foggy Island Bay and parts of Stefansson Sound, was successfully calibrated and validated against field measurements collected at point locations within the Bay and the Sound. Modeled waves, water levels, and currents exhibit root-mean-square differences of about 15 cm, 13 cm, and < 10 cm/s, respectively. Depth-averaged currents are biased somewhat low overall (<-5 cm/s), which likely contribute to the overall negative bias of modeled TSS concentrations (on the order of -2.52 ± 6.29 mg/L). Whereas the model results are biased low, the order of magnitude and overall pattern of higher and lower values appear well represented during the open water and winter landfast ice seasons. Under recent conditions (2010 through 2019), full ice cover typically occurs during November through May/June. The

open-water season (when sea ice concentrations are less than 5%) has on average increased from just a few days per year in 1979 to more than 3 months (110 days) in 2019. A linear trend analysis reveals a statistically significant decrease in the median sea ice concentrations of -1.3% per year and -1.7% per year for the summer (June through July) and fall (September through November), respectively. Over the same analyzed time-period from 1979 to 2019, no statistically significant trends in wind speed were found (Nederhoff et al. 2022).

Model results and field measurements show that under-ice currents are weak (< 6 cm/s) and poorly correlated with winds. The slow current speeds are reflected in both measured and modeled total suspended sediment concentrations, which are on the order of 1 – 2 mg/L within Foggy Island Bay (Figure 3.25).

During the approximate 3-month long open water season, currents are swift (40-70 cm/s) and well correlated with winds (Figure 2.9). When wind speeds reach ~10 m/s, currents become sufficiently strong (≥~15 cm/s) to initiate and transport the finer sediment fractions. Whereas wind-driven currents are capable of mobilizing sediment from the seabed, most of the sediment resuspension is driven by wave action. For example, model results show that a 12 m/s wind produced near-bed TSS concentrations of ~10 mg/L in ~6 water depth and that under similar conditions that additionally included the influence of 0.60 m 5 s waves, TSS concentrations reached more 60 mg/L at the same location (Figure 3.13). In most cases, clay and silt dominate TSS concentrations (Figure 3.24), with sand transport (suspended and bedload) only occurring during higher wave events (>1 m). Silt concentrations tend to be greatest due to their high mobility, low fall speed, and relative abundance at the seabed (compared to clay).

The 41-year hindcast of nearshore waves within Foggy Island Bay shows a two-fold increase of the spatial median annual wave height from 1979 to 2019. The highest events typically occurred in mid-September during the first hindcast decade and have since shifted toward early to mid-October (approximately 20 days later in the season). The longer open-water season and expansion of fetch have also affected the frequency of high wave events so that the number of 'rough wave days' (when wave heights exceed 2.5 m) have increased from less than 7 days/year at the start of the time series in 1979-1984 to more than 13 days/year toward the end of the hindcast period. Whereas wave heights and wave power increased significantly over the 1979-2019 time-period, only minor trends in median wave period (0.03 sec/year) and wave steepness (wave height divided by wave period) were found. Mean wave periods rarely exceed 11 s; this in combination with the weak trend suggests that while some increase in swell (waves generated by distant storms and characterized by wave periods greater than 12-15s) energy has occurred, local seas still dominate the full wave energy spectrum. A barrier island chain located <20 km offshore of Foggy Island Bay mitigates offshore wave energy reaching the study area and additionally limits the fetch for local wave growth within Foggy Island Bay. The ephemeral barrier islands changed shape and configuration over the study time-period, but have thus far generally remained intact, effectively filtering offshore wave energy from the north-northwest to the northeast from reaching Foggy Island Bay.

Akin to the increase in frequency of larger waves, the occurrence of surge and setdown events were also found to increase with time due to the longer open-water season. The number of surge and setdown events, relative to the 25th and 75th climatological quantiles (calculated from the 30-year 1980 to 2010 time series), increased at a rate of 0.13 events per day of increase in the open water season (R^2 = 0.79; *pval*<0.05; Figure 3.23b). A small but statistically significant negative trend (-0.2 cm/year) of the 3-year moving mean annual

maximum storm surge was found. Due to the limited length of the analyzed time-period, it was not possible to assess the influence of multi-decadal large scale climate patterns on the negative trend in annual maxima, but a qualitative correspondence between elevated storm surge levels was noted with the negative phase of the Pacific Decadal Oscillation (PDO).

Modeled time series of water levels and waves within Foggy Island Bay were used as inputs to two coastal change models developed for this study. The CoSMoS-COAST numerical model is a transect-based, one-line, data assimilation model capable of simulating long-term (decades) shoreline evolution along unobstructed open coastlines (Vitousek et al. 2017). A thermal component that accounts for thawing permafrost and decreasing ice protection was added to the model. A second two-step transect-based coastal change model (Arctic-XBeach), capable of simulating bluff face thaw / slump erosion and cross-shore transport, was developed to evaluate the fate and transport of eroded bluff material at a storm-event scale.

The CoSMoS-COAST model was calibrated using measured shoreline change rates for the 2007 – 2018 time-period and subsequently applied for years 2019 through 2049 to project changes in coastline change rates. Model results indicate the shoreline is erosional overall and that rates are expected to increase from 1.2 m/year in 2007-2018 to 4.5 m/year by the 2040-2049 period. The relative contribution to the total change was calculated for each of the processes simulated: longshore transport, cross-shore transport due to non-equilibrium wave conditions, relative sea level rise, and thermal processes. For the training period from 2007 – 2018, the cross-shore term contributed positive (accretionary) shoreline change, while both thermal erosion and the sea-level rise term contributed negative shoreline change. Examination of the individual contributions to the increased erosion rate during the latter projected decade (2040-2049) was largely driven by accelerating sea level rise and to a lesser degree, due to a reduced positive contribution from the cross-shore term.

The storm-event scale bluff face thaw / slump erosion model was used to simulate erosion in 2017. The first consequential storm of the summer of 2017 occurred on July 20, resulting in an estimated erosion volume of 1.4 m^3 per alongshore meter in response to warming ground temperatures and an offshore surge and wave height of 0.47 and 6.4 m, respectively. Whereas freeze-up occurred in late August, halting the transport and movement of eroded bluff material, the fate and transport of eroded bluff material was investigated under the hypothetical scenario that landfast sea ice did not set in until mid-October. The eroded sediment was placed as a mound on the beach in the 3D wave-hydrodynamic-sediment transport model Tier 2C and run using ambient wind, and atmospheric pressures. Had the region been free of ice, the resulting tide, surge and wave conditions are predicted to have caused the eroded bluff material to move alongshore with the predominant concentrations toward the northwest over large parts of the Boulder Patch region (Figure 4.25).

Future directions

There are three distinct oceanographic seasons within the nearshore region of Stefansson Sound and across the U.S. Beaufort Shelf (Weingartner et al. 2017): the “winter” landfast ice season that at present typically extends from October/November through May/June, a month-long melting season in June when landfast ice and runoff interact with one another, and the open water season that extends from mid-July through October/November. The primary focus of this study has been to simulate conditions during the open water season when most wave action occurs and second, during the winter landfast ice season. The influence of partial ice cover on wave energy attenuation was accounted for in the standalone nearshore

wave model (Tier 2A), but due to a lack of high-resolution ice concentration products (particularly for the projection time-period), the inclusion of wave mitigation physics in the model are limited.

The finest resolution sea ice products for Foggy Island Bay are on the order of 25 km at daily time-steps for the projection time-period. While it is possible to replace the 25 km-resolution ERA5 reanalysis sea ice fields with finer resolution sea ice products (such as ~5 km GOFS, Metzger 2014), doing so would likely introduce a scaling bias. Because there is a strong dependency of cumulative nearshore wave energy on timing, duration, and concentration of landfast ice, comparing a wave hindcast with sea ice resolved at a 5-fold finer scale compared to the projections would introduce additional uncertainty in the change analyses. Hosekova et al. (2021) showed that while ERA5 reanalysis compares well with observed offshore wave heights, it fails to reproduce the delayed onset of wave energy at the coast caused by unresolved landfast ice. Concerning coastal change, they point out that landfast ice causes persistent coastal protection from wave action that is not resolved by global climate models; whether this modulation in wave energy reaching the coast is an essential factor in the retreat of permafrost coasts remains unclear.

Another direction for future study is improvements to the local scale wave-hydrodynamic-sediment transport model (Tier 2C) developed for this study. The model was run in three dimensions resolving both horizontal and vertical transports but has not been set up and thoroughly tested to simulate vertical shear associated with density-driven salinity and temperature gradients. While density driven flows are most prominent during the break-up and freeze-up seasons, there are indications that salinity and temperature along with other larger scale possibly pressure-driven gradients impart vertical shear during other times of the year as well (Weingartner et al. 2017; Curchister et al. 2018). Inspection of vertically binned current measurements at the UAF and UAA mooring sites suggest that vertical shear is most prominent during low current regimes and breaks down during high flows. The influence of this on the overall and net transport of fine sediment is unknown. To better capture density-driven flows and vertical shear, some modifications to the current model setup are required. This could include for example, parameterizations of vertical density gradients derived from multi-year observations and model results from the coupled sea ice ocean circulation model (Curchister et al. 2018 and Hedstrom et al. 2018).

6 References

Amante C, Eakins BW. 2009. ETOPO1 1 Arc-Minute Global Relief Model: Procedures, Data Sources and Analysis. NOAA Technical Memorandum NESDIS, NGDC-24, 19 p.

Angelopoulos M, Westermann S, Overduin P, Faguet A, Olenchenko V, Grosse G, Grigoriev MN. 2019. Heat and salt flow in subsea permafrost modeled with cryogrid2. Journal of Geophysical Research: Earth Surface. 124(4):920-937.

Ardhuin F, Rogers E, Babanin AV, Filipot J, Magne R, Roland A, van der Westhuysen A, Queffeulou P, Lefevre J, Aouf L, Collard F. 2010. Semiempirical Dissipation Source Functions for Ocean Waves. Part I: Definition, Calibration, and Validation, Journal of Physical Oceanography 40(9): 1917-1941. https://journals.ametsoc.org/view/journals/phoc/40/9/2010jpo4324.1.xml

Ariathurai C. 1974. A Finite Element Model for Sediment Transport in Estuaries. (PhD Dissertation) UC Davis, Davis.

Ballinger TJ, Walsh JE, Bhatt US, Bieniek PA, Tschudi MA, Brettschneider B, Eicken H, Mahoney AR, Richter-Menge J, Shapiro LH. 2021. Unusual west arctic storm activity during winter 2020: Another collapse of the Beaufort high? Geophysical Research Letters. 48(13).

Baordo F, Clementi E, Iovino D, Masina S. 2020. Intercomparison and assessement of wave models at global scale. Technical Note TN0287. Lecce, Italy: Centro EuroMediterraneo sui Cambiamenti Climatici. 49p.

Barnhart KR, Overeem I, Anderson RS. 2014. The effect of changing sea ice on the physical vulnerability of arctic coasts. The Cryosphere. 8(5):1777-1799.

Baule WJ, Shulski MD. 2014. Climatology and trends of wind speed in the Beaufort/Chukchi sea coastal region from 1979 to 2009. International Journal of Climatology. 34(8):2819-2833.

Bieniek P, Erikson L, Kasper J. 2022. Atmospheric circulation drivers of extreme high water level events at Foggy Island Bay, Alaska. Atmosphere, 13(11), 1791. https://doi.org/10.3390/atmos13111791

Bieniek, P. A., Bhatt, U. S., Walsh, J. E., Rupp, T. S., Zhang, J., Krieger, J. R., & Lader, R. 2016. Dynamical Downscaling of ERA-Interim Temperature and Precipitation for Alaska, *Journal of Applied Meteorology and Climatology*, *55*(3), 635-654.

Bjerklie, D. 1993. 1990 Endicott Environmental Monitoring Program Final Report, Volume V: River Discharge. Prepared by Dames & Moore and Science Applications International Corp. for U.S. Army Corps of Engineers, Alaska District.

Booij, N, Ris, RC, Holthuijsen, LH. 1999. A third generation wave model for coastal regions. I- Model description and validation, J. Geophys. Res., 104, 7649–7666, https://doi.org/10.1029/98jc02622.

Bonsell C, Dunton KH. 2018. Long-term patterns of benthic irradiance and kelp production in the central beaufort sea reveal implications of warming for arctic inner shelves. Progress in Oceanography. 162:160-170.

Bromwich, D. H., Wilson, A. B., Bai, L., Liu, Z., Barlage, M., Shih, C.-F., Maldonado, S., Hines, K. M., Wang, S.-H., Woollen, J., Kuo, B., Lin, H.-C., Wee, T.-K., Serreze, M. C., & Walsh, J. E. 2018. The Arctic System Reanalysis, Version 2, *Bulletin of the American Meteorological Society*, *99*(4), 805-828.

Buffo, JM. 1972. Direct solar radiation on various slopes from 0 to 60 degrees north latitude (Vol. 142). Pacific Northwest Forest and Range Experiment Station, Forest Service, US Department of Agriculture.

Camus P, Mendez F, Medina R. 2011. A hybrid efficient method to downscale wave climate to coastal areas. Fuel and Energy Abstracts. 58: 851-862. 10.1016/j.coastaleng.2011.05.007.

Casas-Prat M, Wang XL. 2020. Projections of extreme ocean waves in the arctic and potential implications for coastal inundation and erosion. Journal of Geophysical Research: Oceans. 125(8).

Coastal Frontiers Corporation and LGL. 1998. Survey of Boulder Patch Area.

Coastal Frontiers Corporation. 2014. Suspended Sediment Dispersal During the Liberty Development Construction. Coastal Frontiers Corporation, Moorpark, CA.

Coastal Frontiers Corporation. 2016. 2015-2016 Freeze-up study of the Alaskan Beaufort and Chukchi Seas. Final Report. CFC-962/963. Prepared for Shell Offshore Inc. and U.S. Dept. of the Int., Bureau of Safety and Environmental Enforcement. Funded in part by BSEE Contract E15PC0002. 225 pp.

Collins CO., Rogers WE. 2017. A Source Term for Wave Attenuation by Sea Ice in WAVEWATCH III ® : IC4.

Crawford A, Stroeve J, Smith A, Jahn A. 2021. Arctic open-water periods are projected to lengthen dramatically by 2100. Communications Earth & Environment. 2(1):109.

Curchitser EN, Hedstrom K, Danielson S, Kasper J. 2018. Development of a Very High-Resolution Regional Circulation Model of Beaufort Sea Nearshore Areas. OCS Study BOEM 2018-018, 81.

Danek L, Tourtellotte G. 1987. 1985 Final Report for the Endicott Environmental Monitoring Program, Volume V: Sedimentation and Erosion Monitoring. Prepared by Envirosphere Corporation for U. S. Army Corps of Engineers, Alaska District.

De Boer G, Chapman W, Kay JE, Medeiros B, Shupe MD, Vavrus S, Walsh J. 2012. A Characterization of the Present-Day Arctic Atmosphere in CCSM4. J. Clim. 25: 2676-2695. doi:10.1175/JCLI-D-11-00228.1.

Deltares. 2022. Simulation of multi-dimensional hydrodynamic flows and transport phenomena, including sediments. User Manual. Hydro-Morphodynamics. Version 4.05. SVN Revision 75129. Deltares, The Netherlands.

Dickins D, Hearon G, Morris K, Ambrosius K, Horowitz W. 2011. Mapping sea ice overflood using remote sensing: Alaska Beaufort Sea. Cold Regions Science and Technology. 65(3):275-285.

Dunton KH., Reimnitz E., Schonberg S. 1982. An Arctic Kelp Community in the Alaskan Beaufort Sea. Arctic, 35(4):465–484. http://www.jstor.org/stable/40509381

Dunton, KH, Schonberg SV. 2000. The benthic faunal assemblage of the Boulder Patch kelp community. In The natural history of an Arctic oil field: development and the biota, ed. J.C. Truett and S.R. Johnson, 371–397. Boston: Academic.

Engelstad AC, Erikson LH, Reguero BG, Gibbs AE, Nederhoff K. in press. Generating nearshore wave time series with a numerical wave model-derived database along the outer coast of Alaska. U.S. Geological Survey Open-File Report

Erikson LH, Gibbs AE, Richmond BM, Storlazzi CD, Jones BM, Ohman KA. 2020. Changing storm conditions in response to projected 21st century climate change and the potential impact on an arctic

barrier island–lagoon system—A pilot study for Arey Island and Lagoon, eastern Arctic Alaska. U.S. Geological Survey Open-File Report 2020. 1142, 68 p., https://doi.org/10.3133/ofr20201142.

Envirosphere, 1991. 1987 Final Report for the Endicott Environmental Monitoring Program. Report prepared for U.S. Dept. of the Army, Alaska District, Corps of Engineers, Anchorage, AK.

Fechhelm. 1999. The effect of new breaching in a Prudhoe Bay causeway on the coastal distribution of humpback whitefish. Arctic. 52(4):386-394.

Frontiers C. 2014. Suspended sediment dispersal during the liberty development construction. Moorpark, CA.

Gallaway BJ, Britch RP. 1983. Environmental summer studies (1982) for the Endicott development. LGL Alaska Research Associates Northern Technical Services., and Sohio Alaska Petroleum Company, Fairbanks, Alaska.

Garratt JR. 1977. Review of drag coefficients over oceans and continents. Monthly Weather Review. 105(7):915-929.

Gibbs AE, Richmond BM. 2017. National assessment of shoreline change—Summary statistics for updated vector shorelines and associated shoreline change data for the north coast of Alaska, U.S.-Canadian border to Icy Cape. Open-File Report 2017-1107, 21p.

Hachmeister LE, Short KS, Schrader GC., Winnick KB, Johannessen JW. 1985. Oceanographic Monitoring. Endicott Environmental Studies: Envirosphere Company, Bellevue, WA.

Hamilton AI, Gibbs AE, Erikson LH, and Engelstad AC. 2021. Assessment of barrier island morphological change in northern Alaska: U.S. Geological Survey Open-File Report 2021–1074, 28p. https://doi.org/10.3133/ofr20211074.

Hasselmann, S, Hasselmann, K. 1985. Computations and parameterizations of the nonlinear energy transfer in a gravity-wave spectrum. Part i: A new method for efficient computations of the exact nonlinear transfer integral. J Phys Oceanogr. 15:8.

Hedström K. 2018. Technical Manual for a Coupled Sea-Ice/Ocean Circulation Model (Version 5). U.S. Dept. of the Interior, Bureau of Ocean Energy Management, Alaska OCS Region. OCS Study BOEM 2018-007. 182 pp.

Hilcorp Alaska, LLC, Anchorage, AK. 2017. Liberty Development Project. Development and Production Plan. Amendment 3. Originally Submitted December 30, 2014. Amendment 3: May 26, 2017. Submitted to Bureau of Ocean Energy Management, Alaska OCS Region, Anchorage AK. 290 pp.

Hersbach H, Bell B, Berrisford P, Hirahara S, Horányi A, Muñoz-Sabater J, Nicolas J, Peubey C, Radu R, Schepers. D. 2020. The ERA5 global reanalysis: Quarterly Journal of the Royal Meteorological Society. 146(760):1-51. https://doi.org/10.1002/qj.3803

Hošeková L, Eidam E, Panteleev G, Rainville L, Rogers WE, Thomson J. 2021. Landfast ice and coastal wave exposure in northern Alaska. Geophysical Research Letters, 48, e2021GL095103. https://doi.org/10.1029/2021GL095103

Hu H, Argyropoulos SA. 1996. Mathematical modelling of solidification and melting: a review. Modelling and Simulation in Materials Science and Engineering, 4(4):371.

Jakobsson M, Mayer LA, Bringensparr C, Castro CF, Mohammad R, Johnson P, Ketter T, Accettella D, Amblas D, An L et al. 2000. The International Bathymetric Chart of the Arctic Ocean Version 4.0. Sci Data. 7(176). https://doi.org/10.1038/s41597-020-0520-9

Jones BM, Hinkel KM., Arp CD, Eisner, WR. 2008. Modern erosion rates and loss of coastal features and sites, Beaufort Sea coastline, Alaska. Arctic. p. 361-372.

Joyce BR, Pringle WJ, Wirasaet D, Westerin JJ, Van der Westhuysen AJ, Grumbine R, Feyen J. 2019. High resolution modeling of western alaskan tides and storm surge under varying sea ice conditions Ocean Modelling. 141(101421):24.

Kasper JL. Idealized modeling of circulation under landfast ice. University of Alaska Fairbanks; 2010.

Kasper JL, Weingartner TJ. 2012. Modeling winter circulation under landfast ice: The interaction of winds with landfast ice. Journal of Geophysical Research: Oceans. 117(C4).

Kenigson JS, Timmermans ML. 2021. Arctic cyclone activity and the Beaufort high. Journal of Climate. 34(10):4119-4127.

Kernkamp HWJ, Van Dam A, Stelling GS, de Goede ED. 2011. Efficient scheme for the shallow water equations on unstructured grids with application to the continental shelf. Ocean Dynamics. 61(8):1175-1188.

Krone R, 1962. Flume Studies of the Transport of Sediment in Estuarial Shoaling Processes. U.C. Berkeley, Berkeley.

Kupilik M, Ulmgren M, Brunswick D. 2020. Bayesian Parameter Estimation for Arctic Coastal Erosion Under the Effects of Climate Change. IEEE Journal of Selected Topics in Applied Earth Observations and Remote Sensing.13:3595-3604.

Le Roux. JP. 2009. Characteristics of developing waves as a function of atmospheric conditions, water properties, fetch and duration. Coastal Engineering. 56(4):479–483. https://doi.org/10.1016/j.coastaleng.2008.10.007

Lesser GR, Roelvink JA, van Kester JATM, Stelling GS. 2004. Development and validation of a three-dimensional morphological model. Coastal Engineering 51(8–9): 883–915.

Lucero F, Catalán PA, Ossandón Á, Beyá J, Puelma A, Zamorano L. 2017. Wave energy assessment in the central-south coast of Chile. Renewable Energy. 114:120-131.

Lüpkes C, Gryanik VM, Hartmann J, Andreas EL. 2012. A parametrization, based on sea ice morphology, of the neutral atmospheric drag coefficients for weather prediction and climate models. Journal of Geophysical Research: Atmospheres. 117(D13).

Madsen OS, Poon YK, Graber HC. 1988. Spectral wave attenuation by bottom friction: theory. Twenty First Coastal Eng Conf. p. 492–504.

Mahoney AR, Eicken H, Gaylord AG, Gens R. 2014. Landfast sea ice extent in the Chukchi and Beaufort Seas: The annual cycle and decadal variability. Cold Regions Science and Technology. 103:41–56. https://doi.org/https://doi.org/10.1016/j.coldregions.2014.03.003

Metzger EJ, Smedstad OM, Thoppil PG, Hurlburt HE, Cummings JA, Wallcraft AJ. 2014. US Navy Operational Global Ocean and Arctic Ice Prediction Systems. Oceanography, 27, 32– 43. https://doi.org/10.5670/oceanog.2014.66

Meylan MH, Bennetts LG, Kohout AL. 2014. In situ measurements and analysis of ocean waves in the Antarctic marginal ice zone. Geophys Res Lett. 41(14):5046–5051. https://doi.org/10.1002/2014GL060809

Moore GWK, Halfar J, Majeed H, Adey W, Kronz A. 2017. Amplification of the Atlantic Multidecadal Oscillation associated with the onset of the industrial-era warming. Scientific Reports 7(1):40861.

Moore GWK, Schweiger A, Zhang J, Steele M. 2018. Collapse of the 2017 winter Beaufort high: A response to thinning sea ice? Geophysical Research Letters. 45(6):2860-2869.

Nederhoff K, Erikson L, Engelstad A, Bieniek P, Kasper J. 2022. The effect of changing sea ice on nearshore wave climate trends along Alaska's Central Beaufort Sea coast. The Cryosphere. 16:1609-21629. https://doi.org/10.5194/tc-16-1609-2022

NCEP/NWS/NOAA: National Centers for Environmental Prediction/National Weather Service/NOAA/U.S. Department of Commerce (2005), NCEP North American Regional Reanalysis (NARR), https://rda.ucar.edu/datasets/ds608.0/, Research Data Archive at the National Center for Atmospheric Research, Computational and Information Systems Laboratory, Boulder, Colo. (Updated monthly.) Accessed 01 March 2018.

NCAR/UCAR: National Center for Atmospheric Research/University Corporation for Atmospheric Research, and Polar Meterology Group/Byrd Polar and Climate Research Center/The Ohio State University. 2017. Arctic System Reanalysis version 2. Research Data Archive at the National Center for Atmospheric Research, Computational and Information Systems Laboratory. https://doi.org/10.5065/D6X9291B. Accessed 02 March 2018.

Overland JE. 2009. Meteorology of the Beaufort Sea. Journal of Geophysical Research: Oceans, 114(5), 1–10. https://doi.org/10.1029/2008JC004861

Porterfield G. 1980. Sediment transport of streams tributary to san francisco, san pablo, and suisun bays, california, 1909-66. US Geological Survey, Water Resources Division.

Ravens TM, Peterson S. 2021. Geologic Controls on Erosion Mechanism on the Alaska Beaufort Coast. Frontiers in Earth Sciences – Cryospheric Sciences. https://www.frontiersin.org/articles/10.3389/feart.2021.693824/full

Reguero BG., Méndez FJ. Losada IJ. 2013. Variability of multivariate wave climate in Latin America and the Caribbean. Global and Planetary Change, 100:70-84. https://doi.org/10.1016/j.gloplacha.2012.09.005.

Reimnitz E, Kempema EW. 1983. High rates of bedload transport measured from infilling rate of large strudel-scour craters in the Beaufort Sea, Alaska. Continental Shelf Research. 1(3):237-251.

Rinke A, Maturilli M, Graham RM, Matthes H, Handorf D, Cohen L, Hudson SR, Moore JC. 2017. Extreme cyclone events in the arctic: Wintertime variability and trends. Environmental Research Letters. 12(9).

Roelvink D, Reniers AJHM., Van Dongeren A, van Thiel de Vries J, Lescinski J, McCall R. 2010. XBeach model description and manual. 2010.Unesco-IHE Institute for Water Education, Deltares and Delft University of Technology.

Rogers WE, Babanin AV, Wang DW. 2012. Observation-consistent input and whitecapping dissipation in a model for wind-generated surface waves: Description and simple calculations. Journal of Atmospheric and Oceanic Technology, 29(9), 1329–1346. https://doi.org/10.1175/JTECH-D-11-00092.1

Rogers E, Orzech MD. 2013. Implementation and Testing of Ice and Mud Source Functions in WAVEWATCH III

Rogers WE. 2019. Implementation of Sea Ice in the Wave Model SWAN. Naval Research Laboratory, Ocean Dynamics and Prediction Branch, Oceanography Division. NRL/MR/7322—19-9874. 32 p.

Schweiger AJ, Zhang J. 2015. Accuracy of short-term sea ice drift forecasts using a coupled ice-ocean model. J Geophys Res: Oceans. 120(12):7827-7841.

Semtner AJ. 1976. A model for the thermodynamic growth of sea ice in numerical investigations of climate. Journal of Physical Oceanography. 6(3):379-389.

Sepp M, Jaagus J. 2011. Changes in the activity and tracks of arctic cyclones. Climatic Change. 105(3-4):577-595.

Shao W, Yu W, Jiang X, Shi J, Wei Y, Ji Q. 2022. Analysis of wave distributions using the wavewatch-iii model in the arctic ocean. Journal of Ocean University of China. 21(1):15-27.

Short KS, Winnick KB, Schrader GC, Hachmeister LE, van Zee, CJ. 1986. Oceanography 1986. Part II Chapter 3. Envirosphere Company, Bellevue, Washington. 276 pp.

Stegall ST, Zhang J. 2012. Wind field climatology, changes, and extremes in the Chukchi–Beaufort Seas and Alaska North Slope during 1979–2009. Journal of Climate. 25(23):8075-8089.

Stevens A, Mortiz HR, Elias EP, Gelfenbaum G, Ruggiero P, Pearson S, McMillian J, Kaminsky G, 2023. Monitoring and modeling dispersal of a submerged nearshore berm at the mouth of the Columbia River, USA. Coastal Engineering.

Stopa JE, Ardhuin F, Girard-Ardhuin F. 2016. Wave climate in the Arctic 1992-2014: Seasonality and trends. Cryosphere, 10(4):1605–1629. https://doi.org/10.5194/tc-10-1605-2016

Stroeve JC, Crawford AD, Stammerjohn S. 2016. Using timing of ice retreat to predict timing of fall freeze-up in the arctic. Geophysical Research Letters. 43(12):6332-6340.

Overland JE. 2009. Meteorology of the Beaufort Sea. Journal of Geophysical Research: Oceans. 114(C1).

Thomson J, Fan Y, Stammerjohn S, Stopa J, Rogers WE, Girard-Ardhuin F, Ardhuin F, Shen H, Perrie W, Shen H. 2016. Emerging trends in the sea state of the Beaufort and Chukchi seas. Ocean Modelling 105:1–12. https://doi.org/10.1016/j.ocemod.2016.02.009

Toimil, L.J. and J.M. England. 1982. Environmental Effects of Gravel Island Construction, OCSY0191 (BF-7), Beechy Point Block 480, Stefansson Sound, Alaska. Anchorage, AK: Exxon Company U.S.A., 62 pp.

Trefry JH, Trocine RP, Alkire MB, Semmler CM, Savoie M, Rember RD (Florida Institute of Technology, Melbourne, FL). 2009. cANIMIDA tasks 3 and 4: sources, concentrations, composition, partitioning and dispersion pathways for suspended sediments and potential metal contaminants in the coastal Beaufort Sea. Anchorage (AK): U.S. Department of the Interior, Minerals Management Service, Alaska OCS Region. 158 p. Report No.: OCS Study MMS 2009-014.

van Rijn Leo C. 2007a. Unified view of sediment transport by currents and waves. I: Initiation of motion, bed roughness, and bed-load transport. Journal of Hydraulic Engineering. 133(6):649-667.

van Rijn Leo C. 2007b. Unified view of sediment transport by currents and waves. II: Suspended transport. Journal of Hydraulic Engineering. 133(6):668-689.

Vitousek S, Barnard PL, Limber P, Erikson L, Cole B. 2017. A model integrating longshore and cross-shore processes for predicting long-term shoreline response to climate change. J Geophys Res, Earth Sur, 122:782–806. doi:10.1002/2016JF004065

Wadhams P, Squire VA, Goodman DJ, Cowan AM, Moore SC. 1988. The attenuation rates of ocean waves in the marginal ice zone. Journal of Geophysical Research: Oceans. 93(C6):6799-6818.

Wan EA, Van der Merwe R. 2000. The Unscented Kalman Filter Nonlinear Estimation. Proc IEEE 2000 Symp Adaptive Syst Signal Process, Commun Contr Symposium, p. 153-158. doi: 10.1109/ASSPCC.2000.882463.

The WAVEWATCH III ® Development Group (WW3DG). 2016. User manual and system documentation of WAVEWATCH III R version 5.16. Tech. Note 329, NOAA/NWS/NCEP/MMAB, College Park, MD, USA, 326 pp. + Appendices

Weingartner T, Danielson SL, Kasper JL, Okkonen SR. 2009. Circulation and water property variations in the nearshore Alaskan Beaufort Sea (1999-2007). Institute of Marine Science, Univ. of Alaska Fairbanks. June Final Report prepared for the Dept. of Interior Minerals Management Service. OCS Study MMS 2009-035.

Weingartner T, Kasper JL. 2011. Idealized modeling of circulation under landfast ice. Anchorage, AK: School of Fisheries & Ocean Sciences, University of Alaska Fairbanks.

Weingartner TJ, Danielson SL, Potter RA, Trefry JH, Mahoney A, Savoie M, Irvine C, Sousa L. 2017. Circulation and water properties in the landfast ice zone of the Alaskan Beaufort Sea. Continental Shelf Research. 148:185-198.

White F, Spaulding M, Gominho L. 1980. Theoretical estimates of the various mechanisms involved in iceberg deterioration in the open ocean environment. US Coast Guard Research and Development Center. Report No: CG-D-62-80.

Wilce RT, Dunton KH. 2014. The boulder patch (North Alaska, Beaufort Sea) and its benthic algal flora. Arctic. 67(1):43-56.

Wilcock P, Crowe J. 2003. Surface-based transport model for mixed-size sediment. Journal of Hydraulic Engineering 129(2): 120-128.

Winterwerp JC, van Kesteren WGM. 2004. *Introduction to the physics of cohesive sediment in the marine environment*. 1st Ed. Elsevier.

The WAVEWATCH III ® Development Group (WW3DG), 2016: User manual and system documentation of WAVEWATCH III ® version 5.16. Tech. Note 329, NOAA/NWS/NCEP/MMAB, College Park, MD, USA, 326 pp + Appendices.

Yager, GC. 2011. The impact of the Endicott causeway on sediment transport in the Sagavanirktok River Delta, North Slope Alaska. Master's Thesis. University of Alaska Anchorage, 189 pp.

Yates ML, Guza RT, O'Reilly WC. 2009. Equilibrium shoreline response: Observations and modeling, J Geophys Res. 114(C09014). doi:10.1029/2009JC005359.

Zimmermann M, Erikson LH, Gibbs AE, Prescott MM, Escarzaga SM, Tweedie CE, Kasper JL, Duvoy PX. 2022. Nearshore bathymetric changes along the alaska beaufort sea coast and possible physical drivers. Continental Shelf Research. 242.

Appendix A: Field Work Summary Reports

Central Beaufort Sea Wave and Hydrodynamic Modeling Study 2018 Field Report

UAF Cooperative Agreement M17AC00020/ USGS CFDA No. 15.423

Report Contributors:

Dr. Jeremy Kasper
Ms. Stephanie Jump
Mr. Paul Duvoy

Field Personnel

Dr. Jeremy Kasper, UAF PI
Mr. Nicholas Konefal, UAF Research Engineer
Ms. Stephanie Jump, UAF Research Professional
Mr. Paul Duvoy, UAF Research Engineer

Table of Contents

List of Figures

List of Tables

Table i. Acronyms used in this report.

ADCP	ACOUSTIC DOPPLER CURRENT PROFILER
ADV	ACOUSTIC DOPPLER VELOCIMETER
CTP	CONDUCTIVITY/TEMPERATURE/PRESSURE
CTD	CONDUCTIVITY/TEMPERATURE/DEPTH
GNSS	GLOBAL NAVIGATION SATELLITE SYSTEM
GPS	GLOBAL POSITION SYSTEM
IARC	INTERNATIONAL ARCTIC RESEARCH CENTER
IMU	INERTIAL MOTION UNIT
TSS	TOTAL SUSPENDED SOLIDS
UAA	UNIVERSITY OF ALASKA ANCHORAGE
UAF	UNIVERSITY OF ALASKA FAIRBANKS
USGS	UNITED STATES GEOLOGICAL SURVEY
VMDAS	VESSEL MOUNT DATA ACQUISITION SYSTEM

Summary

Persistent ice delayed the start of fieldwork in July 2018 by ~1 week and prevented most work outside of the barrier islands, except for a short foray outside the barrier islands to deploy a mooring, for the duration of the 10-day cruise between July 17 and July 26. While ice was a challenge, the weather was generally good throughout the 10-day cruise which allowed us to accomplish a great deal of survey work and to install multiple oceanographic moorings.

Between July 15th and July 30th, 2018 two bottom founded oceanographic moorings equipped with various sensors to measure currents, surface wave spectra, near-bottom velocity and hydrography and water levels were deployed in support of the Central Beaufort Sea Wave and Hydrodynamic Modeling Study project inside of Foggy Island Bay. A third, seasonally deployed shallow water oceanographic mooring, the "shore-face" mooring was deployed to measure shore face sediment fluxes at the southern end of Foggy Island Bay. A fourth mooring, the "LTER Cross Island mooring" equipped with sensors to measure currents, wave spectra and near bottom hydrography was deployed offshore of the barrier islands enclosing Foggy Island Bay for the Beaufort Lagoons LTER project. Data from this LTER mooring will be incorporated into results for the Central Beaufort Sea Wave and Hydrodynamic Modeling Study. Specifically, the LTER mooring will provide information on the "boundary conditions" for wave and hydrographic conditions within Foggy Island Bay.

Water column hydrographic information were collected (conductivity, temperature and pressure) during the cruise in order to provide sound speed corrections for multibeam sonar data and information on the origin and characteristics of the water masses in the study area. A total of 14 CTD+discrete water samples stations (using a Seabird Electronics SBE25/55 CTD +Water Sampler) and 50 sensor only stations (using an AML Oceanographic CTD+Turbidity probe) were completed during the cruise. The complex hydrography of the region (multiple small-scale frontal features between riverine, ambient shelf water and sea ice melt derived waters) means that high resolution hydrographic information is required to ensure the accuracy of the multibeam sonar mapping efforts.

Multibeam sonar data (seafloor depth and backscatter strength) gathered within and outside of Foggy Island Bay will be used for creating a Digital Elevation Model for the ocean and wave modeling portion of the study. When compared to existing and repeat measurements, the multibeam sonar data will also provide information on changes in seafloor topography between survey years within the region which can then be used to estimate sediment fluxes due to bedload transport. Approximately 224 km were surveyed during the 10-day cruise including lines previously surveyed for comparison between years.

A total of 18 seafloor samples were collected during the cruise using a "Ponar"-type grab. The grab samples will be analyzed by UAA to determine sediment size distributions in the area for use in the modeling efforts in order to understand sediment transport within the bay. Multibeam acoustic backscatter measurements will also be calibrated against the in-situ seafloor sediment information so that maps of sediment size derived from the multibeam acoustic backscatter measurements can be created.

A sled-mounted Acoustic Doppler Current Profiler (ADCP) was towed alongside the survey vessel to measure water column velocity and acoustic backscatter. Approximately 167 km of ADCP surveys were completed during the cruise.

A met station was also installed on the southern coast of Foggy Island Bay to measure wind speed and direction, barometric pressure, temperature and relative humidity. Two cameras mounted on the met station provide hourly images of the nearby coast for quantifying coastal change over the course of the project. The met-station and cameras will remain deployed for the duration of the field-portion of the project. In addition, a small drone was deployed to image coastal position and topography. Technical problems with the drone prevented a complete drone survey. A Spoondrift “spotter” buoy for measuring surface wave spectra in real-time could not be deployed this summer due to persistent ice in the region.

Survey Platforms

The R/V Ukpik (Figure 1), a 16m vessel well-suited for work in the region was chartered for the July work. The Ukpik is equipped with an articulating A-frame with a 2,000 lb. capacity winch with 450 meters of cable and a 6" deck mounted capstan winch. Prior to the beginning of the cruise, UAF commissioned a local machinist to design and fabricate an adapter to mount UAF's multibeam transducer to the port-side gunwale of the Ukpik so that a multi-beam survey could be carried out from the Ukpik. Duvoy, Kasper and Konefal undertook the work on the R/V Ukpik during summer 2018. Captain Mike Fleming operated the Ukpik for the duration of the cruise.

The M/V Leeway (Figure 2), a 11m x 4m Catamaran was used during the September 24th -26th 2018. On September 25th, the shallow, seasonal "Shore-face" mooring was retrieved and the met-station was accessed for maintenance; a wind turbine was installed on the met-station to supplement solar power throughout the winter at this time and camera images were also downloaded. Jump and Kasper undertook the September field work. Captain Heather Ronek operated the Leeway for the duration of the cruise. Due to weather and ice conditions, only a half a day on the boat was doable on the 25th. Captain Heather Ronek reported on September 26th that she was unable to make it out to open water.

Figure 1. R/V Ukpik.

Figure 2. M/V Leeway.

Shipboard Instrumentation

1. UAF-owned AML Oceanographic MinosX Conductivity/Temperature/Pressure (CTP)+Turbidity sensor
2. UAF-owned Seabird Electronics SBE25+ CTP equipped with an SBE 55 water sampler and SBE33 deck box. The SBE25+ system was equipped with the following ancillary sensors: Teledyne Benthos Altimeter, Wetlabs FLNTUS (Flourometer/Turbidity), QSP2300 (PAR sensor). A Sequoia Scientif Laser In situ Sediment Size and Transmissivity sensor (a LISST) 100x for measuring sediment size distribution and transmissivity was mounted to the SBE55 water sampler. Data was recorded and archived using Seabird's Seasave software program (Seasave v 7.21f).
3. UAF-owned 600 kHz RD Instruments Sentinel Workhorse Acoustic Doppler Current Profiler (ADCP) mounted on a Biosonics Inc. "acoustic sled". Data was recorded and archived during the cruise using Teledyne RD Instrument's VMDAS software (V. 1.49).
4. UAF-owned Reson 7125 Seabat Multibeam Echosounder and Applanix POSMV GNSS+Inertial Navigation System. Reson's PDS2000 software was used to collect and archive the multibeam sonar data during the cruise (PDS2000 V 4.3.0.5). Multibeam data was backed-up to an external hard drive on a daily basis.
5. Wildco Stainless Steel Ponar Grab (0.1 m^2 sample area).
6. UAF-owned Trimble R8 GNSS base station, Trimble R10 GNSS receiver + Trimble GNSS base station.

Sampling Stations

Fourteen stations were sampled in Foggy Island Bay using the Seabird Electronics SBE25/SBE55+LISST sensor package. Discrete water samples at multiple depths were collected at this time for analysis of total suspended solids (TSS), macronutrients, and stable oxygen isotope ratios (delO18). Water samples for DelO18 were collected following REFXX. Nutrient samples were gathered following MUNDYREFFXX. TSS samples were gathered following STANDARDSXX.

Station names, depth and locations are shown in Table ii and Figure 3. Information on "sensor-only" stations, sampled using the AML CTP+Turbidity sensor package is given in Table iii and Figure 4. Locations of the bottom grab stations are shown in Table iv and Figure 5.

Table ii. Name, depth and locations for the 14 sampling stations where CTD, TSS, and DelO18 samples were collected.

Station Name	Depth (m)	Latitude (DD)	Longitude (DD)
FIB2	6	70.2989	147.1881
FIB2	0.56	70.2989	147.1881
FIB3	5.5	70.2741	147.3605
FIB3	0.56	70.2741	147.3605
FIB5	6	70.3668	147.4978
FIB5	0.46	70.3668	147.4978
FIB6	2	70.2064	147.4939
FIB6	0.462	70.2064	147.4939
FIB7	8	70.3305	147.0904
FIB7	0.36	70.3305	147.0904
FIB8	1.898	70.2279	147.3669
FIB8	0.3594	70.2279	147.3669
FIB9	1.59	70.2065	147.4932
FIB9	0.36	70.2065	147.4932
FIB10	3.23	70.2417	147.6438
FIB10	0.36	70.2417	147.6438
FIB11	9.18	70.4278	147.6472
FIB11	0.46	70.4278	147.6472
FIB12	2.92	70.4202	147.7977
FIB12	0.56	70.4202	147.7977
FIB13	1.39	70.2962	147.7926
FIB13	0.26	70.2962	147.7926
FIB14	4.46	70.3677	147.9142
FIB14	0.36	70.3677	147.9142
FIB15	6.2	70.4535	147.9188
FIB15	0.36	70.4535	147.9188
FIB16	11.75	70.4685	147.7220
FIB16	0.76	70.4685	147.7220

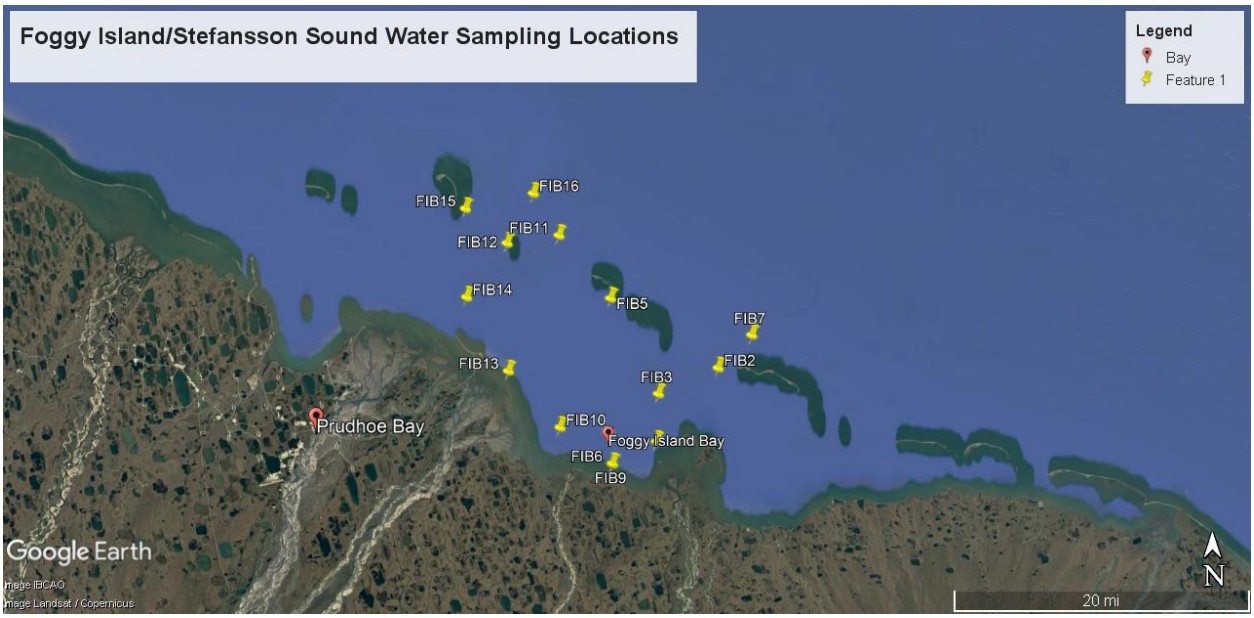

Figure 3. CTD Locations where total suspended solids (TSS), and macronutrients were collected.

Table iii. Sample ID, Dates, Time and location of AML Probe data was collected. Times are UTC.

Number	Area	Date	Time	Latitude (DD)	Longitude (DD)
1	Stef. Sound	7/20/2018	12.25	70.27636667°N	147.2079694°W
2	Stef. Sound	7/20/2018	13.39	70.30183056°N	147.3629139°W
3	Stef. Sound	7/20/2018	14.08	70.32480278°N	147.3619611°W
4	Stef. Sound	7/20/2018	15.36	70.33870833°N	147.4954778°W
5	Stef. Sound	7/20/2018	15.53	70.31411667°N	147.4945528°W
6	Stef. Sound	7/20/2018	16.12	70.28655°N	147.4946972°W
7	Stef. Sound	7/20/2018	16.45	70.26007778°N	147.4943361°W
8	Stef. Sound	7/20/2018	17.07	70.23306944°N	147.4942556°W
9	Stef. Sound	7/21/2018	10:57	70.35558889°N	147.2340778°W
10	Stef. Sound	7/21/2018	11:31	70.32801667°N	147.1209833°W
11	Stef. Sound	7/21/2018	12:09	70.30130278°N	147.2315944°W
12	Stef. Sound	7/21/2018	12:24	70.29868056°N	147.1873694°W
13	Stef. Sound	7/21/2018	12:55	70.27649722°N	147.233°W
14	Stef. Sound	7/21/2018	14:33	70.24807222°N	147.3657056°W
15	Stef. Sound	7/21/2018	14:56	70.27532778°N	147.3625306°W
16	Stef. Sound	7/21/2018	15:44	70.31386111°N	147.4959306°W
17	Stef. Sound	7/21/2018	16:09	70.28669444°N	147.4949806°W
18	Stef. Sound	7/21/2018	16:39	70.26076944°N	147.495025°W
19	Stef. Sound	7/21/2018	17:02	70.23356667°N	147.4947333°W
20	Stef. Sound	7/21/2018	17:27	70.20661111°N	147.4929083°W
21	Stef. Sound	7/22/2018	8:42	70.21366111°N	147.6448028°W
22	Stef. Sound	7/22/2018	9:20	70.24201111°N	147.6436833°W
23	Stef. Sound	7/22/2018	10:14	70.29546111°N	147.6436833°W

24	Stef. Sound	7/22/2018	10:41	70.321725°N	147.6445278°W
25	Stef. Sound	7/22/2018	11:03	70.350375°N	147.6435917°W
26	Stef. Sound	7/22/2018	11:25	70.37601944°N	147.642625°W
27	Stef. Sound	7/22/2018	11:48	70.40384167°N	147.6466306°W
28	Stef. Sound	7/22/2018	12:09	70.42575°N	147.6469722°W
29	Stef. Sound	7/22/2018	13:06	70.41999444°N	147.7976417°W
30	Stef. Sound	7/22/2018	13:31	70.400275°N	147.7969639°W
31	Stef. Sound	7/22/2018	13:53	70.373375°N	147.7958528°W
32	Stef. Sound	7/22/2018	14:13	70.34606944°N	147.7954917°W
33	Stef. Sound	7/22/2018	14:39	70.31783611°N	147.7974194°W
34	Stef. Sound	7/22/2018	15:03	70.29601944°N	147.7921139°W
35	Stef. Sound	7/22/2018	15:57	70.359925°N	147.8442083°W
36	Stef. Sound	7/22/2018	16:22	70.36731111°N	147.9139889°W
37	Stef. Sound	7/22/2018	16:51	70.39870833°N	147.9143111°W
38	Stef. Sound	7/22/2018	17:16	70.42630833°N	147.9154194°W
39	Stef. Sound	7/22/2018	17:42	70.4535°N	147.9180083°W
40	Stef. Sound	7/23/2018	9:34	70.46305278°N	147.7982139°W
41	Stef. Sound	7/23/2018	10:17	70.42524722°N	147.9159833°W
42	Stef. Sound	7/23/2018	10:57	70.39168333°N	147.7969778°W
43	Stef. Sound	7/23/2018	11:47	70.34778333°N	147.6411278°W
44	Stef. Sound	7/23/2018	12:38	70.35951389°N	147.8452694°W
45	Stef. Sound	7/23/2018	12:57	70.36749444°N	147.9150778°W
46	Stef. Sound	7/25/2018	13:25	70.468625°N	147.7227389°W
47	Stef. Sound	7/25/2018	14:52	70.42741944°N	147.6378278°W
48	Stef. Sound	7/25/2018	15:46	70.36662778°N	147.4934722°W
49	Stef. Sound	7/25/2018	17:19	70.34422778°N	147.7966583°W
50	Stef. Sound	7/25/2018	17:42	70.359°N	147.8426861°W

Figure 4. AML cast locations.

Table iv. Sample ID, Date and location of Ponar Grabs to collect ocean floor sediment samples.

Number	Area	Date	Latitude (DD)	Longitude (DD)
1	Stef. Sound	7/21/2018	70.29931667°N	147.1868111°W
2	Stef. Sound	7/21/2018	70.22791667°N	147.3665278°W
3	Stef. Sound	7/21/2018	70.313725°N	147.4962056°W
4	Stef. Sound	7/22/2018	70.24250833°N	147.6447139°W
5	Stef. Sound	7/22/2018	70.29576389°N	147.6448444°W
6	Stef. Sound	7/22/2018	70.40370278°N	147.6465639°W
7	Stef. Sound	7/22/2018	70.41985556°N	147.7972583°W
8	Stef. Sound	7/22/2018	70.39996389°N	147.7971333°W
9	Stef. Sound	7/22/2018	70.34500278°N	147.7945694°W
10	Stef. Sound	7/22/2018	70.31762778°N	147.7963°W
11	Stef. Sound	7/22/2018	70.29669167°N	147.7938°W
12	Stef. Sound	7/22/2018	70.36001944°N	147.8453639°W
13	Stef. Sound	7/22/2018	70.398975°N	147.9158333°W
14	Stef. Sound	7/22/2018	70.42614444°N	147.9148139°W
15	Stef. Sound	7/22/2018	70.45346111°N	147.9186722°W
16	Stef. Sound	7/25/2018	70.46853889°N	147.7223778°W
17	Stef. Sound	7/25/2018	70.42746111°N	147.6385444°W
18	Stef. Sound	7/25/2018	70.35672778°N	147.8383306°W

Figure 5. Location map of ponar bottom grabs.

Table v. DelO18 station locations.

Station Name	Latitude (DD)	Longitude (DD)
FIB2	70.2989°N	147.1881°W
FIB2	70.2989°N	147.1881°W
FIB3	70.2741°N	147.3605°W
FIB3	70.2741°N	147.3605°W
FIB5	70.3668°N	147.4978°W
FIB5	70.3668°N	147.4978°W
FIB6	70.2064°N	147.4939°W
FIB6	70.2064°N	147.4939°W
FIB7	70.3305°N	147.0904°W
FIB7	70.3305°N	147.0904°W
FIB8	70.2279°N	147.3669°W
FIB8	70.2279°N	147.3669°W
FIB9	70.2065°N	147.4932°W
FIB9	70.2065°N	147.4932°W
FIB10	70.2417°N	147.6438°W
FIB10	70.2417°N	147.6438°W

FIB11	70.4278°N	147.6472°W
FIB11	70.4278°N	147.6472°W
FIB12	70.4202°N	147.7977°W
FIB12	70.4202°N	147.7977°W
FIB13	70.2962°N	147.7926°W
FIB13	70.2962°N	147.7926°W
FIB14	70.3677°N	147.9142°W
FIB14	70.3677°N	147.9142°W
FIB15	70.4535°N	147.9188°W
FIB15	70.4535°N	147.9188°W
FIB16	70.4685°N	147.7220°W
FIB16	70.4685°N	147.7220 °W

Oceanographic Moorings

Three year-round oceanographic moorings were deployed on July 20th and July 25th during the cruise. One temporary, shallow "shore face" mooring was deployed on July 20th and retrieved September 25th. Details of the mooring instruments and locations are shown in Table vi and

Table vii.

Table vi. Oceanographic mooring name, locations and deployment date and time.

Name	Latitude (DD)	Longitude (DD)	Date	Time (UTC)
UAF Dinkum	70.29313611°N	147.5432694°W	7/20/2018	16:15
Shore face	70.21078056°N	147.5730778°W	7/20/2018	16:57
UAA Newport	70.29878611°N	147.1876833°W	7/20/2018	18:16
LTER Cross Island	70.46906944°N	147.7245889°W	7/25/2018	10:15 AM

Table vii. Mooring name, instrument types and serial numbers for each mooring.

UAF Dinkum Mooring		
Equipment	Serial Number	Parameters Measured
RDI 1.2MHZ ADCP	16203	Water column velocities, surface wave spectra, water column acoustic backscatter
SBE Microcat 37	16502	Conductivity/temperature/pressure
Acoustic Release	74381	
UAA Newport Mooring		
Equipment	Serial Number	Parameters Measured
RDI 1.2MHZ ADCP	2018	Water column velocities, surface wave spectra, water column acoustic backscatter
SBE Microcat 37	16496	Conductivity/temperature/pressure
Acoustic Release	74278	
ADV	3145	Near bottom turbulence velocity and acoustic backscatter
Campbell OBSx2	NA	Optical backscatter
Shallow Water Temp Mooring (Shoreface)		
Equipment	Serial Number	Parameters Measured
ADV	VEC 11074	Near bottom turbulence velocity and acoustic backscatter
RBR Virtuoso Tu	54272	Optical backscatter
LTER Cross Island Mooring		
Equipment	Serial Number	Parameters Measured
Nortek AD2CP	AD2CP199	Water column velocities, surface wave spectra, water column acoustic backscatter, turbulence velocities
SBE 16Plus	16-50170	Conductivity/temperature/pressure
CART (acoustic release)	30600	

The shallow water shore face mooring (Figure 6) was deployed with a Nortek Acoustic Doppler Velocimeter (ADV), and an RBR Virtuoso Turbidity sensor. The RBR Virtuoso broke off on retrieval of the mooring and was unable to be recovered. An effort will be made to determine whether the acoustic backscatter recorded by the ADV, calibrated against in-situ particle size and turbidity information from the SBE25+55 and LISST sensor package will be adequate for determining sediment fluxes past the shoreface mooring. The UAA Newport mooring (Figure 7) was deployed with an ADCP, Seabird Microcat 37, Nortek ADV and dual Campbell OBS3+ sensors. The UAF Dinkum mooring (Figure 8) was deployed with an acoustic Doppler current profiler (ADCP), a Seabird Microcat 37, and an acoustic release. Mooring deployment locations are shown in Figure 9.

Figure 6. Shallow water shore face mooring

Figure 7. UAA Newport mooring

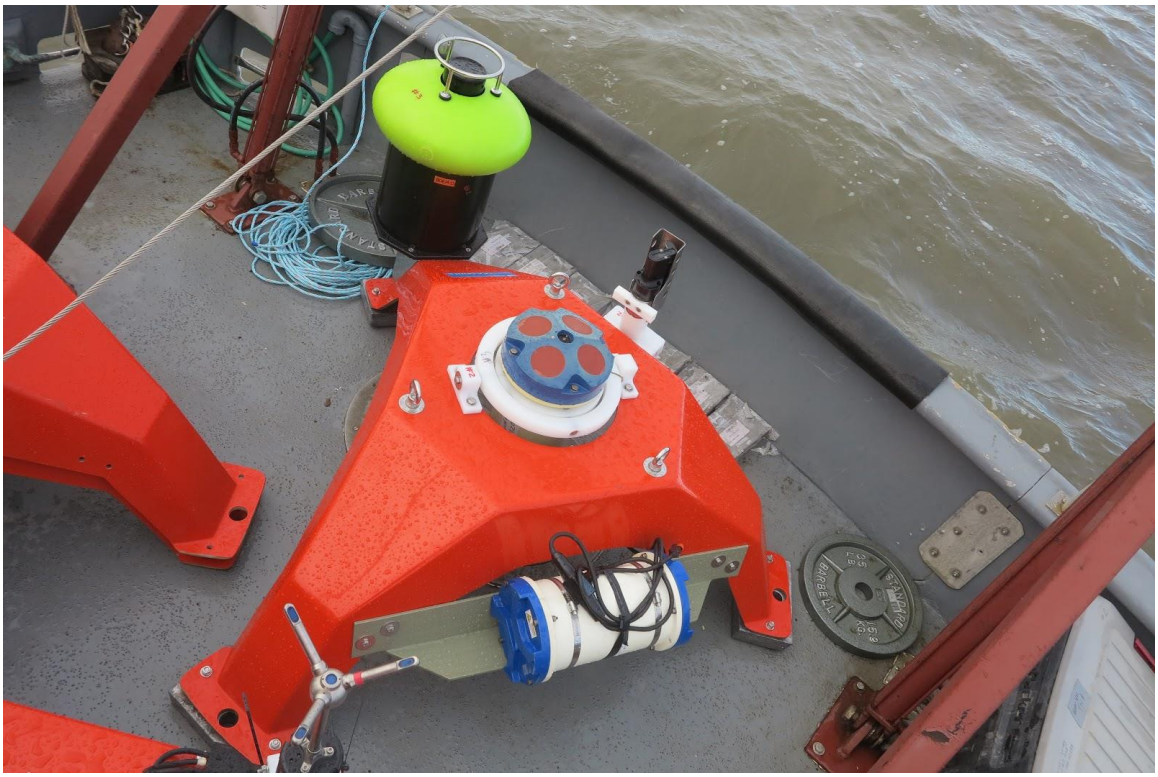

Figure 8. UAF Dinkum mooring

Figure 9. Location of the four moorings deployed during the 2018 Central Beaufort Sea Study cruise.

Survey Equipment

The Reson 7125 Seabat Multibeam Echosounder was deployed daily on July 20th – 23rd and July 25th with a total of 224 km surveyed (Figure 10).

The 600 kHz RD Instruments Sentinel Workhorse ADCP mounted on a Biosonics Inc. "acoustic sled" was also deployed in the morning and retrieved at end of day on July 21st, 22nd, and 25th. A total of 167 km were surveyed (Figure 11) using the ADCP including across the mouth of the Sag. River, a large source of sediments for the region.

In addition to gathering multibeam bathymetry on tracks overlapping with previous bathymetric surveys in the region, several strudel scours were surveyed. Snapshots from the multibeam display of these seafloor are shown in Figure 12, Figure 13 and Figure 14.

The sled mounted ADCP and Reson multibeam and accompanying equipment are shown in Figure 15, Figure 16and Figure 17.

Figure 10. Coverage map of the 224 km surveyed by the Reson 7125 Seabat Multibeam Echosounder deployments

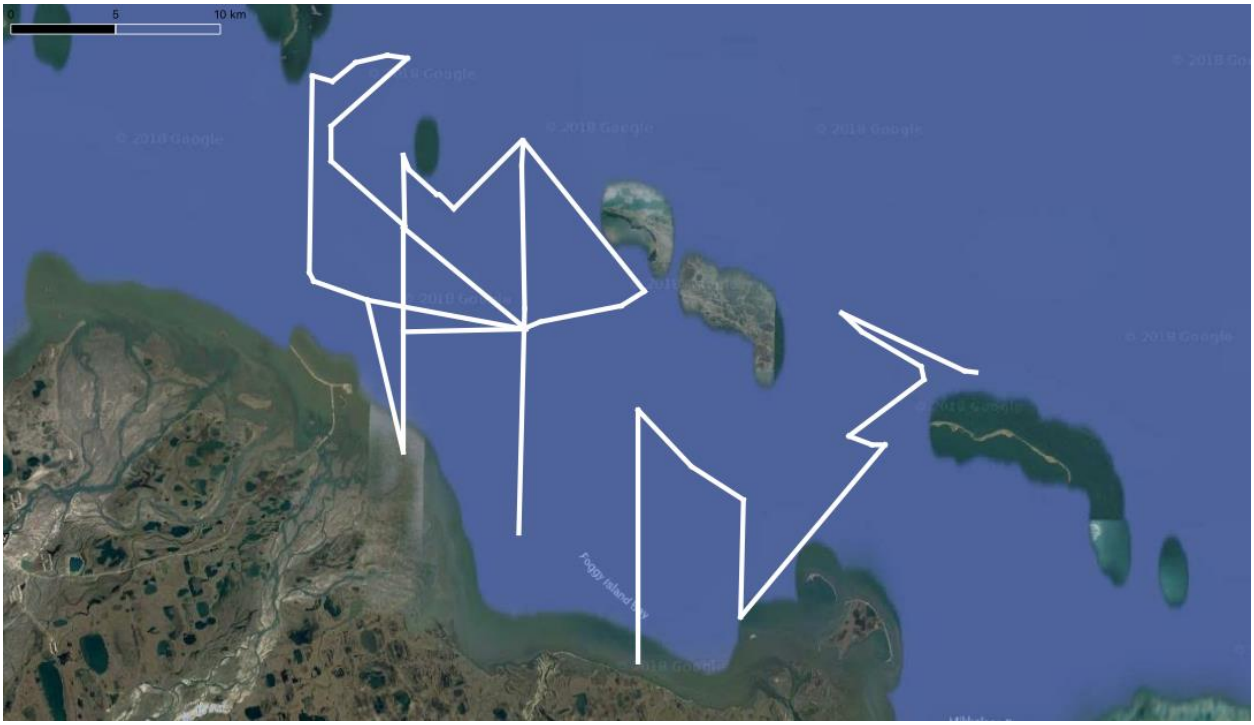

Figure 11. Coverage map of the 167 km that the sled mounted 600 kHz RD Instrument sentinel workhorse ADCP traveled

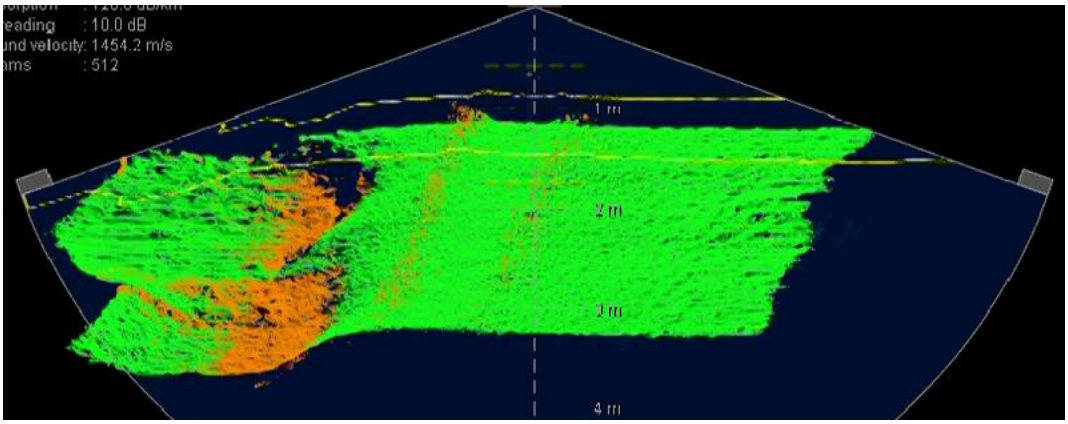

Figure 12. Snapshot of Reson 7125 Seabat multibeam Echosounder image.

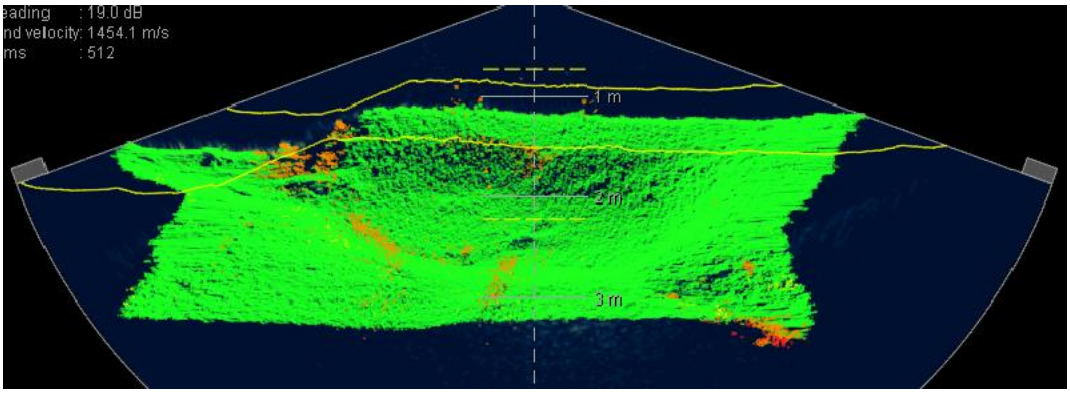

Figure 13. Second image from Reson 7125 Seabat multibeam Echosounder taken in Foggy Island Bay.

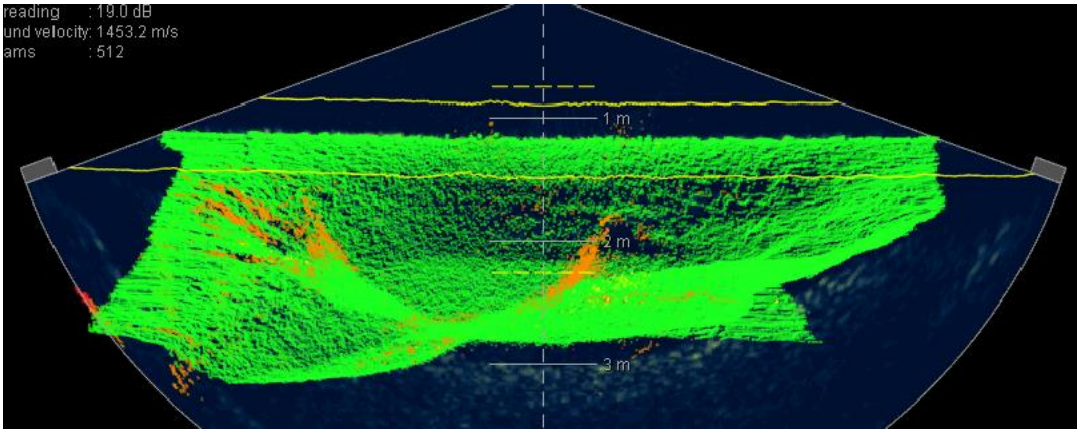

Figure 14. Third image taken with the Reson 7125 multibeam sonar in Foggy Island Bay.


Figure 15. 600 kHz RD Instrument Sentinel Workhorse ADCP mounted on Biosonics Inc., acoustic sled.

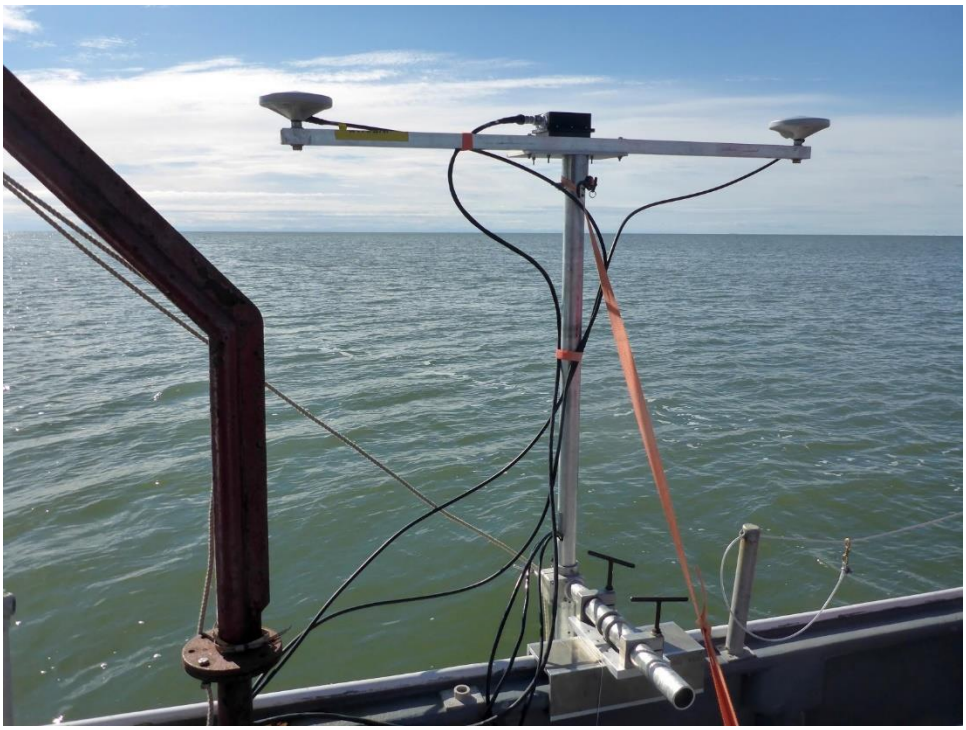

Figure 16. Reson 7125 Seabat Echosounder deployed with inertial motion unit (IMU) and primary and secondary antenna mounted to echosounders support beam.

Figure 17. Deployed Reson 7125 Seabat Echosounder from the R/V Ukpik.

Met Station

A Campbell meteorological station (met station) was installed on July 27th and began logging at 20:00 UTC (12:00 PM AKST) July 27. The met station is powered by a 12V battery that is charged via solar panel and a wind turbine. The met station monitors air temperature in °C, average wind speed in MPH, wind direction in degrees (true north), barometric pressure in milibars, and relative humidity in % Atm. Two cameras were installed facing each side of the coast. These are each programmed to take one picture per hour.

Location: 70.204075°N , 147.701386°W
Components:

1. Campbell Tripod CM110
2. RM Young Wind Sensor 05108-L9-CWS
3. Relative Humidity Sensor 083E-L6-PW
4. 2-CC5MPX Cameras
5. Temperature Sensor with Solar Radiation Shield
6. Micro Specialties satellite control and antenna
7. Sun Xtender PVX-1040T 104AH Battery
8. 2-80W Solar Panels
9. Rutland 914i Windcharger 12V wind turbine with low temperature bearings

Figure 16. Met Station

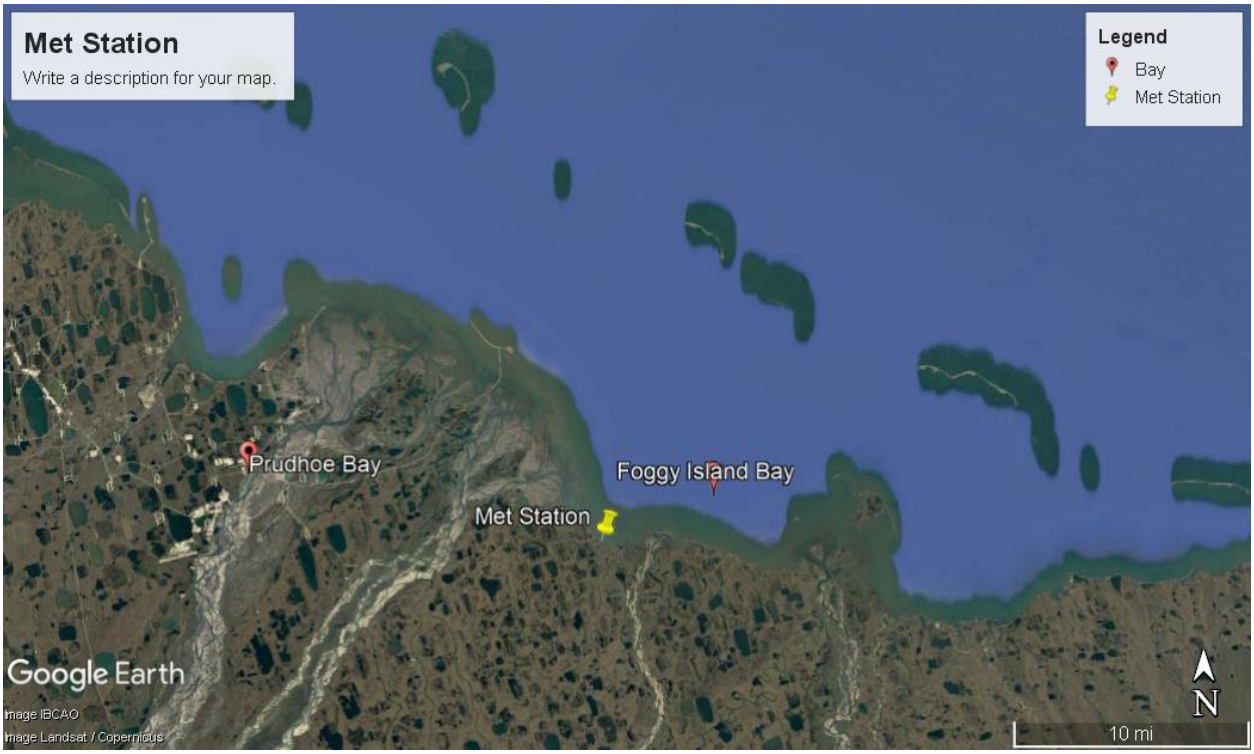

Figure 17. Meteorological weather station location

3D Mapping

3D mapping of Foggy Island Bay coast was attempted, but due to technical issues with the drone's gimbal and compass, only one of the three pre-defined transect lines could be completed. Thus we were not able to complete the mapping of coastal elevations at this time.

Figure 18. Aerial shot of met station location in Foggy Island Bay taken during 3D mapping.

Ice Conditions

Throughout the cruise, MODIS imagery from NASA's Worldview platform was used to provide updates on ice condition. Additionally, the National Weather's Ice Desk provided additional web-based updates as well.

Several MODIS images from the cruise period are included below. While we have not conducted an analysis of winds during the cruise, anecdotally, it appears that ice persisted in the region due to a lack of strong upwelling favorable winds (winds from East to West) that have moved ice further offshore during this time of year in recent years.

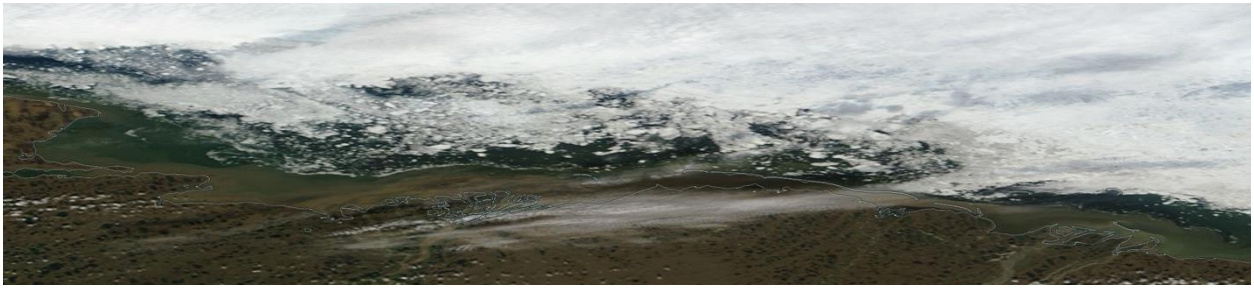

Figure 18. NASA Worldview MODIS image from 7/20/2018 showing persistent sea ice offshore of Prudhoe Bay and Foggy Island Bay.

Figure 19. NASA Worldview MODIS image from 7/27/208.

Preliminary Results

Thirty-nine discrete water samples were collected for analysis of Total suspended solid (TSS). Just after collection, water samples were filtered through a 1.5 µm binder free, glass microfiber filter that was vacuum rinsed three times with 20mL aliquots of reagent free water and dried at 105°C for at least one hour. Samples were processed using standard methods (2005), 2540D and EPA (1983) Method 160.2 (Residue, non-filterable) in the WERC lab on UAF campus after the completion of the cruise. Results are given in Table viii

Table viii. Location, collection date, filter dry weight, volume processed, dried filter weight, and TSS results.

Station Name	Date Collected	Filter Tare Weight (mg)(B)	Volume Filtered (L) (V)	Oven Dry Mass (mg) (A)	TSS (mg/L) [(A-B/V]
FIB12	22-Jul	128.6	1	137.07	8.47
FIB10	22-Jul	127.3	1	139.25	11.95
FIB9	21-Sep	127.9	1	139.23	11.33
FIB3	20-Jul	129.5	1	153.95	24.45
FIB1	20-Jul	127	1	135.29	8.29
FIB3	20-Jul	128.1	1	137.27	9.17
FIB17	28-Jul	128	1	147.48	19.48
FIB21	29-Jul	130.4	1	149.76	19.36
FIB11	22-Jul	129.3	1	148.9	19.6
FIB19	28-Jul	126.6	1	145.5	18.9
FIB6	20-Jul	127.6	1	149.47	21.87
FIB18	28-Jul	127.4	1	154.18	26.78
FIB7	21-Jul	127.6	1	136.59	8.99
FIB8	21-Jul	128.5	1	141.65	13.15
FIB5	20-Jul	128.1	1	146.15	18.05
FIB13	22-Jul	126.7	1	144.09	17.39
FIB6	20-Jul	128.5	1	148.74	20.24
FIB14	23-Jul	128.6	1	149.35	20.75
FIB5	20-Jul	128.3	1	134.61	6.31
FIB12	22-Jul	129	1	140.05	11.05
FIB8	21-Jul	127.6	1	138.32	10.72
FIB1	20-Jul	128.9	1	146.34	17.44

FIB15	23-Jul	128.6	1	160.83	32.23
FIB2	20-Jul	127.6	1	136.6	9
FIB11	22-Jul	128.5	1	156.88	28.38
FIB17	28-Jul	127.1	1	148.71	21.61
FIB7	21-Jul	127.5	1	158.41	30.91
FIB10	22-Jul	127.1	1	141.88	14.78
FIB15	23-Jul	127.3	1	139.91	12.61
FIB13	22-Jul	128.2	1	143.09	14.89
FIB2	20-Jul	126.8	1	144.43	17.63
FIB21	29-Jul	130.9	1	157.99	27.09
FIB9	21-Jul	127.2	1	139.54	12.34
FIB20	28-Jul	129.7	1	153	23.3
FIB20	28-Jul	127.5	1	152.33	24.83
FIB14	23-Jul	129	1	142.42	13.42
FIB16	25-Jul	127	1	137.61	10.61
FIB19	28-Jul	128.5	1	151.84	23.34
FIB SB	25-Sep	129.6	0.1	263.32	133.72

DelO18 samples were analyzed by Cornell Isotope Laboratory (COIL) in Ithaca, New York. The analysis was preformed on a Thermo Delta V isoptope ratio mass Spectrometer (IRMS) interfaced to a Gas Bench II. Delta values are measured in units of per mil (‰). The overall deviation for the internal DI standard 0.18 ‰ $\delta^{18}O$.

Table ix. DelO18 Station where sample was taken and DelO18 Results.

Station Name	DelO 18
FIB2	-4.75
FIB2	-13.85
FIB3	-4.08
FIB3	-12.58
FIB5	-4.03
FIB5	-12.40
FIB6	-16.40
FIB6	-16.43
FIB7	-3.58
FIB7	-13.42
FIB8	-13.32
FIB8	-14.26
FIB9	-16.09
FIB9	-16.39
FIB10	-11.70

FIB10	-14.48
FIB11	-3.14
FIB11	-8.16
FIB12	-11.19
FIB12	-12.23
FIB13	-15.15
FIB13	-18.47
FIB14	-6.00
FIB14	-15.47
FIB15	-4.52
FIB15	-12.91
FIB16	-3.13
FIB16	-6.98

Figure 20. TSS results by location. Note that more than one sample was taken per location.

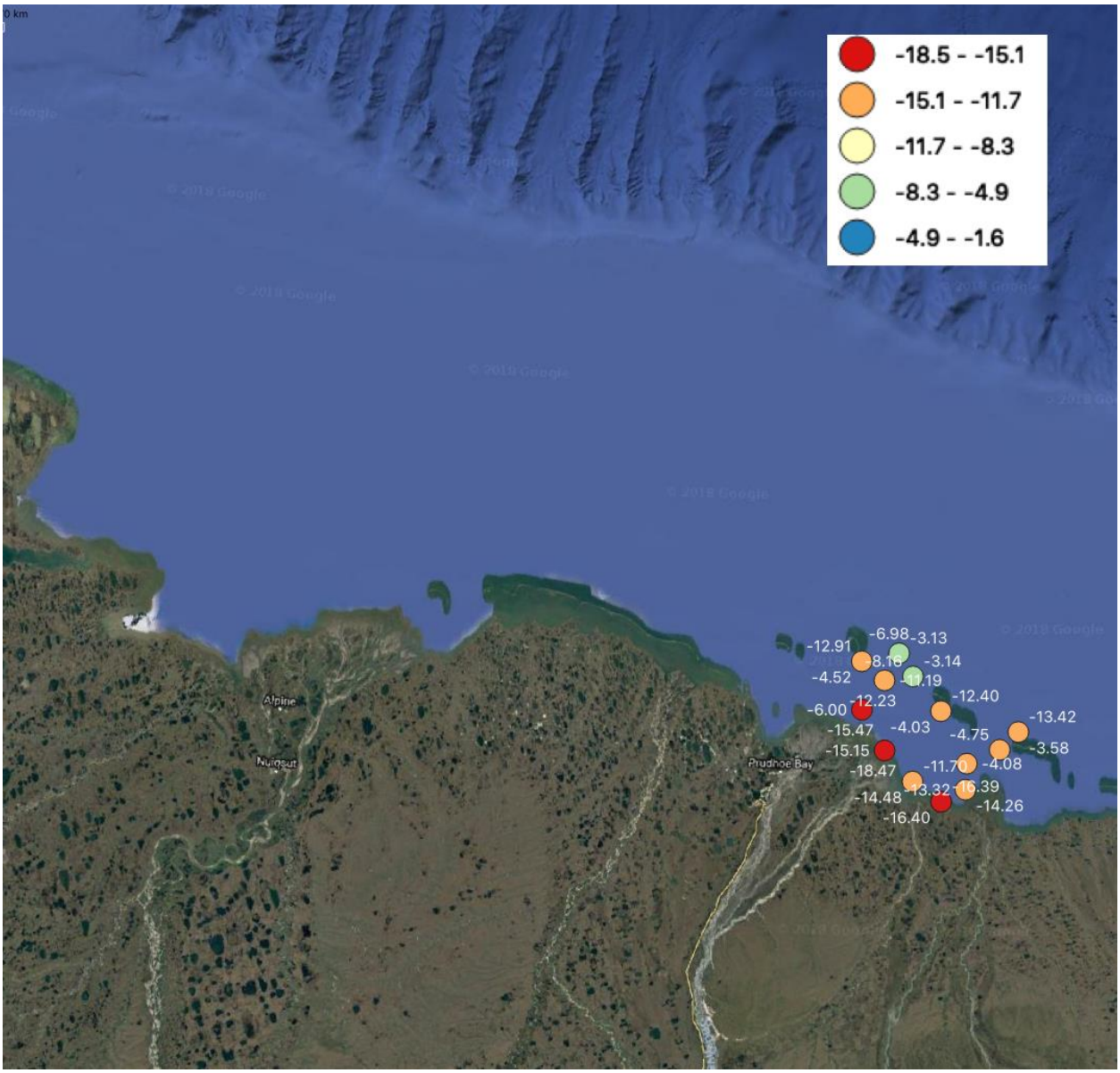

Figure 21. DelO18 results by location.

Supplemental Photos

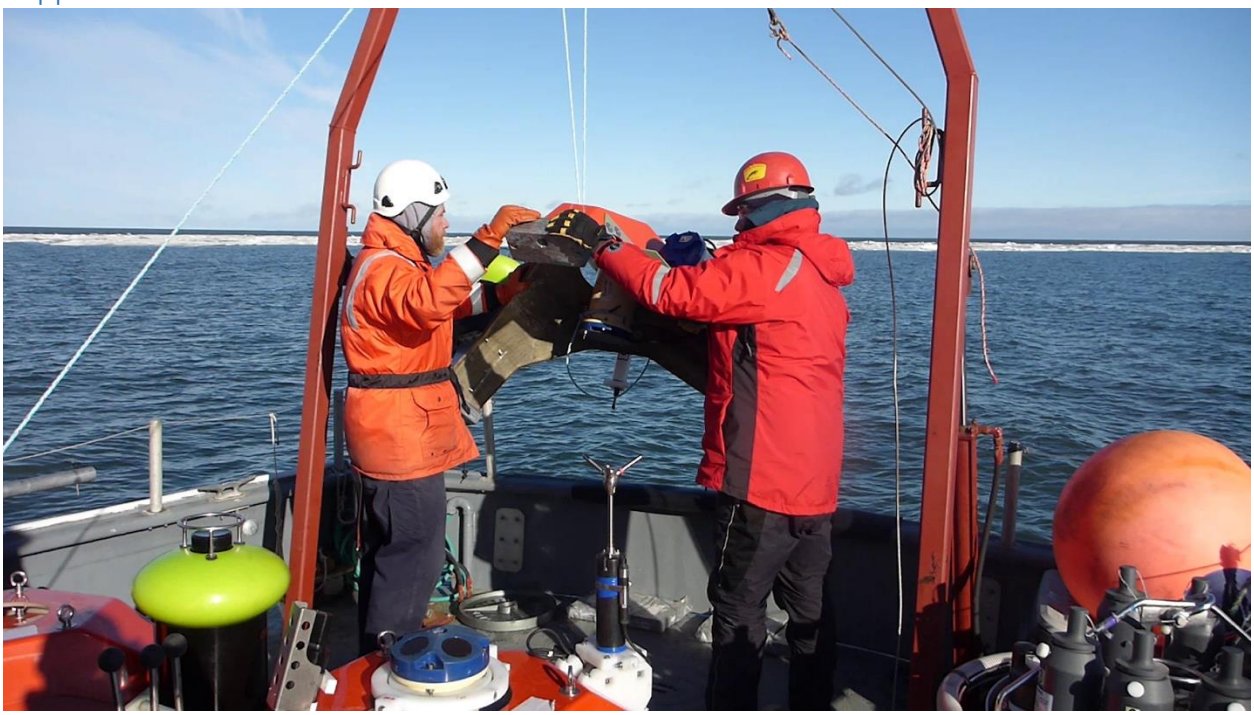

Figure 22. Dr. Jeremy Kasper and Research Engineer Nicholas Konefal deploying one of the oceanographic moorings.

Figure 23. Seabird Electronics SBE25+ equipped with an SBE 55 water sampler and ancillary sensors.

Figure 24. Seabird SBE25+ with LISST attached to carousel being retrieved at a sampling station.

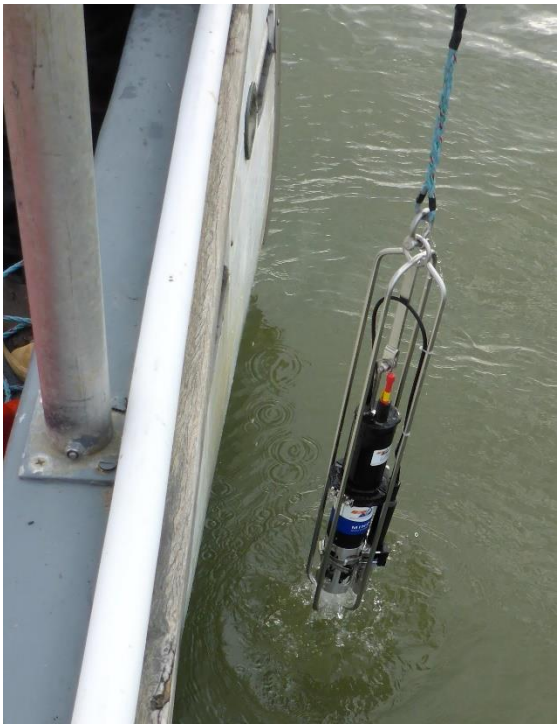

Figure 25. AML MinosX probe.

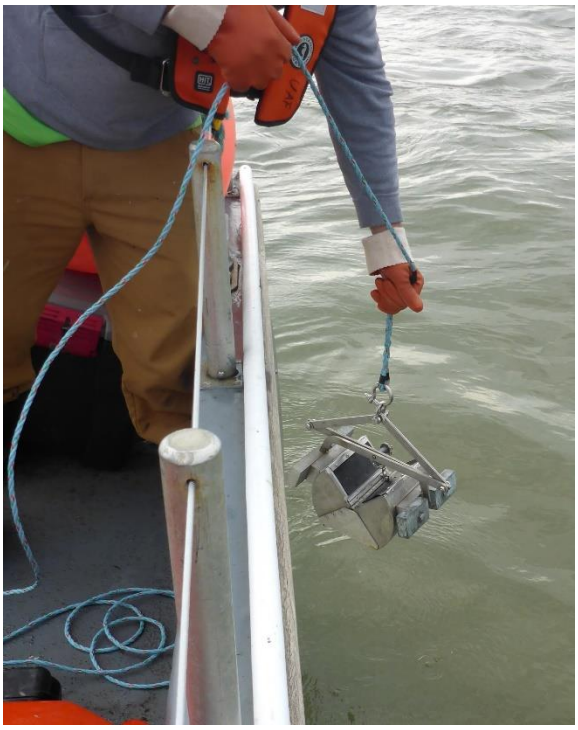

Figure 26. Wildco stainless teel Ponar grab.

Timeline of Foggy Island/Stef Sound Cruise

Table x. Timeline of daily activity and personnel present.

7/15/2018	Arrived in Deadhorse. Arrival delayed by ~1 week due to persistence of ice within the barrier islands. Begin unpacking and setup	Duvoy, Kasper, Konefal
7/16/2018	Unpacking and setup continues. Shuttling 5 pallets worth of gear between Deadhorse and West Dock.	Duvoy, Kasper, Konefal
7/17/2018	Finished moving equipment from hanger to West Dock and onto R/V Ukpik. Set up equipment and instrumentation.	Duvoy, Kasper, Konefal
7/18/2018	Mounting and connection of all equipment. Configured PDS 2000	Duvoy, Kasper, Konefal
7/19/2018	Conducted 2 calibrations for multibeam, and diagnosed and repaired faulty IMU antenna cable.	Duvoy, Kasper, Konefal
7/20/2018	Deployed UAF Dinkum, Shore-face, and UAA Newport Moorings. Multibeam logged for the day, 5 water sampling and CTD cast completed, and 8 AML probe cast conducted. Anchored at Tigvariak Island for the night.	Duvoy, Kasper, Konefal

7/21/2018	Departed Tigvariak Island and went north of Newport entrance, due to ice the entrance going south was surveyed. Multibeam and ADCP on acoustic sled deployed for the day. 12 AML MinosX probe cast taken, one CTD cast, and six ponar grabs with three producing samples.	Duvoy, Kasper, Konefal
7/22/2018	Multibeam started, surveyed multiple strudel scours, thirteen ponar grabs with eleven samples collected. Seventeen AML MinosX probe casts completed.	Duvoy, Kasper, Konefal
7/23/2018	Multibeam started in am. Six AML MinoX probe cast completed. Arrived back to West Dock at 2:25pm (AKST)	Duvoy, Kasper, Konefal
7/24/2018	Spend day at hanger in Deadhorse AK. Working on Met. Station Setup and Testing, Campbell Controller Programming and Met. station parts and setup for Campbell controller. Kasper departs for conflicting LTER field work.	Duvoy, Kasper, Konefal
7/25/2018	Multibeam and ADCP on acoustic sled deployed for day. Cross Island mooring deployed. Five AML MinosX probe cast taken, 3 ponar grabs samples taken.	Duvoy, Konefal
7/26/2018	The met station was installed, Acquired two 15-minute Ground Control Points (GCPs) for 3D Mapping with the Trimble R8 GPS. 1 of 3 transect lines completed before gimble malfunction	Duvoy, Konefal
7/27/2018-7/29/2018	Sandia National Lab Drew Point Project Work	Duvoy, Konefal
7/30/2018	Demob and pack gear for shipment. Truck gear between West Dock and Deadhorse	Duvoy, Kasper, Konefal
7/31/2018	Depart Deadhorse for Fairbanks	Duvoy, Konefal

Central Beaufort Sea Wave and Hydrodynamic Modeling Study 2019 Field Report

UAF Cooperative Agreement M17AC00020/ USGS CFDA No. 15.423

Report Contributors:
Dr. Jeremy Kasper
Ms. Stephanie Jump
Mr. Paul Duvoy

Field Personnel
Jeremy Kasper, UAF PI
Stephanie Jump, UAF Research Professional
Paul Duvoy, UAF Research Engineer
Taylor Poirrier, UAF Research Technician

Table of Contents

List of Figures

List of Tables

Table 1. Acronyms used in this report.

ADCP	ACOUSTIC DOPPLER CURRENT PROFILER
ADV	ACOUSTIC DOPPLER VELOCIMETER
CTP	CONDUCTIVITY/TEMPERATURE/PRESSURE
CTD	CONDUCTIVITY/TEMPERATURE/DEPTH
GNSS	GLOBAL NAVIGATION SATELLITE SYSTEM
GPS	GLOBAL POSITION SYSTEM
IARC	INTERNATIONAL ARCTIC RESEARCH CENTER
IMU	INERTIAL MOTION UNIT
TSS	TOTAL SUSPENDED SOLIDS
UAA	UNIVERSITY OF ALASKA ANCHORAGE
UAF	UNIVERSITY OF ALASKA FAIRBANKS
USGS	UNITED STATES GEOLOGICAL SURVEY
VMDAS	VESSEL MOUNT DATA ACQUISITION SYSTEM

Summary

Between August 12th and August 29th, 2019 two bottom founded oceanographic moorings equipped with various sensors to measure currents, surface wave spectra, near-bottom velocity and hydrography and water levels were retrieved and redeployed in support of the Central Beaufort Sea Wave and Hydrodynamic Modeling Study project inside of Foggy Island Bay (FIB). A third, seasonally deployed shallow water oceanographic mooring, the "shoreface" mooring was deployed to measure shore face sediment fluxes along with wave spectra at the southern end of Foggy Island Bay.

A fourth mooring, the "LTER Cross Island mooring" equipped with sensors to measure currents, wave spectra and near bottom hydrography deployed offshore of the barrier islands enclosing Foggy Island Bay for the Beaufort Lagoons LTER project in 2018 was not able to be recovered in 2019. If recovered, data from this LTER mooring will be incorporated into results for the Central Beaufort Sea Wave and Hydrodynamic Modeling Study. Specifically, the LTER mooring would provide information on the "boundary conditions" for wave and hydrography within Foggy Island Bay.

Water column hydrographic information were collected (conductivity, temperature and pressure) during the cruise in order to provide sound speed corrections for multibeam sonar data and information on the origin and characteristics of the water masses in the study area. A total of 3 water samples were collected in 2019 using a 3.2L Van Dorn water sampler and 4 "sensor only" stations were completed during the 2019 cruise (using an AML Oceanographic CTP+Turbidity probe).

Multibeam sonar data (seafloor depth and backscatter strength) gathered within and outside of Foggy Island Bay will be used for creating a Digital Elevation Model for the ocean and wave modeling portion of the study. When compared to existing and repeat measurements, the multibeam sonar data will also provide information on changes in seafloor topography between survey years within the region which can then be used to estimate sediment fluxes due to bedload transport. Multibeam acoustic backscatter measurements will also be calibrated against the in-situ seafloor sediment information collected so that maps of sediment size derived from the multibeam acoustic backscatter measurements can be created.

In 2019, a pole-mounted Acoustic Doppler Current Profiler (ADCP) was deployed from the gunwale of the R/V Ukpik to measure water column velocity and acoustic backscatter.

A met station installed in 2018 on the southern coast of Foggy Island Bay to measure wind speed and direction, barometric pressure, temperature and relative humidity was serviced in 2019. Two cameras mounted on the met station provide hourly images of the nearby coast for quantifying coastal change over the course of the project. The met-station and cameras will remain deployed for the duration of the field-portion of the project. A small drone, an unmanned aerial vehicle was deployed at this time as well to image coastal position and topography.

Two Spoondrift “spotter” buoy for measuring surface wave spectra in real-time were deployed on August 6th and 7th and retrieved on September 7th, 2019.

Work took place on the R/V between August 16 and August 26. Between August 22 and August 25, work on other projects was carried out from the same platform, the R/V Ukpik. After demobilization was complete, UAF personnel returned to Fairbanks on August 29. UAF researchers S. Jump and T. Poirrier returned to Deadhorse in early September to pack-up the shoreface mooring and wave buoys that were recovered by the R/V Ukpik.

Survey Platforms

The R/V Ukpik (Figure 1), a 16m vessel well-suited for work in the region was chartered for the work. The R/V Ukpik is equipped with an articulating A-frame with a 2,000 lb. capacity winch with 450 meters of cable and a 6" deck mounted capstan winch. UAF commissioned a local machinist to design and fabricate an adapter to mount UAF's multibeam transducer to the starboard-side gunwale of the R/V Ukpik so that a multibeam sonar survey could be carried out from the R/V Ukpik. A similar mount was fabricated in order to use a pole mount for the ADCP rather than the sled system used in 2018. Duvoy, Kasper and Jump undertook the work on the R/V Ukpik during summer 2019. Captain Mike Fleming operated the R/V Ukpik for the duration of the cruise.

Figure 1. R/V Ukpik.

Shipboard Instrumentation

1. UAF-owned AML Oceanographic MinosX Conductivity/Temperature/Pressure (CTP)+Turbidity sensor
2. UAF-owned 600 kHz RD Instruments Sentinel Workhorse Acoustic Doppler Current Profiler (ADCP).
3. UAF-owned Reson 7125 Seabat Multibeam Echosounder and Applanix POSMV GNSS+Inertial Navigation System.
4. 3.2L Van Dorn water sampler
5. UAF-owned Trimble R8 GNSS base station, Trimble R10 GNSS receiver + Trimble GNSS base station.

Sampling Stations

Two stations were sampled in Foggy Island Bay using a 3.2L Van Dorn. Discrete water samples at 2 depths were collected at this time for analysis of total suspended solids (TSS), macronutrients, and stable oxygen isotope ratios (delO18). Station names, depth and locations are shown in Table 2 and Figure 2 Information on "sensor-only" stations, sampled using the AML CTP+Turbidity sensor package is given in Table 3and Figure 3. Note a UAF-owned Seabird 55/25 system failed to initialize dockside and was therefore not brought on the cruise. Four stations were sampled using the AML CTP+Turbidity sensor package (Figure 3).

Table 2.Name, depth and locations for the 2 sampling stations where CTD, TSS, and DelO18 samples were collected.

Station Name	Depth (m)	Latitude (DD)	Longitude (DD)
STL_JLK_0	7	70.402858°N	147.841533°W
FIB17	30 cm below surface	70.34667222°N	147.6439944°W

Figure 2. CTD Locations where total suspended solids (TSS), and macronutrients were collected.

Table 3. Sample ID, Dates, Time and location of AML Probe data was collected. Times are UTC.

Number	Area	Date	Time (UTC)	Latitude (DD)	Longitude (DD)
1	Stef. Sound	8/18/2019	5:02:00 PM	70.27636667°N	147.2079694°W
2	Stef. Sound	8/18/2019	6:25:00 PM	70.30183056°N	147.3629139°W
3	Stef. Sound	8/18/2019	10:06:00 PM	70.32480278°N	147.3619611°W

4	Stef. Sound	9/11/2019	9:17:00 PM	70.402272°N	147.835883°W

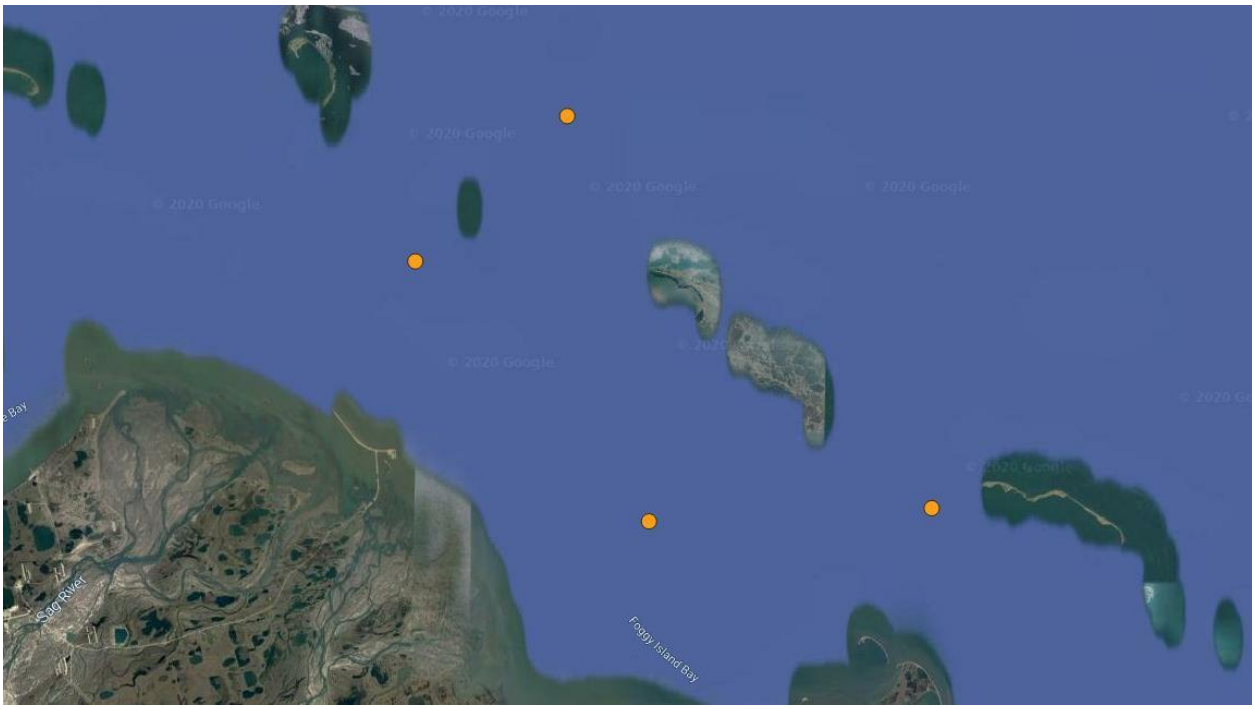

Figure 3. Location of AML "sensor-only" stations.

Table 4. DelO18 and Nutrient sample Station locations.

Station Name	Latitude (DD)	Longitude (DD)
STL_JLK_0	70.402858°N	147.841533°W
FIB17	70.34667222°N	147.6439944°W

Oceanographic Moorings

Two year-round oceanographic moorings were retrieved on August 18th and re-deployed on August 19th . One temporary, shallow "shoreface" mooring was deployed on August 18th and retrieved September 7th. The year-round LTER oceanographic mooring was not recovered due to an apparent failure of the acoustic release. A multibeam survey of the area was conducted in an unsuccessful attempt to locate the mooring.

Table 5. Oceanographic Mooring Name, Locations, deployment date and time.

Name	Latitude (DD)	Longitude (DD)	Date	Time (UTC)
UAF Dinkum	70.29315°N	147.543019°W	8/19/2019	22:52
Shore face	70.2110944°N	147.573631°W	8/18/2019	19:30

UAA Newport	70.2992028°N	147.187625°W	8/19/2019	23:46
Cross Island	70.46906944°N	147.7245889°W	7/25/2018	10:15 AM

Table 6. Mooring name and instrument type and serial number for each mooring.

UAF Mooring		
Equipment	Serial Number	Parameters Measured
ADCP	2018	Water Column Velocity, Surface Wave Spectra, Acoustic Backscatter
RBR Concerto	60717	Conductivity, Temperature, Pressure
Acoustic Release	74379	
UAA Newport Mooring		
Equipment	Serial Number	Parameters Measured
ADCP	2018	Water Column Velocity, Surface Wave Spectra, Acoustic Backscatter
RBR Concerto	60717	Conductivity, Temperature, Pressure
Acoustic Release	76056	
ADV	3145	Near Bottom Velocities
Campbell OBS	S8016	Optical Backscatter
Campbell OBS	S8018	
Shallow Water Temp Mooring (Shoreface)		
Equipment	Serial Number	Parameters Measured
ADV	VEC5095	Near Bottom Velocities
Campbell OBS	T9377	Optical Backscatter
Campbell OBS	T9376	Optical Backscatter
RBR TD.Wave	51094	Pressure and Temperature
LTER Cross Island Mooring		
Equipment	Serial Number	Parameters Measured
ADCP		Water Column Velocity, Surface Wave Spectra, Acoustic Backscatter
SBE 16Plus		Conductivity, Temperature, Pressure
CART (Acoustic Release)		

The shallow water shoreface mooring (Figure 5) was deployed with a Nortek Acoustic Doppler Velocimeter (ADV), two OBS sensors, and an RBR Duo TDWave sensor. The UAF mooring was deployed with an acoustic Doppler current profiler (ADCP), an RBR Concerto CTD, and an acoustic release. The UAA Newport mooring was deployed with an ADCP, RBR Concerto CTD, Nortek ADV with OBS sensors.

Sofar Ocean "Spotter" Wave Buoys

Two Sofar Ocean® wave buoys were deployed at two separate locations for the ~30 days in August-September. The buoys were deployed from the R/V Ukpik prior to the arrival of UAF researchers and retrieved after their departure from the Prudhoe area. The buoys transmit their data once an hour via satellite and track significant wave height, peak and mean period, direction, and spread in near real-time. The data was made available in realtime via the AOOS Project Data Portal. One buoy was placed near the LTER Mooring site STL_JLK0 (SPOT – 0107, T. Weingartner's "Dinkum" mooring-site) and the other (SPOT -0156) six miles SE in Stefansson Sound Lagoon at LTER mooring site STLDS2 (K. Dunton's long-term Boulder Patch "DS2" Site).

Table 7. Wave buoy deployment locations, dates, and times.

Sofar Ocean® wave buoys						
Name	**Latitude (DD)**	**Longitude (DD)**	**Date In**	**Date Out**	**Time In (UTC)**	**Time Out (UTC)**
Spot – 0156	70.319167°N	147.760750°W	8/5/2019	9/7/2019	22:21	19:25
Spot – 0107	70.393250°N	147.832767°W	8/6/2019	9/7/2019	01:14	19:00

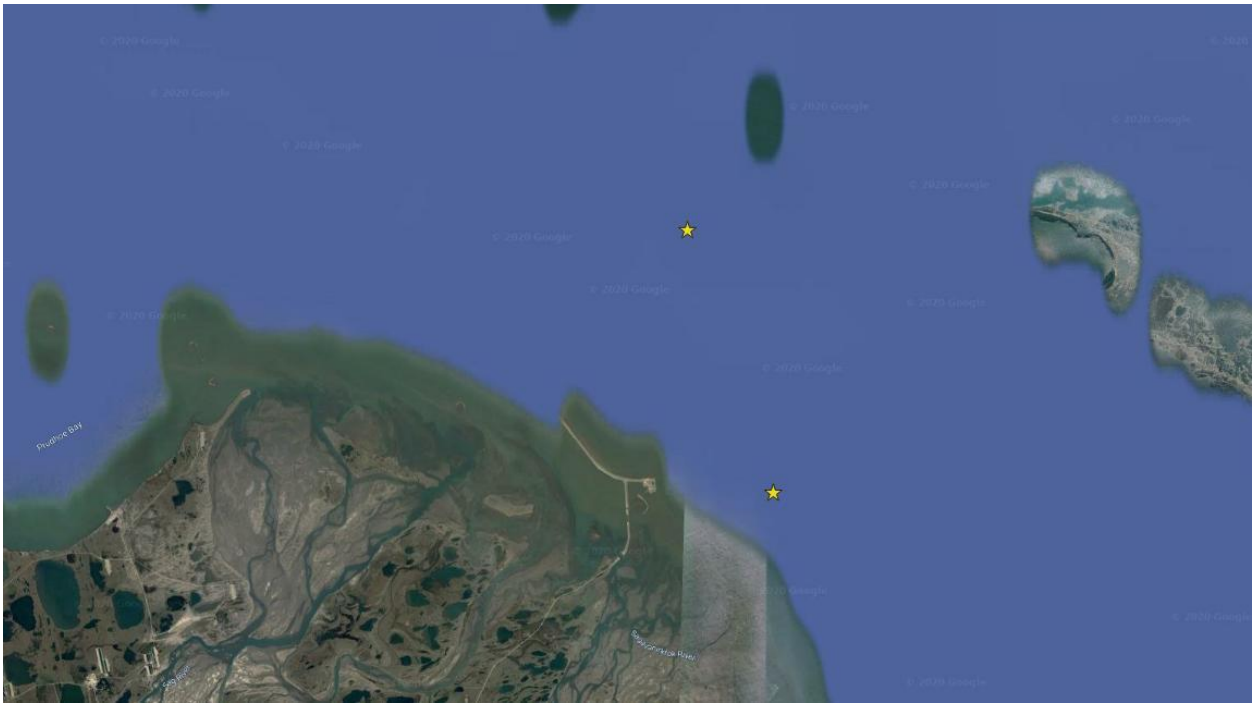

Figure 4. Location of wave buoy deployments.

Figure 5. The shoreface mooring.

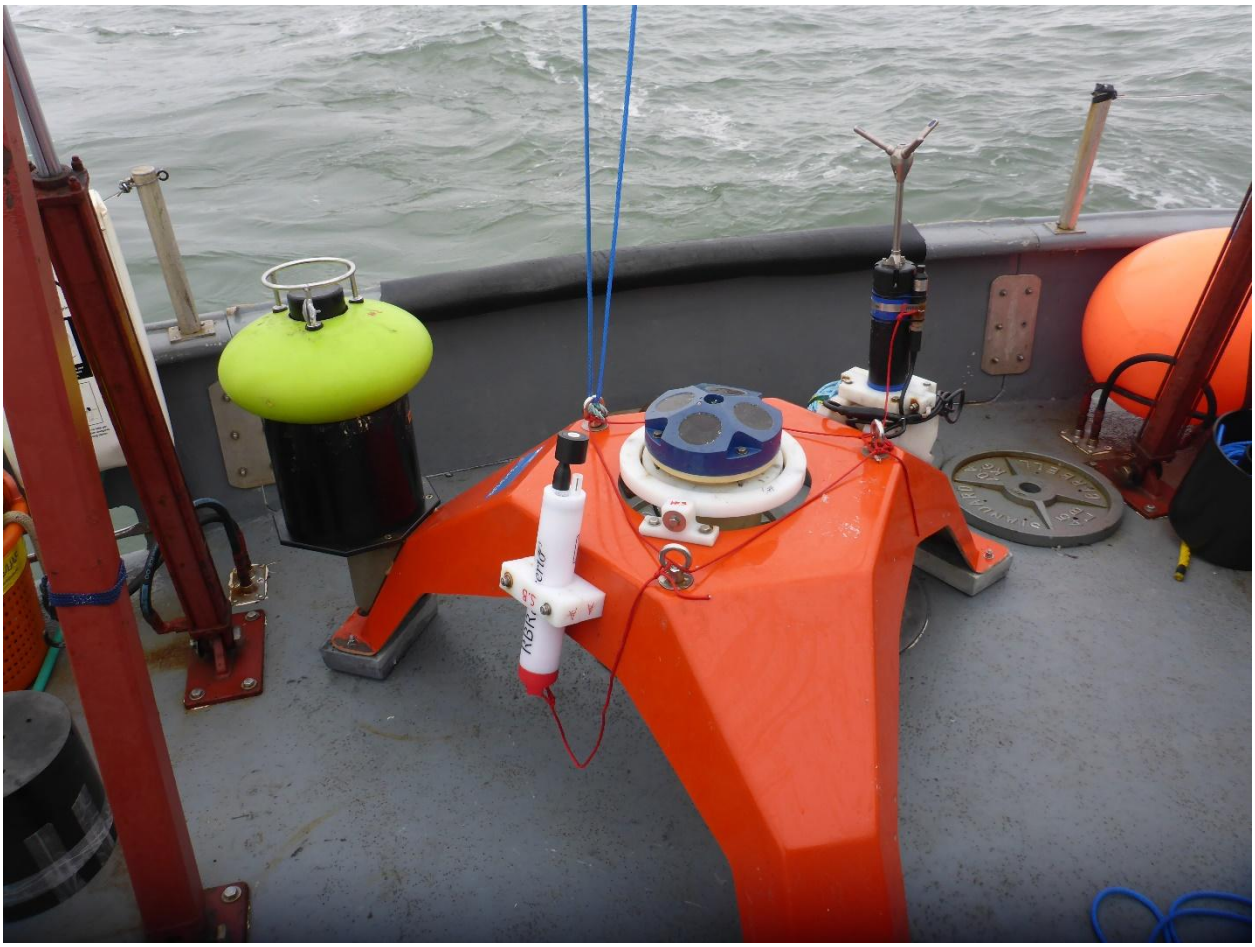

Figure 6. UAA Newport mooring.

Figure 7. UAF mooring.

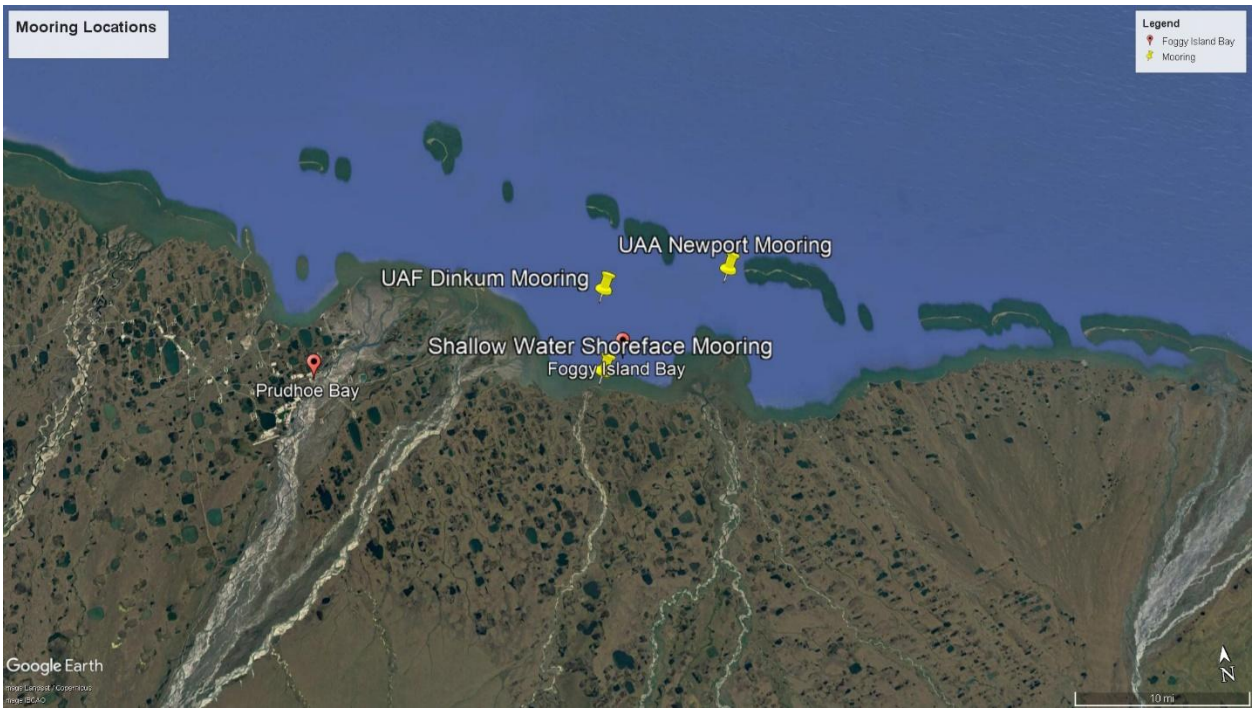

Figure 8. Location of the three mooring deployments in Foggy Island Bay.

Survey Equipment

The Reson 7125 Seabat Multibeam Echosounder was deployed on 8/17-8/18. The 600 kHz RD Instruments Sentinel Workhorse ADCP was deployed on 8/17-8/18 via a gunnel mounted pole.

Figure 9. Coverage map of the pole mounted 600 kHz RD Instrument sentinel workhorse ADCP and approximate multibeam sonar coverage.

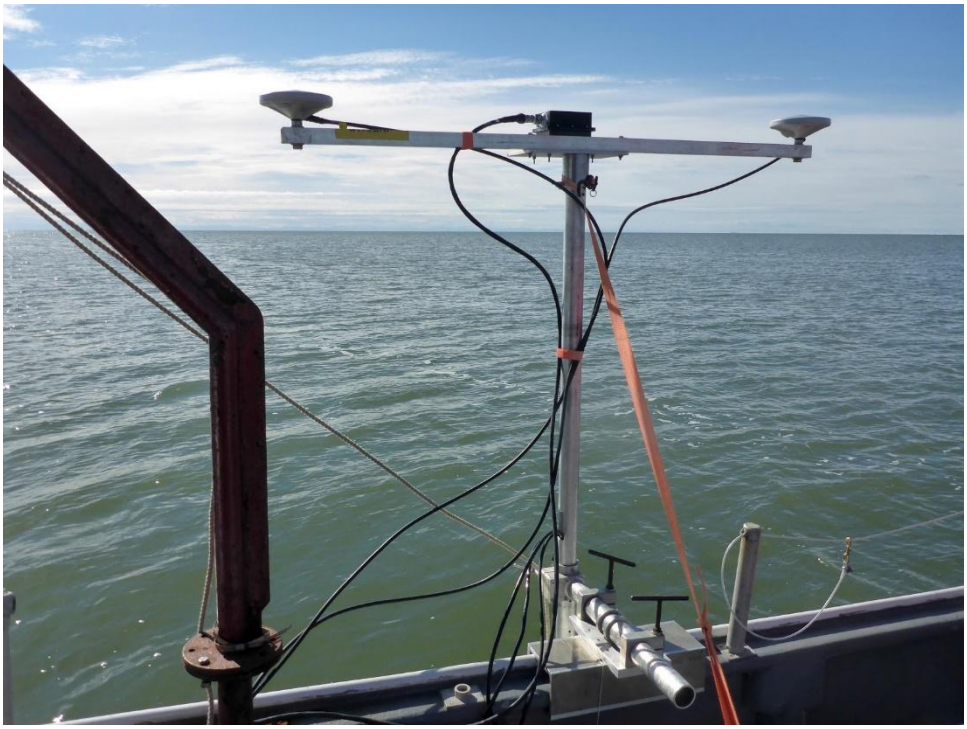

Figure 10. Reson 7125 Seabat Echosounder deployed with inertial motion unit (IMU) and primary and secondary antenna mounted to echosounder support beam.

Figure 11. 600 kHz RD Instrument Sentinel Workhorse ADCP pole mounted off the R/V Ukpik

Met Station

A Campbell meteorological station (met station) installed in 2018 was revisited for repairs in 2019. The met station is powered by a 12V battery that is charged via solar panels and a wind turbine. The met station monitors air temperature in °C, average wind speed in miles per hour, wind direction in degrees (true north), barometric pressure in milibars, and relative humidity in % Atm. Two cameras were installed facing each side of the coast and programmed to take a picture every hour. The met-station failed in December 2018. Upon inspection in summer 2019 it

was determined that a wire between the power system and an exposed connector corroded. The wires between the power system and the logger were replaced with continuous wires (no exposed connectors) and the system resumed functioning. A new wind turbine was also installed to power the system since it was unclear whether the previous turbine was providing adequate power to the system.

Location: 70.204075°N , 147.701386°W
Components:

1. Campbell Tripod CM110
2. RM Young Wind Sensor 05108-L9-CWS
3. Relative Humidity Sensor 083E-L6-PW
4. 2-CC5MPX Cameras
5. Temperature Sensor with Solar Radiation Shield
6. Micro Specialties satellite control and antenna
7. Sun Xtender PVX-1040T 104AH Battery
8. 2-80W Solar Panels
9. Primus Windpower Air 40 12V.

Figure 12. Met station at the southern end of Foggy Island Bay.

Figure 13. The new wind turbine installed to power the met-station over winter.

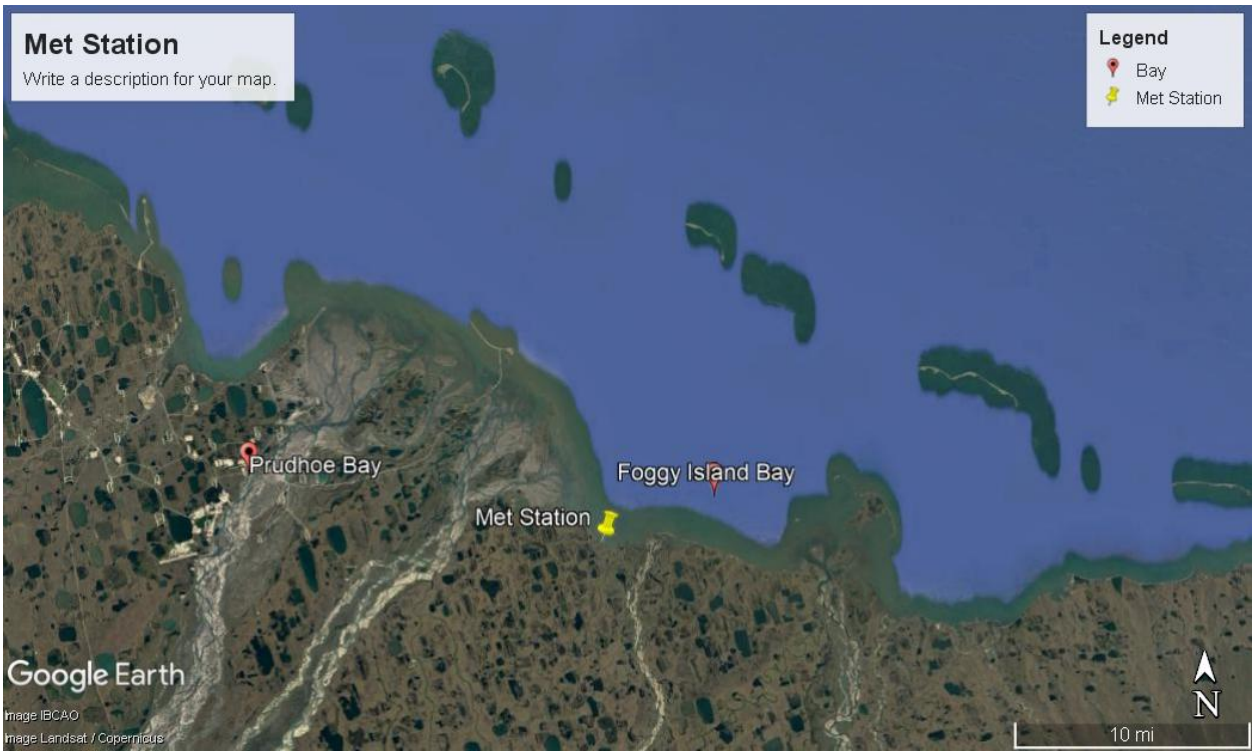

Figure 14. Location of the met station.

3D Mapping

A drone survey of the area immediately surrounding the met-station was successfully executed using a UAF-owned DJI Phantom 3 UAV. The digital elevation map produced using the Agisoft photogrammetric software package of the surveyed area is shown in Figure 19. Three survey lines were occupied using a survey-grade GPS system (a UAF-owned Trimble R10 base and rover). GPS survey lines are shown overlain on the UAV survey area in Figure 20.

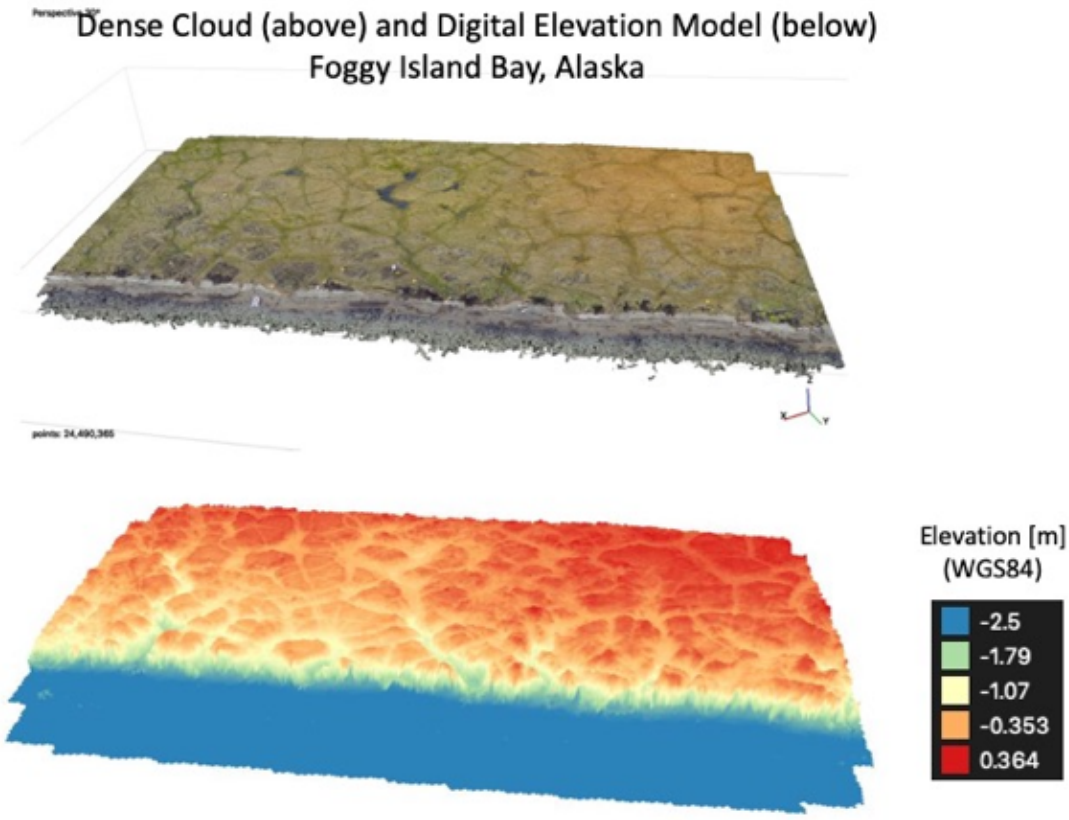

Figure 15. Digital elevation model of FIB produced from drone imagery.

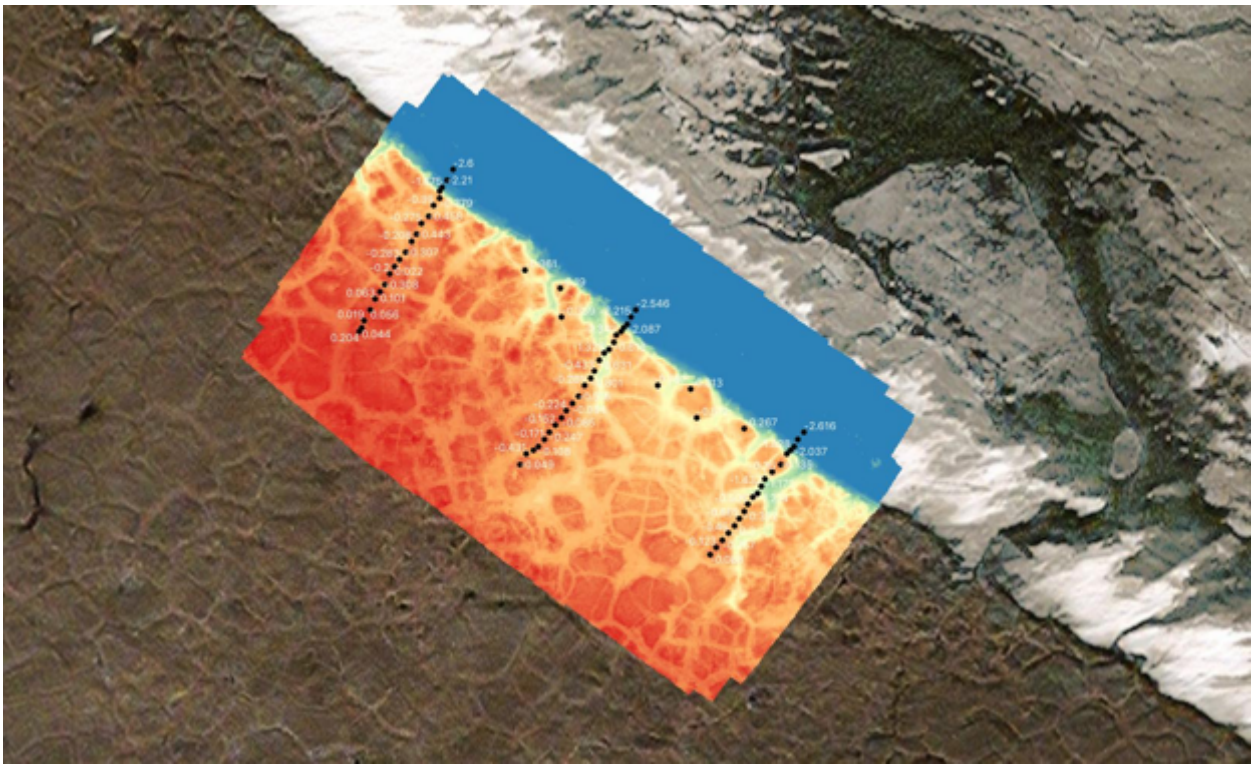

Figure 16. Location of GNSS transects draped over the digital elevation model produced from the UAV imagery.

Sample analysis protocol

Two water samples were collected and analyzed for Total Suspended Solid (TSS). Water samples were filtered through a 1.5 µm binder free, glass microfiber filter that was vacuum rinsed three times with 20mL aliquots of reagent free water and dried at 105°C for at least one hour. The samples will be processed using standard methods (2005), 2540D and EPA (1983) Method 160.2 (Residue, non-filterable) in the UAF WERC lab.

The 2 samples collected for analysis of stable oxygen isotopes (δ^{18}O) will be analyzed by Cornell Isotope Laboratory (COIL) in Ithaca, New York. The analysis is performed on a Thermo Delta V isoptope ratio mass Spectrometer (IRMS) interfaced to a Gas Bench II. Delta values are measured in units of per mil (‰). The overall deviation for the internal DI standard 0.18 ‰ δ^{18}O.

Analyses of nutrients (nitrate plus nitrite, nitrite, phosphate, silicate, and ammonia) in the 2 samples collected will be performed at UAF using a Seal Analytical continuous-flow QuAAtro39 AutoAnalyzer. Following each run, peaks are reviewed for any problems, any blank is subtracted and final concentrations (in micromoles per liter) are calculated based on a linear curve fit using Seal Analytical AACE 7.07 software by the UAF Nutrient Analytical Facility.

ADCP Preliminary Results

The ADCP data was post-processed using the University of Hawaii developed CODAS software package. Preliminary results are shown in Figures 17-23.

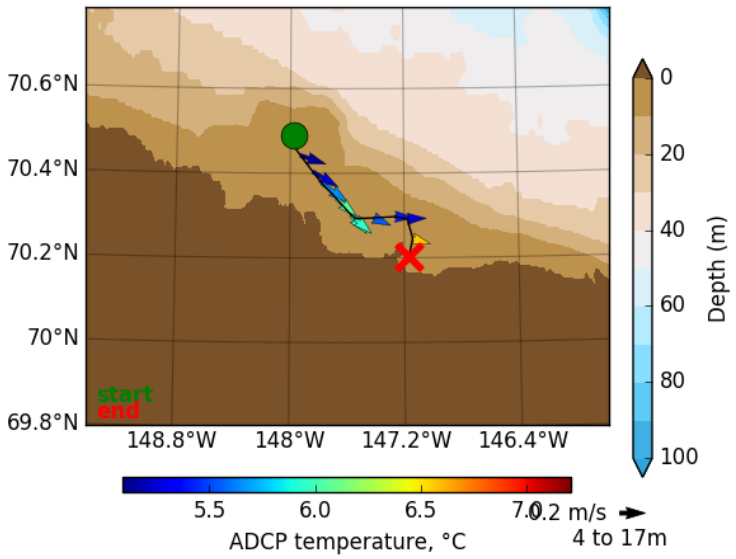

Figure 17. Plot of surface temperature measured by the ADCP.

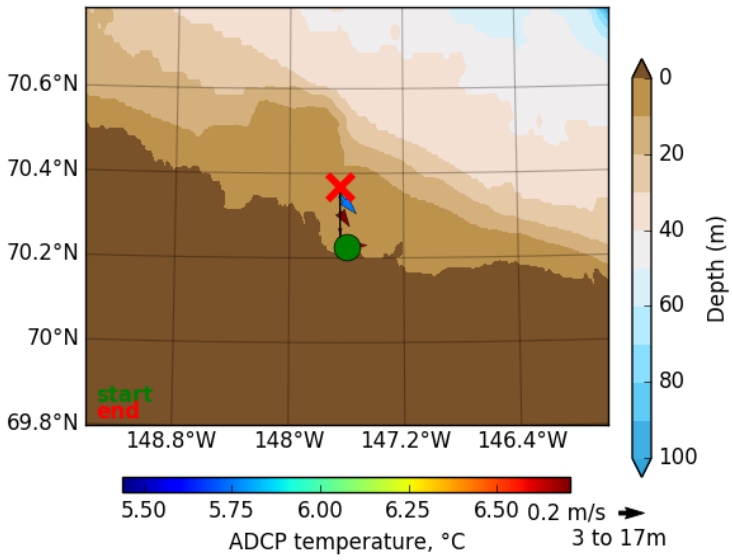

Figure 18. Plot of surface temperature from the ADCP.

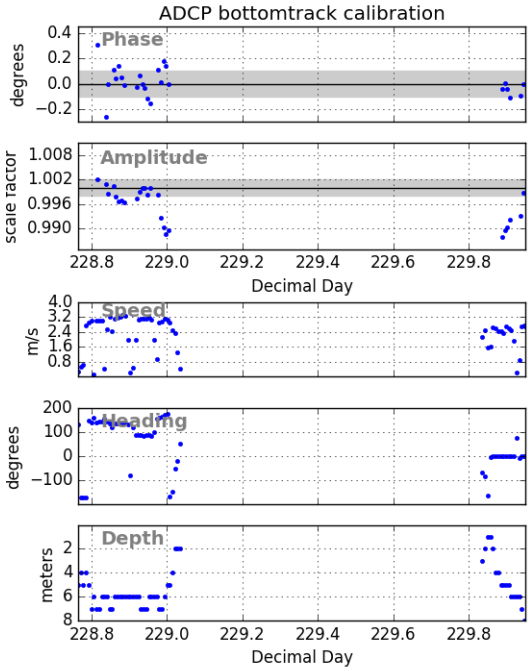

Figure 19. ADCP bottom track calibration.

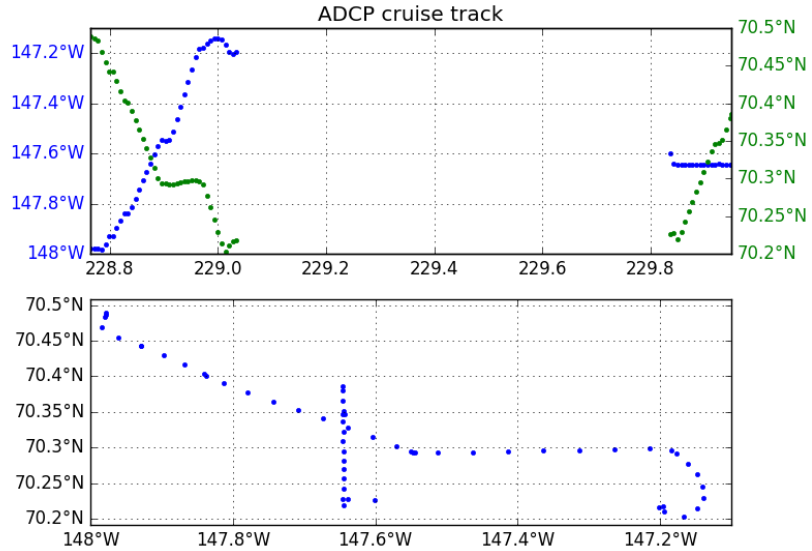

Figure 20. ADCP cruise track.

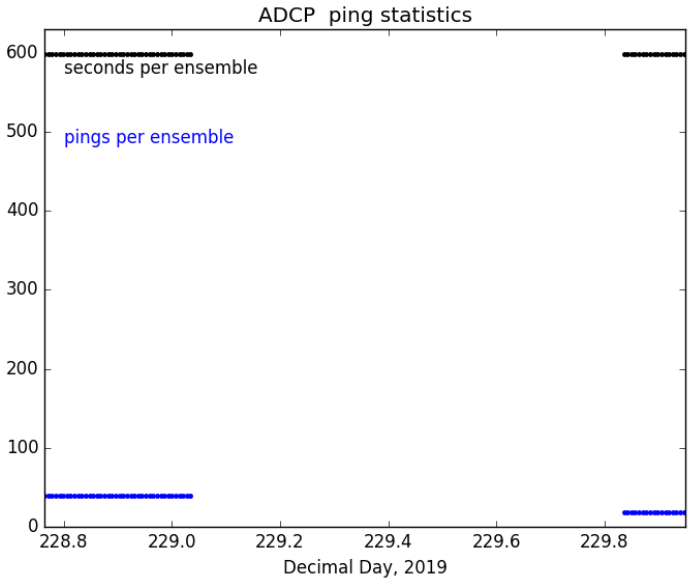

Figure 21. ADCP ping statistics.

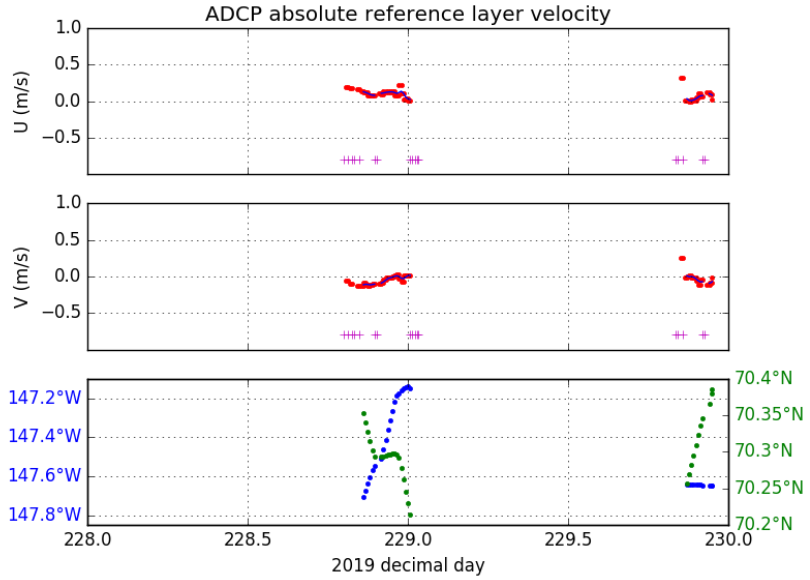

Figure 22. . ADCP absolute reference layer showing velocity and coordinates.

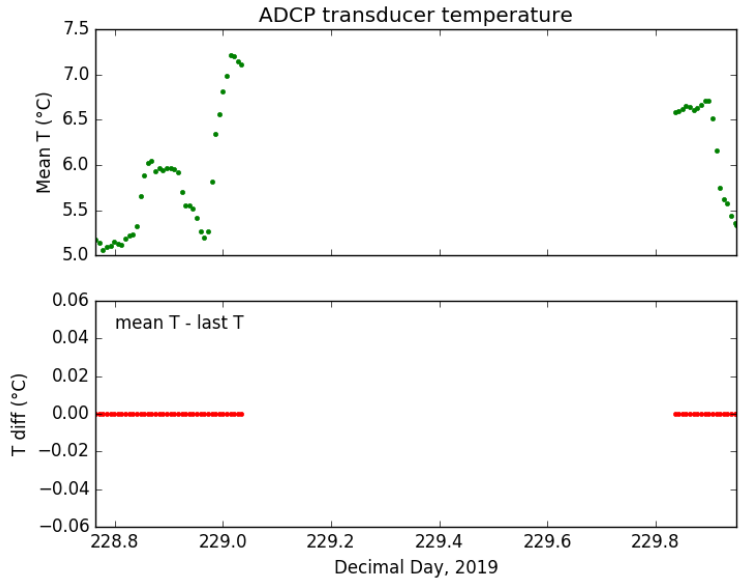

Figure 23. . ADCP transduce mean temperature (top) and temperature difference by day.

Supplemental Photos

Figure 24. Reson 7125 Seabat multibeam sonar head mounted to the starboard side of the R/V Ukpik.

Figure 25. Reson 7125 Seabat Echosounder ready for deployment off the R/V Ukpik.

Figure 26. Dr. Jeremy Kasper and Research Professional Stephanie Jump deploying one of the oceanographic moorings.

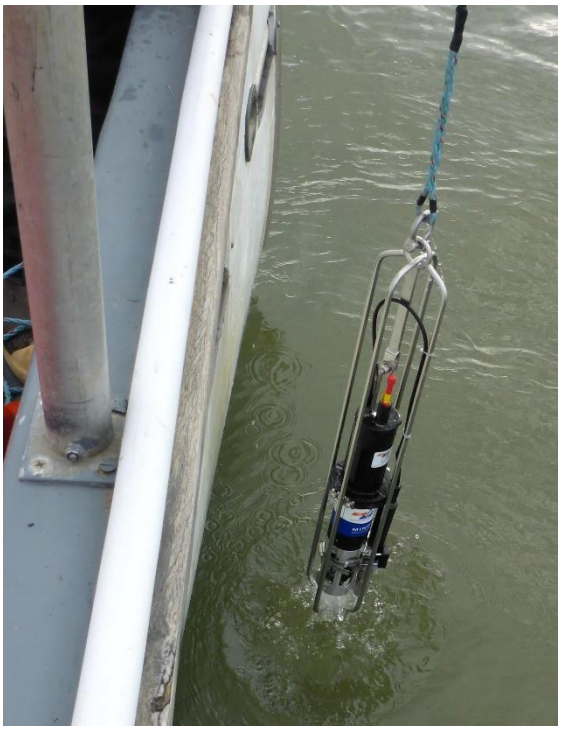

Figure 27. AML CTP probe being deployed from the R/V Ukpik.

Figure 28. Researcher Stephanie Jump deploying the 3.2L Van Dorn water sampler

Figure 29. DJI Phantom 3 unmanned aerial vehicle ready to conduct the aerial survey of FIB.

Appendix A: Narrative Timeline of Foggy Island/Stef Sound Cruise

Table 8. Timeline of daily activity and personnel present.

8/15/2019	Moved equipment from Dalton pad warehouse space to West Dock. Set up equipment and instrumentation.	Dr. Jeremy Kasper, Stephanie Jump, Paul Duvoy
8/16/2019	Finished loading equipment onto vessel. Setup and calibrated shoreface mooring. Anchored at Cross Island for night.	Dr. Jeremy Kasper, Stephanie Jump, Paul Duvoy
8/17/2019	Completed multibeam calibration by doing figure eights and patch test near Cross Island. Surveyed UAA and UAF moorings. Ran Survey line from LTER mooring station STL_JLK_0 -> UAF -> UAA and anchored up at Tigvariuk.	Dr. Jeremy Kasper, Stephanie Jump, Paul Duvoy
8/18/2019	Retrieved UAA and UAF moorings. Put multibeam and ADCP down and surveyed strudel scour. Ran survey line north from FIB. Did AML cast and collected water sample. Cross Island acoustic release did not release, surveyed deployment location with multibeam. Anchored at Cross Island. Started downloading instrument data from moorings and replaced ADCP batteries.	Dr. Jeremy Kasper, Stephanie Jump, Paul Duvoy
8/19/2019	Headed to West Dock to retrieve additional equipment and continued working on downloading data and replacing batteries on mooring instruments. Programed mooring instruments and measured instrument heights on mooring. Deployed UAA and UAF moorings. Anchored at Tigvariuk.	Dr. Jeremy Kasper, Stephanie Jump, Paul Duvoy
8/20/2019	Beach survey day 1. Set up ground control points for drone survey and started troubleshooting and repairing met station. Replaced wind turbine. Completed surveying ground control points.	Dr. Jeremy Kasper, Stephanie Jump, Paul Duvoy
8/21/2019	Completed aerial survey and north/south transect lines with Trimble survey equipment. Headed back to Cross Island and did more multibeam surveys but were unable to locate mooring. Headed back to West Dock.	Dr. Jeremy Kasper, Stephanie Jump, Paul Duvoy
8/22/2019 - 8/25/2019	Work on other projects	
8/26/2019	Unloaded gear off vessel using zodiac due to high water conditions at West Dock and transported it back to Dalton pad in Deadhorse. Packed gear onto pallets for shipment back to Fairbanks.	Dr. Jeremy Kasper, Stephanie Jump, Paul Duvoy

Central Beaufort Sea Wave and Hydrodynamic Modeling Study 2020 Field Report

UAF Cooperative Agreement M17AC00020/ USGS CFDA No. 15.423

Report Contributors:
Dr. Jeremy Kasper
Mrs. Stephanie Fisher
Mr. Paul Duvoy
Ms. Taylor Poirrier

Field Personnel
Stephanie Fisher, UAF Research Professional
Taylor Poirrier, UAF Research Technician

Table of Contents

List of Figures

List of Tables

Table 1. Acronyms used in this report.

ADCP	Acoustic Doppler Current Profiler
ADV	Acoustic Doppler Velocimeter
CTP	Conductivity/Temperature/Pressure
CTD	Conductivity/Temperature/Depth
GNSS	Global Navigation Satellite System
GPS	Global Position System
IARC	International Arctic Research Center
IMU	Inertial motion unit
TSS	Total Suspended Solids
UAA	University of Alaska Anchorage
UAF	University of Alaska Fairbanks
USGS	United States Geological Survey
VMDAS	Vessel Mount data acquisition system

Summary

Between August 3rd and August 13th, 2020 two bottom founded oceanographic moorings equipped with various sensors to measure currents, surface wave spectra, near-bottom velocity and hydrography and water levels were successfully retrieved in support of the Central Beaufort Sea Wave and Hydrodynamic Modeling Study project inside of Foggy Island Bay (FIB). A third, seasonally deployed shallow water oceanographic mooring, the "shoreface" mooring was deployed to measure shore face sediment fluxes along with wave spectra at the southern end of Foggy Island Bay.

A fourth mooring, the "LTER Cross Island mooring" equipped with sensors to measure currents, wave spectra and near bottom hydrography deployed offshore of the barrier islands enclosing Foggy Island Bay for the Beaufort Lagoons LTER project in 2018 was not able to be recovered in 2019 or 2020 and is presumed unrecoverable at this time.

Water column hydrographic information were collected (conductivity, temperature and pressure) during the cruise in order to provide sound speed corrections for multibeam sonar data and information on the origin and characteristics of the water masses in the study area. A total of 31 water samples were collected in 2020 using a 3.2L Van Dorn water sampler and 41 "sensor only" stations were completed during the 2020 cruise (using an AML Oceanographic CTP+Turbidity probe).

In 2020, a pole-mounted Acoustic Doppler Current Profiler (ADCP) was deployed from the gunwale of the R/V Ukpik to measure water column velocity and acoustic backscatter.

A met station installed in 2018 on the southern coast of Foggy Island Bay to measure wind speed and direction, barometric pressure, temperature and relative humidity was serviced in 2019. Two cameras mounted on the met station provide hourly images of the nearby coast for quantifying coastal change over the course of the project. The met-station and cameras will remain deployed for the duration of the field-portion of the project. A small drone, an unmanned aerial vehicle was deployed at this time as well to image coastal position and topography. Work at the met station was unable to be completed in 2020 and is planned to be completed in 2021.

Two Sofar Ocean "spotter" wave buoys for measuring surface wave spectra in real-time were deployed prior to the start of our cruise from the R/V Ukpik on July 16th. The shoreface mooring was deployed at this time as well. The spotter buoys were recovered on August 12th, 2020.

With the exception of the deployments noted above, work took place on the R/V Ukpik between August 3 and August 13. Between August 3 and August 6, work on other projects was carried out from the same platform. After demobilization was complete, UAF personnel returned to Fairbanks on August 15.

Survey Platforms

The R/V Ukpik (Figure 1), a 16m vessel well-suited for work in the region was chartered for the work. The R/V Ukpik is equipped with an articulating A-frame with a 2,000 lb. capacity winch with 450 meters of cable and a 6" deck mounted capstan winch. UAF commissioned a local machinist to design and fabricate an adapter to mount UAF's multibeam transducer to the starboard-side gunwale of the R/V Ukpik so that a multibeam sonar survey could be carried out from the R/V Ukpik. A similar mount was fabricated in order to use a pole mount for the ADCP rather than the sled system used in 2018. Jump and Poirrier undertook the work on the R/V Ukpik during summer 2020. Captain Mike Fleming operated the R/V Ukpik for the duration of the cruise.

Figure 1. R/V Ukpik

Shipboard Instrumentation

1. UAF-owned AML Oceanographic MinosX Conductivity/Temperature/Pressure (CTP)+Turbidity sensor
2. UAF-owned 600 kHz RD Instruments Sentinel Workhorse Acoustic Doppler Current Profiler (ADCP).
3. 3.2L Van Dorn water sampler
4. Wild Petite Ponar Grab 6"x6"
5. BlueView P900-2250-45 Sonar
6. Edgetech 4125 Side Scan Sonar

Sampling Stations

14 stations were sampled in Foggy Island Bay using a 3.2L Van Dorn sampling bottle. Discrete water samples at 2 depths were collected at this time for analysis of total suspended solids (TSS), macro and trace nutrients, and stable oxygen isotope ratios (delO18). Station names, depth and locations are shown in Table 2 and Figure 2. Information on the 37 "sensor-only" stations, sampled using the AML CTP+Turbidity sensor package is given in Table 3 and Figure 3.

Table 2. Name, depth and locations for the 14 sampling stations where CTD, TSS, macronutrients, and DelO18 samples were collected

Station Name	Depth (m)	Latitude (DD)	Longitude (DD)
UAF Dinkum	7.01	70.29313889°N	147.5438083°W
UAA Newport	6.95	70.29877778°N	147.1892056°W
Shoreface	1.77	70.21096389°N	147.5735806°W
FIB3	7.32	70.27800278°N	147.3625972°W
FIB5	6.58	70.36743056°N	147.4955694°W
FIB6	2.87	70.20663056°N	147.4941806°W
FIB7	11.13	70.33089444°N	147.0972028°W
FIB8	3.05	70.22907778°N	147.3641111°W
FIB10	4.51	70.24232500°N	147.6446556°W
FIB11	10.97	70.42809444°N	147.6509444°W
FIB13	2.74	70.30040278°N	147.7961278°W
FIB14	5.79	70.36783611°N	147.9115306°W
FIB15	7.00	70.45299167°N	147.9179889°W
FIB16	14.00	70.46779722°N	147.7216167°W

Figure 2. CTD Locations where total suspended solids (TSS), DelO18, and macronutrients were collected.

Table 3. Sample ID, Dates, Time and location of AML Probe data collected. Times are UTC.

Number	Area	Date	Time (UTC)	Latitude (DD)	Longitude (DD)
1	Stef. Sound	8/8/2020	20:49:00	-70.29342°N	-147.54381°W
2	Stef. Sound	8/8/2020	22:00:00	-70.29878°N	-147.18921°W
3	Stef. Sound	8/9/2020	23:02:00	-70.4678°N	-147.72145°W
4	Stef. Sound	8/10/2020	00:06:00	-70.45299°N	-70.45299°W
5	Stef. Sound	8/10/2020	18:32:00	70.42538°N	147.91218°W
6	Stef. Sound	8/10/2020	18:53:00	70.39888°N	147.91497°W
7	Stef. Sound	8/10/2020	19:17:00	-70.36784°N	-147.91153°W
8	Stef. Sound	8/10/2020	19:33:00	70.35960°N	147.84522°W
9	Stef. Sound	8/10/2020	20:15:00	70.30040°N	147.79613°W
10	Stef. Sound	8/10/2020	20:34:00	70.31719°N	147.79628°W
11	Stef. Sound	8/10/2020	21:02:00	70.34535°N	147.79537°W
12	Stef. Sound	8/10/2020	21:32:00	70.37833°N	147.79606°W
13	Stef. Sound	8/10/2020	22:05:00	70.41540°N	147.79848°W
14	Stef. Sound	8/10/2020	22:57:00	-70.42809°N	-147.65094°W
15	Stef. Sound	8/10/2020	23:48:00	70.37725°N	147.64452°W
16	Stef. Sound	8/11/2020	00:10:00	70.34922°N	147.64922°W
17	Stef. Sound	8/11/2020	00:30:00	70.32194°N	147.64535°W
18	Stef. Sound	8/11/2020	00:49:00	70.29556°N	147.64468°W
19	Stef. Sound	8/11/2020	01:09:00	70.26742°N	147.64488°W
20	Stef. Sound	8/11/2020	01:28:00	-70.24233°N	-147.64466°W
21	Stef. Sound	8/11/2020	17:06:00	-70.33089°N	-147.0972°W
22	Stef. Sound	8/11/2020	17:56:00	70.35520°N	147.23088°W

23	Stef. Sound	8/11/2020	18:39:00	70.30176°N	147.23152°W
24	Stef. Sound	8/11/2020	18:59:00	70.27719°N	147.23177°W
25	Stef. Sound	8/11/2020	19:51:00	-70.22908°N	-147.36411°W
26	Stef. Sound	8/11/2020	20:10:00	70.24768°N	147.36499°W
27	Stef. Sound	8/11/2020	20:32:00	-70.278°N	-147.3626°W
28	Stef. Sound	8/11/2020	20:54:00	70.30098°N	147.36332°W
29	Stef. Sound	8/11/2020	21:11:00	70.32289°N	147.36291°W
30	Stef. Sound	8/11/2020	22:00:00	-70.36743°N	-147.49557°W
31	Stef. Sound	8/11/2020	22:25:00	70.34034°N	147.49508°W
32	Stef. Sound	8/11/2020	22:45:00	70.31481°N	147.49543°W
33	Stef. Sound	8/11/2020	23:07:00	70.28723°N	147.49466°W
34	Stef. Sound	8/11/2020	23:29:00	70.26076°N	147.49454°W
35	Stef. Sound	8/11/2020	23:51:00	70.23355°N	147.49349°W
36	Stef. Sound	8/12/2020	00:05:00	-70.20663°N	-147.49418°W
37	Stef. Sound	8/12/2020	00:48:00	-70.21096°N	-147.57358°W

Figure 3. Location of AML "sensor-only" stations.

Oceanographic Moorings

Two year-round oceanographic moorings were retrieved on August 8th, 2020. One temporary, shallow "shoreface" mooring was deployed on July 16th and retrieved August 11th. The year-round LTER oceanographic mooring was not recovered due to an apparent failure of the acoustic release. A survey of the area was conducted using a Blue View imaging sonar in an unsuccessful attempt to locate the mooring.

Table 4. Oceanographic Mooring Name, Locations, deployment date and time.

Name	Latitude (DD)	Longitude (DD)	Date	Time (UTC)
UAF Dinkum	70.2931500°N	147.543019°W	8/19/2019	22:52
Shore face	70.2109170°N	147.573233°W	7/16/2020	19:30
UAA Newport	70.2992028°N	147.187625°W	8/19/2019	23:46
Cross Island	70.4690694°N	147.724589°W	7/25/2018	10:15

Table 5. Table 6. Mooring name and instrument type and serial number for each mooring.

UAF Mooring		
Equipment	Serial Number	Parameters Measured
ADCP	16203	Water Column Velocity, Surface Wave Spectra, Acoustic Backscatter
RBR Concerto	60716	Conductivity, Temperature, Pressure
Acoustic Release	74379	
UAA Newport Mooring		
Equipment	Serial Number	Parameters Measured
ADCP	2018	Water Column Velocity, Surface Wave Spectra, Acoustic Backscatter
RBR Concerto	60717	Conductivity, Temperature, Pressure
Acoustic Release	76056	
ADV	3145	Near Bottom Velocities
Campbell OBS	S8016	Optical Backscatter
Campbell OBS	S8018	
Shallow Water Temp Mooring (Shoreface)		
Equipment	Serial Number	Parameters Measured
ADV	14521	Near Bottom Velocities
Campbell OBS	T9381	Optical Backscatter
RBR TD Wave	204207	Pressure and Temperature
RBR Virtuoso	204121	Turbidity

LTER Cross Island Mooring		
Equipment	Serial Number	Parameters Measured
ADCP	AD2CP199	Water Column Velocity, Surface Wave Spectra, Acoustic Backscatter
SBE 16Plus	16-50170	Conductivity, Temperature, Pressure
CART (Acoustic Release)	30600	

The shallow water shoreface mooring (Figure 4) was deployed with a Nortek Acoustic Doppler Velocimeter (ADV), one OBS sensors, an RBR Duo TDWave sensor, and a RBR Virtuoso Tu sensor. The UAF mooring was deployed with an acoustic Doppler current profiler (ADCP), an RBR Concerto CTD, and an acoustic release. The UAA Newport mooring was deployed with an ADCP, RBR Concerto CTD, Nortek ADV with OBS sensors. These moorings are shown in Figures 5 through 7, below.

Figure 4. Locations of the three mooring deployments in Foggy Island Bay.

Figure 5. The shoreface mooring.

Figure 6. UAA Newport mooring.

Figure 7. UAF mooring.

Sofar Ocean "Spotter" Wave Buoys

Two Sofar Ocean® wave buoys were deployed at two separate locations (Figure 4) for the ~30 days in July through August. The buoys were deployed from the R/V Ukpik prior to the arrival of UAF researchers and retrieved at the end of the cruise. The buoys transmit their data once an hour via satellite and track significant wave height, peak and mean period, direction, and spread in near real-time. The data was made available in realtime via the AOOS Project Data Portal. One buoy was placed near the LTER Mooring site STL_JLK0 (SPOT – 0518, T. Weingartner's "Dinkum" mooring-site) and the other (SPOT -0519) six miles SE in Stefansson Sound Lagoon at LTER mooring site STLDS2 (K. Dunton's long-term Boulder Patch "DS2" Site).

Table 6. Wave buoy deployment locations, dates, and times.

Sofar Ocean® wave buoys						
Name	**Latitude (DD)**	**Longitude (DD)**	**Date In**	**Date Out**	**Time In (UTC)**	**Time Out (UTC)**

Spot – 0518	70.392707°N	147.833682°W	7/17/2020	8/12/2020	01:57	18:45
Spot – 0519	70.319104°N	147.761135°W	7/17/2020	8/13/2020	00:58	01:25

Figure 8. Wave buoy deployment locations.

Survey Equipment

The 600 kHz RD Instruments Sentinel Workhorse ADCP was deployed on 8/17-8/18 via a gunnel mounted pole (Figure 9). The cruise track within FIB is shown in Figure 10.

Figure 9. 600 kHz RD Instrument Sentinel Workhorse ADCP pole mounted off the R/V Ukpik

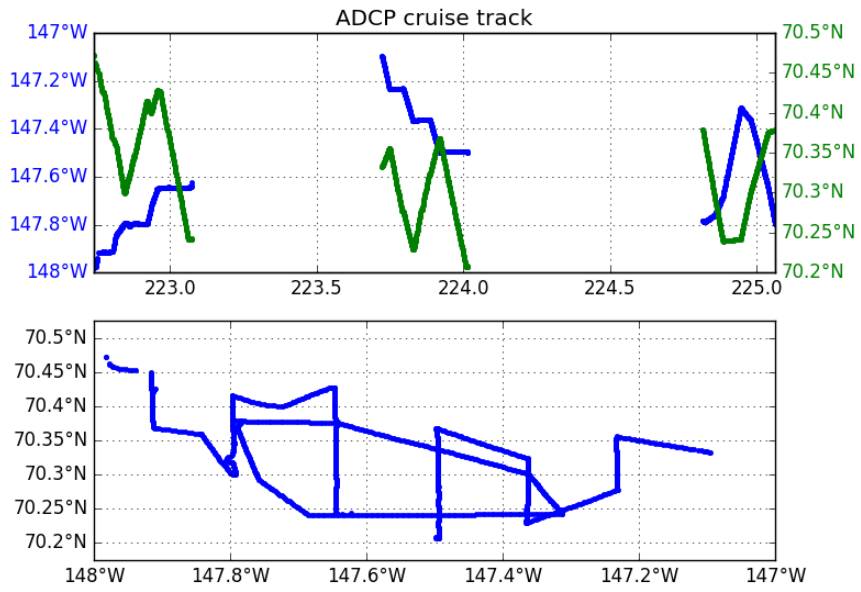

Figure 10. ADCP navigation plot.

Met Station

A Campbell meteorological station (met station) installed in 2018 was revisited for repairs in 2019 but was unable to be serviced in 2020. The met station is powered by a 12V battery that is charged via solar panels and a wind turbine. The met station monitors air temperature in °C, average wind speed in miles per hour, wind direction in degrees (true north), barometric pressure in milibars, and relative humidity in % Atm. Two cameras were installed facing each side of the coast and programmed to take a picture every hour. The met-station failed in December 2018 and again in Janurary 2020. Plans to visit the met station location are in place for 2021.

Location: 70.204075°N , 147.701386°W
Components:

1. Campbell Tripod CM110
2. RM Young Wind Sensor 05108-L9-CWS
3. Relative Humidity Sensor 083E-L6-PW
4. 2-CC5MPX Cameras

5. Temperature Sensor with Solar Radiation Shield
6. Micro Specialties satellite control and antenna
7. Sun Xtender PVX-1040T 104AH Battery
8. 2-80W Solar Panels
9. Primus Windpower Air 40 12V.

Figure 11. Met Station at the southern end of Foggy Island Bay.

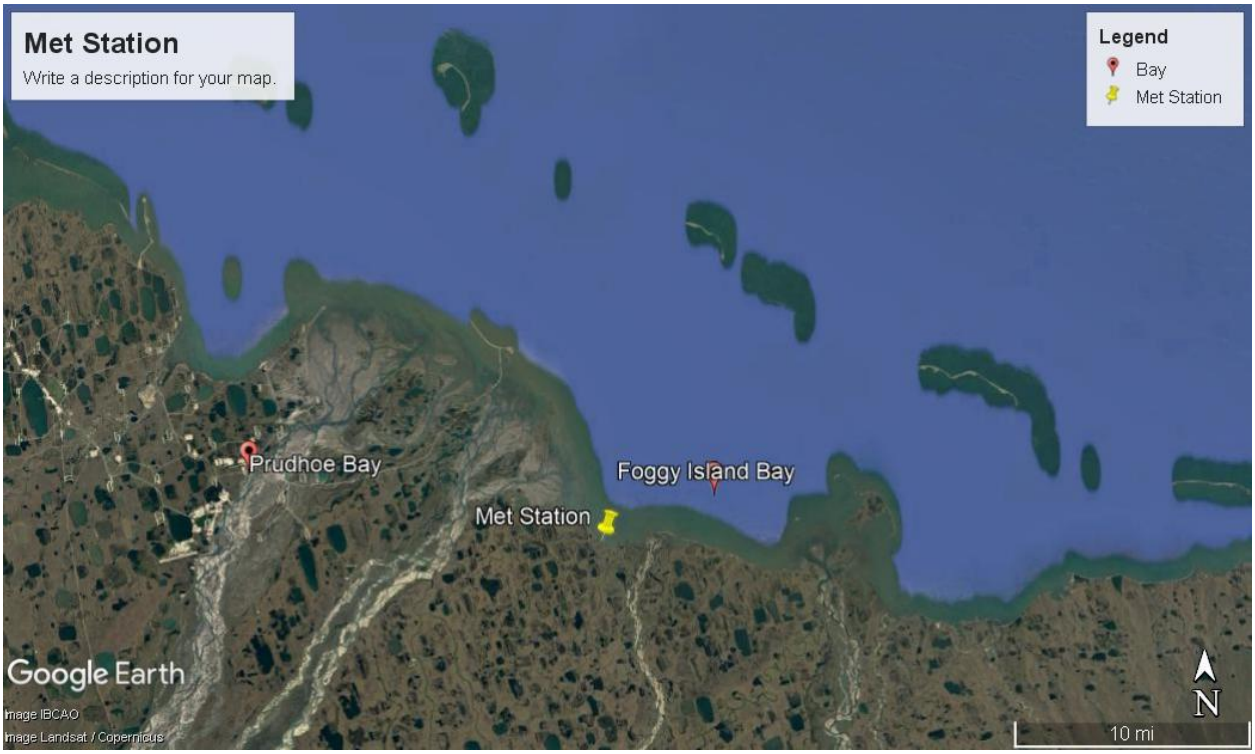

Figure 12. Location of the met station.

3D Mapping

A drone survey of the area immediately surrounding the met-station was successfully executed using a UAF-owned DJI Phantom 3 UAV in 2019. The digital elevation map produced using the Agisoft photogrammetric software package of the surveyed area is shown in Figure 19. Three survey lines were occupied using a survey-grade GPS system (a UAF-owned Trimble R10 base and rover). GPS survey lines are shown overlain on the UAV survey area in Figure 20. A repeat aerial survey is scheduled for 2021.

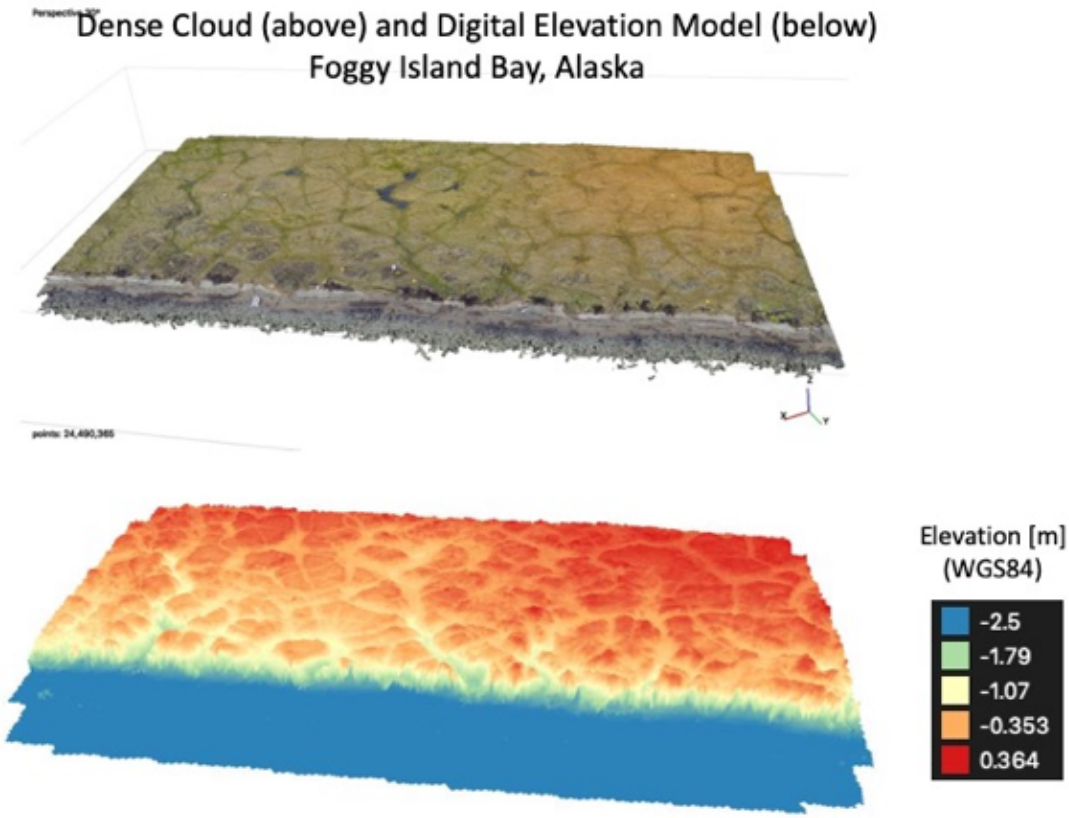

Figure 13. 2019 Digital elevation model of FIB produced from drone imagery.

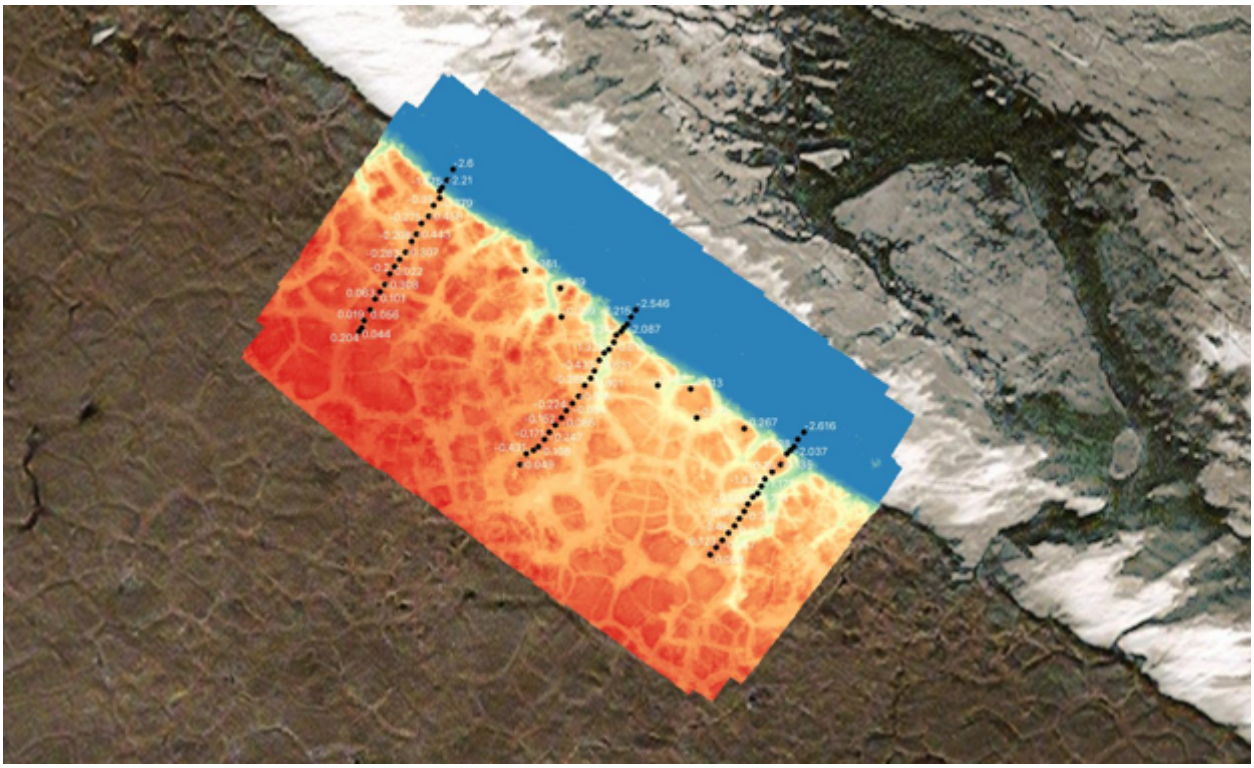

Figure 14. Location of GNSS transects draped over the digital elevation model produced from the UAV imagery.

Sample analysis protocol

24 water samples were collected and analyzed for Total Suspended Solid (TSS). Water samples were filtered through a 1.5 µm binder free, glass microfiber filter that was vacuum rinsed three times with 20mL aliquots of reagent free water and dried at 105°C for at least one hour. The samples will be processed using standard methods (2005), 2540D and EPA (1983) Method 160.2 (Residue, non-filterable) in the UAF WERC lab.

The 24 samples collected for analysis of stable oxygen isotopes (δ^{18}O) will be analyzed by Cornell Isotope Laboratory (COIL) in Ithaca, New York. The analysis is performed on a Thermo Delta V isoptope ratio mass Spectrometer (IRMS) interfaced to a Gas Bench II. Delta values are measured in units of per mil (‰). The overall deviation for the internal DI standard 0.18 ‰ δ^{18}O.

Analyses of nutrients (nitrate plus nitrite, nitrite, phosphate, silicate, and ammonia) in the 24 samples collected will be performed at UAF using a Seal Analytical continuous-flow QuAAtro39 AutoAnalyzer. Following each run, peaks are reviewed for any problems, any blank is subtracted and final concentrations (in micromoles per liter) are calculated based on a linear curve fit using Seal Analytical AACE 7.07 software by the UAF Nutrient Analytical Facility.

Three seafloor sediment samples were collected using the Ponar grab and sent to the Central Analytical Laboratory at Oregon State University for analysis. Procedures are documented in Appendix.

Preliminary Analyses of Samples

Table 7. Grain size analysis results.

Sample ID	%	% Clay	% Silt		% Sand				
Customer ID	Moisture	Clay (<2mm)	Silt (2 - 20mm)	Silt (20 - 50mm)	Sand (1000 - 2000 mm)	Sand (500 - 1000mm)	Sand (250 - 500mm)	Sand (100 - 250mm)	Sand (50 - 100mm)
Fib 10	30	0.0847	0.1255	0.0965	0.0007	0.0107	0.1944	0.3967	0.0906
SILD 1	69	0.1703	0.3774	0.2355	0.0002	0.0022	0.0117	0.0474	0.1553
EWL_JLK_0	81	0.3336	0.3764	0.1915	0.0002	0.0031	0.0093	0.0268	0.0591
FIB 6	83	0.2023	0.3695	0.0790	0.0182	0.0308	0.1786	0.1018	0.0199
Fib 8	24	0.0253	0.0081	0.0040	0.0002	0.0005	0.7083	0.2487	0.0049

Table 8. Total suspended solids results.

Sample ID	DEPTH (m)	Filter ID	TSS Final	Latitude	Longitude
FIB 14 Surface	Surface	Y1642	8	70.36783611	-147.9115306
FIB 13 Surface	Surface	Y1641	7.934782609	70.30040278	-147.7961278
FIB 13 Bottom	2.74	Y1639	7.582417582	70.30040278	-147.7961278
FIB 10 Surface	Surface	Y1626	8.095238095	70.242325	-147.6446556
FIB 10 Bottom	4.51	Y1627	7.252747253	70.242325	-147.6446556
FIB 6 Surface	Surface	Y1635	5.111111111	70.20663056	-147.4941806
FIB 6 Bottom	2.87	Y1636	5.058823529	70.20663056	-147.4941806
FIB 8 Surface	Surface	Y1629	5.111111111	70.22907778	-147.3641111
FIB 8 Bottom	3.05	Y1630	5.052631579	70.22907778	-147.3641111
FIB 3 Surface	Surface	Y1631	4.782608696	70.27800278	-147.3625972
FIB 3 Bottom	7.32	Y1632	12.6744186	70.27800278	-147.3625972
FIB 7 Surface	Surface	Y1628	5.108695652	70.33089444	-147.0972028
FIB 5 Surface	Surface	Y1633	3.406593407	70.36743056	-147.4955694
FIB 15 Surface	Surface	Y1647	3.571428571	70.45299167	-147.9179889
FIB 15 Bottom	7	Y1646	5.257731959	70.45299167	-147.9179889
FIB 15 Bottom #2	7	Y1645	3.666666667	70.45299167	-147.9179889
FIB 11 Surface	Surface	Y1640	4.888888889	70.42809444	-147.6509444
FIB 16 Surface	Surface	Y1644	2.959183673	70.46779722	-147.7216167
FIB 16 Bottom	14	Y1643	7.052631579	70.46779722	-147.7216167
EEL JLK Surface	Surface	Y1259	10.93023256	71.21924167	-155.8947028

EEL JLK Bottom	3.2	Y1260	17.61904762	71.21924167	-155.8947028
EWL JLK Surface	Surface	Y1262	5.591397849	71.34249722	-156.3335222
EWL JLK Bottom	2.74	Y1261	15.71428571	71.34249722	-156.3335222
SILD1 Surface	Surface	Y1263	13.26315789	70.53669444	-147.77565
SILD1 Bottom	2.74	Y2917	22.65306122	70.53669444	-147.77565
Shoreface	1.77	Y1637	6.30952381	70.21096389	-147.5736806
Barrow Surface	Surface	Y1258	4.128440367	71.32621111	-155.6468917
UAF Surface	Surface	Y1257	14.77272727	70.29313889	-147.5438083
UAF Bottom	7.01	Y1256	10.21052632	70.29313889	-147.5438083
UAA Surface	Surface	Y1255	4.489795918	70.29877778	-147.1892056
UAA Bottom	6.95	Y1254	19.12087912	70.29877778	-147.1892056

ADCP Preliminary Results

The ADCP data was post-processed using the University of Hawaii developed CODAS software package. Preliminary results are shown in Figures 15-20.

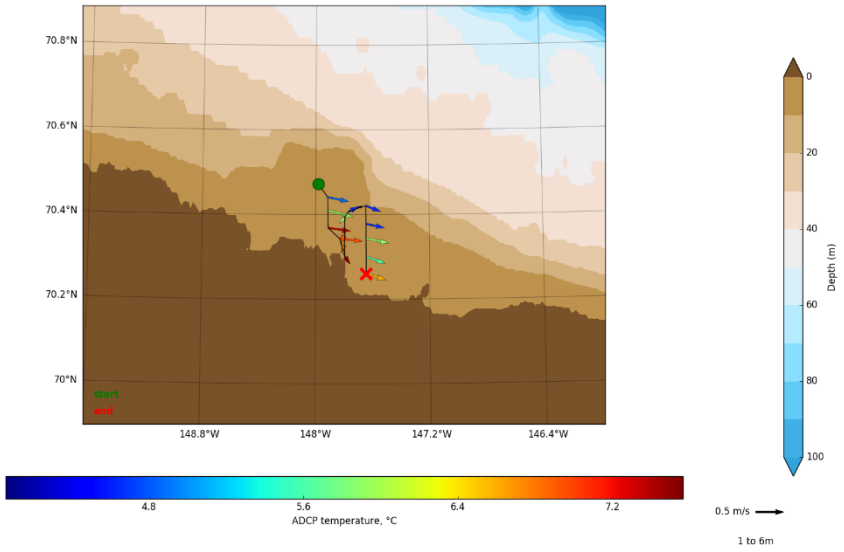

Figure 15. Plot of surface temperature measured by the ADCP.

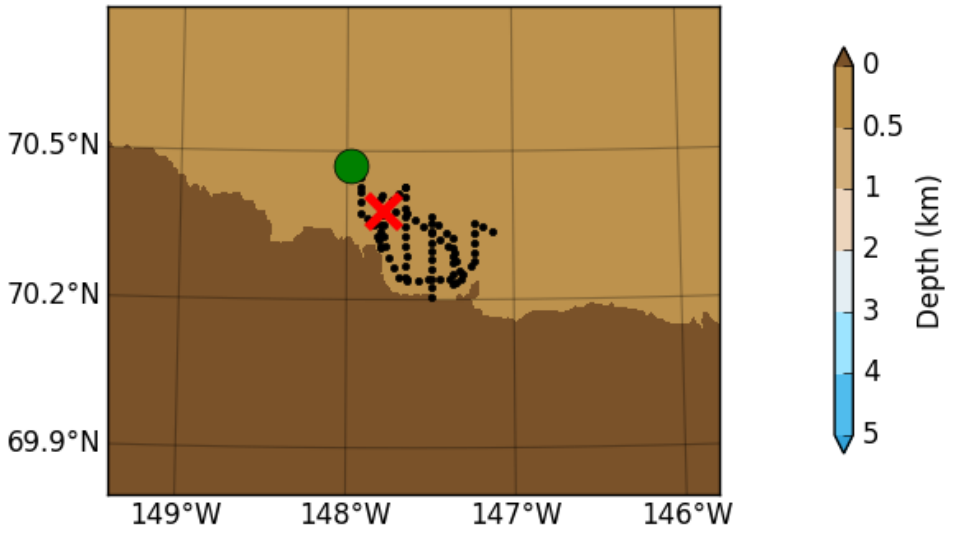

Figure 16. Plot of ADCP path.

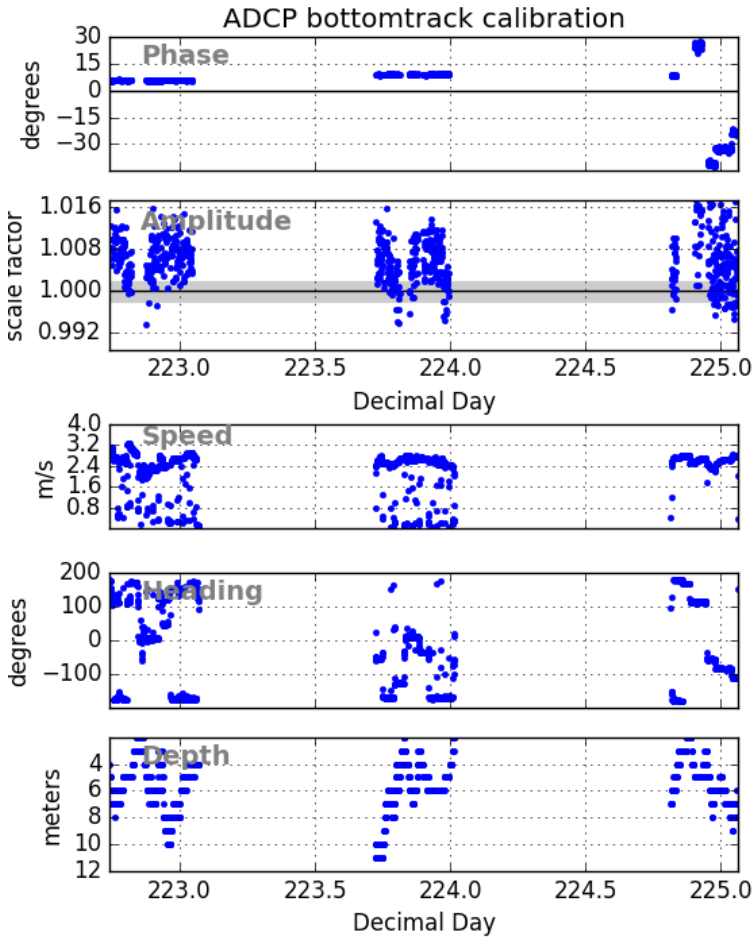

Figure 17. ADCP bottom track calibration.

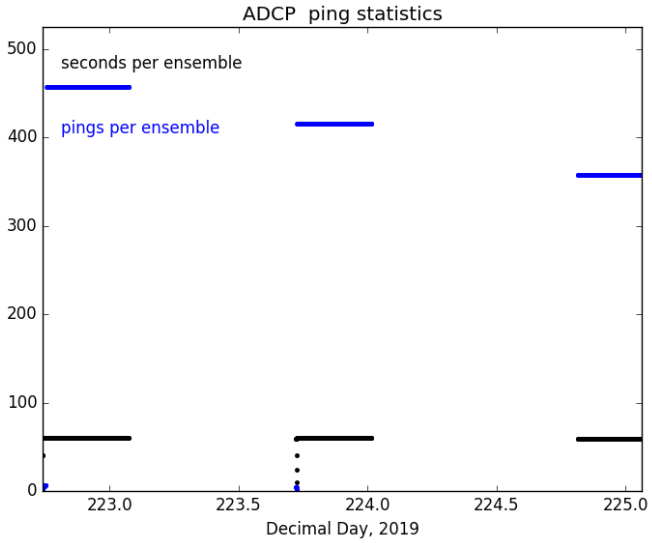

Figure 18. ADCP ping statistics.

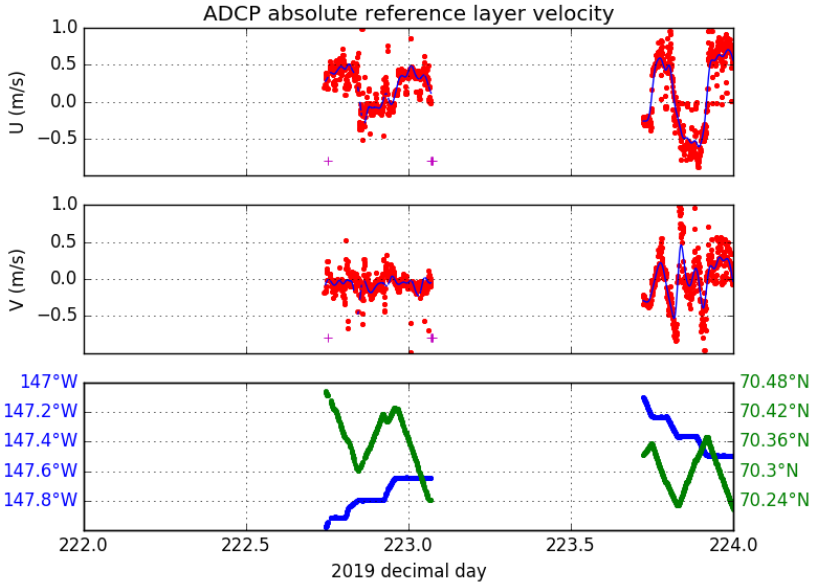

Figure 19. ADCP absolute reference layer showing velocity and coordinates.

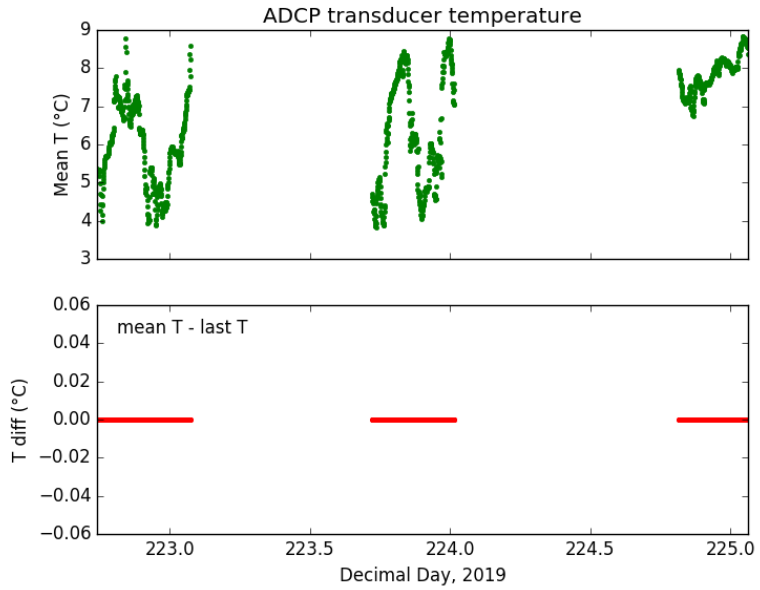

Figure 20. ADCP transduce mean temperature (top) and temperature difference by day.

Supplemental Photos

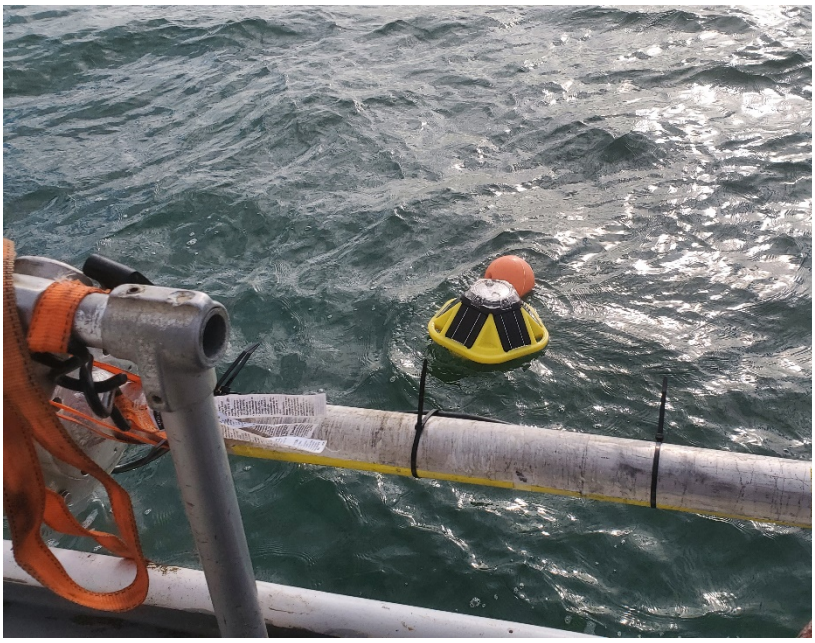

Figure 21. SPOT-0518 mooring upon recovery.

.

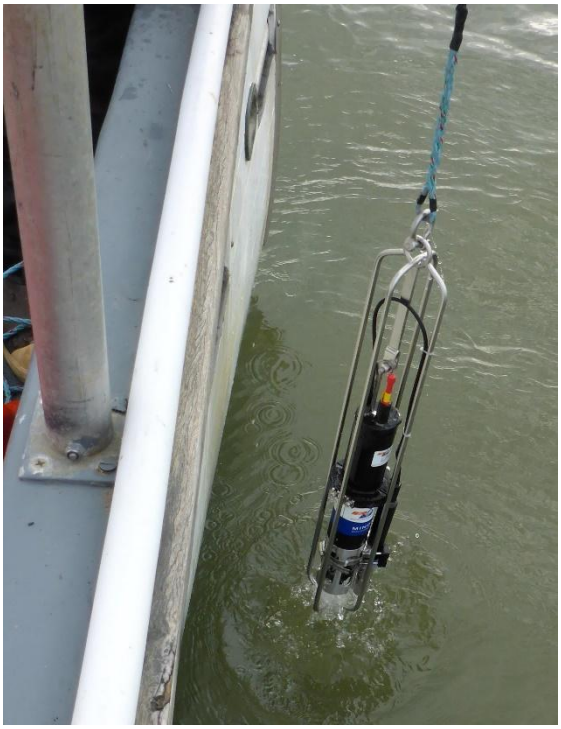

Figure 28. AML CTP probe being deployed from the R/V Ukpik.

Figure 22. Researcher Stephanie Jump deploying the 3.2L Van Dorn water sampler

Appendix A: Narrative Timeline of Foggy Island/Stef Sound Cruise

Table 8. Timeline of daily activity and personnel present.

7/31/2020	Arrive in Deadhorse Alaska	Stephanie Jump, Taylor Poirrier
8/1/2020	Pickup gear from Lynden and transport to Dalton Pad storage space in Deadhorse.	Stephanie Jump, Taylor Poirrier
8/2/2020	Prepped gear at Dalton Pad.	Stephanie Jump, Taylor Poirrier
8/3/2020	Load gear at Dalton Pad and transport it to Westdock. Load gear onto boat and start setting vessel for cruise. Transit to Oliktok and anchor for night.	Stephanie Jump, Taylor Poirrier
8/4/2020	Depart Oliktok and transit to SILD1 (LTER Site) and drag for mooring – no luck. Collect water and sediment samples along with CTD cast. Spent day traveling to Barrow AK, Anchored at Plover Point for night.	Stephanie Jump, Taylor Poirrier
8/5/2020	Dragged for and retrieved EWL_JLK_0 mooring and took water samples along with CTD cast. Downloaded data and replaced batteries on mooring. Put sea spider together and did field repair on deck box. Deployed EWL_JLK_0 mooring and retrieved EEL_JLK_0.	Stephanie Jump, Taylor Poirrier
8/6/2020	Deployed EEL_JLK_0 and transited to out Ekilukruak Entrance to "Eki" sea spider mooring deployment location. Deployed Eki mooring. Transited to Drew Point and attempted to establish communications with mooring, no response from acoustic release. Deployed Blue View and Side scan sonar to look for Drew Point mooring. Anchored at Cape Halkett	Stephanie Jump, Taylor Poirrier
8/7/2020	Depart Cape Halkett and attempt to drag for SILD1 again, no luck. Anchor up at West Dock for the night.	Stephanie Jump, Taylor Poirrier
8/8/2020	Retrieve UAA and UAF sea spider moorings and return to West Dock to disassemble moorings and download data. Anchor at West Dock for the night.	Stephanie Jump, Taylor Poirrier

8/9/2020	Load UAA and UAF moorings into truck. Transit to Cross Island and set up Blue View. Attempt to release acoustic release with Edgetech and Teledyne deckbox's. No response. Surveyed deployment location with Blue View sonar. Anchor at Cross Island for night.	Stephanie Jump, Taylor Poirrier
8/10/2020	Setup ADCP onto pole mount. Spend day doing ADCP transect lines and collecting water and sediment samples along with doing CTD cast. Anchored at Tigvariak Island.	Stephanie Jump, Taylor Poirrier
8/11/2020	Conducted remaining ADCP transect lines. Retrieved Shoreface mooring and both spotters (wave buoys). Dragged for STLD1 with no luck. Anchored by Endicott for night.	Stephanie Jump, Taylor Poirrier
8/12/2020	Attempted dragging for STLD1 again, no luck. Conducted additional ADCP transects and anchored at West Dock for the night.	Stephanie Jump, Taylor Poirrier
8/13/2020	Demobilize boat and transport gear back to Dalton pad in Deadhorse AK.	Stephanie Jump, Taylor Poirrier
8/14/2020	Pack gear and have Lynden pick up pallets of gear for shipping.	Stephanie Jump, Taylor Poirrier
8/15/2020	Depart Deadhorse and return to Fairbanks.	Stephanie Jump, Taylor Poirrier

Appendix B: *Sieve and Pipette Method for Analyzing Sediment Texture*

Scope and Application

This method is recommended for academic research that is investigating properties related specifically to texture. The method employed by CAL splits the sand sized fraction into five classes, and splits silt into two size classes. Generally, the reproducibility is considered to be ± 2%.

Summary

Prior to starting the particle size separation steps the sample is dried and particles greater than 2 mm are removed, the sample is precisely weighed, then organic matter and any other potential cementing-agents are removed. Sodium hexametaphosphate is added to the suspension and placed on a shaker overnight to overcome flocculation during settling. Sand size fractions are separated through a wet sieve, oven dried, and sieved through a series of sieves. The silt and clay suspension is brought to a volume of 1L and specific aliquots of the fluid are removed by pipette at a specific depth at specific time points to capture the silt and clay sized particles in accordance with Stokes' Law. The fluid is dried, weighed, and the weight used in calculations to determine the final texture.

Equipment and Materials

- 2 mm sieve
- 0.05 mm sieve
- Sieve stack (US or FAO size grouping)
- Accujet pipette dispenser
- 20 mL glass pipettes
- Analytical balance (0.0001g accuracy)
- 30 mL beakers
- 1000 mL graduated cylinders
- Pipette slide apparatus
- Stop watch
- Large funnel
- Squirt bottle
- 500 mL texture bottles
- 500 mL bottle lids
- Data sheet
- 105C oven
- Thermometer
- Flat bottomed stirring rod

Reagents

- 30% Hydrogen peroxide (H_2O_2)
- Sodium Hexametaphosphate $Na_6P_6O_{18}$ (solution of 10% $Na_6P_6O_{18}$)

Procedure

A: Sample Preparation

1. Weigh approximately 50g of air dried soil that has been sieved through a 2 mm sieve and place into a labeled 500 mL texture bottle

B: Sample dispersion and removal of cementing agents

2. Assess sample for need to remove carbonates (pH greater than 7.3) or iron cementing agents (visual inspection for iron oxides).
3. Add 100 mL of deionized water using a bottletop dispenser.
4. Add 8 mL of 30% H_2O_2 using repeater pipette.
5. Gently swirl the bottle to mix the soil, water, and H_2O_2 together. Use a squirt bottle of deionized water to rinse the sides of the texture bottle to make sure all soil particles are in contact with the water and H_2O_2 slurry.
6. Let stand ~4 hours while periodically swirling the texture bottle and rinsing the sides of the bottle with deionized water. Do not let the soil dry out.
7. After ~4 hours, add 50 mL of $Na_6P_6O_{18}$ solution using a bottletop dispenser.
8. Secure cap on bottle, and place on reciprocating shaker set to "Low".
9. After ~2 hours, take the bottles off the shaker and open each bottle to allow H_2O_2 fumes to release.
10. Put the lids back on the bottles and place the bottles back on the shaker. Set the shaker to "Low" and shake overnight.
11. Pull bottles off the shaker the following morning and proceed with 'Separation of fractions'.

C: Separation of fractions

12. Remove samples from reciprocating shaker.
13. Label a 100 to 150 mL glass beaker with sample ID, place beaker in 105C oven for 5 minutes, then dessicate for 5 minutes, and record weight of empty beaker with a 0.0001g balance.
    a. This beaker will be used to collected sand sized particles after silt and clay are rinsed through the sieve.
14. Set up sand sieving apparatus:
    a. Place ring stand in the sink with funnel holder.
    b. Place large funnel in funnel holder.
    c. Place a 50μm sieve above the funnel.
    d. Place a 1000 mL graduated cylinder below the funnel.
15. While the sample is still in the texture bottle, gently shake the bottle to ensure that none of the sample is stuck to the bottom of the bottle.
16. Pour dispersed sample over the sieve screen ensuring all smaller particles enter cylinder.
17. Use a rinse bottle with deionized water to rinse all particles out of the texture bottle and onto the sieve screen.
18. **Pay special attention to the volume of liquid in the graduated cylinder as you are transferring the sample from the texture bottle to the sieve screen. Do not fill the cylinder over the 1000 mL mark.**

19. Use a rinse bottle with deionized water to rinse all remaining particles on top of the sieve screen until there is only sand-sized particles left on top of the sieve screen.
20. Remove the sieve from the sand sieving apparatus and use a rinse bottle with deionized water to carefully transfer the remaining sand into pre-labeled and pre-weighed beaker. Place beaker onto a heat-safe tray and place the tray into 105C oven.
21. Dry beaker with sand fraction overnight in a 105C oven. After 24 hours, place the beakers in a dessicator for 20 minutes, then weigh beakers to 0.0001g.
22. Keep the sample in the beaker and prepare to separate the sand into different particle size classes using a sieve stack.
23. Stack the sieve sizes of choice with the largest on top, with decreasing sieve openings
    a. We will use 1000, 500, 250, 106, 53um sieve openings for our stack
24. After ensuring that you have recorded the weight of the dried beaker, transfer the dried sample onto the top sieve (1000 um). You will need to scrape the sides and bottom of the beaker to ensure that all of the sample has been transferred from the beaker into the sieve stack.
25. Using your hands or a Vortex shaker, shake the sieve stack for 30 – 60 seconds. Apply pressure to the top and bottom of the sieve stack to ensure that no sample is being lost between sieves.
26. After shaking, place each individual sieve onto a 0.0001g balance and record the weight. Repeat this process for all sieves of the sieve stack.
27. If any material makes it through **ALL** of the sand sieves, it should be transferred to the graduated cylinder for the pipette determination.
28. After ensuring that you have recorded a weight for each sieve in the sieve stack, use the sieve brush to thoroughly clean each sieve before reassembling the sieve stack. Proceed with the remaining samples.

D: Pipette fine fractions from depth

29. Gather enough 30 mL beakers needed for taking 3 aliquots of each texture sample
30. Label each 30 mL beaker with sample ID and pipette time point (i.e. 0 min, 5 min, 5.5 hr). Be sure to label a trio of beakers for Blank determination. (i.e. Blank 0 min, Blank 5 min, Blank 5.5 hr).
31. Place all 30 mL beakers in 105C oven for at least 10 minutes. After a minimum of 10 minutes, place beakers in dessicator, and then record the weight for each empty beaker to 0.0001g.
32. In the Texture room, line up all cylinders directly behind the yellow line on the bench. Using DI water, fill graduated cylinders to exactly 1000 mL.
33. Place the 0 min and 5 min oven dried, weighed, and labeled 30 mL beakers in front of each cylinder. Set the 5.5 hr 30 mL beakers aside.
34. Install a 20 mL glass pipette in the pipette slide apparatus.
35. Check the temperature of the room to determine appropriate sampling depth.
36. Set the pipette apparatus depth according to Table 1 at the end of this protocol. It is helpful to use a piece of lab tape to mark the 0 min and 5 min pipette depths on the pipette slide apparatus.

37. Rigorously stir/pump the silt and clay fraction with the flat bottomed stirring rod until thoroughly mixed. Do not break the surface of the water, focus on getting sediment up from the bottom of the cylinder and making sure the suspension is well distributed.
38. Immediately after mixing the suspension, lower the pipette to the desired sampling depth inside the graduated cylinder using the slide apparatus.
39. Remove 20 mL using the top button on the Accujet automatic pipetter. Pull the slide apparatus up and deposit the suspension into the 30 mL beaker labeled "0 min" using the down button on the Accujet. Ensure all of the suspension is dispensed by hitting the down button again after all of the suspension has been dispensed.
40. Proceed to stirring the next cylinder.
41. Carefully follow the timing schedule in Table 2 **at the end of this protocol.**
42. Precisely five minutes after you stop stirring each cylinder, pipette a second sample from the cylinder and deposit into the 30 mL beaker labeled "5 min".
43. Place the 0 min and 5 min 30 mL beakers with suspension onto a heat safe tray and place tray into a 105C oven.
44. Precisely 5.5 hours after the first sample is removed from the cylinder, pipette a third sample from the cylinder and deposit into the 30 mL beaker labeled "5.5 hr".
45. Place the beakers with suspension onto a heat safe tray and place in 105C oven.
46. The next day, remove all 30 mL beakers from the 105C oven and place in a dessicator for at least 30 minutes.
47. Weigh all 30 mL beakers and record the sample mass onto the datasheet.
48. Enter all data into the spreadsheet.

E: Blank Determination

1. Make a blank solution using 50 mL of 10% NaHMP and dilute to 1000 mL with DI water.
2. Follow pipetting steps 37 - 44 for this blank sample at each measurement point.
3. Determine the weight of salts added to the soil suspension for calculation purposes by drying and weighing each 30 mL beaker of the pipetted blank sample.

Calculations

1. A spreadsheet has been developed and provided to help make calculations
2. Enter all weights into the spreadsheet
3. Determine relative portion of fractions as follows; very coarse sand <2-1 mm, coarse sand <1-0.5 mm, medium sand <0.5-0.25 mm, fine sand <0.25-0.1 mm, and very fine sand <0.1-0.05 mm, coarse silt <0.05-0.02 mm, fine silt <0.02-0.002 mm, and clay <0.002 mm.

Table 1. Appropriate depth at which to take the sample with pipette by temperature

Temperature	Depth (cm)	Depth (cm)
°C	5 min.	5½ hrs.
19	10.5	6.9
20	10.8	7.1
21	11.0	7.2
22	11.3	7.4
23	11.6	7.6
24	11.9	7.8
25	12.1	8.0
26	12.4	8.2
27	12.7	8.4
28	13	8.6
29	13.3	8.8
30	13.6	9
31	13.9	9.1
32	14.2	9.3
33	14.4	9.5
34	14.8	9.7
35	15.1	9.9
36	15.4	10.1

Table 2. Timing schedule for pipette procedure

Minutes	Sample #	Action
0	1	Start Stir
0.5	1	Stop stir, start timer, & pull sample 1.1 (0 min)
2.5	2	Start stir
3	2	Stop stir and pull sample 2.1 (0 min)
5	1	Pull sample 1.2 (5 min)
5.5	3	Star Stir
6	3	Stop stir & pull sample 3.1 (0 min)
8	2	Pull sample 2.2 (5 min)
8.5	4	Start stir
9	4	Stop stir and pull sample 4.1 (0 min)
11	3	Pull sample 3.2 (5 min)
16	4	Pull sample 4.2 (5 min)
333 (5.5 hr)	1	Pull sample 1.3 (5.5 hr)
336	2	Pull sample 2.3 (5.5 hr)
339	3	Pull sample 3.3 (5.5 hr)
342	4	Pull sample 4.3 (5.5 hr)

Appendix B: Hydrodynamic, Wave and Sediment Transport Modeling Supplementary Information

In Section 3.3.2.2 the use of different CMIP6 GCM wind projections for computing projected wave conditions is discussed. Analysis of waves computed with the Tier 1 WaveWatchIII model indicated a discrepancy in the wave time series computed with the CMCC winds and sea ice fields near Stefansson Sound, compared to six other downscaled wave time series. To evaluate if any large discrepancies of the CMCC product exist, we compared historical winds to the ERA reanalysis (Figures B1 through B2) and found that the winds were biased high. The bias appears to persist for the future time-period as well (Figure B3).

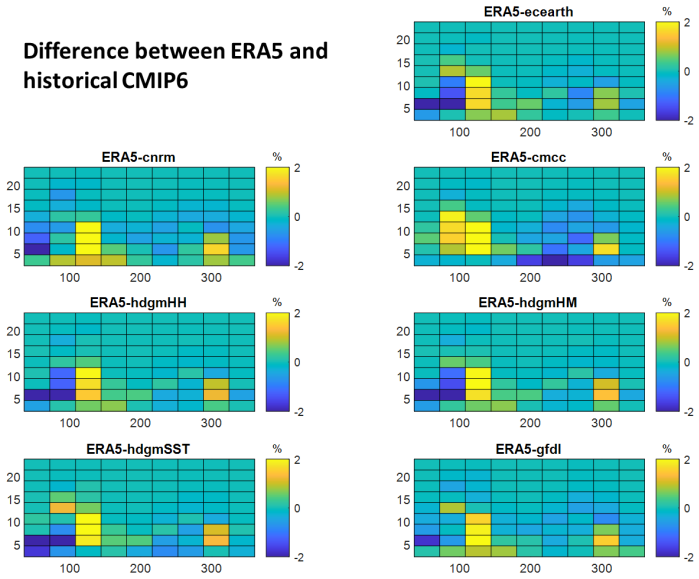

Figure B.1 Difference between ERA5 and historical winds (1979-2014).
Colors denote the difference in probability of occurrence of each binned wind speed and direction between ERA5 reanalysis 6 GCMs.

ERA5 and CMIP6 historical

Wind speed for each month (May to December)

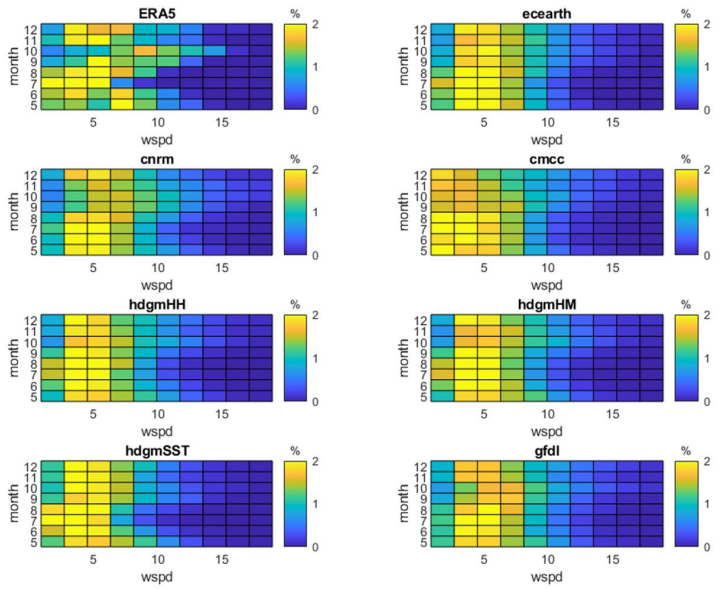

Figure B.2 Monthly probability of occurrence of binned wind speeds for the ERA5 reanalysis and historical CMIP6 winds (1979-2014).

Colors denote the probability of occurrence of each binned wind speed (horizontal axis ('wspd') in meters/second) by month (vertical axis, May through December).

CMIP6 projections

Wind speed for each month (May to December)

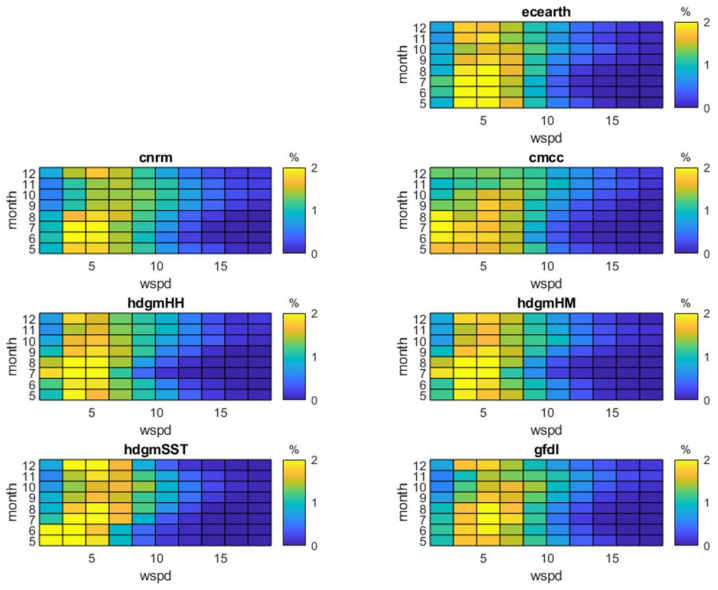

Figure B.3 Monthly probability of occurrence of binned wind speeds for the projected CMIP6 winds (2020-2050).

Colors denote the probability of occurrence of each binned wind speed by month.

Model Settings

Model settings for the Tier 2 models are shown in this section and are additionally provided as separate files within the data release that accompanies this report.

```
[MorphologyFileInformation]
  FileCreatedBy    = Delft3D FLOW-GUI, Version: 3.59.01.57433
  FileCreationDate = Tue Apr 19 2022, 20:05:22
  FileVersion      = 02.00
[Morphology]
  EpsPar       = false            [-]    Vertical mixing distribution according to van Rijn (overrules k-epsilon model)
  IopKCW       = 1                [-]    Flag for determining Rc and Rw
  RDC          = 1.0000000e-02    [m]    Current-related roughness height (only used if IopKCW <> 1)
  RDW          = 2.0000000e-02    [m]    Wave-related roughness height (only used if IopKCW <> 1)
  MorFac       =  1.0000000e+000  [-]    Morphological scale factor
  MorStt       =  1.4400000e+003  [min]  Spin-up interval from TStart till start of morphological changes
  Thresh       =  5.0000001e-002  [m]    Threshold sediment thickness for transport and erosion reduction
  MorUpd       = false                   Update bathymetry during FLOW simulation
  EqmBc        = true                    Equilibrium sand concentration profile at inflow boundaries
  DensIn       = false                   Include effect of sediment concentration on fluid density
  AlfaBs       =  1.0000000e+000  [-]    Streamwise bed gradient factor for bed load transport
  AlfaBn       =  1.5000000e+000  [-]    Transverse bed gradient factor for bed load transport
  Sus          =  1.0000000e+000  [-]    Multiplication factor for suspended sediment reference concentration
  Bed          =  1.0000000e+000  [-]    Multiplication factor for bed-load transport vector magnitude
  SusW         =  2.0000000e-001  [-]    Wave-related suspended sed. transport factor
  BedW         =  2.0000000e-001  [-]    Wave-related bed-load sed. transport factor
  SedThr       =  1.0000000e-001  [m]    Minimum water depth for sediment computations
  ThetSD       =  0.0000000e+000  [-]    Factor for erosion of adjacent dry cells
  HMaxTh       =  1.5000000e+000  [m]    Max depth for variable THETSD. Set < SEDTHR to use global value only
  FWFac        =  1.0000000e+000  [-]    Vertical mixing distribution according to van Rijn (overrules k-epsilon
model)
  AksFac       =  1.0000000e+000  [-]    van Rijn's reference height = AKSFAC * KS
  RWave        =  2.0000000e+000  [-]    Wave related roughness = RWAVE * estimated ripple height. Van Rijn
                                          Recommends range 1-3
[underlayer]
  IUnderLyr   = 1
[output]
  AverageAtEachOutputTime= true
  HidExp      = true
  Dm          = true
  Percentiles  = 10 50 90
```

Figure B.4 Tier 2C model settings for the morphology (*.mor).

```
[MorphologyFileInformation]
  FileCreatedBy    = Delft3D FLOW-GUI, Version: 3.59.01.57433
  FileCreationDate = Tue Apr 19 2022, 20:05:22
  FileVersion      = 02.00
[Morphology]
  EpsPar         = false              [-]     Vertical mixing distribution according to van Rijn (overrules k-epsilon
model)
  IopKCW         = 1                  [-]     Flag for determining Rc and Rw
  RDC            = 1.0000000e-02      [m]     Current-related roughness height (only used if IopKCW <> 1)
  RDW            = 2.0000000e-02      [m]     Wave-related roughness height (only used if IopKCW <> 1)
  MorFac         =  1.0000000e+000    [-]     Morphological scale factor
  MorStt         =  1.4400000e+003    [min]   Spin-up interval from TStart till start of morphological changes
  Thresh         =  5.0000001e-002    [m]     Threshold sediment thickness for transport and erosion reduction
  MorUpd         = false                      Update bathymetry during FLOW simulation
  EqmBc          = true                       Equilibrium sand concentration profile at inflow boundaries
  DensIn         = false                      Include effect of sediment concentration on fluid density
  AlfaBs         =  1.0000000e+000    [-]     Streamwise bed gradient factor for bed load transport
  AlfaBn         =  1.5000000e+000    [-]     Transverse bed gradient factor for bed load transport
  Sus            =  1.0000000e+000    [-]     Multiplication factor for suspended sediment reference concentration
  Bed            =  1.0000000e+000    [-]     Multiplication factor for bed-load transport vector magnitude
  SusW           =  2.0000000e-001    [-]     Wave-related suspended sed. transport factor
  BedW           =  2.0000000e-001    [-]     Wave-related bed-load sed. transport factor
  SedThr         =  1.0000000e-001    [m]     Minimum water depth for sediment computations
  ThetSD         =  0.0000000e+000    [-]     Factor for erosion of adjacent dry cells
  HMaxTh         =  1.5000000e+000    [m]     Max depth for variable THETSD. Set < SEDTHR to use global
value only
  FWFac          =  1.0000000e+000    [-]     Vertical mixing distribution according to van Rijn (overrules k-
epsilon model)
  AksFac         =  1.0000000e+000    [-]     van Rijn's reference height = AKSFAC * KS
  RWave          =  2.0000000e+000    [-]     Wave related roughness = RWAVE * estimated ripple height. Van
Rijn Recommends range 1-3
[underlayer]
  IUnderLyr      = 1
[output]
  AverageAtEachOutputTime= true
  HidExp         = true
  Dm             = true
  Percentiles    = 10 50 90
```

Figure B.5 Tier 2C model settings for the sediment descriptor file (*.sed).

```
[Constants]
   WaterLevelCorrection =  0.0000000e+000
   Gravity              =  9.8299999e+000
   WaterDensity         =  1.0260000e+003
   NorthDir             =  9.0000000e+001
   MinimumDepth         =  5.0000001e-002
[Processes]
   GenModePhys          = 3
   Breaking             = true
   BreakAlpha           =  1.0000000e+000
   BreakGamma           =  7.3000002e-001
   Triads               = true
   TriadsAlpha          =  1.0000000e-001
   TriadsBeta           =  2.2000000e+000
   BedFriction          = collins
   BedFricCoef          =  2.0000000e-002
   Diffraction          = false
   DiffracCoef          =  2.0000000e-001
   DiffracSteps         = 5
   DiffracProp          = true
   WindGrowth           = true
   WhiteCapping         = Westhuysen
   Quadruplets          = true
   Refraction           = true
   FreqShift            = true
   WaveForces           = dissipation
[Numerics]
   DirSpaceCDD          =  5.0000000e-001
   FreqSpaceCSS         =  5.0000000e-001
   RChHsTm01            =  2.0000000e-002
   RChMeanHs            =  2.0000000e-002
   RChMeanTm01          =  2.0000000e-002
   PercWet              =  9.8000000e+001
   MaxIter              = 30
[Output]
   TestOutputLevel      = 0
   TraceCalls           = false
   UseHotFile           = true
   MapWriteInterval     =  6.0000000e+001
   WriteCOM             = true
   COMWriteInterval     =  6.0000000e+001
   Int2KeepHotfile      = 0.0000000e+00
   AppendCOM            = false
   IceOut               = true
   MapWriteNetCDF       = false
```

Figure B.6 Summary of main model parameter settings in the Tier 2 (A-C) WAVE module

Ag = 9.8300000e+000
Rhow = 1.0260000e+003
Tempw = 1.5000000e+001
Salw = 3.1000000e+001
Rouwav = #FR84#
Wstres = 7.5000000e-004 0.0000000e+000 2.5000000e-003 1.0000000e+002 2.5000000e-003
1.0000000e+002
Rhoa = 1.0000000e+000
Betac = 5.0000000e-001
Equili = #N#
Tkemod = #K-epsilon #
Ktemp = 0
Fclou = 0.0000000e+000
Sarea = 0.0000000e+000
Temint = #Y#
Commnt =
Roumet = #M#
Filrgh = #fib_detail.rgh#
Xlo = 0.0000000e+000
Vicouv = 2.0000000e+000
Dicouv = 1.0000000e+001
Htur2d = #N#
Vicoww = 0.0000000e+000
Dicoww = 0.0000000e+000
Irov = 0
Filsed = #fib.sed#
Filmor = #fib.mor#
Commnt =
Iter = 2
Dryflp = #YES#
Dpsopt = #MEAN#
Dpuopt = #MOR#
Dryflc = 1.0000000e-001
Dco = -9.9900000e+002
Tlfsmo = 6.0000000e+001
ThetQH = 0.0000000e+000
Forfuv = #Y#
Forfww = #N#
Sigcor = #N#
Trasol = #Cyclic-method#
Momsol = #Cyclic#

Figure B.7 Summary of main model parameter settings in the Tier 2C FLOW module

Appendix C: Coastal Change Modeling Supplementary Information

This appendix provides additional details on the two coastal change models described in Section 4.

Figure C.1 shows time series data used as inputs to the CoSMoS-COAST model (Section 4.1) that was used to hindcast and project long-term shoreline change within Foggy Island Bay. The wave time series are from model Tier 2B described in Section 3.

Figure C.2 shows hindcasted and forecasted erosion when the surface temperature formulation is used instead of the is White formulation in the CoSMoS-COAST model.

The remaining text and figures within this appendix describe formulations and inputs to the process-based event-driven erosion model in Section 4.2.

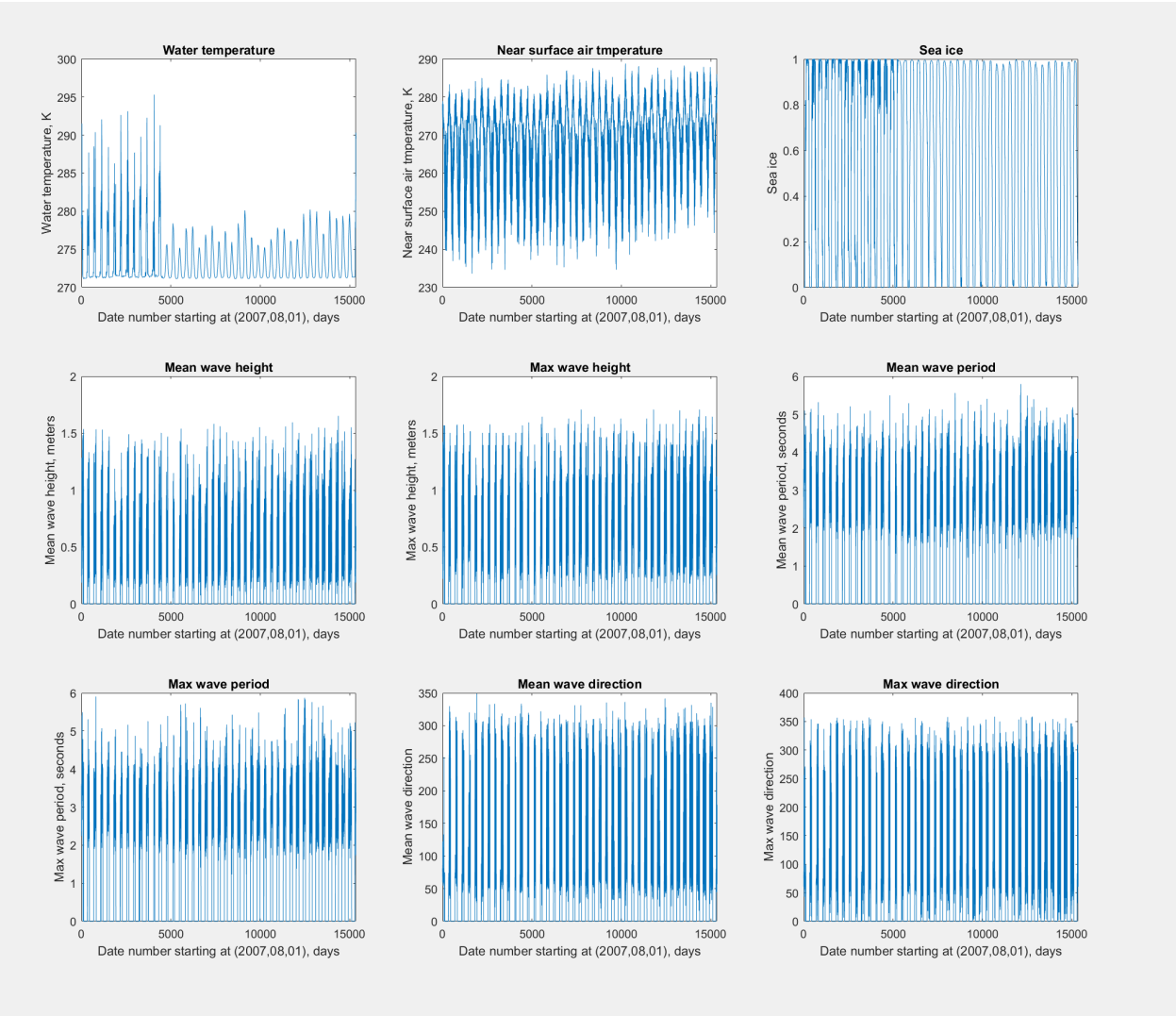

Figure C.1 Input data for the CoSMoS-COAST model from 2007 to 2049.

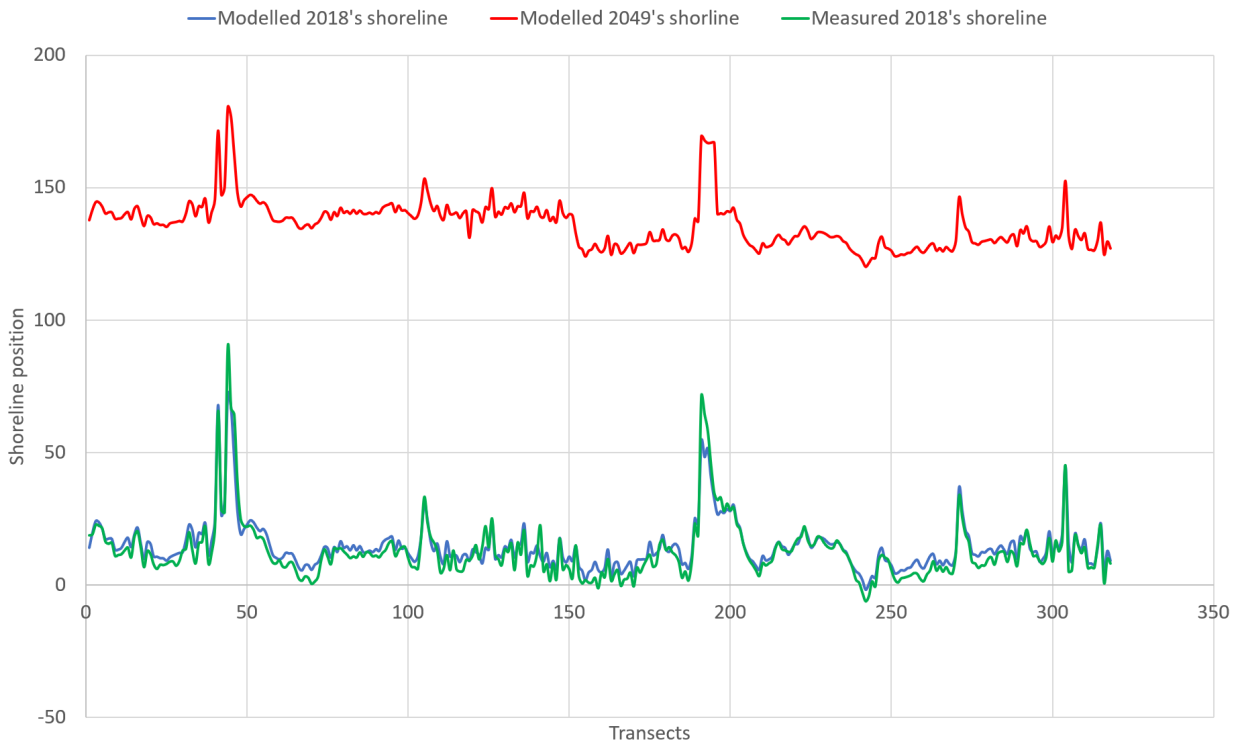

Figure C.2 Observed and modeled 2018 shoreline position and forecasted 2049 shoreline position (relative to the 2007 shoreline) assuming a thermal erosion formulation using land surface temperature as a proxy.

How to calculate solar flux on an angled slope

Solar flux is a measurement of how much solar energy is falling on a given area (kW/m^2). This calculation is simple on a clear day with the sun directly over a flat surface but becomes more complex as the angle between the rays and the surface change - due to time of day or year, weather, or surface of the slope. This write-up describes the development of a basic calculator to determine an estimate of solar radiation on a slope, optimized for a latitude 70.2˚ in Prudhoe Bay. It is based on prior similar work, included in the references section.

The calculator uses the latitude, slope, and aspect from the North of an observation point to determine the solar flux at that point for each hour of the year. It uses historical data from latitude 70.2˚ to estimate the effect of weather (the transmission coefficient), and also reports the results if a general transmission coefficient is used.

Operating equations

The equation for solar flux on a surface is

I_0 = solar constant

p = atmospheric transmission coefficient (varies depending on altitude, weather) A = altitude angle between the sun's rays and a horizontal surface on the earth θ = angle between the surface and the radiation

Essentially it is an equation which reduces the radiation received at the top of the atmosphere by the losses during transmission through the atmosphere and spread of the rays due to the angle it hits the earth. We will take a closer look at the individual parts of this equation, and then its derivation. This explanation has been modified from the derivation in Reference [1].

The solar constant (I0)

The first step of calculating solar flux is determining what flux is received at the top of the atmosphere, before being modified by transmission through atmosphere and clouds and time of day. This is done by using the Stefan-Boltzmann equation for black body radiation, assuming the sun is a black body with a temperature of about 5800 K.

$S_S = (5.67 \times 10^{-8}\ W \bullet m^{-2} \bullet K^{-4})(5778\ K)^4 \approx 6.3 \times 10^7\ W \bullet m^{-2}$

S_S = solar flux at the surface of the sun 5.67×10^{-8} = Stefan-Boltzmann constant

The energy spreads out as it radiates away from the sun, but the total quantity is unchanged. The solar flux at the planet (S_P) can therefore be given by:

$S_P = S_S(r_S/d_p)^2 = 6.3 \times 10^7\ W \bullet m^{-2}\ (700{,}000\ km/150{,}000{,}000\ km)^2 \approx 1370\ W \bullet m^{-2}$

r_S = radius of the sun d_p = Average distance from the earth to the sun

This is the solar flux at the top of earth's atmosphere closest to the sun and is known as the solar constant. In these calculations it has been rounded slightly: the widely accepted value is 1366 W/m^2, which is used in the rest of this work. A more detailed explanation of this derivation is available in Reference [2].

Transmission coefficient (p)

The atmospheric transmission coefficient is the fraction of the solar radiation that actually reaches the point of observation, instead of being reflected in the atmosphere. This coefficient is impacted by altitude - radiation must pass through more atmosphere to reach lower points - pollution, and weather. In the work done in reference 3, for example, the transmission coefficient used was 0.9, representative of "conditions on the top of a mountain [...] on a clear day."

Weather and pollution can lead to significant variation in the transmission coefficient, and thus the calculated flux. The USDA has collected solar flux data at a point close to the location of interest (on a horizontal surface). With this information it is possible to back-calculate the transmission coefficient and use it to calculate what the flux would be on an angled surface at that point. This is why the developed calculator is optimized for a particular location; it used this training data to inform the coefficient. The calculator also allows input of a different coefficient, like 0.9.

Altitude angle (A)

The altitude angle is the angle off of the horizontal that the sun's rays strike a horizontal surface. It is defined as follows:

$\sin(A) = \sin(\phi)\sin(\delta) + \cos(\phi)\cos(\delta)\cos(h)$ ϕ = latitude

δ = declination (i.e., time of year)

h = hour angle (e.g., time of day)

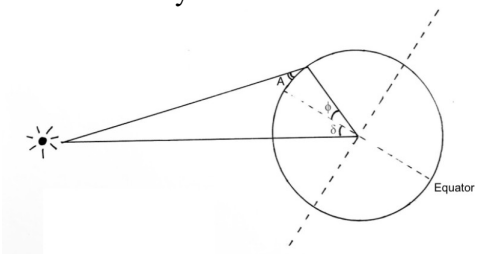

Latitude is given by the observation point's angle with the equation, and declination varies from about 23.45˚ north to 23.45˚ south (creating seasons). These are shown in the figure at the right. The hour angle describes the 24-hour spin of the earth, with 0˚ indicating noon and 180˚ indicating midnight - local solar time.

This formula is derived either with spherical trigonometry or vector analysis. With vector analysis, we define the latitude and longitude of the point of observation and of the subsolar point (the point where the sun is perceived to be exactly overhead, with an altitude angle of 90˚) to be (ϕ_O,λ_O) and (ϕ_S,λ_S), respectively, with vectors that point up from them called V and S. These vectors are:

$V = \cos\phi_O\cos\lambda_O\mathbf{i} + \cos\phi_O\sin\lambda_O\mathbf{j} + \sin\phi_O\mathbf{k}$ $S = \cos\phi_S\cos\lambda_S\mathbf{i} + \cos\phi_S\sin\lambda_S\mathbf{j} + \sin\phi_S\mathbf{k}$

I,j,k = basis vectors from the Earth-Centered Earth-Fixed (ECEF) cartesian coordinate system. The sine of the altitude angle is the dot product of V and S:

$\sin(A) = \sin\phi_O \sin\phi_S + \cos\phi_O \cos\phi_S \cos(\lambda_S - \lambda_O)$

Because ϕ_S is equivalent to δ and $(\lambda_S - \lambda_O)$ is equivalent to h, this is the same formula as first described.

Angle between the surface and radiation (θ)

As will be described later, the intensity of rays received at the surface depend on the tilt of the surface (see the figure below, taken from reference 1, on irradiation on sloping surfaces). The angle of the slope impacts how many rays will hit it. In the figure, with rays striking perpendicular to the horizontal surface, fewer rays will hit a surface if it is sloped.

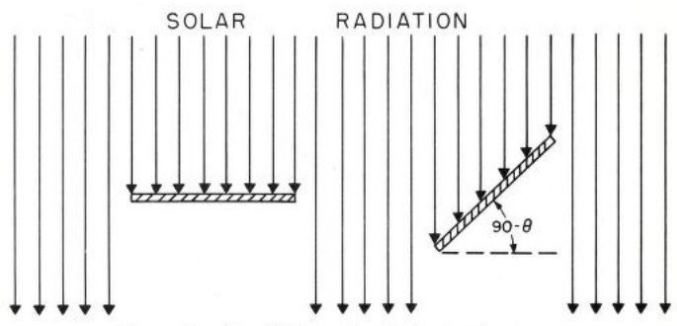

We need to calculate the angle between the sun's rays and the surface. The equation for this is $\sin\theta = \sin A \cos \alpha - \cos A \sin \alpha \sin (Z - \beta)$

α = angle between the surface and the horizontal Z = azimuth of the sun clockwise from the east

β = slope aspect clockwise from north (0 is north facing: a vector orthogonal to the slope face would point north)

Azimuth

The mathematical expression for the solar azimuth is measured clockwise from the south in the northern hemisphere, and clockwise from the north in the southern hemisphere. In order to get the expression for the azimuth measured clockwise from the east, we must add 90 degrees to the equation. The resulting equation is below:

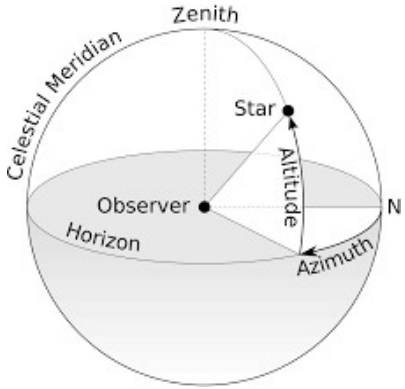

$AZ = \cos(\delta)\sin(h)/\cos(A)$

$Z = \text{asin}(\cos(\delta)\sin(h)/\cos(A)) + 90^\circ$

AZ = azimuth clockwise from south δ = declination

h = hour angle

A = altitude angle

This equation holds true as long as the sun does not cross the east-west line, or cos(h) > tan(δ)/tan(ϕ) where ϕ is latitude. When the sun does cross the line (as it does near the solstices in the far north and south), the equation for the azimuth is modified by pi: -π + |AZ| in the morning hours and π-AZ in the afternoon. This equation and modification are from Reference [5].

Base flux equation derivation

With the individual parts of the solar flux equation defined, we can look more closely at how they come together in the final equation $I = I_0 p^{1/\sin(A)} \sin(\theta)$.

I_0 = solar constant

p=transmission coefficient

L = effective length of the path through the atmosphere

p^L is the fraction of radiation able to pass through distance L of the atmosphere: over shorter distances, it will be larger.

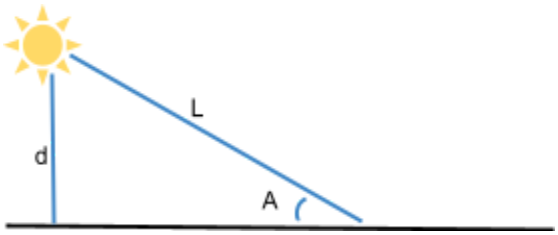

Neglecting atmospheric refraction, L is related to the altitude angle and the effective depth of the atmosphere (d). The effective depth has units of "unit atmosphere depths" with a value of 1. The equation for L is therefore approximately

$L = d/\sin(A) = 1/\sin(A)$

Substituting this into the basic expression above, we get

$I' = I_0 p^{1/\sin(A)}$

This equation must be further modified to account for the angle between the incident beams and the target surface. As previously shown, when rays are not orthogonal to the surface, their intensity is reduced. It is reduced as following:

$I = I' \cos(90-\theta) = I' \sin\theta$
I = Intensity indecent on a unit surface
I' = Intensity of rays when orthogonal to a surface θ = angle between the surface and the radiation
This is combined with the previous equation to get the final equation:
$I = I_0 p^{1/\sin(A)} \sin(\theta)$

Limitations

This calculation works best with direct solar rays; it does not accurately calculate surface solar flux due to reflected light. For example, twilight, when the sun is below the horizon but light is still reflected over the earth, is not well accounted for. In the calculator, it is assumed that the calculated transmission coefficient may help to account for some natural reflection from clouds and natural features. This results in some instances where the calculated transmission coefficient is greater than 1.

One part of the calculator's function not previously described here is determining declination based on the day of the year. This is assumed to be a steady oscillation between -23.45 and 23.45 over the year.

References for the solar flux calculator

[1] Equation derivation: Fons, W. L., H. D. Bruce, and Alan McMasters 1960. Tables for estimating direct beam solar irradiation on slopes at 30" to 46" latitude. USDA Forest Serv. Pac. Southwest Forest & Range Exp. Stn., 298 p. Berkeley, Calif. https://archive.org/details/CAT10664076/page/4/mode/2up

[2] Black body solar radiation: https://www.acs.org/content/acs/en/climatescience/energybalance/energyfromsun.html

[3] "Direct Solar Radiation on Various Slopes from 0 to 60 Degrees North Latitude." https://www.fs.fed.us/pnw/pubs/pnw_rp142.pdf

[4] Tuning Data https://wcc.sc.egov.usda.gov/nwcc/site?sitenum=1177

[5] Azimuth angle, Soteris A. Kalogirou, in Solar Energy Engineering (Second Edition), 2014, https://www.sciencedirect.com/topics/engineering/solar-azimuth-angle

This page intentionally left blank

U.S. Department of the Interior (DOI)
DOI protects and manages the Nation's natural resources and cultural heritage; provides scientific and other information about those resources; and honors the Nation's trust responsibilities or special commitments to American Indians, Alaska Natives, and affiliated island communities.

Bureau of Ocean Energy Management (BOEM)
BOEM's mission is to manage development of U.S. Outer Continental Shelf energy and mineral resources in an environmentally and economically responsible way.

BOEM Environmental Studies Program
The mission of the Environmental Studies Program is to provide the information needed to predict, assess, and manage impacts from offshore energy and marine mineral exploration, development, and production activities on human, marine, and coastal environments. The proposal, selection, research, review, collaboration, production, and dissemination of each of BOEM's Environmental Studies follows the DOI Code of Scientific and Scholarly Conduct, in support of a culture of scientific and professional integrity, as set out in the DOI Departmental Manual (305 DM 3).